

이학박사학위논문

Study of Multi-Nucleon Transfer Reaction of  
 $^{136}\text{Xe} + ^{198}\text{Pt}$  Above the Coulomb Barrier

쿨롱 장벽 위에서  $^{136}\text{Xe} + ^{198}\text{Pt}$ 의  
다중 핵 전달 반응의 연구

2015 년 8 월

서울대학교 대학원

물리 천문 학부

김 용 희

# Abstract

The neutron-rich isotopes far from stability, around the mass number  $A \sim 200$  forms the last waiting point of the r-process towards the synthesis of uranium. But, the difficulty of producing such nuclei with conventional methods, limited the current knowledge of such nuclides (e.g. half-life, mass, etc.) to the region close to the valley of stability. The multi-nucleon transfer (MNT) reaction recently attracts much attentions as the candidate to produce nuclides in this neutron-rich region. The MNT reactions with the combination of heavy neutron-rich projectile, such as  $^{136}\text{Xe}$  with target nucleus (e.g.  $^{208}\text{Pb}$  or  $^{198}\text{Pt}$ ) is anticipated to have large cross sections for the producing neutron-rich target-like fragments (TLF's) [9, 14, 26]. However, the MNT reactions in such heavy systems have not been studied well.

We performed an experiment using  $^{136}\text{Xe} + ^{198}\text{Pt}$  system with the beam energy 8MeV/u ( $\sim 55\%$  above the Coulomb barrier). The large acceptance VAMOS++ spectrometer [83] and the EXOGAM Ge-detector array [96] at GANIL were used. First, to investigate the feasibility of the MNT reaction for producing neutron-rich exotic nuclei. Second, to study reaction mechanism between heavy neutron-rich beam, and target with similar N/Z ratio.

The event-by-event particle identification of projectile-like fragments (PLF's)

were successfully carried out [119]. The cross sections of PLF, and TLF (calculated from information of PLF) will be presented, comparison with the GRAZING code [20] and TDHF [35] calculation. The evolution of reaction concerning nucleon transfer by moment analysis of correlation between mass and atomic number distribution(e.g. mean, width, and correlation of atomic number/mass distribution) will be discussed.

This experimental result confirmed the MNT reaction between  $^{136}\text{Xe} + ^{198}\text{Pt}$  above the Coulomb barrier can produce neutron rich nuclides with  $N = 126$  magic number for the first time. And observed neutron rich nuclides are produced from reaction with low excitation energy before N/Z-equilibrium is reached.

This result will offer new possiblity to explore astronomically and nuclear physically important new territory of nuclear chart. And encourage new facilities that use MNT reactions for producing new isotope beam.

**Keywords:** Multi-nucleon transfer reaction, reaction between heavy ions, reaction mechanism,r-process, neutron magic number  $N = 126$ ,  $^{136}\text{Xe}$ ,  $^{198}\text{Pt}$ , cross section measurement, N/Z equilibrium

*Student Number:* **2009-20404**

# Contents

<b>1</b>	<b>Introduction</b>	<b>1</b>
1.1	Motivation of the experiment . . . . .	1
1.2	Production of N~126 nuclides . . . . .	4
1.3	Previous studies of reaction mechanism:Reaction mechanism of MNT reaction . . . . .	13
1.4	Perspective of this experiment . . . . .	24
<b>2</b>	<b>Theory of Multi-nucleon Transfer Reaction</b>	<b>25</b>
2.1	Characteristics of Multi-nucleon Transfer Rection . . . . .	25
2.1.1	Partial statistical equilibrium (Q-value dependence) . . . . .	25
2.1.2	N/Z equilibrium . . . . .	31
2.2	Reaction kinematics . . . . .	36
2.3	Quasi-elastic and Deep Inelastic Reaction . . . . .	40
2.3.1	Deep inelastic collision (D.I.C.) . . . . .	41
2.4	Unified models MNT reactions . . . . .	45
2.4.1	Grazing model . . . . .	45
2.4.2	Time dependent Hartree Fork (TDHF) theory . . . . .	48

## *CONTENTS*

<b>3 Experimental Setup</b>	<b>56</b>
3.1 Accelerator Facility . . . . .	56
3.2 Beam target combination consideration . . . . .	58
3.2.1 Beam and target nuclei . . . . .	58
3.2.2 Beam energy . . . . .	58
3.2.3 Spectrometer angle . . . . .	60
3.2.4 Target thickness . . . . .	60
3.2.5 $B\rho$ of spectrometer . . . . .	61
3.2.6 Beam time . . . . .	65
3.3 VAMOS++ septicrometer . . . . .	65
3.3.1 Electro-Magmentic elements of VAMOS++ . . . . .	66
3.3.2 Detectors of VAMOS++ . . . . .	66
3.3.3 Event Reconstruction . . . . .	79
3.4 EXOGAM Ge-clover Array . . . . .	81
3.4.1 Electric circuit and trigger system . . . . .	86
3.5 Tandem experimental result . . . . .	95
<b>4 Presorted Experimental Data: Calibration, PID, and Corrections</b>	<b>100</b>
4.1 Calibration . . . . .	100
4.1.1 Multi-wire parallel plate avalanche counter calibration . . . . .	100
4.1.2 Drift chamber calibration . . . . .	103
4.1.3 Si, IC energy calibration . . . . .	105
4.1.4 Ge detector . . . . .	110
4.1.5 Timing calibration . . . . .	110
4.2 Particle Identification . . . . .	118

## CONTENTS

4.2.1	Total Energy Calibration and Charge state identification . . . . .	118
4.2.2	Mass number identification . . . . .	127
4.2.3	Atomic number identification . . . . .	130
4.3	Spectrometer Detection Efficiency . . . . .	134
4.3.1	Simulation . . . . .	134
4.3.2	Beam position uncertainty . . . . .	138
4.3.3	Detection efficiency correction using charge state . . . . .	144
4.3.4	Restoration of events out side of the acceptance . . . . .	154
<b>5</b>	<b>Analyzed Results and Discussion</b>	<b>165</b>
5.1	Elastic Scattering . . . . .	165
5.1.1	Selection of elastic scattering channel from $^{136}\text{Xe}$ . . . . .	166
5.1.2	Conversion factor calculation . . . . .	169
5.1.3	Optical potential fitting . . . . .	170
5.1.4	Comparison with tandem experiment . . . . .	172
5.2	Cross section of projectile-like fragments . . . . .	172
5.3	Decomposition of Q.E. and D.I.C. . . . .	177
5.3.1	Different factors of nucleon transfer dependency in Q.E. and D.I.C. . . . .	178
5.4	Reaction kinematics of PLFs . . . . .	183
5.4.1	Wilczynski plot . . . . .	183
5.4.2	n,p-transfer dependence of Wilzynski plot . . . . .	186
5.5	pre-evaporation fragment and Excitation Energy Determination . . . . .	191
5.5.1	Iteration method . . . . .	196
5.5.2	Resolution of the $E_{total}^*$ calculation . . . . .	203

## CONTENTS

5.5.3	Limit of the $E_{total}^*$ calculation . . . . .	203
5.5.4	Pre-evaporated fragment cross section . . . . .	205
5.5.5	Pre-evaporation fragment cross section $E_{total}^* < 100\text{MeV}$ . . .	210
5.6	Evolution of Reaction as Function of $E_{total}^*$ . . . . .	213
5.6.1	$\langle M \rangle$ , $\langle Z \rangle$ and $\langle N \rangle$ of the distribution . . . . .	213
5.6.2	$\langle M(E_{TOT}^*, Z) \rangle$ distance from N/Z equilibrium mass . . .	218
5.6.3	Variance of proton, neutron distribution . . . . .	222
5.6.4	Correlation of proton and neutron transfer . . . . .	228
5.7	TLF cross section and feasibility of n-rich nuclides . . . . .	229
5.7.1	TLF cross section after evaporation . . . . .	230
5.7.2	Evolution of TLF as function of excitation energy . . . . .	236
5.7.3	TLF PID confirmation . . . . .	236
5.7.4	Feasibility of producing n-rich TLF . . . . .	242
5.7.5	The kinematics of the TLF . . . . .	244
<b>6</b>	<b>Conclusions</b>	<b>250</b>

# List of Figures

1.1	The schematic picture of MNT reaction. The nucleons are exchanged during projectile collides with the target. Meanwhile the kinetic energy is converted to internal excitation energy during the collision. After separation of projectile-like fragment (PLF) and target-like fragment (TLF), the excitation energy is consumed by secondary processes (dominated by light particle emission). The reaction fragments after the secondary process is detected. . . . .	3
1.2	The table of nuclides with r-process path.[126] The sudden change of path near $N \sim 126$ can be observed, which is responsible for $A \sim 200$ peak in abundance distribution. . . . .	5
1.3	The production cross section of fragmentation reaction products of $^{208}\text{Pb}$ beam with energy of 1 GeV/u impinging on $^8\text{Be}$ target. . . . .	6
1.4	The calculated production cross section(arb. unit) of MNT reaction of $^{154}\text{Xe}(\text{top}), ^{136}\text{Xe}(\text{middle}), ^{118}\text{Xe}(\text{bottom}) + ^{208}\text{Pb}$ at $E_{CM}=700$ MeV.	8

## LIST OF FIGURES

1.5 (top left) The pre-evaporation fragment(before evaporation) distribution of target-like fragments. (top right) Cross section of N = 126 nuclides from calculation after evaporation, compared with fragmentation of $^{208}\text{Pb}$ . (bottom left) cross section of Pt isotopes of different incident energy. . . . .	10
1.6 The GRAZING code [20] calculated cross section of N=126 isotones from $^{136}\text{Xe} + ^{198}\text{Pt}$ MNT reaction with different beam energy. . . .	12
1.7 The cross sections of $^{136}\text{Xe} + ^{208}\text{Pb}$ at energy of $E_{CM}=450\text{MeV}$ of N=126. (Black square) experimental result, (red dashed line)Langevin equation calculation, (black solid line) GRAZING code [20] calculation, ( blue dotted line) $^{64}\text{Ni} + ^{208}\text{Pb}$ experimental result . . . . .	14
1.8 (left)The atomic number distribution of $^{136}\text{Xe} + ^{209}\text{Bi}$ at energy of $E_{Beam}=940\text{MeV}$ with different total kinetic energy of 26 MeV wide bin. (right) The angular distribution with different total kinetic energy of same reaction. . . . .	16
1.9 The mass vs atomic number distribution of $^{64}\text{Ni} + ^{238}\text{U}$ with $E_{Beam} = 390\text{MeV}$ (6.10 MeV/u). . . . .	17
1.10 Mass distribution of $^{136}\text{Xe} + ^{208}\text{Pb}$ with (top) $E_{CM} = 617\text{MeV}$ ( $E_{Beam} = 1020\text{MeV}$ ), (bottom) $E_{CM} = 526\text{MeV}$ ( $E_{Beam} = 870\text{MeV}$ ) of different total kinetic energy loss. [49] . . . . .	18
1.11 Most probable N/Z ratio of $^{129}\text{Xe}, ^{132}\text{Xe}, ^{136}\text{Xe} + ^{197}\text{Au}$ for different atomic number. $^{129}\text{Xe}, ^{132}\text{Xe}, ^{136}\text{Xe}$ are indicated with circle, black square, black dot respectively. The typical error bars are presented (Z ~ 56, 65, 75 and 79). . . . .	20

## LIST OF FIGURES

1.12 The target-like fragments identified by gamma-rays produced from $^{136}\text{Xe} + ^{198}\text{Pt}$ $E_{beam}=850$ MeV. [41] . . . . .	21
1.13 The mass vs atomic number distribution of PLFs from $^{144}\text{Sm} + ^{208}\text{Pb}$ with $E_{beam} = 5.8$ MeV/u reaction. . . . .	23
2.1 The cross section vs Q value of reaction between $^{22}\text{Ne} + ^{222}\text{Th}$ at energy of $E_{Beam}=174$ MeV. . . . .	26
2.2 (left)Ground-to-ground state Q-value distribution of this experiment. (right) Effective Q-value calculated from V. V. Volkov's formula. . .	29
2.3 The mean isotope ( $\langle Z \rangle, \langle A \rangle$ ) as fuction of total excitation energy, with calculated potential energy surface(1MeV spaced).The crosses conneted with solid line represents mean isotope ( $\langle Z \rangle, \langle A \rangle$ ) without considering neutron evaporation. The black dot conneted with dashed line represents mean isotope ( $\langle Z \rangle, \langle A \rangle$ ) considering neutron evaporation. . . . .	32
2.4 The (top) $^{144}\text{Sm} + ^{144}\text{Sm}$ and (bottom) $^{154}\text{Sm} + ^{154}\text{Sm}$ at energy of mean mass( $\langle A \rangle$ ) as fuction of atomic number(black dot) with potential energy surface(indicated as contour) and N/Z ratio(scatterd line).[72] . . . . .	35
2.5 Wilczynski plot(TKE(assuming two body kinematics) vs $\theta_{CM}$ ) of $^{136}\text{Xe} + ^{209}\text{Bi}$ with $E_{beam}=1130$ MeV.[55] . . . . .	37

## LIST OF FIGURES

2.6	The calculated potential energy between $^{136}\text{Xe} + ^{209}\text{Bi}$ [3]with $E_{beam}=1130$ MeV assuming classical trajectory with spherical nuclei. (left) Potential energy as function of distance between two nuclei for different incident angular momentum. (right) Correlation of incident angular momentum and deflection angle. . . . .	38
2.7	The total kinetic energy (assuming two body kinematics) vs atomic number distribution of $^{136}\text{Xe} + ^{209}\text{Bi}$ at energy $E_{Beam}=1422$ MeV .	39
2.8	(right)Flow of reaction chart showing classification of the diffent reaction change as reaction evolves and the characteristics of reaction from [3]. (left) Reaction mechanism change as function of angular momentum(i.e. impact parameter) using sharp cutoff model. . . . .	40
2.9	(left)Angular,(middle) energy-loss and (right)charge distributions of the Xe-like fragments obtained in the $^{136}\text{Xe}+^{209}\text{Bi}$ reaction at $E_{CM} = 568$ MeV. The experimental result[58] are presented with circle while the result from the theory[28] is represented with solid line. . . . .	44
2.10	Total cross sections of pure proton stripping (left frames)pure neutron and pick-up (right frames) channels for the $^{40}\text{Ca} + ^{208}\text{Pb}$ and $^{58}\text{Ni} + ^{208}\text{Pb}$ systems. The Complex WKB(CWKB) model calculations with take into account the effect of the evaporation, (dashed lines) results of calculations with only independent particle transfers,(full lines) including a pair transfer mode for both neutrons and protons . . . . .	46

## *LIST OF FIGURES*

2.11 (top) Cross section of $^{64}\text{Ni} + ^{238}\text{U}$ of $-6\text{p} \sim +2\text{p}$ channel, compared with GRAZING calculation.(bottom) Cross section of $^{58}\text{Ni} + ^{208}\text{Pb}$ of $-6\text{p} \sim 0\text{p}$ channel, compared with GRAZING calculation. The under estimation can be observed in proton pickup channels and proton stripping channels with number of proton stripping $> 3$ . . . . .	49
2.12 The cross section of $^{58}\text{Ni} + ^{208}\text{Pb}$ (red solid line) TDHF calculation result compared with (red circle) experimental result. . . . .	55
3.1 Accelerator facility at GANIL. C01 and C02 are the injector cyclotrons. CSS1 and CSS2 are the separated $K = 380$ cyclotrons. TIS is the ISOL target for SPIRAL. CIME is the $K = 265$ cyclotron for the radioactive beam. The RIBs are delivered after selection by the $\alpha$ -shaped spectrometer. . . . .	57
3.2 Bragg curve of selected isotopes. The isotope with larger proton number shows larger energy loss with same incident energy. The energy difference between different channels becomes less than 0.3 MeV for $E < 400$ MeV. . . . .	59

## *LIST OF FIGURES*

3.3	Simulation result of $^{134}\text{Ce} + ^{200}\text{W}$ for efficiency estimation with beam energy 7MeV/u. (top leftmost) Angular distribution of produced event and detected events. (top, second from left) Detection efficiency of $^{134}\text{Ce}$ correlated to angle. (top, third from left/rightmost) Mass/proton number of fragment( $=^{134}\text{Ce}$ ). (bottom, leftmost) Accepted angular distribution(magnification from top leftmost figure). (bottom, second from left) Charge state distribution of produced event and detected events. (bottom, third from left) Fragment kinetic energy correlated with angle. (bottom, rightmost) Accepted charge state distribution (magnification from top leftmost figure). . . . .	62
3.4	Magnetic rigidity in T·m (middle row) and detection efficiency (bottom row) for proton pickup channels of PLFs produced by MNT reactions of $^{136}\text{Xe}+^{198}\text{Pt}$ at the incident energy of 7 MeV/u. For the $^{136}\text{Xe}$ scattering, the elastic cross section accepted by the VAMOS is shown, which imposes a limit to the projectile beam intensity. The hatched area covers PLFs to be detected with good statistics within the proposed beam time. [121] . . . . .	63
3.5	The setup of VAMOS spectrometer. Incoming beam direction is indicated as an arrow at the left side. The reaction fragments pass through electro-magnetic component consist of two quadrupoles, Wien filter ,and dipoles. Then detected by MWPPAC, two set of drift chambers, three sets of ionization chamber. and Si detector wall. The angle between electro-magnetic component axis and axis perpendicular to the detector face was $45^\circ$ . . . . .	67

## *LIST OF FIGURES*

3.6 Schematic view of detector set of VAMOS near focal plane.The projectile from the reaction passes two PPACs near the target and near the focal plane detects the ToF. After the PPAC, the two sets of drift chamber detects position and angle of incident particle. Then the projectile travels and stops inside the series of ionization chamber, and Si detector to measure energy. [83] . . . . .	69
3.7 Schematic of multi-wire parallel plate avalanche chamber(MWPPAC) at focal plane. . . . .	72
3.8 (right) Side view of drift chamber structure. Drift region, and amplification region is separated by Frisch grid can be seen.(left) Pad design of drift chamber for horizontal (X) position measurement. Two rows of pads are shifted to each other by half pad size. . . . .	73
3.9 Schematic for demonstration of working principle of the drift chamber. Incident projectile passing through drift region creates ion pair. Electrons from ion pair travel through field inside drift region with constant speed. Then electrons are accelerated after Frisch grid and creates avalanche near the amplification wire inducing charge signal at the segmented pads. The drift time inside drift region is measured for position in vertical axis (Y), and charge induced in segmented pads decides horizontal position(X). . . . .	74

## LIST OF FIGURES

3.10 Schematic view showing working principle of ionization chamber. The energetic charged particle passes through gas,ion pair created proportional to the energy loss inside the gas. electrons are drifed inside drift region then accelerated in series by electric field from Frisch grid and acceleration grid. Finally electrons are collected at the pads. [83] . . . . .	76
3.11 Si detector configuration inside the VAMOS spectrometer . . . . .	78
3.12 Flow chart showing reconstruction procedure . . . . .	80
3.13 Correlation between generated event and analysed result using simplified database ( $B\rho$ , $\theta$ ) and fitting ( $\phi$ ). (top left) Correlation between generated $B\rho$ and analysed $B\rho$ typical width was $\Delta B\rho=4.5\times10^{-3}$ T·m (FWHM).The red dashed line is $Y=X$ . (top right) Correlation between generated $\theta$ and analysed $\theta$ typical width was $\Delta\theta=0.15^\circ$ (FWHM).(bottom left) Correlation between generated $\phi$ and analysed $\phi$ typical width was $\Delta\phi = 0.35^\circ$ (FWHM). . . . .	82
3.14 Clover crystal structure inside the EXOGAM Ge-clover detector.Set of 4 crystal consist one Ge-detector, each crystal has 4 electrode segments.(left figure) Side-view of crystal.(right figure)front view of Crystal. [96] . . . . .	83
3.15 EXOGAM surrounding target chamber.Total seven Ge-clover detector near $90^\circ$ can be seen . . . . .	84
3.16 The Compton shielding of EXOGAM Ge-clover detector.Side ,and rear side shielding of the detector was made by BGO crystal which have large stopping power. While back catcher is made of CsI crystal(lower stopping power than CsI) which have larger space is available.[97]	85

## *LIST OF FIGURES*

3.17 The electric circuit of two set of MWPPACs . . . . .	89
3.18 The electric circuit of two set of MWPPACs to the TDC and Scaler	89
3.19 The electric circuit of ionization chamber(top), and Si detector (bottom)	90
3.20 The electric circuit of drift chamber . . . . .	91
3.21 The electric circuit of EXOGAM . . . . .	92
3.22 The electric circuit of trigger system . . . . .	93
3.23 The electric system of scyncronization of different detector system .	94
3.24 The setup of Tandem experiment. The $^{198}\text{Pt}$ target with $1.6 \text{ mg}/\text{cm}^2$ is placed at the center. Two set of detectors with consist of SSSD sandwiched with SSD was placed at $30\sim50^\circ$ ( $6.0\sim7.0 \text{ MeV/u}$ )/ $20\sim40^\circ$ ( $7.5\sim8.0 \text{ MeV/u}$ ) and $50\sim70^\circ$ . Two Si detectors for monitoring elastic scattering was placed at $\pm20^\circ$ . Faraday cup was placed at $0^\circ$ deg to monitor the beam current. . . . .	96
3.25 The angular distribution of elastic scattering channels with different beam energy. Angular distribution was normalized by Rutherford scattering at the $20^\circ$ counts. Sudden decrease of cross section at the grazing angle can be observed. . . . .	97
3.26 (left)dE-E distribution of one segment( $\sim24^\circ$ ) in SSSD placed at $40^\circ$ . (right)The energy distribution of Xe channels. The elastic scattering was decomposed from the rest of the reaction fragments by Gaussian fitting to the elastic channel and reaction channels. Both figures the beam energy was $8 \text{ MeV/u}$ . . . . .	98

## *LIST OF FIGURES*

4.1 Time of flight calibration between two MWPPAC at focal plane and target using elastic scattered $^{136}\text{Xe}$ near $0^\circ$ . Different channels from 4 <sup>th</sup> (top leftmost) 15 <sup>th</sup> (bottom rightmost) is shown . . . . .	101
4.2 The correlation between energy deposit in Si (channel 7) and time of flight between two MWPPAC at focal plane and target. The fast timing event from MWPPAC showed similar energy distribution as the normal events indicating the false timing. . . . .	102
4.3 The correlation between time of flight between MWPPAC at focal plane and target and time of flight between MWPPAC at target and Si. the parallel transition shows that the timing in MWPPAC at the target had problem . . . . .	103
4.4 The drift chamber using pulser signal before calibration. The pulser with different signal height was used for better resolution. . . . .	104
4.5 The hit position at the focal plane (30 mm in-front of MWPPAC at focal plane). The clear vertical shadows from the supporting pole inside the MWPPAC, and vertical/horizontal shadows from the field wires between exit of MWPPAC and entrance of drift chamber can be observed. . . . .	106
4.6 The hit position at the Si plane. The clear vertical shadows from the gap between different Si detector can be seen. The blank region in the left lower side is due to broken Si detector. . . . .	107

## *LIST OF FIGURES*

4.7 The ionization chamber(IC) energy peak from elastic scattering as function of run number. The unstalbe gain in the channel 2 can be seen, the other channels showed very small fluctuation order of few MeV. The gain was corrected run by run using the fitting result . . .	108
4.8 The Si detector energy peak(except for Si detector channel :15~24 which used mean of energy distribution) from elastic scattering as function of run number. The sudden change in the gain for different Si detectors can be observed.The instability of Si detectors in low $B\rho$ regions (Si detector channel: 15~24) due to absent of elastic peak. . .	109
4.9 The timing of gamma-ray considering time of flight of PLF. The major peak from in beam gamma-ray events. The small peaks due to off coincident event with same period of RF signal from cyclotron . . .	111
4.10 The energy dependence of timing in different Ge clover detectors. (top) timing dependence of energy of Clover detector 1 which shows almost no dependence. And (bottom) Clover detector 5 which shows $\sim 1$ ns decrease in timing from 1000keV to 0keV . . . . .	112
4.11 The energy dependence of timing in different Ge clover detectors. (top) timing dependence of energy of Clover detector 1 which shows almost no dependence. And (bottom) Clover detector 5 which shows $\sim 1$ ns decrese in timing from 1000keV to 0keV . . . . .	115
4.12 The energy of gamma-ray Doppler corrected for projectile-like fragment with angular distribution $10^\circ$ cut from (top left) $70\sim80^\circ$ to (bottom right) $140\sim150^\circ$ . . . . .	116

## LIST OF FIGURES

4.13 The graph of angular dependence of energy resolution $\sigma$ ) of gamma-ray peak 1313keV of $^{136}\text{Xe}$ , Doppler corrected for projectile-like fragment . The graph was fitted with formula 4.9 . . . . .	117
4.14 The flow chart of particle identification process. Each parameters were divided in to two by resolution (detection, requirement). The energy detected by Si and IC had low resolution, while time of flight, $B\rho$ , and travel length from reconstruction had high resolution. While the particle identification parameters charge state and atomic number which is integer value required low resolution, while the energy and mass needs good resolution. The detected parameters were combined to produce PID parameters to satisfy the required resolution . . . . .	119
4.15 The total energy calibration using charge state distribution of events hitting Si detector channel 17. (top left) The correlation of charge state and $\frac{M}{Q}$ from rough calibrated energy, the charge states dependence can be seen. The events selected by two dimensional cuts, which have clear charge states were used for fitting. (top right) The same histogram with applying fitting result using equation 4.12. (bottom left) The additional correction using equation 4.14. . . . .	121
4.16 (left) Field leak of IC near the cathode. (right) Field leak of IC between Frisch grid, Amplification grid, and anode. The field leak in each regions showed different pattern. . . . .	123
4.17 The correlation between charge state and X hit position at the exit position of IC. The sudden decrease in charge state at the edge of the IC chamber exit can be observed . . . . .	124

## LIST OF FIGURES

4.18 The correlation between charge state and Y hit position at the exit position of IC for typical Si detector(channel 17, 22) events before and after position dependence correction. (top left) Si detector channel :17 events before correction,overall tilt in the charge state and sudden change at the edge can be seen (top right) Si detector channel :17 after correction. (bottom left) Si detector channnel : 22 before correction, gradual decrease in the charge state can be seen due to different field leak pattern. (bottom right) Si detector channel : 22 after correction.	125
4.19 (top)The correlation of charge state and $\frac{M}{Q}$ for all events.(Bottom) Charge state distribution fitted with multiple Gaussian function, resolution of $\frac{\Delta Q}{Q} = \frac{1}{77}$ (FWHM) was achived after all corrections. . . . .	126
4.20 The correlation of charge state and $\frac{M}{Q}$ in Si detector channel 7. Right above elastic peak smaller peak can be seen. . . . .	128
4.21 The correlation of charge state and Mass of Xe channels in Si detector channel 7.(right) Distribution before correction, the mis-identification of charge state of blob events (can be seen 2~4 neutron pickup channels)results mass dependence of charge state(red dotted line). The two dimensional cut for selecting blob events are shown as box. (left)The distribution after correction blob events by correcting charge state by -1. . . . .	129
4.22 (left)Mass distribution of Si detector channel 11, with charge state 38 before fine calibration of time of flight. (right) Mass distribution after the fine calibration. The after the mass was aligned at the integer value	130

## LIST OF FIGURES

4.23 Mass distribution including all events. The mass peak are aligned at the integer indicating successful mass calibration. The distribution was fitted with multiple Gaussian function. The resolution from the fitting result was $\frac{\Delta M}{M} = \frac{1}{203}(FWHM)$ . . . . .	131
4.24 The correlation of dE and E. The each atomic numbers can be identified by curved bands. . . . .	132
4.25 The two dimensional histogram of atomic number vs E. The each atomic numbers can be identified as parallel lines. . . . .	133
4.26 The energy sliced atomic number distribution. The each atomic numbers can be identified using fitting using multi Gaussian function. The width of fitting function was limited to the same value for all histograms with the resolution $\frac{\Delta Z}{Z} = \frac{1}{60}$ . . . . .	135
4.27 The correlation between atomic number and E with two dimensional cut based on the fitting result from energy sliced atomic number distribution. . . . .	136
4.28 (top) The two dimensional histogram $B\rho$ vs $\theta$ (LAB frame) of generated events. Isotropic distribution of $\theta$ , and uniform distribution of $B\rho$ can be seen. (bottom) The two dimensional histogram $B\rho$ vs $\theta$ (LAB frame) of accepted events of VAMOS. The shadows from supporting pole and missing Si detectors can be seen as curved bands. . . . .	137

## LIST OF FIGURES

4.29 The two dimensional histogram of detection efficiency ( $B\rho$ vs $\theta$ (LAB frame)) calculated by taking the ratio accepted events over generated events. The maximum acceptance shown as the curved band showed lowest $B\rho$ near the $30\sim 31^\circ$ at $\sim 1.05 \text{ T}\cdot\text{m}$ while angle at the side showed maximum acceptance at higher $B\rho \sim 1.18 \text{ T}\cdot\text{m}$ . . . . .	138
4.30 Correlation between generated event assuming beam position of $X = -2$ , $Y = -2 \text{ mm}$ at the target and analyzed result assuming beam position $X=0$ , $Y=0 \text{ mm}$ by simplified database( $B\rho$ , $\theta$ ) and fitting ( $\phi$ ). (top left) Correlation between generated $B\rho$ and analyzed $B\rho$ typical width was $\Delta B\rho = 7.0 \times 10^{-3} \text{ Tm}$ (FWHM).The red dashed line is $Y=X$ . (top right) Correlation between generated $\theta$ and analyzed $\theta$ typical width was $\Delta\theta=0.27^\circ$ (FWHM).(bottom left) Correlation between generated $\phi_{generated}$ and analyzed $\phi_{analyzed}$ typical width at the $\phi_{generated} = 0^\circ$ was $\Delta\phi_{analyzed} = 4.9^\circ$ (FWHM) . . . . .	140
4.31 The angular distribution of elastic scattering compared with Rutherford angular distribution(scaled to experimental distribution in forward angle of $24\sim 26^\circ$ ). . . . .	142
4.32 The two dimensional histogram of acceptance range ( $\theta$ vs $\phi$ (LAB frame)) of different $B\rho$ range.(top left) $B\rho=0.95\sim 1.05$ , (top right) $B\rho=1.05\sim 1.15$ , (bottom left) $B\rho=1.15\sim 1.25$ , (bottom right) $B\rho=1.25\sim 1.35 \text{ T}\cdot\text{m}$ . . . . .	143
4.33 The method for detection efficiency using typical case of $^{134}\text{Xe}$ with $\beta=0.1110$ at $30^\circ$ . (See the explanation in the text) . . . . .	147

## LIST OF FIGURES

4.34 (Not normalized) Detection efficiency using $^{134}\text{Xe}$ events with different velocity at $30^\circ$ compared with scaled detection efficiency. (See the explanation in the text) . . . . .	148
4.35 The normalization process of detection efficiency using typical case of $^{132}\text{Xe}$ at $30^\circ$ .(top left) the velocity distribution using simulated acceptance correction(red diamond) and empirically corrected velocity distribution(black square).(top right) The ratio between different corrections.(bottom) each correction factors from different velocities were normalized by ratio of velocity distribution. (see the explanation in the text) . . . . .	149
4.36 Averaged detection efficiency using $^{134}\text{Xe}$ events with different velocity at $30^\circ$ compared with (scaled) X-2Y-2 efficiency. (See the explanation in the text) . . . . .	150
4.37 (scaled) Averaged detection efficiency of various isotopes ( $^{134}\text{Xe}$ , $^{132}\text{Xe}$ , $^{132}\text{Cs}$ , $^{134}\text{Cs}$ , $^{130}\text{I}$ , $^{136}\text{Ba}$ , $^{134}\text{Ba}$ , $^{130}\text{Te}$ )compared with (scaled) X-2Y-2 efficiency . . . . .	151
4.38 Two dimensional histogram of detection efficiency averaging over many isotopes. . . . .	152
4.39 (top) (black square) calculated efficiency of $^{134}\text{Xe}$ at $\beta = 0.1075$ , $\theta = 27^\circ$ using the original formula from [103] and (red diamond) X-2Y-2 efficiency. (bottom) calculated efficiency by shifting which minimize the chi-square between X-2Y-2 efficiency and calculated efficiency. . . . .	155

## LIST OF FIGURES

- 4.40 The calculated charge state shift of  $^{134}\text{Xe}$  of different velocity and (even number) angles of 26~34 (shown in order from top left to bottom right) the error bars indicate the calculated chi-squares after minimization with the X-2Y-2 efficiency described in the text. The bottom left figure is the distribution of the charge state shift. . . . . 156
- 4.41 The averaged charge state shift of different isotopes indicated as the blue square ( $^{126,124}\text{Sb}$ ,  $^{130,128}\text{Te}$ ,  $^{130}\text{I}$ ,  $^{134,132}\text{Xe}$ ,  $^{134,132}\text{Cs}$ ,  $^{136,134}\text{Ba}$ ,  $^{138,136}\text{La}$ ,  $^{140,139}\text{Ce}$ ) with the linear fitting (red solid line). The error bars indicate the FWHM of the charge state shift distribution shown in the figure 4.40. . . . . 157
- 4.42 The ratio between charge state of  $^{136}\text{Xe}$  with  $\beta=0.107\sim0.108$  at different angle (left)using X-2Y-2 detection efficiency,(right)using averaged detection efficiency by charge states. The error bars include the statistical errors and the error from detection efficiency . . . . . 158
- 4.43 The ratio between charge state of  $^{136}\text{Xe}$  with  $\beta=0.113\sim0.114$  at different angle (left)using X-2Y-2 detection efficiency,(right)using averaged detection efficiency by charge states. . . . . 159
- 4.44 The charge state of  $^{133}\text{Ba}$  from  $\beta=0.089$ (top left) to  $\beta=0.094$ (bottom right). The width was fixed using theoretical value[103].The experimental value and Gaussian function showed good agreement within error bar. . . . . 161

## LIST OF FIGURES

4.45 The velocity distribution of $^{131}Ba$ from $\theta=24$ (top left) to $\theta=34$ (bottom right).The accepted yield are indicated as black square and yield including restored events are indicated as red diamond. The peak position and the yield of velocity changes, especially at the angle far from grazing angle. . . . .	162
4.46 The angular distribution of $^{131}Ba$ .The accepted yield are indicated as black square and yield including restored events are indicated as red diamond. . . . .	163
4.47 The two dimensional $B\rho$ vs $\theta$ distribution of $^{136}Xe$ . (top left) Accepted events inside detection efficiency using charge states.(top right) Restored events outside the acceptance.(bottom left)Combined distribution of accepted distribution and restored distribution. . . . .	164
5.1 The energy distribution of $^{136}Xe$ (from top left to bottom right) at even number angles of $\theta_{LAB} = 24, 26, 28, 30, 32$ , and $34$ deg, fitted with three Gaussian distributions representing elastic, quasi-elastic, and deep inelastic collision. . . . .	167
5.2 The energy distribution of $^{136}Xe$ (from top left to bottom right) even number angles of $\theta_{LAB} = 24, 26, 28, 30, 32$ , and $34$ deg, fitted with three Gaussian distribution representing elastic, quasi-elastic, deep inelastic collision. The width of the Gaussian function which represents elastic scattering, was fixed to the value from angle 24. . . . .	168
5.3 (black square) The angular distribution of elastic scattering component of $^{136}Xe$ and (red dashed line) Rutherford scattering angular distribution normalized to $\theta_{LAB}=24 \sim 27$ deg. . . . .	169

## *LIST OF FIGURES*

5.4 (black square) The angular distribution of elastic scattering component of $^{136}\text{Xe}$ normalized by Rutherford scattering and (red dashed line) optical potential fitting result by program PTOLEMY. . . . .	171
5.5 The angular distribution of elastic scattering (black square) and elastic and quasi elastic component (green square) of Xe normalized by Rutherford scattering and tandem experimental result (red circle). . .	173
5.6 The production cross section of projectile-like fragment from 0p to 2p transfer channels indicated as black square with GRAZING code calculation [20] indicated as red solid line. The Xe (top left), I (middle left), Cs (middle right), Te (bottom left), Ba (bottom right) isotopes are presented. The black dashed line indicates pure proton transfer channel (channel without neutron transfer) and blue dashed line indicates isotope with maximum cross section. . . . .	175
5.7 The production cross section of projectile-like fragment from 3p to 4p transfer channels. The Sb (top left), La (top right), Sn (bottom left), Ce (bottom right) isotopes are presented. The figures use same indication as the figure 5.6 . . . . .	176
5.8 The cross section of Cs ( $Z = 55$ ) fitted with two Gaussian distribution. The narrow distribution was assigned as a reaction from Q.E. and wider width was assigned as a reaction fragments from D.I.C. . . .	179
5.9 The result of decomposition of Q.E. and D.I.C. component of the cross section in proton transfer channels. The error bars indicate uncertainty of cross sections from the fitting errors. . . . .	180

## LIST OF FIGURES

5.10 The distance of mean mass number of Q.E. component from mass of largest ground-to-ground state Q-value and N/Z equilibrium (See table 2.1). . . . .	181
5.11 The distance of mean mass number of D.I.C. component from mass of largest ground-to-ground state Q-value and N/Z equilibrium (See table 2.1). . . . .	182
5.12 The Wilczynski plot of this system. drift to backward angle in TKEL<350 was due to the acceptance cut off of the spectrometer. . . . .	184
5.13 The Wilczynski plot (TKE (or E <sub>CM</sub> ) vs θ <sub>CM</sub> ) of typical cases of light projectile system ( <sup>40</sup> Ar + <sup>232</sup> Th = K + Ac [65]) (top) and very heavy projectile system ( <sup>208</sup> Pb + <sup>208</sup> Pb) [66] (bottom ). . . . .	185
5.14 The atomic number vs TKE distribution . The potential energy (V <sub>Interaction</sub> ) at the distance of the closest approach (red solid line) and fully damped energy calculated by Viola systematics [108] (blue dotted line) are indicated. . . . .	187
5.15 The mean position of <TKEL> and <θ <sub>CM</sub> > of proton stripping channels (left figure) and proton pickup channels (right figure). The isotope with even number of transferred neutrons are marked to indicate the position of different nuclides. . . . .	188
5.16 The FWHM of angular distribution of different proton transfer channels.	190
5.17 (right) Schematics of MNT reaction and secondary process. Evaporated light particles are indicated as an blue circle. (left) Schematics of kinematical calculation without correcting secondary process. . . .	192

## LIST OF FIGURES

5.18 (left) Experimental result of fusion evaporation of $^4\text{He} + ^{209}\text{Bi} \rightarrow ^{213}\text{At}$ $\rightarrow ^{213-x}\text{At} + \text{xn-evaporation}$ with PACE4 calculation. [114] (right) Experimental result of fusion evaporation of $^8\text{Be} + ^{124}\text{Sn} \rightarrow ^{132}\text{Xe}$ $\rightarrow ^{132-x}\text{Xe} + \text{xn-evaporation}$ and $^{126}\text{Te} + \alpha + 2\text{n-evaporation}$ with PACE4 calculation [115]. . . . .	196
5.19 (right) The PACE4 calculation of evaporation curve ( $E_{TOT}^*$ as an x-axis) of $^{136}\text{Xe}$ (mean mass after evaporation as function of excitation energy) which are indicated with black solid circle with 7th order polynomial fitting (solid line) (left) The ratio of $^{136}\text{Xe}$ evaporation channel without any particle evaporation (neutron evaporation only) from total cross section as function of excitation energy. . . . .	197
5.20 (left) The PACE4 calculation of evaporation curve of $^{193}\text{Os}$ (mean mass after evaporation as function of excitation energy) which are indicated with black solid circle with 7th order polynomial fitting (solid line) (right) The ratio of $^{193}\text{Os}$ evaporation channel without any particle evaporation (neutron evaporation only) to the total cross section as function of excitation energy. . . . .	198
5.21 Evaporation curve of $^{193}\text{Os}$ with one proton and multiple neutrons, (top left) mean mass , (top right) ratio to the total evaporation channels as function of excitation energy of TLF, with two proton and multiple neutrons, (bottom left) mean mass , (bottom right) ratio to the total evaporation channels as function of excitation energy of TLF.	199

## LIST OF FIGURES

5.22 Mass number of the nucleus after neutron evaporation from $^{136}\text{Xe}$ calculated by PACE4 (black solid circle) with 7th order polynomial fitting (black solid line) red/green solid circle indicate upper/lower limit deduced by adding/subtracting standard deviation of the mass distribution after evaporation with fitting result (solid line). . . . .	200
5.23 The flow chart describing the iteration method for correcting neutron evaporation and deducing excitation energy of the system. (See text for more detailed explanation) . . . . .	201
5.24 The charge state vs total exciation energy ( $E_{TOT}^*$ ) distribution of pre-evaporation fragment(left figure) $^{138}\text{Ba}$ , (right figure) $^{132}\text{Ba}$ . The cutoff below $E_{TOT}^* < 200$ MeV are indicated as a red triangle. The missing event in $^{132}\text{Ba}$ distribution at $E_{TOT}^* > 200$ MeV are due to the (integer) mass identification was not determined, isotopes in that mass range after evaporation (isotope with mass smaller than $^{126}\text{Ba}$ ) due to the small statistic. . . . .	204



## LIST OF FIGURES

5.27 The cross section of pre-evaporation fragments before secondary process with limit range of $E_{total}^* < 100$ MeV. The (top left) Xe ( $Z = 54$ ), (middle left) I ( $Z = 53$ ), (middle right) Cs ( $Z = 55$ ), (bottom left) Te ( $Z = 52$ ), (bottom right) Ba ( $Z = 56$ ) isotopes are presented. Experimental results are indicated as an black solid circle. The theoretical calculation of GRAZING are indicated as and red solid line. The black vertical dashed line indicates the pure proton transfer channel. The isotope with local Q-value maximum are indicated as red arrows, and global Q-value maximum (N/Z equilibrium) isotope are indicated as black arrows. . . . .	211
5.28 The cross section of pre-evaporation fragments before secondary process with limit range of $E_{total}^* < 100$ MeV. The (top left) Sb ( $Z = 51$ ), (top right) La ( $Z = 57$ ), (bottom left) Sn ( $Z = 50$ ), (bottom right) Ce ( $Z = 58$ ) isotopes are presented . The figure follows the same notation as figure 5.27. . . . .	212

## LIST OF FIGURES

5.29 The two dimensional pre-evaporation fragment cross section of atomic number versus mass number for different total excitation energy range ( $E_{total}^*$ ). (top left) $-10 < E_{total}^* < 10$ , (top middle) $10 < E_{total}^* < 30$ , (top right) $30 < E_{total}^* < 50$ , (bottom left) $50 < E_{total}^* < 70$ , (top middle) $70 < E_{total}^* < 90$ , and (top right) $90 < E_{total}^* < 110$ . The range of cross section in the top row was matched from $0.05 < \sigma < 1000$ mb, while the bottom row the range of cross section was matched from $0.05 < \sigma < 100$ mb. The red dashed line indicates N/Z equilibrium mass and magenta dashed line indicates isotope with largest Q-value (Mgg)	214
5.30 The two dimensional pre-evaporation fragment cross section of atomic number versus mass number for different total excitation energy range ( $E_{total}^*$ ). (top left) $110 < E_{total}^* < 130$ , (top middle) $130 < E_{total}^* < 150$ , (top right) $150 < E_{total}^* < 170$ , (bottom left) $170 < E_{total}^* < 190$ , (top middle) $190 < E_{total}^* < 210$ , and (top right) $210 < E_{total}^* < 230$ . The the range of cross section was matched from $0.05 < \sigma < 100$ mb. The red dashed line indicates N/Z equilibrium mass and magenta dashed line indicates isotope with largest Q-value (Mgg)	215
5.31 The mean of atomic number distribution as function of $E_{TOT}^*$ with 20 MeV bin.	216
5.32 The mean of neutron number distribution as function of $E_{TOT}^*$ with 20 MeV bin.	217

## LIST OF FIGURES

5.33 The TDHF calculated mean of (left) neutron number distribution (right) proton number distribution as function of closest distance approach. The black dashed line indicates the closest distance approach corresponds to the $E_{TOT}^* < 200$ MeV. . . . .	218
5.34 The distance of mean of mass distribution of different isotopic channels from N/Z equilibrium mass as function of $E_{TOT}^*$ . . . . .	219
5.35 The effective Q-value distribution of (top) Ce (Z = 58) , (bottom) Sn (Z = 50). The vertical dashed line indicates the pure proton transfer channel, black arrow indicates the mass of global maximum effective Q-value, red arrow indicates the mass of local maximum of effective Q-value. . . . .	221
5.36 The variance of (red diamond) atomic number, (black square) mass, (blue triangle) neutron number as function of excitation energy. . . .	223
5.37 The atomic number variance as function of normalized total kinetic energy over grazing angular momentum compared with vast number of references[60] and reference therein. The green line indicates the exponential fitting of different references, while the red line indicates the exponential function fitting result of this experiment. . . . .	224
5.38 The ratio variance of mass number over atomic number as function of excitation energy indicated as a black square. The yellow dashed line indicates $A/Z$ , and the red dashed line indicates $(A/Z)^2$ of compound system. . . . .	226
5.39 The correlation coefficient of neutron and proton variance as function of excitation energy. . . . .	228

## LIST OF FIGURES

5.40 The two dimensional TLF cross section of atomic number versus mass number with limit of $E_{total}^* < 200$ MeV. The range of cross section was matched from $0.05 < \sigma < 1000$ mb. . . . .	231
5.41 The two dimensional TLF cross section of atomic number versus mass number with no limit of $E_{total}^*$ . The range of cross section was matched from $0.05 < \sigma < 1000$ mb. . . . .	231
5.42 The one dimensional cross section of TLF of (top left) Pt (0p), (middle left) Au (-1p), (middle right) Ir (+1p), (bottom left) Hg (-2p), and (bottom right) Os (-2p) without cutoff or restoration. The proton transfer channel without neutron transfer are indicated as a black dashed line. The isotope with $N = 126$ are indicated with blue dashed line. And the most neutron richest isotope ever produced are indicated as a green dashed line. . . . .	233
5.43 The one dimensional cross section of TLF of (top left) Tl (-3p), (top right) Re (+3p), (bottom left) Pb (-4p), and (bottom right) W (-4p) without cutoff or restoration. The isotope with $N=126$ are indicated with blue dashed line. And the most neutron richest isotope ever produced are indicated as a green dashed line. . . . .	234
5.44 The different causes of errors of (top left) statistical, (top right) detection efficiency (middle left) conversion factor, (middle right) atomic number PID, (bottom left) secondary process, and (bottom left) sum of all errors in unit of %. . . . .	235

## LIST OF FIGURES

- 5.45 The one dimensional cross section of TLF of (top left) Pt (0p), (middle left) Au (-1p), (middle right) Ir (+1p), (bottom left) Hg (-2p), and (bottom right) Os (-2p) without cutoff or restoration. For each figures, cross section with different excitation energy range are indicated with (black solid circle) Sum of all cross section, (red square)  $-25 < E_{total}^* < 25$  (green triangle)  $25 < E_{total}^* < 75$  MeV, (blue inverted triangle)  $75 < E_{total}^* < 125$ , (magenta empty circle )  $125 < E_{total}^* < 175$  MeV, (skyblue empty square)  $175 < E_{total}^* < 225$  MeV, (forest green empty triangle)  $225 < E_{total}^* < 275$  MeV. The proton transfer channel without neutron transfer are indicated as a black dashed line. The isotope with  $N = 126$  are indicated with blue dashed line. And the most neutron richest isotope ever produced are indicated as a green dashed line. . . . . 237
- 5.46 The one dimensional cross section of TLF of (top left) Tl (-3p), (top right) Re (+3p), (bottom left) Pb (-4p), and (bottom right) W (-4p) without cutoff or restoration. The maker and lines follow same notation as figure 5.45. . . . . 238
- 5.47 (top left) level diagram of  $^{196}\text{Os}$  [123]. (top)  $\gamma$ -ray energy distribution gated on  $^{138}\text{Ba}$  in  $-40 < \text{TKEL} < 30$  MeV. (bottom) additional gate in TLF  $^{196}\text{Os}$ . Blue dotted line indicates  $\gamma$ -ray energy of  $^{196}\text{Os}$ , and red dotted line indicates  $\gamma$ -ray energy from  $^{194}\text{Os}$ . . . . . 239

## LIST OF FIGURES

5.48 (top left) level diagram of $^{196}\text{Os}$ []. (top) $\gamma$ -ray energy distribution gated on $^{137}\text{Ba}$ in $15 < \text{TKEL} < 40$ MeV. (middle) Additional gate with TLF $^{196}\text{Os}$ on the top figure. (bottom) Additional gate with TLF $^{197}\text{Os}$ on the top figure. Blue dotted line indicates $\gamma$ -ray energy of $^{196}\text{Os}$ , and red dotted line indicates $\gamma$ -ray energy from $^{194}\text{Os}$ . . . . .	240
5.49 (top) $\gamma$ -ray energy distribution gated on $^{136}\text{Ba}$ in $20 < \text{TKEL} < 60$ MeV. (bottom) Additional gate with TLF $^{196}\text{Os}$ on the top figure. Blue dotted line indicates $\gamma$ -ray energy of $^{196}\text{Os}$ , and red dotted line indicates $\gamma$ -ray energy from $^{194}\text{Os}$ . . . . .	241
5.50 (top) $\gamma$ -ray energy distribution gated on $^{140}\text{Ba}$ and gated on $^{194}\text{Os}$ . (bottom) $\gamma$ -ray energy distribution gated on $^{142}\text{Ba}$ and gated on $^{192}\text{Os}$ . . . . .	242
5.51 The cross section of $N=126$ isotones of $Z=75$ <i>sim</i> 81 channels. (black square) This experiment, (blue diamond) Fragmentation experimental result [42], (red inverse triangle) GRAZING code calculation ( $^{136}\text{Xe}+^{198}\text{Pt}$ , 8 MeV/u), (magenta triangle) Langevin equation calculation [27] ( $^{136}\text{Xe}+^{208}\text{Pb}$ , $E_{CM}$ 450 MeV). . . . .	243
5.52 The excitation energy distributions of Os isotopes with (black solid line) ninth order polynomial fit of (top left) $^{200}\text{Os}$ , (top middle) $^{198}\text{Os}$ , (top right) $^{196}\text{Os}$ , (bottom left) $^{194}\text{Os}$ , (bottom middle) $^{192}\text{Os}$ , (bottom right) $^{190}\text{Os}$ . . . . .	245
5.53 The excitation energy distributions of Os isotopes with (black solid line) ninth order polynomial fit of (top left) $^{204}\text{Hg}$ , (top middle) $^{202}\text{Hg}$ , (top right) $^{200}\text{Hg}$ , (bottom left) $^{198}\text{Hg}$ , (bottom middle) $^{196}\text{Hg}$ , (bottom right) $^{194}\text{Hg}$ . . . . .	246

## *LIST OF FIGURES*

5.54 Mean excitation energy correlated with mean angular distribution of TLF nuclides (left) in proton stripping channels of (black square) Pt (0p), (blue diamond) Au (-1p), (red inverse triangle) Hg (-2p), (green triangle) Tl (-3p), and (yellow rotated triangle) Pb (-4p). (right) The same graph as the left figure with proton stripping channels of (black square) Pt (0p), (blue diamond) Ir (+1p), (red inverse triangle) Os (+2p), (green triangle) Re (+3p), and (yellow rotated triangle) W (+4p). The lines are drawn to guide eyes. The channels with even number neutron transferred are indicated with same color of the graph. . . . .	248
--	-----



# List of Tables

1.1	GRAZING-F calculation result of $^{136}\text{Xe} + ^{198}\text{Pt}$ reaction channel with N = 126.[23]. Production rate calculation assumed beam energy of 9 MeV/u, beam current $1\mu\text{A}$ , and target thickness equivalent to the range from the entrance energy to the interaction barrier. The cross section was reverse calculated by reverse calculating the target thickness to be $18.4 \text{ mg/cm}^2$ (range of $^{198}\text{Pt}$ Ecm=723 ~ 416 MeV)	9
2.1	The tabulated isotope with maximum ground-to-ground state Q-value ( $M(Q_{gg}) _{MAX}$ ), and N/Z equilibrium position ( $M _{N/Zequilibrium}$ ) using fitting of effective Q-value distribution calculated by equation of V. V. Volkov [13]	36
3.1	Specification of CSS1 cyclotron used in the experiment [91]	57
3.2	Acceptance calculation result from simulation. Both accepted events from elastic scattering and detection efficiency of reaction fragments increases proportional to the $B\rho$	61

## LIST OF TABLES

3.3	Rate calculation result from simulation and GRAZING calculation assuming beam intensity of 0.2pnA target thickness of 1.3 mg/cm <sup>2</sup> . Both accepted events from elastic scattering and reaction fragments increases proportional to the $B\rho$	63
3.4	Specification of electro-magnetic elements of VAMOS [90]	68
3.5	Detector setup and potion of VAMOS near focal plane.	70
3.6	Photo peak efficiency, peak-to-total efficiency cases close to this experimental configuration[97]	82
3.7	Resolution of $\gamma$ -ray with cases close to this experimental configuration[97]	83
3.8	Angular geometry coverage of each EXOGAM Clover detector 1 ~ 5.	87
3.9	Angular geometry coverage of each EXOGAM Clover detector 6 ~ 11.	88
4.1	Fitting result of Doppler correction resolution.	115
5.1	The optical potential fitting result of elastic scattering angular distribution. The Real/Imaginary potential parameters are indicated with label. The V indicates the depth of potential, R indicates the radius parameter (Radius of nuclei = $R^* A^{1/3}$ ), A is the diffusion parameter of Woods-Saxon potential ( $V(R) = \frac{V_0}{1-exp(\frac{r-R}{A})}$ ). The depth and the diffusion constant of the both real and imaginary potential were fixed and only the radii of the potential were set as the free parameter. . .	171



# **Chapter 1**

## **Introduction**

### **1.1 Motivation of the experiment**

The experiment of multi-nucleon transfer(MNT) reaction between  $^{136}\text{Xe}$  beam and  $^{198}\text{Pt}$  target at the energy  $\sim 55\%$  above Coulomb barrier was carried out, with full event-by-event identification of PLF with wide angular and momentum acceptance. Which distinguishes this experiment with previous experiments with similar beam and target combination with this experiment. This was possible by the VA-MOS++ spectrometer combined with gamma-ray detector array EXOGAM.

The Multi-nucleon transfer (MNT) reaction is the reaction between heavy ions (i.e,  $A > 15 \sim 20$ ) mechanisms with system energy near the Coulomb barrier. The main properties of MNT reaction from other reactions in this energy region such as fusion-fission, and Coulomb excitation are first, the nucleon is transferred. And second the reaction fragments retains the information from the entrance channel (i.e. reaction

### *1.1. MOTIVATION OF THE EXPERIMENT*

fragments are close to the entrance channel and kinetic energy is larger than the fully damped energy) [13]. The full process of the MNT reaction can be described by schematically by figure 1.1.

The experiment was carried out in the interest of first, to test the feasibility of producing neutron rich target-like fragments(TLF) with MNT reaction vicinity of neutron magic number 126. The neutron rich nuclei can be accessed via proton pickup, neutron stripping channels. The di-nuclear property of the MNT reaction, the TLF cross section could be determined from the measurement of reaction projectile-like fragments (PLF). The full identification PLF partner provides the cross section of the TLF side.

The second topic of the interest is the reaction mechanism between heavy neutron rich beam, and target system with similar N/Z ratio concerning proton and neutron transfer.

In more specification manner, the second topic of reaction mechanism can be classified as three categories first, how the nucleon transfer change as the MNT reaction evolves. By investigating the direction, strength of nucleon transfer, and when the reaction system reaches N/Z equilibrium. And diffusion of the nucleon transfer change as reaction (i.e. width).

Second, investigate how the reaction kinematics is correlated to the nucleon transfer. Such as how the angular distribution and excitation energy changes as the number of nucleon exchange. This can indicate the interplay between repulsive Coulomb force and attractive nuclear force and dissipative interaction.

Third, how the two different reaction mechanism of quasi elastic (direct) and deep inelastic (di-nuclear system with neck) which consists multi nucleon transfer

### 1.1. MOTIVATION OF THE EXPERIMENT

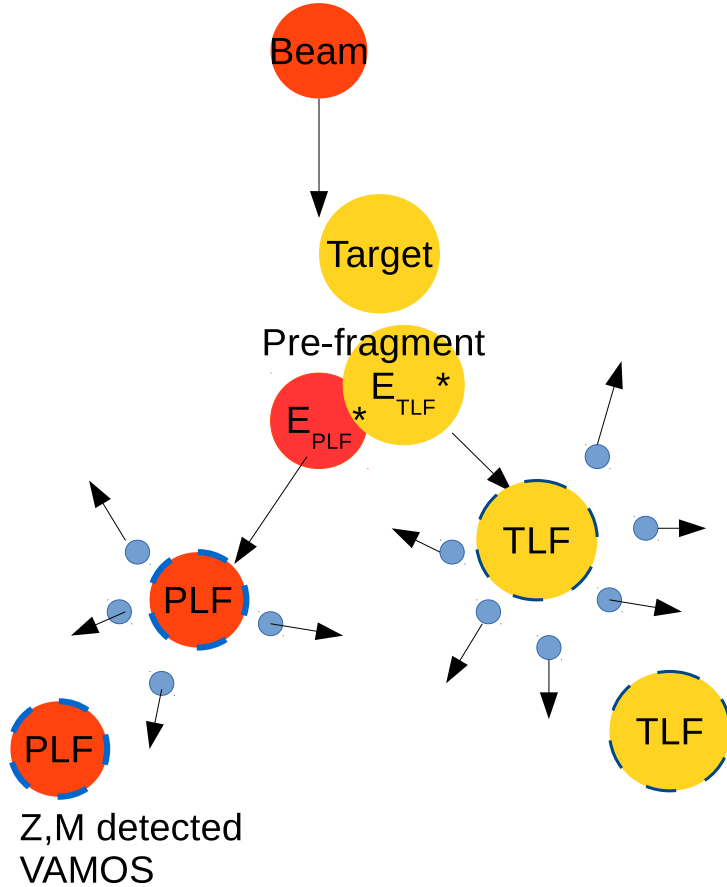


Figure 1.1 The schematic picture of MNT reaction. The nucleons are exchanged during projectile collides with the target. Meanwhile the kinetic energy is converted to internal excitation energy during the collision. After separation of projectile-like fragment (PLF) and target-like fragment (TLF), the excitation energy is consumed by secondary processes (dominated by light particle emission). The reaction fragments after the secondary process is detected.

## *1.2. PRODUCTION OF N~126 NUCLIDES*

(MNT) reaction compete in different channels.

### **1.2 Production of N~126 nuclides**

The rapid neutron capture process(r-process) which was suggested from historical paper of E.M. Burbridge and G.R. Burbridge, Fowler, Hoyle [7], is the process which explains the synthesis of heavy elements from Iron to Uranium. The r-process are presumed to happen in the extreme condition which can provide energetic and strong flux of neutrons. The astronomical site which satisfies such condition are presumed to be the type || supernovae and neutron star merger [8]. The r-process pass through (see figure 1.2) neutron rich nuclei. The actual path is very sensitive to the nuclear physical information such as the life time of the nuclei, neutron, and proton separation energy( $\tau_{1/2}, S_n, S_p$ ), especially at the nuclei near magic number. This is due to the nuclide at the shell closure have smaller level density causing smaller neutron capture cross section . This low cross section stalls the r-process towards the heavier side, forming the waiting point. The isotopes near neutron number  $\sim 126$  is the last waiting point of the r-process towards uranium, governing the synthesis of actinides. And important normalization point for theoretical model predictions. [14] The nuclei near  $N\sim 126$  are also very attractive region for nuclear physical interest, for testing the understanding of the shell models such as the quenching of shell structures from increasing neutron number. But the research related to nuclides at  $N\sim 126$  is limited from the fact that accessible isotopes is very close to the stable nuclei, so called “blank spot” [26] of table of nuclides as presented in figure 1.2.

Thus the production of  $N\sim 126$  nuclides are the first step to explore this frontier in the nuclear chart. Conventionally, fission or fragmentation reactions are used as

## 1.2. PRODUCTION OF $N \sim 126$ NUCLIDES

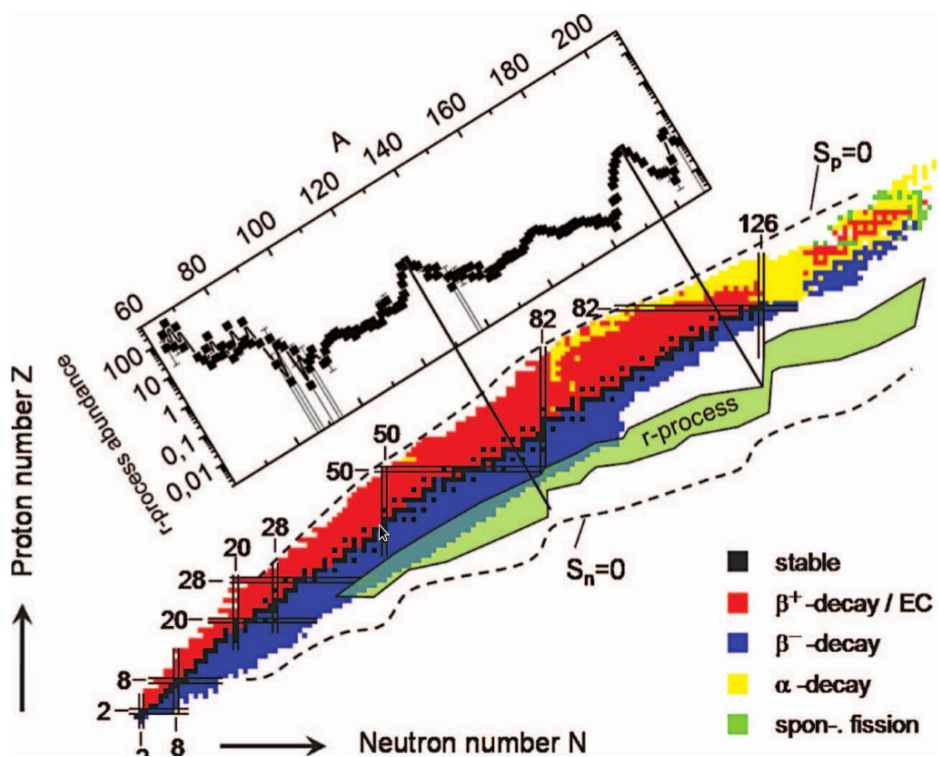


Figure 1.2 The table of nuclides with r-process path.[126] The sudden change of path near  $N \sim 126$  can be observed, which is responsible for  $A \sim 200$  peak in abundance distribution.

## 1.2. PRODUCTION OF $N \sim 126$ NUCLIDES

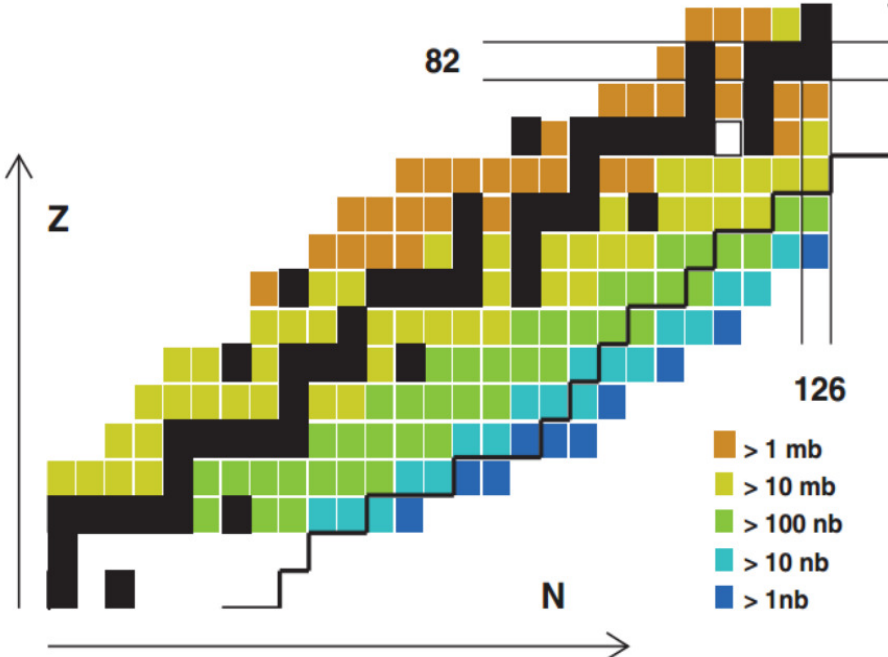


Figure 1.3 The production cross section of fragmentation reaction products of  $^{208}\text{Pb}$  beam with energy of 1 GeV/u impinging on  $^8\text{Be}$  target.

the driving reaction mechanisms for the production of n-rich nuclides. But applying the same method for producing n-rich nuclei near  $N \sim 126$  seems to be quite difficult. Very recently experiment was carried out at GSI using cold fragmentation reaction between  $^{208}\text{Pb}$  (1 GeV/u) +  $^8\text{Be}$  in order to reach  $N \sim 126$  nuclides [42, 43]. The production cross section were presented.(shown in figure 1.3) They showed very small cross section of nb order around targeted nuclei ( ex)  $^{203}\text{Ir}$  cross section 3.9 nb). This result well agreed with theoretical calculation of EPAX, ABRABLA, COFRA. Which predicted production cross section of  $^{202}\text{Os}$  was less than 1 nb for all calculations.

## 1.2. PRODUCTION OF N~126 NUCLIDES

The difficulties of producing N~126 nuclei using conventional method, brought spotlight to alternative reaction mechanism of multi-nucleon transfer (MNT) reaction between heavy nuclides close to Coulomb barrier.

The recent development of reaction mechanism theories and experiments presented new possibility.[14, 9] The theoretical prediction of C. H. Dasso et, al. [21], using GRAZING calculation model by A. Winther [20], first explored the possibility of production of such heavy n-rich nuclides. By systematically changing the projectile's neutron number they showed the combination of  $^{136}\text{Xe} + ^{208}\text{Pb}$  near Coulomb barrier. The resulting reaction cross section symmetric around the target, presented the possibility to reach n-rich nuclei. (See figure 1.4)

Very recently GRAZING including fission and more sophisticated evaporation treatment was presented (GRAZING-F )[23]. The code incorporated GRAZING calculated result to newly developed fission, particle evaporation code. This incorporation results better prediction in the reaction involving heavy nuclei ( $A > 200$ ). The transfer induced fission of heavy fragment one of the major part of the exit channel due to the massive excitation energy. The calculation of beam target combination of  $^{136}\text{Xe} + ^{198}\text{Pt}$ ,  $^{208}\text{Pb}$  was calculated with various system energy. This calculation result also presented positive result for producing neutron rich nuclides near  $N \sim 126$ . Due to the fact that  $^{208}\text{Pb}$  case the decay probability for fission existed, on the other hand  $^{198}\text{Pt}$  had almost no probability of fission. Thus increasing survival probability of neutron rich nuclei in  $^{136}\text{Xe} + ^{198}\text{Pt}$  combination, factor two larger than the  $^{136}\text{Xe} + ^{208}\text{Pb}$ . (See table 1.1)

V. Zagrebaev and W. Greiner [28] predicted the reaction cross section of the  $^{136}\text{Xe} + ^{208}\text{Pb}$  combination at the  $E_{CM}=450\text{MeV}$  using the model based on Lagevin

1.2. PRODUCTION OF  $N \sim 126$  NUCLIDES

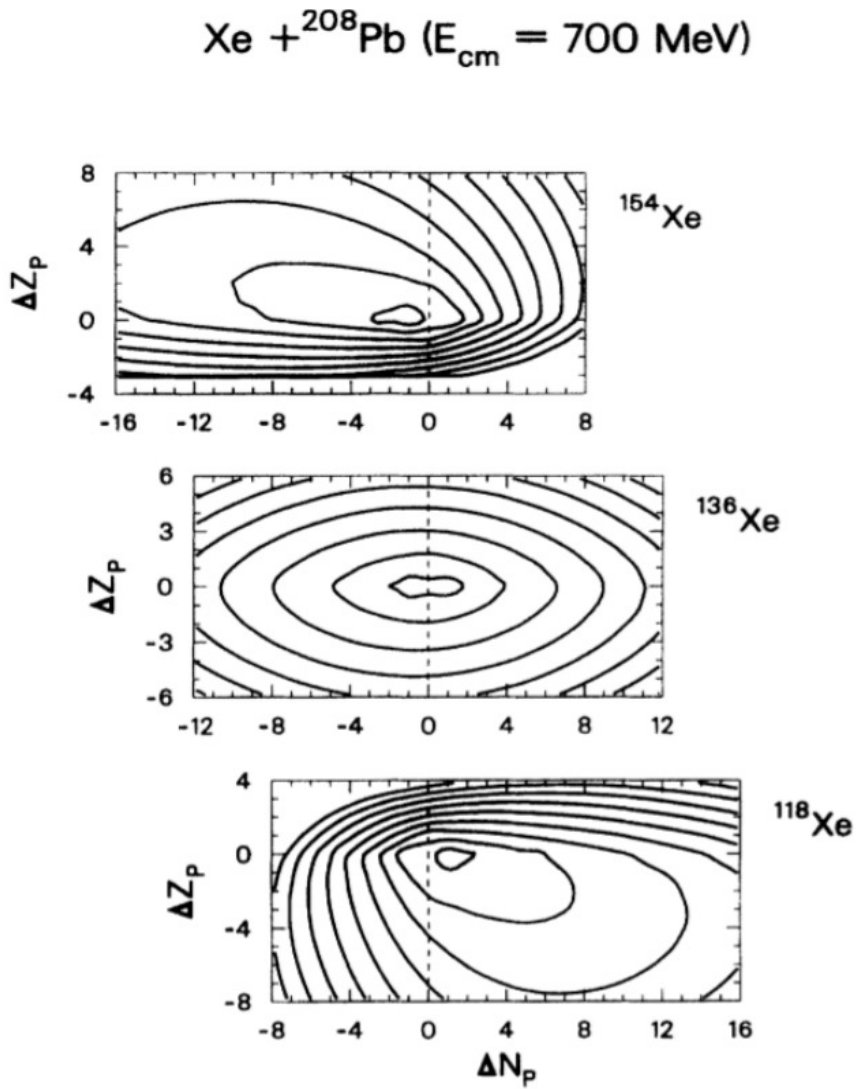


Figure 1.4 The calculated production cross section(arb. unit) of MNT reaction of  $^{154}Xe$ (top),  $^{136}Xe$ (middle),  $^{118}Xe$ (bottom) +  $^{208}Pb$  at  $E_{CM}=700$  MeV.

## 1.2. PRODUCTION OF $N \sim 126$ NUCLIDES

Isotope	production rate [ $s^{-1}$ ]	(estimated)average cross section [mb]
$^{204}\text{Pb}$	$2.6 \times 10^6$	0.74
$^{203}\text{Ir}$	$4.7 \times 10^5$	0.14
$^{202}\text{Os}$	$5.5 \times 10^4$	0.016
$^{201}\text{Re}$	$4.0 \times 10^3$	0.0014

Table 1.1 GRAZING-F calculation result of  $^{136}\text{Xe} + ^{198}\text{Pt}$  reaction channel with  $N = 126$ .[23]. Production rate calculation assumed beam energy of 9 MeV/u, beam current  $1\text{p}\mu\text{A}$ , and target thickness equivalent to the range from the entrance energy to the interaction barrier. The cross section was reverse calculated by reverse calculating the target thickness to be  $18.4 \text{ mg/cm}^2$  (range of  $^{198}\text{Pt}$  Ecm=723 ~ 416 MeV)

equation. Their result also showed isotropic distribution around the target nuclei. (See figure 1.5) The predicted cross section of  $n=126$  nuclides was around  $\sim 100 \mu\text{b}$  order for  $^{203}\text{Ir}$  and  $\sim \mu\text{b}$  order for  $^{202}\text{Os}$  before evaporation. The authors insisted the system energy should be low to avoid the large effect from the evaporation in order to produce neutron rich nuclei. (see left right figure of 1.5)

The two theoretical predictions of MNT reaction presented cross section more than 2~4 orders of magnitude larger than the conventional method. But if we inspect the different theories more closely, the optimum conditions for producing neutron rich nuclides are very different from each other. First the optimum choice of the beam and target combination was different. The GRAZING based calculations presents the  $^{136}\text{Xe} + ^{198}\text{Pt}$  combination presented factor two larger cross section than  $^{136}\text{Xe} + ^{208}\text{Pb}$  [23]. This is mainly due to the transfer probability of proton is smaller than the neutron. On the other hand, the Langevin equation calculation [28] predicts the  $^{136}\text{Xe} + ^{208}\text{Pb}$  combination results better cross section in  $n=126$  isotones over  $^{136}\text{Xe}$

## 1.2. PRODUCTION OF $N \sim 126$ NUCLIDES

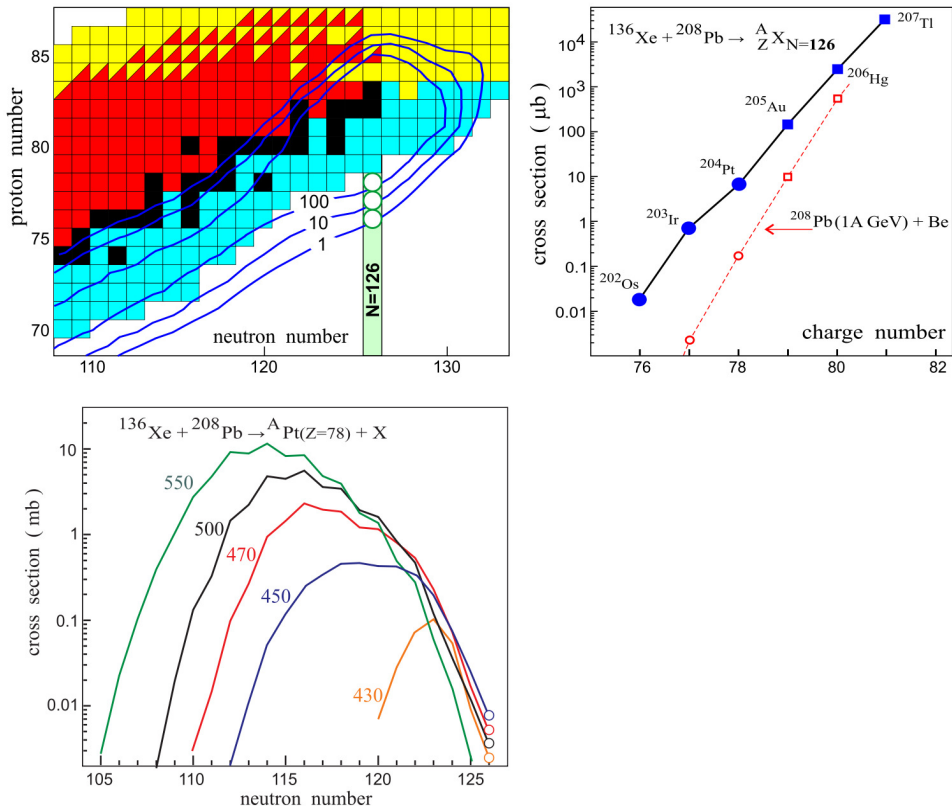


Figure 1.5 (top left) The pre-evaporation fragment(before evaporation) distribution of target-like fragments. (top right) Cross section of  $N = 126$  nuclides from calculation after evaporation, compared with fragmentation of  $^{208}\text{Pb}$ . (bottom left) cross section of Pt isotopes of different incident energy.

## 1.2. PRODUCTION OF $N \sim 126$ NUCLIDES

+  $^{198}\text{Pt}$ . This result was due to the shell closure of  $N=126$  in  $^{208}\text{Pb}$  making smaller neutron transfer than the non-magic number beam target combination.

The predicted optimum system energy was also diverse between different theories. The GRAZING code calculation [20] including particle evaporation predicted saturated cross section from beam energy  $6 \sim 10$  MeV/u. (See figure 1.6)

In the Langevin equation based calculation [28, 26] predicted the energy close to the Coulomb barrier  $4.5 \sim 5$  MeV/u, in order to avoid the massive particle evaporation. On the other hand Y. Iwata *et al.* [34] indicated that the fast charge equilibrium in reaction close to the Coulomb barrier will suppress the possibility for producing neutron rich nuclides, using time dependent Hartree-Fork (TDHF) calculation. They suggested that the energy of the system need to be much higher than Coulomb barrier in order to produce neutron rich nuclei. Since the higher energy decreases the reaction time therefore preventing the charge equilibrium.

These controversial predictions of theoretical predictions are partially due to the limited information from the several experimental results in this region. Experimentally the use MNT reaction, as a tool for producing neutron rich nuclides firstly carried out by Arutkh *et al.*[45].

In this heavy region using  $^{136}\text{Xe}$  was first done in the early 80's [46] using  $^{Nat}\text{W}$  +  $^{Nat}\text{Th}$  target, in the interest of producing neutron rich nuclides near the target nucleus. Which were able to produce new isotopes  $^{179}\text{Yb}$ ,  $^{181,182}\text{Lu}$  by  $\beta - \gamma$  decay spectroscopy.

The recent experiment by P. H. Regan *et al.* [47, 41], and E. M. Kozulin *et al.* [49] (which is already introduced in previous sections) was carried out of interest to produce neutron rich nuclides. They showed promising result, but due to the

## 1.2. PRODUCTION OF $N \sim 126$ NUCLIDES

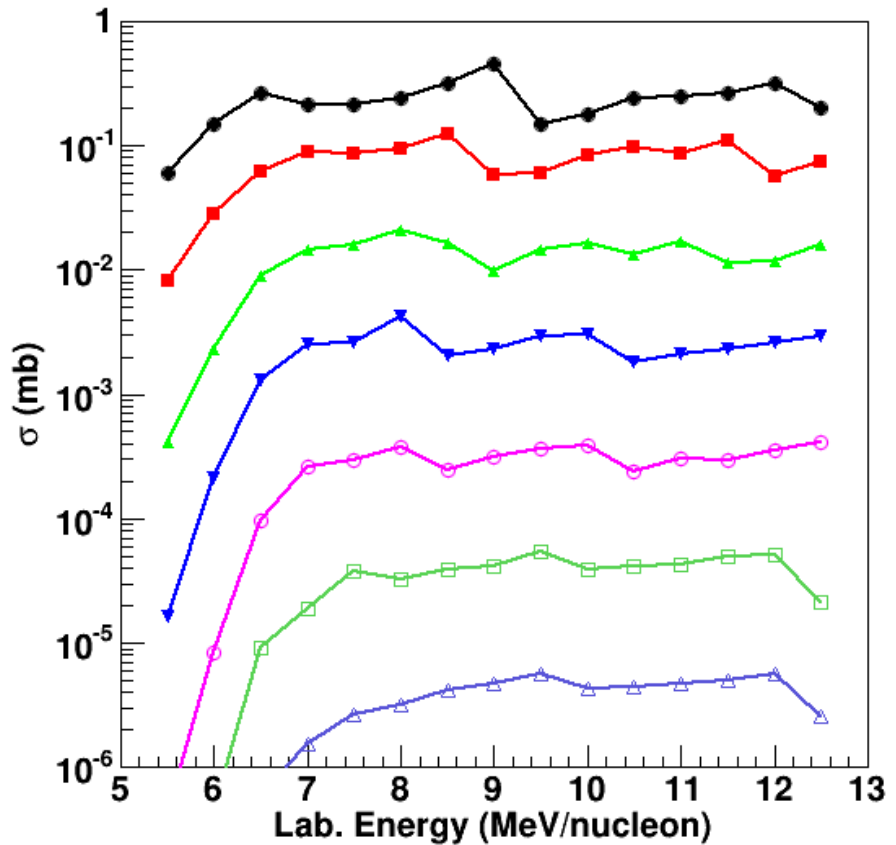


Figure 1.6 The GRAZING code [20] calculated cross section of  $N=126$  isotones from  $^{136}\text{Xe} + ^{198}\text{Pt}$  MNT reaction with different beam energy.

### **1.3. PREVIOUS STUDIES OF REACTION MECHANISM:REACTION MECHANISM OF MNT REACTION**

PID methodology no definite evidence for enhancement of producing neutron rich nuclides was not presented. (See figure 1.10, and 1.12) Thus more experimental evidence with full particle identification and kinematic information is necessary to test the feasibility of producing N~126.

Very recently experiment by with GAMMA sphere[48] with  $^{136}\text{Xe} + ^{208}\text{Pb}$  of  $E_{CM} = 450$  MeV (similar setup with P. H. Regan *et al.* [47]) with reported the cross section with full particle identification of nuclei with known  $\gamma$ -ray scheme. The result indicated the cross section coincide with Langevin equation[26], confirming the large cross section of MNT reaction in n-rich side. But the cross sections of N=126 isotones were smaller than the Langevin equation calculation. (See figure 1.7)

## **1.3 Previous studies of reaction mechanism:Reaction mechanism of MNT reaction**

The study of reaction mechanism of multi-nucleon transfer reaction fragments with very heavy beam and target system were limited in the previous studies due to the following difficulties,

- (1) The full identification of the reaction fragment is very hard even for the light projectile-like fragments due to resolution of detectors. Especially the mass identification for such heavy system is very challenging. And also the typical detector resolution of proton number is  $\frac{\Delta Z}{Z} = \frac{1}{60}$  (FWHM) which is close to this experimental system.

The experimental difficulties from the characteristics of MNT reaction mechanisms such as,

### 1.3. PREVIOUS STUDIES OF REACTION MECHANISM:REACTION MECHANISM OF MNT REACTION

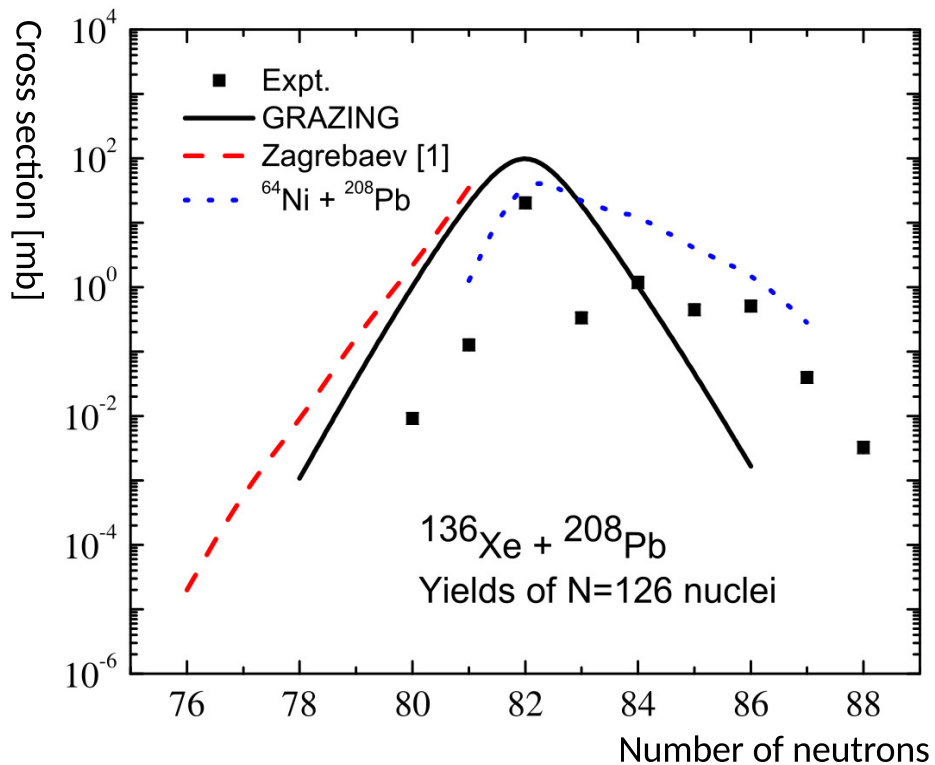


Figure 1.7 The cross sections of  $^{136}\text{Xe} + ^{208}\text{Pb}$  at energy of  $E_{CM}=450\text{MeV}$  of  $N=126$ . (Black square) experimental result, (red dashed line)Langevin equation calculation, (black solid line) GRAZING code [20] calculation, ( blue dotted line)  $^{64}\text{Ni} + ^{208}\text{Pb}$  experimental result

### 1.3. PREVIOUS STUDIES OF REACTION MECHANISM:REACTION MECHANISM OF MNT REACTION

- (2) The wide momentum distribution ranging from elastic to fully damped energy, which is caused by the massive energy dissipation of the system.
- (3) The wide angular distribution which is typically few~several $\times$ 10 degrees depending on the system.

The intensive investigation of  $^{136}\text{Xe} + ^{209}\text{Bi}$  were carried out with different energy (940, 1130, 1422 MeV). [55, 56, 57, 58, 59, 60]. The projectile fragment partial identification of atomic number was executed using dE-E method. The energy dependence of reaction dynamics related to p-transfer was presented. It showed symmetric transfer of protons were presented with angular distribution concentrated near grazing angle for all beam energy. (See figure 1.8)

This is different from most experiments performed with light or medium mass projectiles at energies around the Coulomb barriers, which favored neutron pickup and proton stripping channels. Even with the neutron-rich medium mass projectile (e.g.  $^{64}\text{Ni} + ^{238}\text{U}$  [51]), the proton pickup channels were accessible but the proton stripping channels were still dominant. (See figure 1.9) This suppression is owing to the different N/Z ratio between heavy and light systems. The angular distribution of light nuclei + heavy systems tends to move forward as dissipated energy increases. This is due to the stronger nuclear force than Coulomb force at the smaller distance approach.

The recent experiment of E. M. Kozulin *et al.* [49] studied  $^{136}\text{Xe} + ^{198}\text{Pt}$  with beam energy of 700 (5.15), 870 (6.40), and 1020 (7.5) MeV ( MeV/u) reported mass distributions(without proton number)of both reaction fragments. The mass was detected by ToF and energy measurement. They showed rather symmetric transfer of mass over all energy regions. (See figure 1.10)

### 1.3. PREVIOUS STUDIES OF REACTION MECHANISM:REACTION MECHANISM OF MNT REACTION

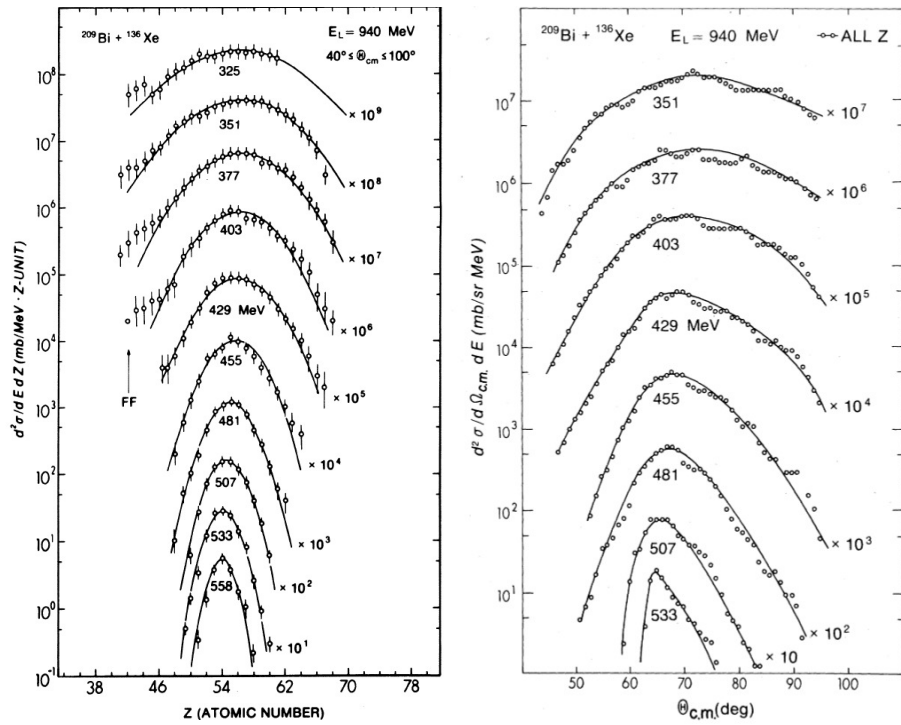


Figure 1.8 (left) The atomic number distribution of  $^{136}\text{Xe} + ^{209}\text{Bi}$  at energy of  $E_{\text{Beam}}=940\text{MeV}$  with different total kinetic energy of 26 MeV wide bin. (right) The angular distribution with different total kinetic energy of same reaction.

### 1.3. PREVIOUS STUDIES OF REACTION MECHANISM:REACTION MECHANISM OF MNT REACTION

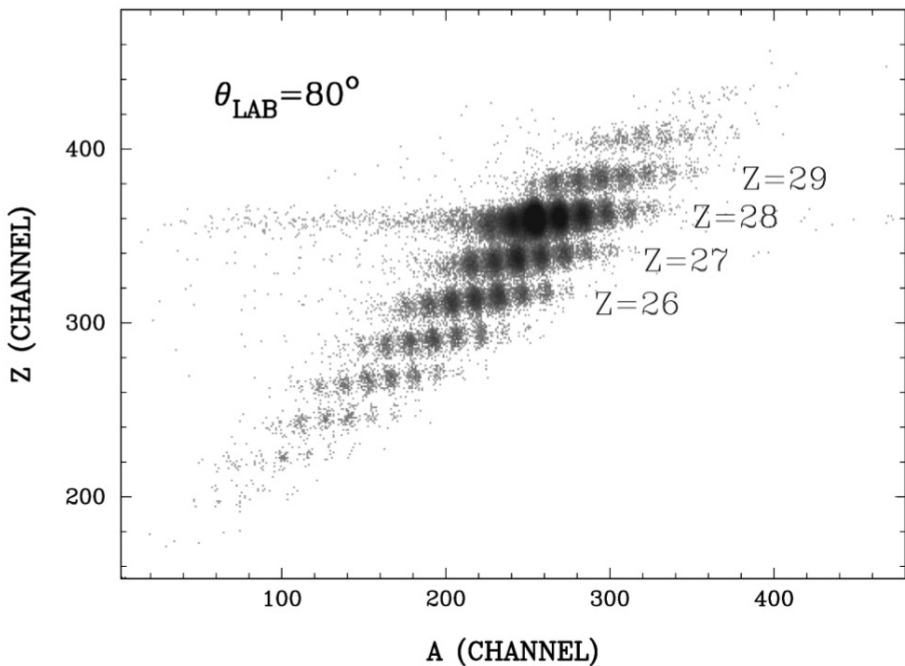


Figure 1.9 The mass vs atomic number distribution of  $^{64}\text{Ni} + ^{238}\text{U}$  with  $E_{\text{Beam}} = 390\text{MeV}$  (6.10 MeV/u).

1.3. PREVIOUS STUDIES OF REACTION MECHANISM:REACTION MECHANISM OF MNT REACTION

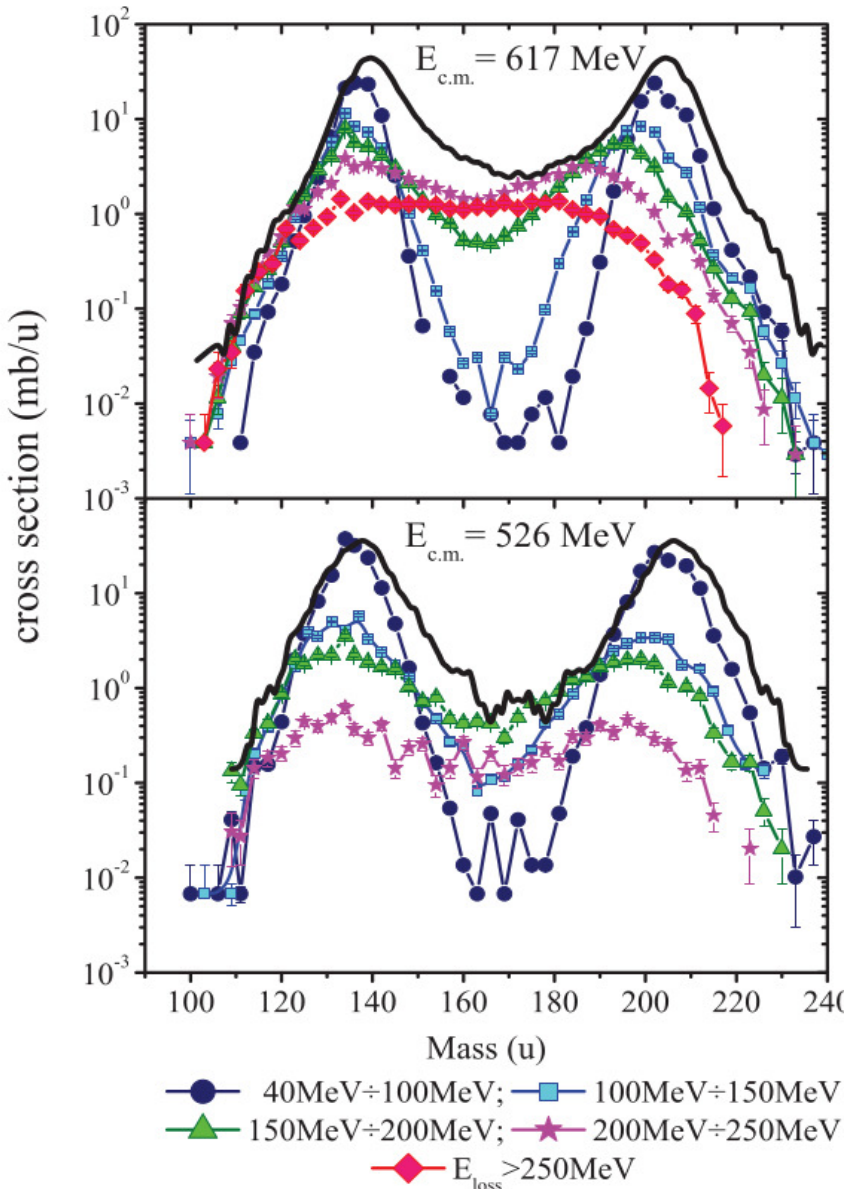


Figure 1.10 Mass distribution of  $^{136}\text{Xe} + ^{208}\text{Pb}$  with (top)  $E_{CM} = 617\text{MeV}$  ( $E_{Beam} = 1020\text{MeV}$ ), (bottom)  $E_{CM} = 526\text{MeV}$  ( $E_{Beam} = 870\text{MeV}$ ) of different total kinetic energy loss. [49]

### 1.3. PREVIOUS STUDIES OF REACTION MECHANISM:REACTION MECHANISM OF MNT REACTION

Both proton and mass distribution between heavy ions with similar N/Z ratio showed symmetric distribution. But partial identification of reaction fragment is not enough in order to see the direction of nucleon transfer both protons and neutrons.

The systematic study of  $^{129}\text{Xe}$  (761MeV),  $^{132}\text{Xe}$  (764MeV),  $^{136}\text{Xe}$  (787MeV) +  $^{197}\text{Au}$  combination were carried out by Kratz *et al.*. They used radio chemical method which separates reaction fragments by atomic number by chemically and measured decay  $\gamma$ -rays for full identification of nuclei with long life time [68]. It showed the wide range of reaction products which followed N/Z equilibrium by potential energy surface. (See figure 1.11) But due to the limit of the technique, only the limited information of reaction dynamics was obtained.

P. H. Regan *et al.* [47] used same beam target combination of this experiment with beam energy of 850 MeV (6.25 MeV/u). The de-excitation  $\gamma$ -rays were used for direct identification of target-like fragments (TLF) and the direction and  $\Delta\text{ToF}$  between PLF and TLF were detected by PPACs covering  $4\pi$ . The experimental result presented gamma-rays from n-rich nuclei outside of the valley of stability. (See figure 1.12). But due to the identification was done only in the region with known gamma-ray decay. The reaction mechanism and the neutron rich side outside unknown region were not explored. Since their main interest was to examine the high spin states of nuclides.

The MNT reactions in the heavy neutron rich systems with energy near the Coulomb barrier were extensively studied. But the previous experiments mostly even the recent ones, only partial identification (usually atomic number) were carried out due to the difficulties stated above. (e.g. reference [49, 55, 58, 59, 61]) And the experiments with full identifications were done in other methods like radio

### 1.3. PREVIOUS STUDIES OF REACTION MECHANISM:REACTION MECHANISM OF MNT REACTION

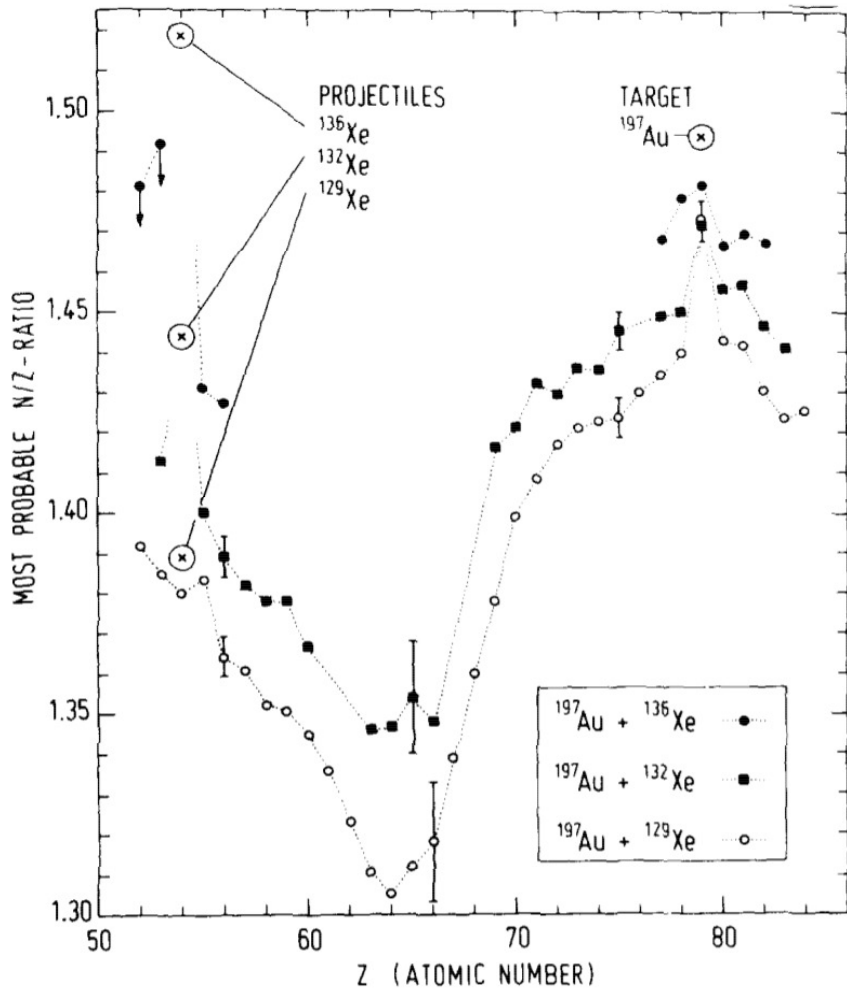


Figure 1.11 Most probable N/Z ratio of  $^{129}\text{Xe}$ ,  $^{132}\text{Xe}$ ,  $^{136}\text{Xe}$  +  $^{197}\text{Au}$  for different atomic number.  $^{129}\text{Xe}$ ,  $^{132}\text{Xe}$ ,  $^{136}\text{Xe}$  are indicated with circle, black square, black dot respectively. The typical error bars are presented (  $Z \sim 56, 65, 75$  and  $79$ ).

### 1.3. PREVIOUS STUDIES OF REACTION MECHANISM:REACTION MECHANISM OF MNT REACTION

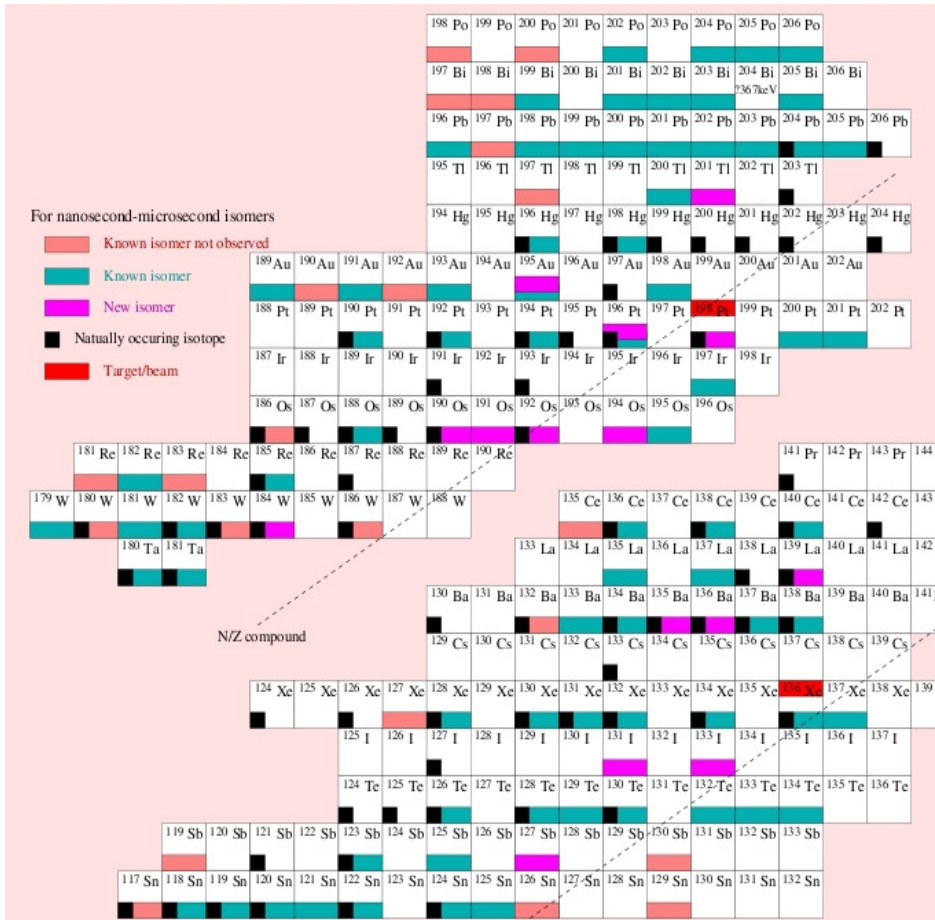


Figure 1.12 The target-like fragments identified by gamma-rays produced from  $^{136}\text{Xe} + ^{198}\text{Pt}$   $E_{beam}=850 \text{ MeV}$ . [41]

### 1.3. PREVIOUS STUDIES OF REACTION MECHANISM:REACTION MECHANISM OF MNT REACTION

chemical processes [68] or detecting the de-excitation gamma-rays from the reaction fragments [47, 48]. This presented limited to known isotopes due to the methodology. Therefore the comprehensive study of the evolution of reaction concerting proton and neutron transfer, full event-by-event identification of reaction fragments with wide range is needed.

The full event-by-event identification of heavy ion with mass resolution was possible by dE-E and ToF measurement but resolution was poor.(e.g. see reference [72] ( $\Delta Z = 1.6$ ,  $\Delta A = 4.0$ )) The full event-by-event identification of heavy ion with mass resolution less than 1/100 was possible using magnetic spectrometer. This method applied to very heavy system by J. Speer *et al.* by  $^{144}\text{Sm} + ^{208}\text{Pb}$  [78] (Ebeam=5.5,5.8 MeV/u at GSI by inverse kinematics and detecting recoiled Sm-like fragments. The even-by-event full identification was possible. (See figure 1.13) The transfer probability of pure proton transfer channels were presented to find enhancement pair proton transfer. But due to small acceptance of the spectrometer regions were limited to direct reactions with small energy dissipation.

In this experiment, setup with the capability of both large acceptance and good resolution enough for particle identification was possible. Due to the development of the modern large acceptance spectrometers like VAMOS++[85], PRISMA[98] ,and MAGNEX[99]. These sepctrometers were designed to study various reactions near the Coulomb barrier. And capable to cover large angular ( $50 \sim 100$  mrad) and momentum acceptance needed to fully detect the reaction fragments with full event-by-event particle identification. (see more details in chapter 3)

Thus extensive study of the MNT reaction with the experiment capable of full identification with measurement of reaction dynamics is very necessary.

### 1.3. PREVIOUS STUDIES OF REACTION MECHANISM:REACTION MECHANISM OF MNT REACTION

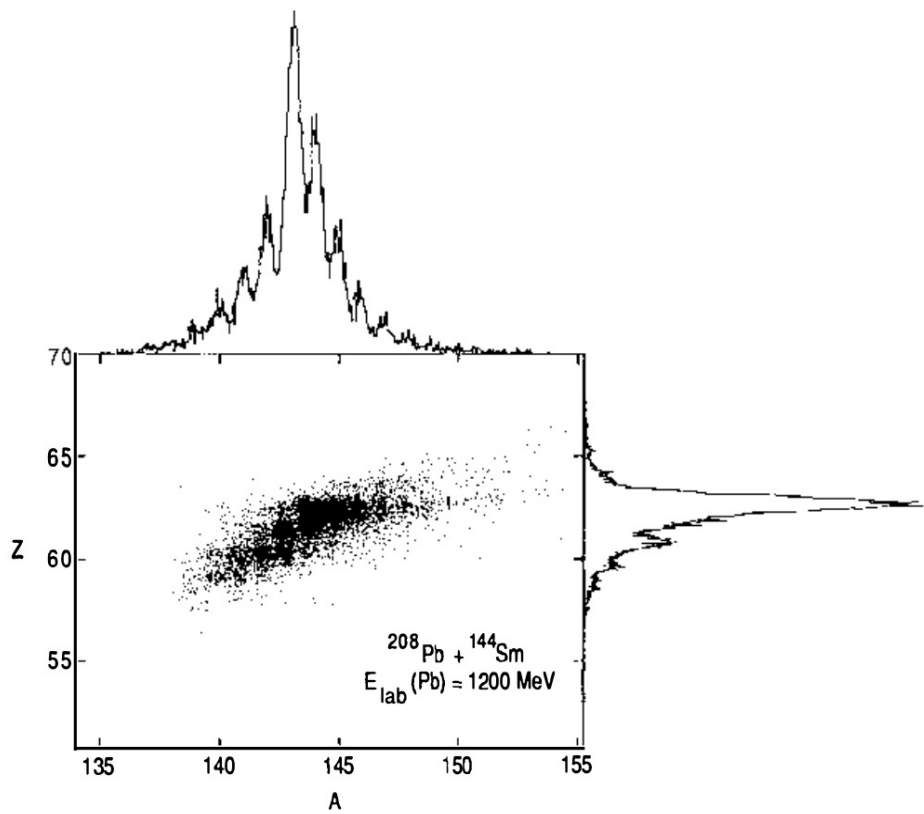


Figure 1.13 The mass vs atomic number distribution of PLFs from  $^{144}\text{Sm} + ^{208}\text{Pb}$  with  $E_{\text{beam}} = 5.8 \text{ MeV/u}$  reaction.

## *1.4. PERSPECTIVE OF THIS EXPERIMENT*

### **1.4 Perspective of this experiment**

The full event-by-event identification of PLFs will provide first, more extensive information of reaction mechanism between heavy neutron rich nuclides with similar N/Z ratio concerning nucleon transfer. And second, test the feasibility for producing neutron rich isotopes, by measuring the target-like fragment cross section using information from projectile-like fragment.

This experimental result is expected enable the theories with more reliable result of feasibility of N~126 isotopes and provide the optimum condition for producing them.

And last reaction kinematics with reaction dynamics, and feasibility information will provide information to upcoming facilities for producing neutron rich N~126 nuclides which utilize MNT reaction between heavy nuclides. (e.g. KEK isotope separation system(KISS) project at RIKEN and reference [14]) And hopefully open a door way to the study the properties of nuclei concerning r-process towards synthesis of uranium.

# Chapter 2

## Theory of Multi-nucleon Transfer Reaction

### 2.1 Characteristics of Multi-nucleon Transfer Reaction

The two main properties arise from the experiment result concerning direction and strength (cross section) of nucleon transfer. First is partial statistical equilibrium ( $Q$  value dependence), and second is  $N/Z$ -equilibrium.

#### 2.1.1 Partial statistical equilibrium ( $Q$ -value dependence)

The strong dependence of  $Q$ -value on cross section of multi-nucleon transfer reaction was first realized by Volkov *et al.* [67] The exponential dependence on cross section of ground-to-ground state  $Q$ -value ( $Q_{gg}$ ) of isotopes for given element were observed. (See figure 2.1) These systematic features are commonly observed in the

## 2.1. CHARACTERISTICS OF MULTI-NUCLEON TRANSFER REACTION

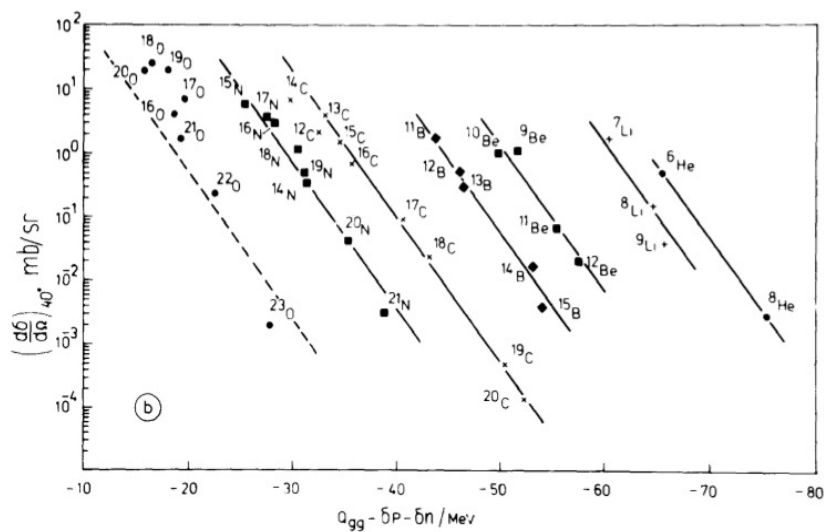


Figure 2.1 The cross section vs  $Q$  value of reaction between  $^{22}\text{Ne} + ^{222}\text{Th}$  at energy of  $E_{Beam}=174$  MeV.

## 2.1. CHARACTERISTICS OF MULTI-NUCLEON TRANSFER REACTION

light projectile ( $A \sim 20$ ) systems with energy near or below the Coulomb barrier [15]. The Q-value dependence means that the reaction fragments retains the information of entrance channels. Partial statistical equilibrium was introduced [19] to explain direct and statistical features of particle exchange and energy dissipation of MNT reactions. The transfer probability is determined by size of phase-space in reaction channels. Which is expressed by level density  $\rho_{tot} = \rho_{PLF} \times \rho_{TLF}$  of the final system. The level density can be inferred from applying thermodynamics to the nuclear system [6] with approximation that light projectile with excitation energy much smaller compared to heavy partner. This assumption is known to better work near closed shell [18]. The exponential relation of cross section can be derived by calculating mean probability of compound system emitting PLF with energy  $e_{PLF} \sim e_{PLF} + de_{PLF}$  per unit time ( $W_{PLF}(e_{PLF})de_{PLF}$ ). First, reversely calculating mean probability of TLF capturing PLF (with  $E = e_{PLF} \sim e_{PLF} + de_{PLF}$ ,  $velocity = v$ ) forming compound system with  $E^* \sim E^* + de_{PLF}$  per unit time ( $W_{Capture}$ ) with cross section  $\sigma(E^*, e_{PLF})$  inside volume V.  $W_{capture}$  can be written as,

$$W_{capture} = \frac{\sigma(E^*, e_{PLF})v(e_{PLF})}{V} \quad (2.1)$$

Dividing  $W_{capture}$  with density of states in compound system  $\rho_{comp}(E^*)$  and multiplying the density of states in target-like fragement  $\rho_{TLF}(E_{TLF} = E^* - e_{PLF} - Q_{gg})$  and number of states inside the volume V ( $dN_{PLF}$ ). Then

$$W(e_{PLF})de_{PLF} = W_{capture} \frac{\rho_{TLF}(E_{TLF}^*)dN_{PLF}}{\rho_{comp}(E^*)} \quad (2.2)$$

Using Fermi gas model, the number of states of PLF can have inside the volume V can be written as,

$$dN = \frac{V(2l_{PLF} + 1)}{2\pi^2\hbar^3} m_{PLF} \sqrt{2m_{PLF}e_{PLF}} de_{PLF} \quad (2.3)$$

## 2.1. CHARACTERISTICS OF MULTI-NUCLEON TRANSFER REACTION

Applying statistical relation

$$S(E_{TLF}^* = E^* - (e_{PLF} - Qgg)) = k_B \log(\rho), (E^* \ll (e_{PLF} - Qgg)) \quad (2.4)$$

$$S(E_{TLF}^*) \simeq S(E^*) - ((e_{PLF}^* - Qgg) \frac{\partial S}{\partial E^*} + \dots) \quad (2.5)$$

$$\rho_{TLF} = e^{S(E^*) + (Qgg - e_{PLF}^*)/T}, (\frac{\partial S}{\partial E^*} = T) \quad (2.6)$$

Finally

$$W(e_{PLF}) de_{PLF} = W_{capture} dN e^{S_{TLF}(E^*) - S(E^*)} e^{(Qgg - e_{PLF}^*)/T} \quad (2.7)$$

Thus the cross section of the exit channels can be expected by

$$\sigma \propto e^{U/T} \quad (2.8)$$

Where U is the available energy at the reaction point, and T is parameter corresponds to the temperature of the system.

The empirical formula introduced by V. V. Volkov [13] utilizes the change of potential at interaction position (two spherical nuclei touching).

$$Q_{eff} = Qgg - \Delta V_C - \Delta V_N - \Delta V_L - \delta(n) - \delta(p) \quad (2.9)$$

$\Delta V_C / \Delta V_N / \Delta V_L$ : Coulomb/Nuclear/Centrifugal potential difference between initial and final channel (at closest distance approach)

$\delta(n), \delta(p)$ : non-pairing corrections

The non-pairing correction energy is included to consider the nucleon transfer through excited states. Since the Qgg value includes the pairing energy. In this experiment for instance, the change of Coulomb potential can be in order of 8 ~ 10 MeV per one

## 2.1. CHARACTERISTICS OF MULTI-NUCLEON TRANSFER REACTION

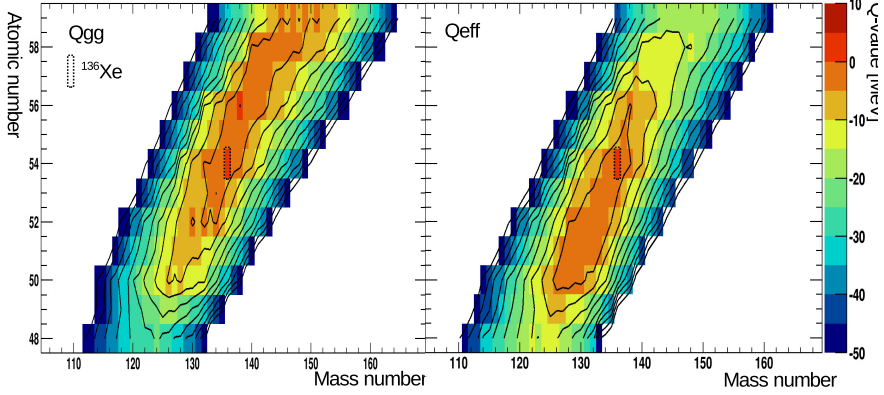


Figure 2.2 (left) Ground-to-ground state Q-value distribution of this experiment. (right) Effective Q-value calculated from V. V. Volkov's formula.

proton exchange and paring energy order of 850keV. While the change in nuclear potential for one nucleon exchange order of 20keV, and change of centrifugal force is smaller than several 100keV order which can be neglected. In this experiment the  $Q_{eff}$ -value using V. V. Volkov's formula is shown in figure 2.2. The proton pickup channels show more favorable Q-value than the proton stripping channels. The local peaks appear due to pairing energy.

The exponential relation of Q-value doesn't apply as the reaction partner becomes heavier and energy of the system increases. But the strong Q-value dependence can still be observed in those regions.(e.g. see reference [9, 10])

Another Q-value dependence arise from the matching condition of initial and final trajectories at the classical turning points (where the transfer probability assumed to be the highest). Using first order Born approximation, the probability of transition from i-th channel to the f-th channel can be written as equation 2.10, using semi-

## 2.1. CHARACTERISTICS OF MULTI-NUCLEON TRANSFER REACTION

classical coupled equations [9].

$$P_{fi} = \left| \frac{i}{\hbar} \int_{-\infty}^{\infty} dt f_{fi}(\mathbf{k}, \mathbf{r}) e^{-i[(E_f - E_i) + (\delta_f - \delta_i)]t/\hbar} \right|^2 \quad (2.10)$$

$f_{fi}(\mathbf{k}, \mathbf{r})$ : Form factor from i-th to f-th channel(i.e.,  $\langle \chi_f | V_{interaction} | \chi_i \rangle$ )

$E_{i,f}$ : incident and exit energy of the system

$\mathbf{k}$ : transferred momentum,  $\mathbf{r}$ : relative distance between two nuclides

$\delta_{i,f}(t)$ : phase accounting relative motion of two particles ( $= \int^t dt L(t)$  L(t):Lagrangian of relative motion)

The form factor  $f(\mathbf{k}, \mathbf{r})$  can be rewritten as equation 2.11

$$f_{fi}(\mathbf{k}, \mathbf{r}) \sim e^{i\sigma_{fi}} f_{fi}(0, \mathbf{r}) \quad (2.11)$$

$$\sigma_{af} \sim \frac{1}{\hbar} \frac{\Delta M}{M_{Beam} + M_{Target}} (R_{Target} M_{PLF} - R_{Beam} M_{TLF}) \quad (2.12)$$

By approximating the true trajectory to the parabolic trajectory the equation 2.10 can be rewritten as,

$$P_{fi} = \sqrt{\frac{1}{16\pi\hbar^2|\ddot{r}|k}} |f_{fi}(0, \mathbf{r})|^2 g(Q) \quad (2.13)$$

Where the adiabatic cutoff function  $g(Q)$  can be written as equation 2.14.

$$g(Q) = e^{-\frac{(Q-Q_{opt})^2}{\hbar^2|\ddot{r}|k}} \quad (2.14)$$

For bombarding energy below or close to the Coulomb barrier the optimum Q-value can be written as equation 2.15.

$$\begin{aligned} Q_{opt} &= \left( \frac{\Delta Z}{Z_{beam}} - \frac{\Delta Z}{Z_{TLF}} \right) V_B + \left( \frac{\Delta M}{M_{TLF}} - \frac{\Delta M}{M_{beam}} \right) (E_{CM} - V_B) \\ &\quad + \frac{\Delta M \ddot{r}}{M_{beam} + M_{PLF}} (R_{beam} M_{TLF} - R_{PLF} M_{target}) \end{aligned} \quad (2.15)$$

## 2.1. CHARACTERISTICS OF MULTI-NUCLEON TRANSFER REACTION

$\Delta Z, \Delta M$  : number of transferred protons, mass

$Z_{beam/target/PLF/TLF}$ : Atomic number of beam/target/PLF/TLF

$M_{beam/target/PLF/TLF}$ : Mass number of beam/target/PLF/TLF

$R_{beam}$ : radius of beam nuclei,  $R_{PLF}$ : radius of PLF

$V_B$ : Coulomb barrier

The exsistance of optmum Q-value suppress or promotes the reaction which have Q-value near or larger than the optimum Q-value. (Since lower Q-value can be accessed by exciation energy of the reaction.) More various models of optimum Q-value from theoretical models can be found in [1].

### 2.1.2 N/Z equilibrium

In the heavily damped regions (i.e. reaction fragment with large dissipation energy) the nucleon transfer is known to move towards N/Z equilibrium determined by potential energy surface (P.E.S.) of composite system [15]. (e.g. see reference figure 2.3)

The potential energy surface (including mass) of composite system can be calculated by assuming two touching spherical nuclide by liquid drop model. It can be written as equation 2.16.

$$V(Z_{PLF}, A_{PLF}, Z_{TLF}, A_{TLF}, R) = M_{LD}(Z_{PLF}, A_{PLF}) + M_{LD}(Z_{TLF}, A_{TLF}) + V_{Coulomb}(R) + V_{Nuclear}(R) + V_L(R) \quad (2.16)$$

$$V_{Coulomb} = \frac{1}{4\pi\epsilon_0} \frac{Z_{TLF}Z_{PLF}e^2}{R} \quad (2.17)$$

$$M_{LD}(Z, A) = ZM_P + (A - Z)M_N - a_V A + a_S A^{2/3}$$

## 2.1. CHARACTERISTICS OF MULTI-NUCLEON TRANSFER REACTION

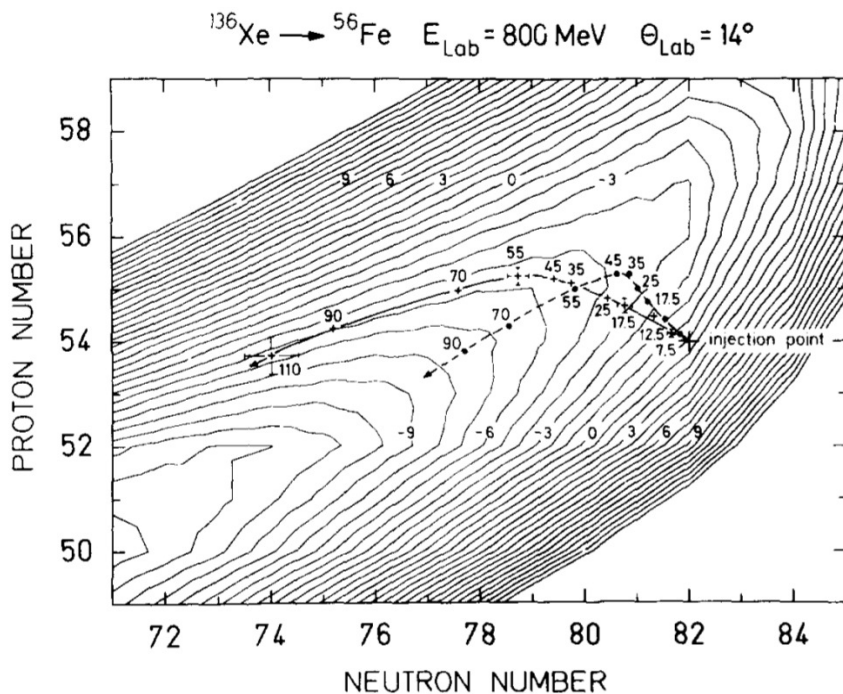


Figure 2.3 The mean isotope ( $\langle Z \rangle, \langle A \rangle$ ) as function of total excitation energy, with calculated potential energy surface(1MeV spaced).The crosses connected with solid line represents mean isotope ( $\langle Z \rangle, \langle A \rangle$ ) without considering neutron evaporation. The black dot connected with dashed line represents mean isotope ( $\langle Z \rangle, \langle A \rangle$ ) considering neutron evaporation.

## 2.1. CHARACTERISTICS OF MULTI-NUCLEON TRANSFER REACTION

$$+ a_C \frac{Z(Z-1)}{A^{1/3}} + a_A \frac{(Z-(A-Z))^2}{A} + \delta \quad (2.18)$$

$a_V/a_C/a_A$ : Volume term (15.5MeV) /Surface term (16.8MeV) /Coulomb repulsion term (0.72MeV)/Symmetric term (24MeV)

$\delta$ : pairing term ( $+a_p/A^{-3/4}$ :even-even,0:even-odd,- $a_p/A^{-3/4}$ :odd-odd, $a_p=34$ MeV) [5]

The most probable atomic number  $\langle Z_{PLF} \rangle$  of TLF for fixed  $A_{PLF}$  can be written as

$$\frac{\partial V(Z_{PLF}, A_{PLF}, (Z_{TLF}), (A_{TLF}), R)}{\partial Z_{PLF}} \Big|_{A_{PLF}} = 0 \quad (2.19)$$

$$\langle Z_{PLF} \rangle = (Z_{PLF} + Z_{TLF})$$

$$\times \frac{2a_C/A_{TLF}^{1/3} + 2a_A/A_{TLF} - e^2/(4\pi\epsilon_0 R)}{2a_C(A_{PLF}^{-1/3} + A_{TLF}^{-1/3}) + 2a_A(A_{PLF}^{-1} + A_{TLF}^{-1}) - 2e^2/(4\pi\epsilon_0 R)} \quad (2.20)$$

The terms from Coulomb repulsion is much smaller than the symmetric terms since  $a_C \ll a_A$ . Therefore the most probable atomic number is determined mostly by symmetric term. If we ignore terms other than symmetric term than it can be written as

$$\langle Z_{PLF} \rangle \approx (Z_{PLF} + Z_{TLF}) \frac{A_{PLF}}{A_{TLF} + A_{PLF}} \quad (2.21)$$

Which is simply determined from N/Z ratio of compound nucleus (named UCD-rule). The curvature of potential (which is related to the width of charge distribution) is also determined mostly by symmetric term which can be written as

$$\begin{aligned} & \frac{\partial^2 V(Z_{PLF}, A_{PLF}, Z_{TLF}, A_{TLF}, R)}{\partial Z_{PLF}^2} \Big|_{A_{PLF}} \\ &= 2a_C \left( \frac{1}{A_{PLF}^{1/3}} + \frac{1}{A_{TLF}^{1/3}} \right) + 2a_A \left( \frac{1}{A_{PLF}} + \frac{1}{A_{TLF}} \right) \end{aligned} \quad (2.22)$$

## 2.1. CHARACTERISTICS OF MULTI-NUCLEON TRANSFER REACTION

Above simple liquid drop model doesn't include nuclear structural information such as shell effects. In more sophistic calculations, the shell model effects and deformations are included for determining potential. Extensive studies showed that the shell effects plays essential role in the potential energy surface, which agreed with experimental results.(See reference [15]) For instance in the study of the reaction between symmetric system of  $^{144,154}\text{Sm} + ^{144,154}\text{Sm}$  showed very different mean mass distribution following potential energy surface [72]. (See figure 2.4) The neutron magic number 82 in  $^{144}\text{Sm} + ^{144}\text{Sm}$  holds neutron transfer reaction, and the reaction evolves through proton transfer. While  $^{154}\text{Sm} + ^{154}\text{Sm}$  on the other hand showed neutron transfer as well as the proton transfer than lighter partner moves towards  $N \sim 82$ .

Both effective Q-value calculation, and potential energy surface calculates the potential energy at the (most possible) reaction point. The distribution of effective Q-value calculation in the previous section presents potential energy surface normalized by entrance channels. The critical difference in N/Z equilibrium calculation is that the effects from entrance channels are only included by total number of protons, and neutrons. While Q-value calculations the entrance channel shell effect is important. Also exponential relation of Q-value the local maximum effects largely in the cross section prediction. On the other hand the N/Z-equilibrium global maximum of potential energy surface will form the most probable isotope. This emphasizes the evolution from direct reaction in the low dissipation energy to the compound reaction like behavior in the large energy dissipation.

The empirical partial statistic equilibrium and simple N/Z-equilibrium description successfully explains many experimental cross section results. But the dynamic

## 2.1. CHARACTERISTICS OF MULTI-NUCLEON TRANSFER REACTION

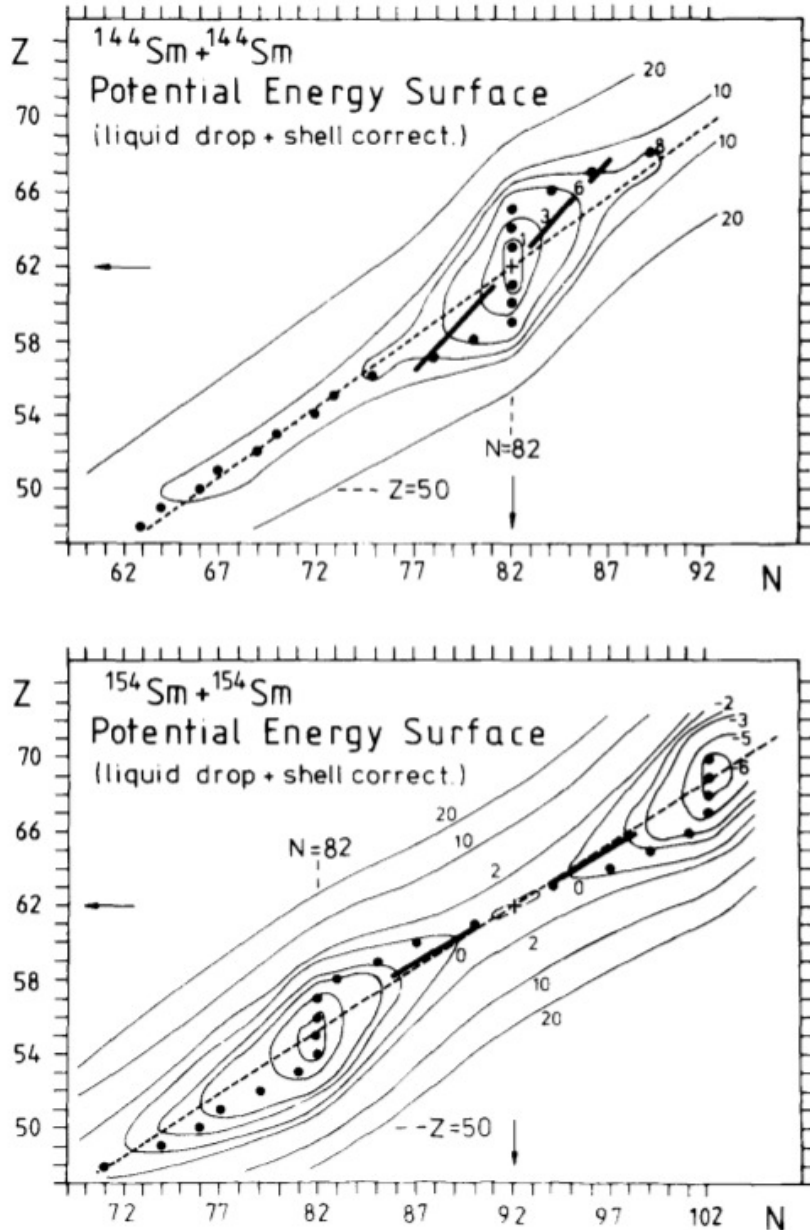


Figure 2.4 The (top) $^{144}\text{Sm} + ^{144}\text{Sm}$  and (bottom) $^{154}\text{Sm} + ^{154}\text{Sm}$  at energy of mean mass( $\langle A \rangle$ ) as function of atomic number(black dot) with potential energy surface(indicated as contour) and  $N/Z$  ratio(scattered line).[72]

## 2.2. REACTION KINEMATICS

Element	$M(Q_{gg}) _{MAX}$	$M _{N/Z equilibrium}$
$\text{Sn} \leftrightarrow \text{Pb } (Z_{PLF}=50)$	126	126.5
$\text{Sb} \leftrightarrow \text{Tl } (Z_{PLF}=51)$	129	128.9
$\text{Te} \leftrightarrow \text{Hg } (Z_{PLF}=52)$	132	130.9
$\text{I} \leftrightarrow \text{Au } (Z_{PLF}=53)$	135	133.2
$\text{Xe} \leftrightarrow \text{Pt } (Z_{PLF}=54)$	136	135.7
$\text{Cs} \leftrightarrow \text{Ir } (Z_{PLF}=55)$	137	138.3
$\text{Ba} \leftrightarrow \text{Os } (Z_{PLF}=56)$	138	141.0
$\text{La} \leftrightarrow \text{Re } (Z_{PLF}=57)$	141	143.8
$\text{Ce} \leftrightarrow \text{W } (Z_{PLF}=58)$	144	146.6

Table 2.1 The tabulated isotope with maximum ground-to-ground state Q-value ( $M(Q_{gg})|_{MAX}$ ), and N/Z equilibrium position ( $M|_{N/Z equilibrium}$ ) using fitting of effective Q-value distribution calculated by equation of V. V. Volkov [13]

properties of reaction mechanism such as angular, energy dissipation, and nucleon transfer along the reaction evolution cannot be described. Therefore more sophisticated theories are developed in order to explain reaction dynamics.

The mass with maximum  $Q_{gg}$ -value and N/Z equilibrium mass of this experiment is summarized in the table 2.1.

## 2.2 Reaction kinematics

The reaction kinematics of MNT reaction can be inferred from the angle and energy loss(total kinetic energy loss) of the reaction fragments so called Wilczynski plot. (See figure2.5) The MNT reaction the reaction starts from grazing angle and develops depending on the system. In case of heavy systems close to this experiment the angular distribution is concentrated near the grazing angle. This behavior can be explained by interplay between repulsive Coulomb interaction and attractive nuclear

## 2.2. REACTION KINEMATICS

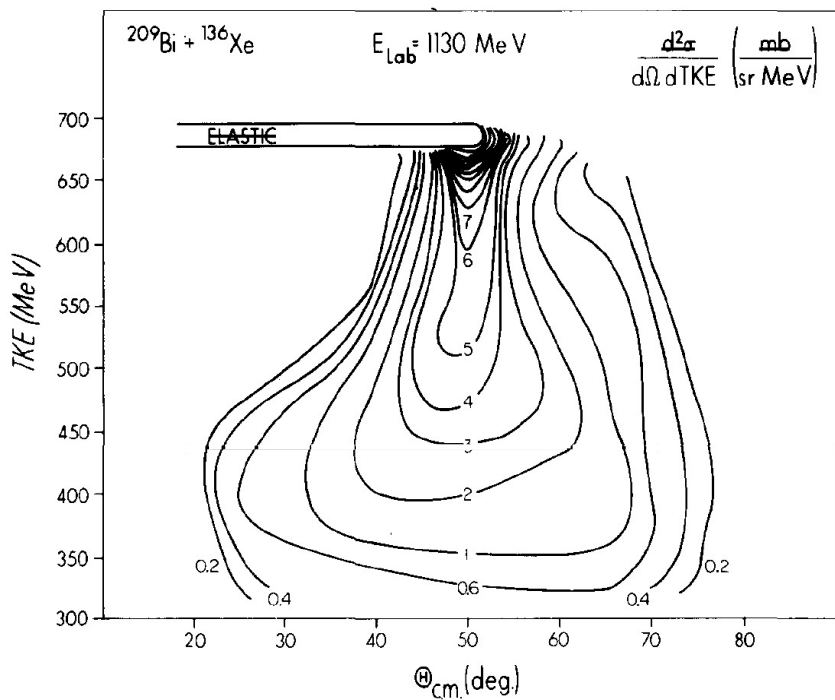


Figure 2.5 Wilczynski plot(TKE(assuming two body kinematics) vs  $\theta_{CM}$ ) of  $^{136}\text{Xe} + ^{209}\text{Bi}$  with  $E_{beam}=1130 \text{ MeV}.$ [55]

## 2.2. REACTION KINEMATICS

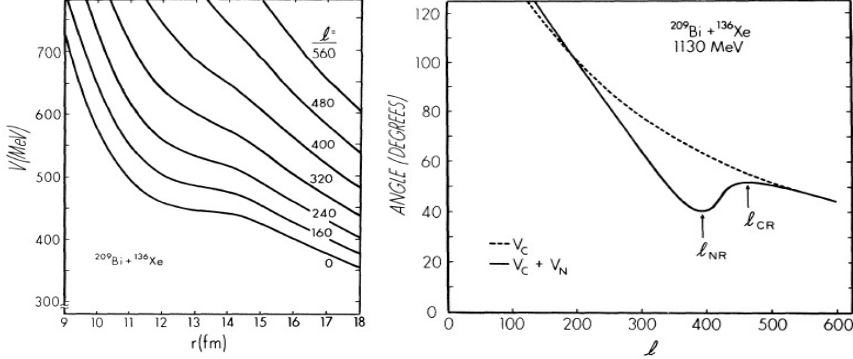


Figure 2.6 The calculated potential energy between  $^{136}\text{Xe} + ^{209}\text{Bi}$  [3] with  $E_{beam}=1130$  MeV assuming classical trajectory with spherical nuclei. (left) Potential energy as function of distance between two nuclei for different incident angular momentum. (right) Correlation of incident angular momentum and deflection angle.

force. (See figure 2.6)

The grazing angle can be calculated from the deflected angle from closest distance approach is same as the sum of the radius of two nuclides. If we assume only Coulomb interaction grazing angle can be described as (See textbook such as [1])

$$R_{Coulomb} = \frac{Z_{beam} Z_{target} e^2}{4\pi\epsilon\mu v_{beam}^2} \left(1 + \csc\left(\frac{\theta_{grazing}}{2}\right)\right) \quad (2.23)$$

$$R_{Coulomb} = 1.12(A_{PLF}^{1/3} + A_{TLF}^{1/3}) - 0.94(A_{PLF}^{-1/3} + A_{TLF}^{-1/3}) + 3[\text{fm}] \quad (2.24)$$

In this experiment case, calculated grazing angle is.

$$\theta_{grazing} = 32.6^\circ \quad (2.25)$$

$A_{beam,target}$ : Mass number beam, target nucleus  $\mu$ : reduced mass

## 2.2. REACTION KINEMATICS

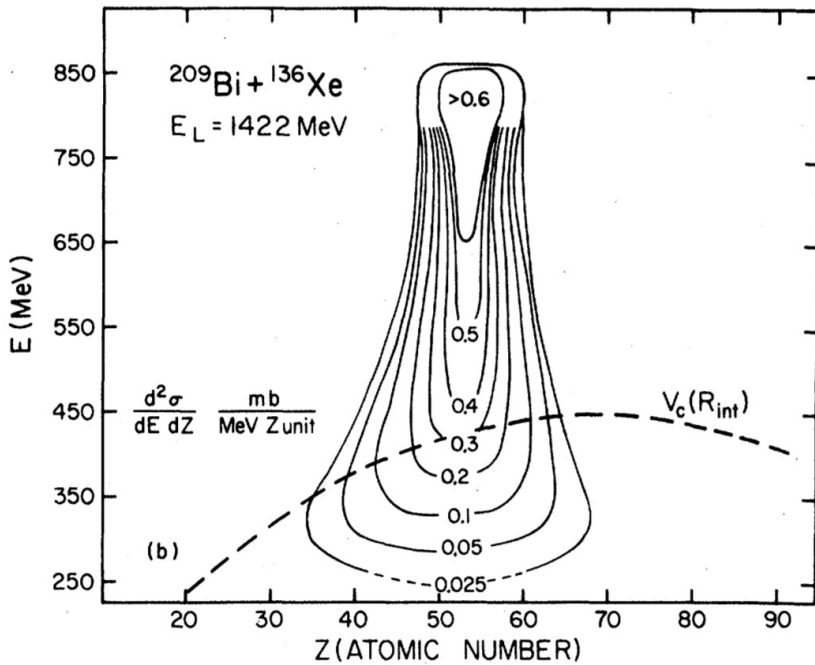


Figure 2.7 The total kinetic energy (assuming two body kinematics) vs atomic number distribution of  $^{136}\text{Xe} + ^{209}\text{Bi}$  at energy  $E_{Beam}=1422 \text{ MeV}$

The MNT reaction occurs mainly from the Coulomb rainbow to the nuclear rainbow point where grazing (or peripheral) collision occurs. Therefore, this experiment the focused angular distribution near grazing angle is expected.

The reaction fragment energy distribution ranging from elastic scattering and well below the Coulomb barrier energy, calculated by  $V_{Coulomb}$  and  $V_{Nuclear}$  using Bass nuclear potential (equation (7.37)~(7.39), (7.51.) of reference [1]) distance at two touching spherical nuclides. (Indicated as scattered line in the figure 2.7) The distribution below the Coulomb barrier energy indicates the large deformation between nuclides.

### 2.3. QUASI-ELASTIC AND DEEP INELASTIC REACTION

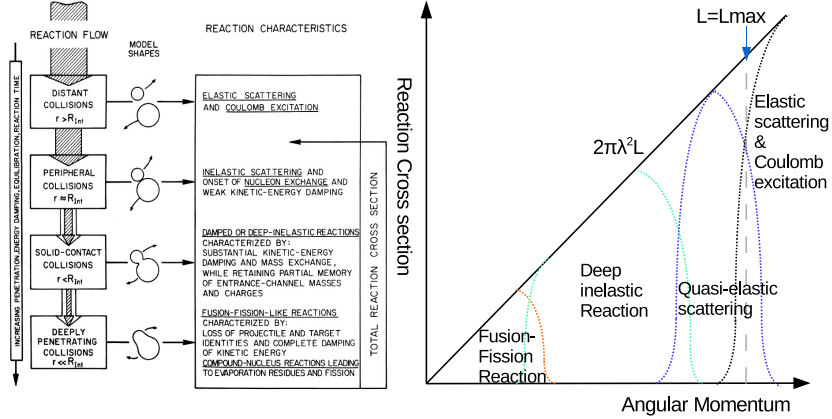


Figure 2.8 (right) Flow of reaction chart showing classification of the different reaction change as reaction evolves and the characteristics of reaction from [3]. (left) Reaction mechanism change as function of angular momentum(i.e. impact parameter) using sharp cutoff model.

### 2.3 Quasi-elastic and Deep Inelastic Reaction

Theoretically reaction mechanism of multi-nucleon transfer reaction can be classified with different reaction mechanisms of, quasi-elastic, deep-inelastic reactions for different impact parameter (i.e. incident angular momentum). (See figure 2.8)

The different reaction mechanisms are vaguely separated depending on reaction details such as impact parameter, number of transferred nucleons and incident energy. Experimentally, artificial energy loss cut, angular distribution differences (in light + heavy systems) and multi-Gaussian fitting of mass distribution(e.g. reference [68]) can be made. The multi-Gaussian fitting method utilizes the fact that mass distributions from direct reactions are narrowly peaked while the mass distribution

### *2.3. QUASI-ELASTIC AND DEEP INELASTIC REACTION*

from compound reaction on the other hand is wide. But there is no clear boundary between D.I.C. and Q.E. reactions especially in very heavy projectile and target systems.

Theoretically, they are treated with very different formalism. The quasi-elastic scattering (Q.E.) were treated with direct reaction picture. While the deep inelastic scattering (D.I.C.) (or referred as quasi-fission, strongly/heavily damped collision) were treated with statistical models.

#### **2.3.1 Deep inelastic collision (D.I.C.)**

The characteristic of deep inelastic transfer reaction of heavy ions, summarized by W. U. Schroder, and J. R. Huizenga [16] are written below.

- (1) Damping of the initial relative kinetic energy of the target and projectile nuclei takes place, resulting in a range of binary-product kinetic energies down to the Coulomb energies for charge centers of highly deformed fragments. The events that are the most relaxed are reminiscent of nuclear fission. What fraction of the kinetic-energy loss initially goes into internal excitation energy rather than into collective degrees of freedom is an open question of current interest.
- (2) Nucleon transfer or diffusion occurs during the short time the two nuclei are in contact and the magnitude of the nucleon exchange is correlated with the kinetic energy dissipation. However, the reaction-product mass distributions are bimodal with centroids near the target and projectile masses.
- (3) The angular distributions for the products with masses in the vicinity of the projectile mass have features characteristic of a fast peripheral or direct re-

### 2.3. QUASI-ELASTIC AND DEEP INELASTIC REACTION

action process occurring on a time scale of approximately  $10^{-21}$  sec or less. Products near the projectile mass produced by reactions for which the relative incident energy above the Coulomb barrier, i.e.  $(E_{CM} - E_{Coulomb})/E_{Coulomb}$ , is small tend to have differential cross sections that are preferentially sideways-peaked at angles slightly forward of  $\theta_{1/4}$  (the angle where the elastic-to-Rutherford cross-section ratio is 1/4).

Theoretically deep inelastic scattering reactions were treated with transportation theories. (See section 2.3.1) Which utilize classical equation of motion with diffusion process for interpretation of nuclear transfer(based on Fokker-Plank, Langevin equation) and treats energy dissipation by introducing friction. (See [3, 13, 15]and reference therein).

#### **Langevin equation model(transport model)**

The characteristics of MNT reaction dynamics(such as the monotonic increase of cross section width function of reaction time, the nuclear motion( $\frac{d\sigma}{dE d\theta}$ ) with huge dissipation energy), showed similar property of classical dynamics with friction and diffusion. The transport model introducing frictional force with classical equation of motion was firstly by developed Wilczynski [29], Beck, and Gross [30]. Recently, the nucleon transfer was described by diffusion process with Langevin equation was developed V. Zagrebaev, and W. Greiner [28]. Which predicted production of N~126 nuclides by  $^{136}\text{Xe} + ^{208}\text{Pb}$ . The theory considers potential change during the collision due to deformation, vibration and rotation of deformed nuclides.

The main term describing the nuclear transfer and change of mass asymmetry

### 2.3. QUASI-ELASTIC AND DEEP INELASTIC REACTION

can be written as equation 2.26

$$\frac{d\eta}{dt} = \frac{2}{A_{CN}}(D_A^{(1)}(\eta) + \sqrt{D_A^{(2)}(\eta)}\Gamma(t)) \quad (2.26)$$

$A_{CN}$ : Mass number of compound system,  $\eta$ :  $(2A_{PLF} - A_{CN})/A_{CN}$  (Mass asymmetry)

$D_A^{(1)/(2)}$ : Transport coefficient,  $\Gamma$ : Random motion(Gaussian distribution)

The transport coefficients are calculated by nuclear level density  $\lambda$ .

$$D_A^{(1)} = \lambda(A \rightarrow A + 1) - \lambda(A \rightarrow A - 1) \quad (2.27)$$

$$D_A^{(2)} = \frac{\lambda(A \rightarrow A + 1) - \lambda(A \rightarrow A - 1)}{2} \quad (2.28)$$

$$\lambda(A \rightarrow A \pm 1) \approx \lambda_0 e^{(V(R,\beta,A \pm 1) - V(R,\beta,A))/2T} \quad (2.29)$$

$$(2.30)$$

$V(R,\beta,A)$ : potential energy between colliding nuclides

The transfer probability is exponentially proportional to the potential energy difference, which coincides with the partial statistical equilibrium 2.1. The theory fairly coincides with experimental cross section of  $^{136}\text{Xe} + ^{209}\text{Bi}$  [58] which is close to this experimental system. (See figure 2.9)

#### Quasi-elastic scattering (Q.E.)

The quasi-elastic reaction refers to inelastic scattering and few nucleon transfers though low-lying states which have small energy losses in heavy ion reaction near Coulomb barrier. It was first used in order to distinguish reaction with small energy loss from more violent deep inelastic reactions which have massive nucleon exchange and energy dissipation [12]. Quasi-elastic reactions induced by light ions are most

### 2.3. QUASI-ELASTIC AND DEEP INELASTIC REACTION

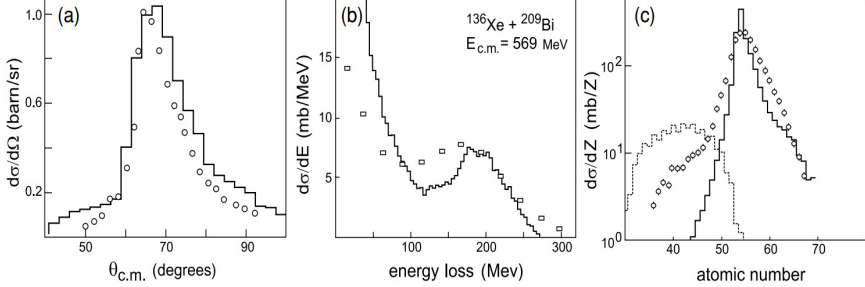


Figure 2.9 (left) Angular,(middle) energy-loss and (right)charge distributions of the Xe-like fragments obtained in the  $^{136}\text{Xe} + ^{209}\text{Bi}$  reaction at  $E_{CM} = 568$  MeV. The experimental result[58] are presented with circle while the result from the theory[28] is represented with solid line.

successfully described by the framework of distorted-wave Born approximation[1]. Where multi-step calculation including low lying states of different nuclides are preceded. Distorted wave theories have been very successful describing the reaction between light( $A < 20$ ) and heavy ( $A > 40$ ) systems.

In these theories it is assumed that elastic scattering is the most important channel. The removal of flux into other channels is treated by the introduction of an imaginary potential, with no individual channel contributing significantly to the absorption. The cross section is then given by [1]

$$\frac{d\sigma}{d\Omega} = \frac{\mu_i \mu_f}{(2\pi\hbar^2)^2} \frac{k_f}{k_i} \frac{1}{(2I_{beam} + 1)(2I_{PLF} + 1)} \sigma_{l,m} |T_{lm}(\theta)|^2 \quad (2.31)$$

$$T_{lm} = \int \chi^*(r_f, k_f) \langle \psi_{nf} | V_{eff} | \psi_{ni} \rangle \chi(r_i, k_i) dr_i dr_f \quad (2.32)$$

$\chi_{i,f}$ : distorted wave functions describing the entrance and exit channel.

$\psi_{ni,nf}$ : bound state wave function of transferred particle at initial and final states.

## 2.4. UNIFIED MODELS MNT REACTIONS

$V_{eff}$ : Effective interaction potential calculated from an optical potential whose parameters have been adjusted to fit data for elastic scattering.

More sophisticated coupled channel calculation was used to include pair transfer of two correlated nucleons. These calculation shows good agreement in the medium mass ( $30 > A > 80$ ) with low excitation energy. (e.g. recent works of Corradi *et al.* [9] see figure 2.10)

The transition between Q.E. and D.I.C. happens continuously in the experiment especially at reaction between heavy isotopes on the other hand, the theory of Q.E. are described in direct reaction picture while the D.I.C. are described by statistical picture.

Thus the theory describing both reactions with unified picture is needed. The two different models are widely used to describe MNT reaction named GRAZING model, and time dependent Hartree-Fork (TDHF) model.

## 2.4 Unified models MNT reactions

### 2.4.1 Grazing model

Grazing model developed by A. Wither [20] is widely used as a standard for cross section measurements. The model is based on microscopic picture of form factor for single nucleon transfer. For multi nucleon transfer with energy damping of the reaction, the semi-classical approach was used. The source of energy dissipation is based on excitation of collective modes of nuclides. (Instead of nucleon exchange) The for given trajectory (assumed as classical trajectory), main part concerning nucleon transfer from i-th channel to f-th channel (including low excitation states and collective modes) can be written as equation 2.33.

## 2.4. UNIFIED MODELS MNT REACTIONS

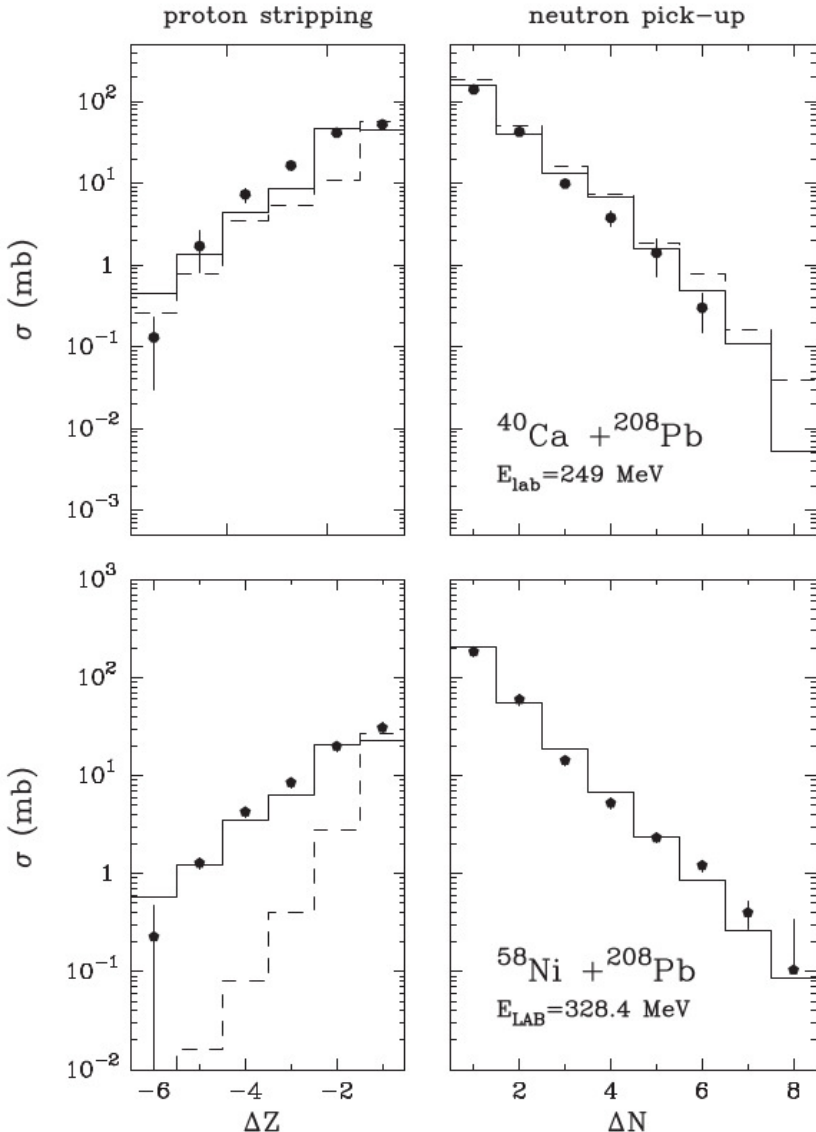


Figure 2.10 Total cross sections of pure proton stripping (left frames) pure neutron and pick-up (right frames) channels for the  $^{40}\text{Ca} + ^{208}\text{Pb}$  and  $^{58}\text{Ni} + ^{208}\text{Pb}$  systems. The Complex WKB(CWKB) model calculations with take into account the effect of the evaporation, (dashed lines) results of calculations with only independent particle transfers,(full lines) including a pair transfer mode for both neutrons and protons

## 2.4. UNIFIED MODELS MNT REACTIONS

$$p_{if}^{NS} = \frac{2\pi}{(\hbar\omega_0)^2} |f_{m_f m_i}^{NS}|^2$$

$$\times \exp\left(-\left(\frac{Q - Q_{opt}^{NS}}{\hbar\omega_0}\right)^2 + (m_i + m_f)\frac{k_\perp}{\kappa} - \frac{k_\perp^2}{4\kappa}R_0\right) \quad (2.33)$$

$f_{m_f m_i}^{NS}$ : Form factor from i-th channel to f-th channel.

$m_{i/f}$ : magnetic quantum number of i/f-th channel  $\omega_o$ : width of reaction window (i.e.  $(collision time)^{-1}$ ).

$Q, Q_{opt}$ : Q-value, optimum Q-value(potential energy difference between initial and exit channel).

$k_\perp$ : recoil momentum at distance  $r_0$

$\kappa$ : exponential slope of form factor

The averaged form factor over single particle quantum numbers with magnetic quantum number  $m_{i/f}$  is calculated based on the empirical parametrization.

$$<|f_{m_f m_i}(r_0)|^2> = \frac{1}{n} \sum l_f j_f l_i j_i |f_{m_f m_i}^{(n_i, l_i, j_i)(n_f, l_f, j_f)}|^2 \quad (2.34)$$

(2.35)

$$= \frac{K}{1 + \exp(\kappa - R_{beam} - R_{target})} < N_{(n_i, l_i, j_i)}^2 > < N_{(n_f, l_f, j_f)}^2 > \varsigma(E)^2$$

$$\times \left(\frac{\hbar^2}{4M}\right)^2 \left(\frac{R_{beam} R_{target}}{R_{beam} + R_{target}}\right)^2 \exp\left(-S_l \left(\frac{m_i m_f}{2}\right)^2\right) \quad (2.36)$$

$$n: \approx 4(l_f^{max} - |m_f|)(l_i^{max} - |m_i|)$$

$< N_{(n, l, j)} >$ : Average amplitude of single particle wave function(1.6/A (neutrons),1.0/A

## 2.4. UNIFIED MODELS MNT REACTIONS

(protons))

$\kappa$ : exponential slope of form factor neutron  $\rightarrow 0.58 + 0.25(A_{beam}^{-1/3} + A_{target}^{-1/3})$

protons  $\rightarrow 0.83 + 0.05(A_{beam}^{-1/3} + A_{target}^{-1/3})$

$K, S_l$ : (empirical adjustable parameter)  $K=0.25$ (neutrons), $0.30$ (protons),  $S_l = \frac{1.6}{l_f^{max} + l_i^{max}}$

Besides the complicated form factor part, the main contribution of transfer probability comes from the exponential dependence of the Q-value corrected with the recoil of the transferred nucleon.

The GRAZING model can be used at rather low energy due to following reasons. The classical trajectory assuming point like nuclei is used, which will deviate near the closest distance approach at energy higher than Coulomb barrier. The main part of the reaction in high excitation energy, associated with single particle states in the continuum cannot be described. Also the actual calculation model assumes potential with no deformation or rotation. Thus in the actual calculations, the impact parameter range was limited to region larger than the nuclear rainbow which is  $\sim 14$  fm in this experiment. The GRAZING models are extensively tested in the region of mid-mass projectile with heavy target systems such as  $^{64}\text{Ni} + ^{238}\text{U}$  [51],  $^{62}\text{Ni}/^{58}\text{Ni} + ^{208}\text{Pb}$  [53, 52]. (See figure 2.11) The GRAZING calculation compared with experimental cross section will be discussed in chapter 5.

### 2.4.2 Time dependent Hartree Fork (TDHF) theory

The time dependent Hartree Fork theory is microscopic model based on mean field theory. (recently reviewed by C. Simenel [31])

The system is described by purely quantum mechanical terms of wave function and operators. The N independent particle wave function inside the mean field po-

## 2.4. UNIFIED MODELS MNT REACTIONS

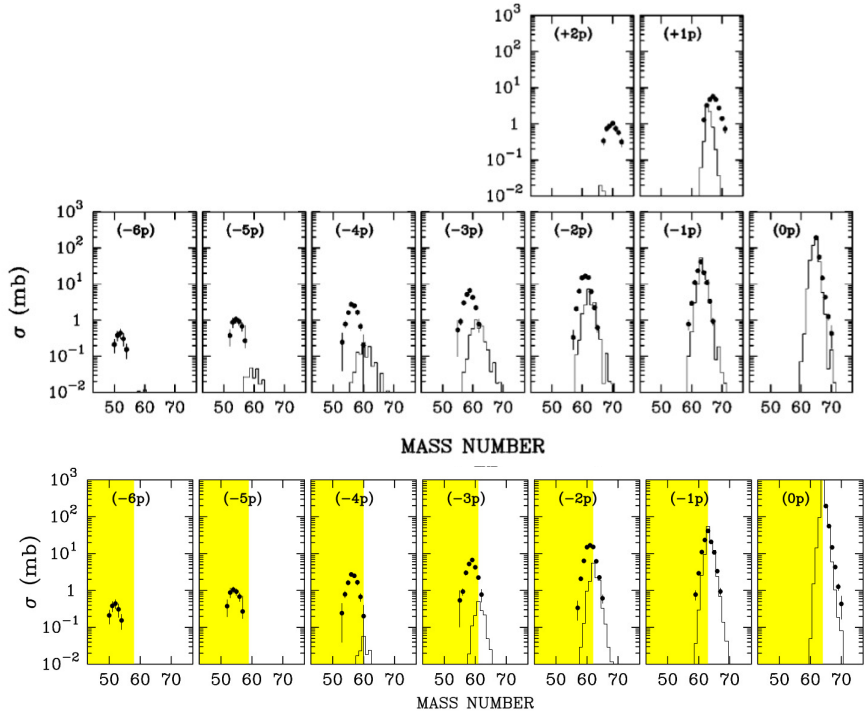


Figure 2.11 (top) Cross section of  $^{64}\text{Ni} + ^{238}\text{U}$  of  $-6\text{p} \sim + 2\text{p}$  channel, compared with GRAZING calculation.(bottom) Cross section of  $^{58}\text{Ni} + ^{208}\text{Pb}$  of  $-6\text{p} \sim 0\text{p}$  channel, compared with GRAZING calculation. The under estimation can be observed in proton pickup channels and proton stripping channels with number of proton stripping  $> 3$ .

## 2.4. UNIFIED MODELS MNT REACTIONS

tential is assumed, which can be written with Slater determinant.

$$|\phi\rangle = \prod_{i=1}^N a_i^\dagger |-\rangle = \prod_{i=1}^N |\varphi_i\rangle \quad (2.37)$$

The Hartree Fork equation can be written as

$$i\hbar \frac{\partial \rho}{\partial t} = [h[\rho], \rho] \quad (2.38)$$

where  $h[\rho]$  is the Hartree-Fork single particle Hamiltonian which can be written as.

$$\rho = \sum_{i=1}^N |\varphi_i\rangle \langle \varphi_i| \quad (2.39)$$

$$h_{ij}[\rho] = \frac{\delta \langle \phi | \hat{H} | \phi \rangle}{\delta \rho_{ij}} \quad (2.40)$$

The Hamiltonian described by full Skyrme energy density functional [36].

$$\begin{aligned} \hat{H}[\rho]\phi_m(\mathbf{r}, \mathbf{s}) &= \sum_{s'} [(-\nabla(\frac{\hbar^2}{2m} + Y_o)\nabla + U_{om}(\mathbf{r}) + iC_{om} \cdot \nabla)\delta_{ss'} \\ &\quad + \mathbf{V}_{om}(\mathbf{r}) \cdot \langle \mathbf{s} | \sigma | \mathbf{s}' \rangle + i\mathbf{W}_{om}(\mathbf{r}) \cdot (\langle \mathbf{s} | \sigma | \mathbf{s}' \rangle \times \Delta)]\phi_m(\mathbf{r}, \mathbf{s}') \end{aligned} \quad (2.41)$$

$$Y_o = A_3\rho + A_4\rho_o \quad (2.42)$$

$$\begin{aligned} U_o(\mathbf{r}) &= 2A_1\rho^2 + 2A_2\rho_i^2 + A_3(\tau + i\nabla \cdot \mathbf{j}) + A_4(\tau_o + i\nabla \cdot \mathbf{j}_o) \\ &\quad + A_5\Delta\rho + 2A_6\Delta\rho_i + (2 + \alpha)A_7\rho^{1+\alpha} + A_8(\alpha\rho^{alpba-1} \sum_o rho_o^2 + 2\rho^\alpha\rho_o) \\ &\quad + A_9(\rho\nabla \cdot J + \nabla \cdot J_o) + 2\rho^\alpha(A_{12}\mathbf{S} + A_{13} \sum_o \mathbf{S}_o) \end{aligned} \quad (2.43)$$

$$V_o = A_9(\nabla \times (\mathbf{j} + \mathbf{j}_o) + 2A_{10}\mathbf{S} + 2A_{11}\mathbf{S}_o + \rho^\alpha(A_{12}\mathbf{S} + A_{13}\mathbf{S}_o)) \quad (2.44)$$

## 2.4. UNIFIED MODELS MNT REACTIONS

$$W_o = -A_9 \nabla(\rho + \rho_o) \quad (2.45)$$

$$C_o = 2A_3 \mathbf{j} + 2A_4 \mathbf{j}_q - A_9 \nabla \times ((S) + (S)_q) \quad (2.46)$$

where  $o$  is isospin, and  $s, s'$  is the spin of single particle,  $A_{1 \sim 13}$  and  $\alpha$  is adjustable parameters.

$$\rho = \sum_{m,s} \varphi_m^*(\mathbf{r}, \mathbf{s}) \varphi_m(\mathbf{r}, \mathbf{s}) \quad (2.47)$$

$$\tau = \sum_{m,s} |\nabla \varphi_m(\mathbf{r}, \mathbf{s})|^2 \quad (2.48)$$

$$\mathbf{j} = \frac{1}{2i} \sum_{m,s} (\varphi_m^*(\mathbf{r}, \mathbf{s}) \nabla \varphi_m(\mathbf{r}, \mathbf{s}) + \varphi_m(\mathbf{r}, \mathbf{s}) \nabla \varphi_m^*(\mathbf{r}, \mathbf{s})) \quad (2.49)$$

$$\mathbf{J} = -i \sum_{m,s,s'} \nabla \varphi_m^*(\mathbf{r}, \mathbf{s}) \times \nabla \varphi_m(\mathbf{r}, \mathbf{s}') < \mathbf{s} | \sigma | \mathbf{s}' > \quad (2.50)$$

$$\mathbf{S} = \sum_{m,s,s'} \varphi_m^*(\mathbf{r}, \mathbf{s}) \varphi_m(\mathbf{r}, \mathbf{s}') < \mathbf{s} | \sigma | \mathbf{s}' > \quad (2.51)$$

The actual calculation using same beam target combination as this experiment was done by work of K, Sekizawa and K, Yabana with the same process presented in the reference of [33]. The wave function of the can be written as independent fermions particles with total number of  $N$  ( $= N_{PLF} + N_{PLF}$ ) nucleons by Slater determinant. The wave function before collision could be expressed by single particle orbital state wave functions.

$$\Phi((\mathbf{x}_1, \mathbf{p}_1), \dots, (\mathbf{x}_N, \mathbf{p}_N)) = \frac{1}{N} \text{Det}(\phi) \quad (2.52)$$

## 2.4. UNIFIED MODELS MNT REACTIONS

In the initial stage, the wave function is localized in each spatial regions formulating the eigenstate of number operator.

The wave function of Hartree-Fork equation is solved iteratively as time by the Hamiltonian. During the collision the single particle wave function is altered by potential from other nuclei, and the wave function extends to the other spatial region (i.e. not eigenstate of number operator).

$$\psi_i((\mathbf{x}_i, \mathbf{p}_i), t + \Delta t) = e^{-i\Delta t/\hbar(t+\Delta t/2)}|\phi(t) > \quad (2.53)$$

$$\Psi((\vec{x}_1, \vec{p}_1), \dots, (\vec{x}_N, \vec{p}_N)) = \frac{1}{N} \text{Det}(\psi) \quad (2.54)$$

Which satisfy normalization condition with notation  $\int d\mathbf{x}_i = \int d\vec{p}_i \int d\vec{x}_i$ .

$$\int_V d\mathbf{x}_1 \dots \int_V d\mathbf{x}_N |\Psi((\mathbf{x}_1, \mathbf{p}_1), \dots, (\mathbf{x}_N, \mathbf{p}_N))|^2 = 1 \quad (2.55)$$

The in the calculation, grid of spacing 0.8 fm with box size of  $60 \times 60 \times 26$  grid points was used. The time evolution of the single orbital wave function was calculated by fourth-order Taylor expansion, with time step of  $\Delta t = 0.2$  fm/c.

The calculation space before (i) and after (f) collision is divided by  $V_{PLF}^{i/f}$  and  $V_{PLF}^{i/f}$  ( $V^{i/f} = V_{PLF}^{i/f} + V_{PLF}^{i/f}$ ). The transfer of the nucleons between target and projectiles are treated by particle number operator [31, 33].

The probability of  $n$  nucleons are in the PLF ( $P_n$ ) can be written as,

$$P_n = \sum_{s(\tau_i : V_{PLF}^n V_{TLF}^{N-n})} \int_{\tau_1} d\mathbf{x}_1 \dots \int_{\tau_N} d\mathbf{x}_N |\Psi((\mathbf{x}_1, \mathbf{p}_1), \dots, (\mathbf{x}_N, \mathbf{p}_N))|^2 \quad (2.56)$$

where  $s(\tau_i : V_{PLF}^n V_{TLF}^{N-n})$  is the combination of nucleons where  $n$  nucleon is in PLF.

This can be simplified when we introduce particle number operator of certain spatial region ( $\hat{N}_\tau$ ), which can be written as,

$$\hat{N}_\tau = \sigma_{i=1}^N \Theta_\tau(\mathbf{r}_i) \quad (2.57)$$

## 2.4. UNIFIED MODELS MNT REACTIONS

where  $\tau = V_{PLF}$  or  $V_{TLF}$ . And  $\Theta_\tau(\mathbf{r}_i)$  space division function which determine the position of each nuclei can be defined as

$$\Theta_\tau(\mathbf{r}_i) = \begin{cases} 1 & \mathbf{r}_i \in \tau \\ 0 & \mathbf{r}_i \notin \tau \end{cases}$$

. Then we can introduce number projection operator  $\hat{P}_n$  for getting  $P_n$ , which can be expressed as,

$$\hat{P}_n = \sum_{s(\tau_i:V_{PLF}^n V_{TLF}^{N-n})} \Theta_{\tau_1}(\mathbf{r}_1) \dots \Theta_{\tau_N}(\mathbf{r}_N)$$

. Then  $P_n$  can be written as,

$$\begin{aligned} P_n = <\Psi|\hat{P}_n|\Psi> &= \int d\mathbf{x}_1 \dots \int d\mathbf{x}_1 \times \psi_1^*(\mathbf{x}_1) \dots \psi_N^*(\mathbf{x}_N) \hat{P} \det(\psi_i \mathbf{x}_j) \\ &= \sum_{s(\tau_i:V_{PLF}^n V_{TLF}^{N-n})} \det <\psi_i|\psi_j>_{\tau_i} \end{aligned} \quad (2.58)$$

In the actual calculation proton and neutrons are calculated separated and the probability is calculated for different impact parameter  $d$ . And the number projection operator uses equivalent expression introduced by [31] for saving computational cost.

The probability  $n_Z$  number of protons and  $n_N$  neutrons in PLF with impact parameter  $b$  can be expressed as,

$$P_{n_Z, n_N}(b) = P_{n_Z}(b) P_{n_N}(b) \quad (2.59)$$

The cross section ( $\sigma_{tr}(n_Z, n_N)$ ) of PLF with  $n_Z$  number of protons and  $n_N$  neutrons can be calculated as

$$\sigma_{tr}(n_Z, n_N) = 2\pi \int_{b_{min}}^{\infty} db b P_{n_Z, n_N}(b) \quad (2.60)$$

The energy dissipation during the reaction is treated by first, collective motions coupled with one particle one hole (1p1h) excitations, and second single particle

#### *2.4. UNIFIED MODELS MNT REACTIONS*

emission to the continuum (particle evaporation). The TDHF calculations assumptions directly related to the nucleon transfer are not embedded in the equation. The TDHF calculation result compared with  $^{40}\text{Ca} + ^{112}\text{Sn}$ ,  $^{58}\text{Ni} + ^{208}\text{Pb}$  experimental results showed fairly good agreement. (See figure 2.12) The comparison between TDHF calculation result[35] and experimental result will be discussed in chapter 5.

## 2.4. UNIFIED MODELS MNT REACTIONS

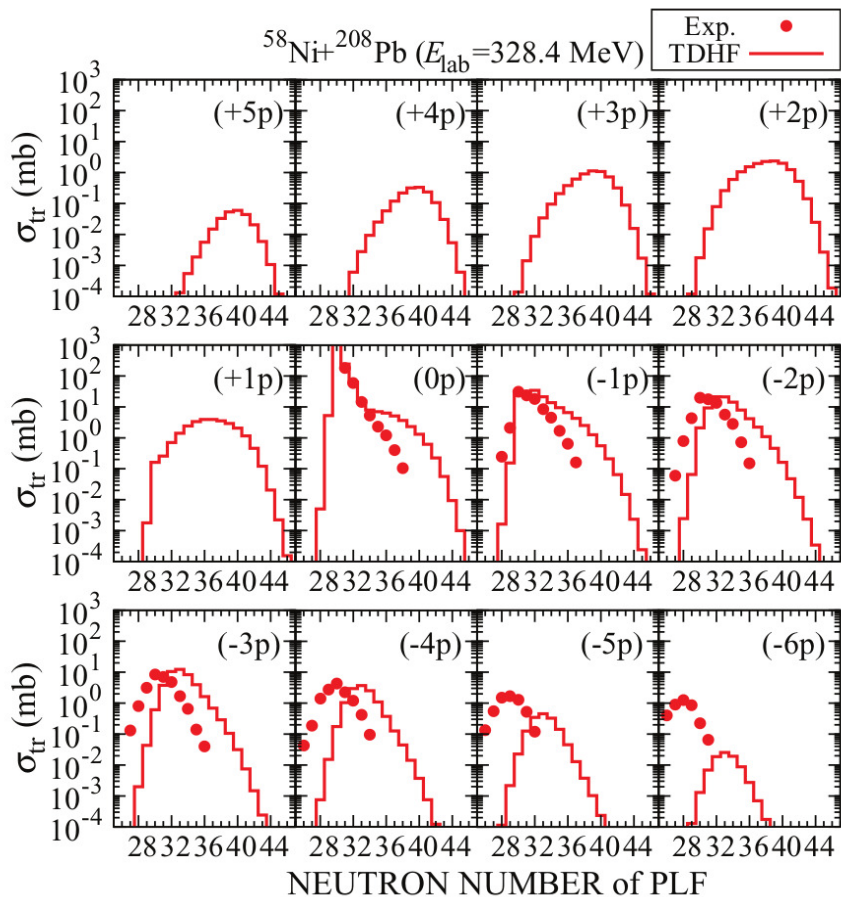


Figure 2.12 The cross section of  $^{58}\text{Ni} + ^{208}\text{Pb}$  (red solid line) TDHF calculation result compared with (red circle) experimental result.

# Chapter 3

## Experimental Setup

In this section, the detailed description of detectors used in the experiment and the experimental conditions during the actual experiment will be discussed.

### 3.1 Accelerator Facility

The experiment was done at G1 experimental hall at GANIL, Cean, France. The ions are produced from ECR ion source, which utilize cyclotron resonance phenomenon. The microwaves with the electron cyclotron resonance are injected. The electrons inside are accelerated and ionize the atoms nearby by transferring energy by collision creating plasma. The ions from plasma are transported to injector cyclotron ( $K=25$ ), electrons in  $^{136}\text{Xe}$  are stripped at the exit of cyclotron by carbon foil with charge state of  $20+$ . Then ions are injected to main cyclotrons.  $K$  value which describes exit kinetic energy of the cyclotron can be written as  $\frac{E}{A} = K(\frac{Q}{A})^2$ .

GANIL has two identical cyclotron accelerators CSS1, CSS2 which has  $K=380$

### 3.1. ACCELERATOR FACILITY

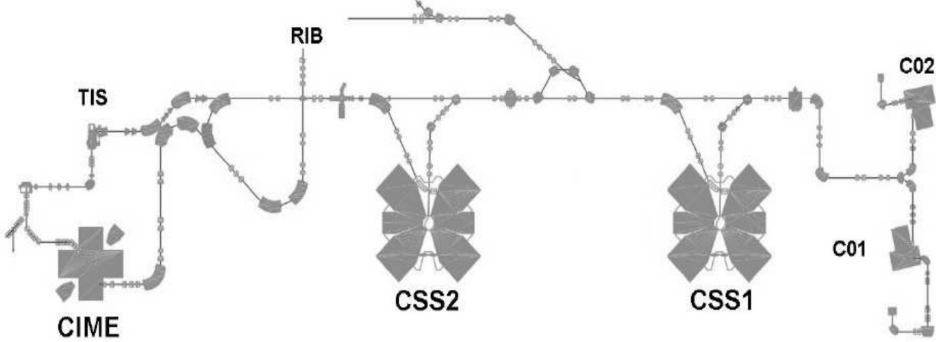


Figure 3.1 Accelerator facility at GANIL. C01 and C02 are the injector cyclotrons. CSS1 and CSS2 are the separated  $K = 380$  cyclotrons. TIS is the ISOL target for SPIRAL. CIME is the  $K = 265$  cyclotron for the radioactive beam. The RIBs are delivered after selection by the  $\alpha$ -shaped spectrometer.

Total emittance	$10\pi$ [ mmrad]
Energy spread	$2 \times 10^{-3}$ [FWHM]
Beam pulse time	$\pm 1.5$ [% of RF period]

Table 3.1 Specification of CSS1 cyclotron used in the experiment [91]

delivers stable heavy-ion to the experimental hall, or bombarded to ISOL target called TIS. The RI beams produced from ISOL is re-accelerated by CIME cyclotron ( $K=265$ ) (See figure. 3.1 and Table. 3.1). CSS1, 2 cyclotrons can be used one next to another to accelerate beam energy up to  $\sim 45$  MeV/u for isotope with mass around  $A \sim 125$ . In this experiment, single CSS1 cyclotron was used to deliver  $^{136}\text{Xe}$  beam to the G1 experimental hall, since stable isotope with relatively low energy is needed. The spec. of CSS1 cyclotron is summarized in Table. 3.1.

### 3.2. BEAM TARGET COMBINATION CONSIDERATION

## 3.2 Beam target combination consideration

### 3.2.1 Beam and target nuclei

The  $^{136}\text{Xe}$  beam was used because the reaction Q-values are strongly depends on the lighter projectile than the target. Therefore the selection of projectile is more important than selection of the target in order to populate the desired transfer channels.  $^{136}\text{Xe}$  is the most n-rich projectile  $Z < 60$  due to  $N = 82$  shell closure and have the similar N/Z ratio of the target nucleus. This N/Z ratio makes potential Q-value isotropic resulting feasibility of target nuclei. (See chapter 2) (From these considerations are also shown in theoretical predictions [21, 28] used  $^{136}\text{Xe}$ .) The last reason is that the  $^{136}\text{Xe}$  beam is easy to produce from the ionsource which makes the ideal experimental condition. The  $^{198}\text{Pt}$  target was chosen since it is the one of most neutron rich nuclides near and closer to the neutron rich side of the black spot near  $N \sim 126$ .

### 3.2.2 Beam energy

The MNT reaction occurs near Coulomb barrier, which determines the order of beam energy to several MeV/u. The total reaction, cross section increases exponentially as the beam energy increases due to the Coulomb barrier. But the increase in the beam energy, results proportional increase of excitation energy of the reaction fragments. This increase of excitation energy, decreases the survival probability of fragments from the secondary processes like particle evaporation (mostly n, p,  $\alpha$ ), and fission. (Very similar to the hot/cold fusion process.) Thus the energy of the system should be decided compromising this contrarily results.

In the original proposal, the beam energy 7 MeV/u was chosen, which is  $\sim$

### 3.2. BEAM TARGET COMBINATION CONSIDERATION

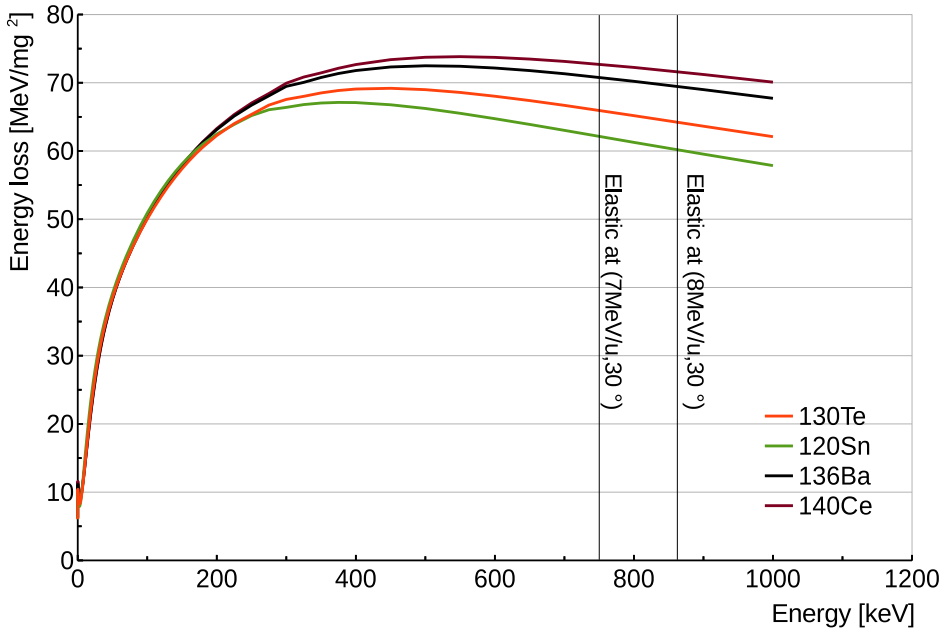


Figure 3.2 Bragg curve of selected isotopes. The isotope with larger proton number shows larger energy loss with same incident energy. The energy difference between different channels becomes less than 0.3 MeV for  $E < 400$  MeV.

35% above the Coulomb barrier ( $E_{Coulomb}=416$  MeV calculated from GRAZING code). But due to the Bragg curve inside the ionization chamber of VAMOS spectrometer beam energy was needed to be increased. Because the sudden decrease of the stopping power after the Bragg peak makes it impossible to recognize the proton number determination using dE-E method in the analysis. (See figure 3.2) The incident energy less than Bragg peak, e.g.  $\sim 400$  MeV the energy loss separation between different nuclides with one proton becomes less than  $0.38$  MeV/ mg/cm<sup>2</sup> in proton pickup channels, corresponding to difference in energy loss 0.5 MeV inside

### **3.2. BEAM TARGET COMBINATION CONSIDERATION**

the one segment of the ionization chamber (See section. While at incident energy near Bragg peak at  $\sim 550$  MeV the energy loss difference between nuclides with one proton difference is  $\sim 1$  MeV. Thus in order to measure cross section from the reactions the most of the reaction fragments should be outside of the Bragg peak. From this reason the actual experiment beam energy was adjusted to 8 MeV/u, which is  $\sim 55\%$  above the Coulomb barrier. In the experiment beam energy measured from the cyclotron  $E_{Beam}=7.95056$  MeV/u from measured  $B\rho=2.76536$  T·m (mass of  $^{136}Xe=135.9072$  amu).

#### **3.2.3 Spectrometer angle**

Once the energy of the beam was fixed, the angle of spectrometer was set to  $30^\circ$ , similar to the calculated grazing angle of the system( $\sim 32^\circ$ ). The spectrometer angle was set as the actual grazing angle was determined also from tandem experiment, which will be explained in detail at subsection 3.5.

#### **3.2.4 Target thickness**

The thickness of the target depends on the characteristic of the material. In order to avoid the contamination of the unwanted reaction fragments, target was made to stand its own weight, but thin enough to have enough energy resolution to separate reactions. Accounting these reasons the thickness was set to  $1.3$  mg/cm $^2$  with the error of 10%. This accuracy of the target thickness limits the effective number of the experiment to two.

### 3.2. BEAM TARGET COMBINATION CONSIDERATION

$B\rho$ [ T.m ]	1.10	1.12	1.13	1.15	1.18
$^{136}\text{Xe}$ [mb/sr]	140	181	195	222	247
$^{142}\text{Xe}$ [%]	3.7	4.8	5.3	6.3	2.7
$^{134}\text{Ce}$ [%]	8.0	8.7		9.2	5.7
$^{138}\text{Ba}$ [%]	5.6	6.6	7.0	7.9	

Table 3.2 Acceptance calculation result from simulation. Both accepted events from elastic scattering and detection efficiency of reaction fragments increases proportional to the  $B\rho$

#### 3.2.5 $B\rho$ of spectrometer

The  $B\rho$  of the spectrometer was deduced, after above physical conditions were fixed. Since the VAMOS cannot accept all the MNT reaction channels due to its wide range of momentum, and angular distribution. The reference  $B\rho$  of spectrometer need to be set to maximize the acceptance of the reaction fragments aimed in this experiment. (i.e. proton pickup, neutron stripping channels of projectile-like fragment which is partner of target-like fragment with neutron rich side.) And to avoid the neutron evaporation, reaction from small excitation energy should be accepted the most. From this, momentum acceptance range of the reaction fragments can be optimized.

The simulation was done to deduce efficiency of different nuclides, In order to find the optimum value of  $B\rho$ . Four reaction channels out of various proton pickup channels (figure 3.4) were calculated to decrease the number of computation and to focus on the proton pickup channels. The two reaction channels far from elastic ( $^{142}\text{Xe} (+6n)$ ,  $^{134}\text{Ce} (+4p, -6n)$ ), one channel at the center ( $^{138}\text{Ba} (+2p, 0n)$ ) and elastic scattering were calculated.(See table 3.3) Event generation of fragments was

### 3.2. BEAM TARGET COMBINATION CONSIDERATION

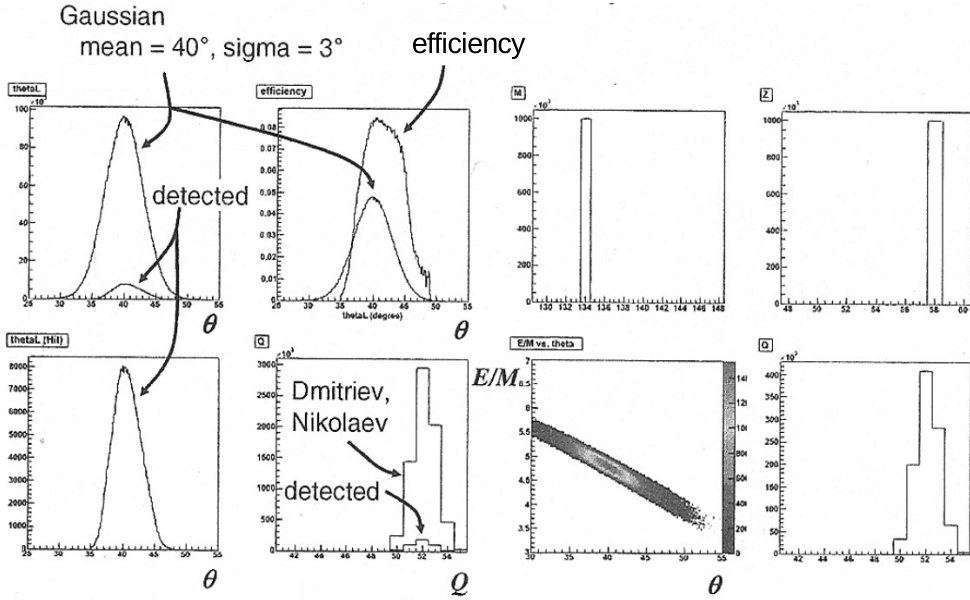


Figure 3.3 Simulation result of  $^{134}\text{Ce} + ^{200}\text{W}$  for efficiency estimation with beam energy 7MeV/u. (top leftmost) Angular distribution of produced event and detected events. (top, second from left)Detection efficiency of  $^{134}\text{Ce}$  correlated to angle. (top, third from left/rightmost) Mass/proton number of fragment( $=^{134}\text{Ce}$ ). (bottom, leftmost) Accepted angular distribution(magnification from top leftmost figure). (bottom, second from left) Charge state distribution of produced event and detected events. (bottom, third from left) Fragment kinetic energy correlated with angle. (bottom, rightmost) Accepted charge state distribution (magnification from top leftmost figure).

### 3.2. BEAM TARGET COMBINATION CONSIDERATION

$^{134}\text{Ce}$	$^{135}\text{Ce}$	$^{136}\text{Ce}$	$^{137}\text{Ce}$	$^{138}\text{Ce}$	$^{139}\text{Ce}$	$^{140}\text{Ce}$	$^{141}\text{Ce}$	$^{142}\text{Ce}$	$^{143}\text{Ce}$	$^{144}\text{Ce}$	$^{145}\text{Ce}$	$^{146}\text{Ce}$	+4p
0.81 6.3%	0.81 6.3%	0.82 6.4%	0.82 6.4%	0.82 6.4%	0.83 6.3%	0.83 6.2%	0.83 6.2%	0.83 6.0%	0.84 5.9%	0.84 5.8%	0.84 5.7%	0.84 5.6%	
$^{133}\text{La}$	$^{134}\text{La}$	$^{135}\text{La}$	$^{136}\text{La}$	$^{137}\text{La}$	$^{138}\text{La}$	$^{139}\text{La}$	$^{140}\text{La}$	$^{141}\text{La}$	$^{142}\text{La}$	$^{143}\text{La}$	$^{144}\text{La}$	$^{145}\text{La}$	+3p
0.82 6.4%	0.82 6.4%	0.83 6.4%	0.83 6.3%	0.83 6.1%	0.83 6.0%	0.84 5.8%	0.84 5.7%	0.84 5.5%	0.84 5.4%	0.85 5.2%	0.85 5.0%	0.85 5.0%	
$^{132}\text{Ba}$	$^{133}\text{Ba}$	$^{134}\text{Ba}$	$^{135}\text{Ba}$	$^{136}\text{Ba}$	$^{137}\text{Ba}$	$^{138}\text{Ba}$	$^{139}\text{Ba}$	$^{140}\text{Ba}$	$^{141}\text{Ba}$	$^{142}\text{Ba}$	$^{143}\text{Ba}$	$^{144}\text{Ba}$	+2p
0.83 6.3%	0.83 6.2%	0.84 6.0%	0.84 5.8%	0.84 5.6%	0.84 5.4%	0.85 5.0%	0.85 5.0%	0.85 4.7%	0.85 4.6%	0.85 4.4%	0.85 4.2%	0.86 4.2%	
$^{131}\text{Cs}$	$^{132}\text{Cs}$	$^{133}\text{Cs}$	$^{134}\text{Cs}$	$^{135}\text{Cs}$	$^{136}\text{Cs}$	$^{137}\text{Cs}$	$^{138}\text{Cs}$	$^{139}\text{Cs}$	$^{140}\text{Cs}$	$^{141}\text{Cs}$	$^{142}\text{Cs}$	$^{143}\text{Cs}$	+1p
0.84 5.9%	0.84 5.8%	0.84 5.5%	0.85 5.3%	0.85 4.9%	0.85 4.7%	0.85 4.3%	0.86 4.2%	0.86 4.0%	0.86 3.9%	0.86 3.7%	0.86 3.7%	0.86 3.6%	
$^{130}\text{Xe}$	$^{131}\text{Xe}$	$^{132}\text{Xe}$	$^{133}\text{Xe}$	$^{134}\text{Xe}$	$^{135}\text{Xe}$	$^{136}\text{Xe}$	$^{137}\text{Xe}$	$^{138}\text{Xe}$	$^{139}\text{Xe}$	$^{140}\text{Xe}$	$^{141}\text{Xe}$	$^{142}\text{Xe}$	
0.85 5.2%	0.85 5.0%	0.85 4.5%	0.85 4.3%	0.86 3.9%	0.86 3.7%	50 mb	0.86 3.3%	0.87 3.1%	0.87 3.1%	0.87 2.9%	0.87 3.0%	0.87 2.8%	
-6n	-5n	-4n	-3n	-2n	-1n		+1n	+2n	+3n	+4n	+5n	+6n	

Figure 3.4 Magnetic rigidity in T·m (middle row) and detection efficiency (bottom row) for proton pickup channels of PLFs produced by MNT reactions of  $^{136}\text{Xe}+198\text{Pt}$  at the incident energy of 7 MeV/u. For the  $^{136}\text{Xe}$  scattering, the elastic cross section accepted by the VAMOS is shown, which imposes a limit to the projectile beam intensity. The hatched area covers PLFs to be detected with good statistics within the proposed beam time. [121]

rate/ $B\rho$	1.10	1.12	1.13	1.15	1.18
$^{136}\text{Xe}$ [pps]	691	893	963	1096	1219
$^{142}\text{Xe}$ [count/day]	$1.03 \times 10^2$	$1.37 \times 10^2$	$1.51 \times 10^2$	$1.80 \times 10^2$	$0.77 \times 10^2$
$^{134}\text{Ce}$ [count/day]	$5.97 \times 10^2$	$6.49 \times 10^2$		$6.87 \times 10^2$	$4.25 \times 10^2$
$^{138}\text{Ba}$ [count/day]	$9.839 \times 10^3$	$1.160 \times 10^4$	$1.230 \times 10^4$	$1.388 \times 10^4$	

Table 3.3 Rate calculation result from simulation and GRAZING calculation assuming beam intensity of 0.2pnA target thickness of 1.3 mg/cm<sup>2</sup>. Both accepted events from elastic scattering and reaction fragments increases proportional to the  $B\rho$

### 3.2. BEAM TARGET COMBINATION CONSIDERATION

carried out by assuming uniform TLF excitation energy distribution ranging from  $0 \sim 40$  MeV with two-body kinematics. (See figure 3.3) The angular distribution for elastic scattering was assumed to be Rutherford angular distribution. And for the reaction fragments the Gaussian distribution with  $\langle \theta \rangle = 32.4^\circ$  with  $\sigma = 3^\circ$  was assumed. The charge state of fragments inside the spectrometer was calculated by the empirical formula.[105] The acceptance calculation was done based on database made from ray-tracing code ZGOUBI[93] which is explained in more detail at Section 3.3.3. Finally, the cross section deduced from GRAZING calculation introduced to the detection efficiency from simulation was used to deduce the rate of reaction fragments.

The  $N \sim 126$  (proton pickup) neutron stripping channel  $^{134}\text{Ce}$  (+4p, -6n) the maximum detection efficiency was at  $1.15 \text{ T}\cdot\text{m}$ . The other channels ( $^{138}\text{Ba}$  (+2p, 0n),  $^{142}\text{Xe}$  (+0p, +6n)) the detection efficiency showed same tendency as  $^{134}\text{Ce}$  (+4p, -6n) channel. But  $B\rho = 1.15 \text{ T}\cdot\text{m}$  the too much event from the elastic scattering rate was expected. The reference  $B\rho = 1.13 \text{ T}\cdot\text{m}$  was chosen which has detection efficiency of targeted nuclei near the maximum value, while limiting elastic scattering rate. (See Table 3.3)

The beam current was chosen from the maximum rate of the detection. The maximum rate was determined from the detector dead time and total capability of data acquisition. Since too much number of events from elastic will increase the dead time of the detector setup and cause malfunction of the detectors. The typical dead time of the data acquisition system of VAMOS is  $150 \mu\text{s}$ , and number of events drift chamber(which has the smallest maximum detection rate) can handle which is  $10 \text{ kHz}$ .[83] But the DAQ handling both VAMOS and EXOGAM had maximum the

### 3.3. VAMOS++ SEPCTROMETER

rate of 1 kHz. Thus the final rate of event detection should be less than 1 kHz to insure the safe data taking during the experiment. From these parameters we can determine the limit of the beam current.

$$I = \frac{1.0 \times 10^3}{\frac{1.3[mg/cm^2]}{198[g]} \times N_{Avogadro} \times \frac{d\sigma}{d\Omega} \times N_{Coulomb}} = 0.2pnA \quad (3.1)$$

$$\frac{d\sigma}{d\Omega} = 195.0 \text{ mb } N_{Coulomb} = 6.24 \times 10^{18}$$

$N_{Avogadro}$  = Avogadro's number

From these calculations, typical beam current during the experiment was limited to  $I = 0.2 \text{ pnA } (^{136}\text{Xe}^{20+})$ .

#### 3.2.6 Beam time

The total beam time needed for this experiment was calculated using expected rate of the  $^{202}\text{Os}$  ( $Z=76, N=126$ ). If we assume considering the detection efficiency of 10% for the gamma rays and the reduction of 20% for the coincidence rate between PLFs and TLFs compared with the single detection of the PLFs, more than  $5 \times 10^3$  events need to be detected by the VAMOS. The direct detection of new isotopes  $^{200}\text{W}$  is unlikely to be detected using  $\gamma$ -ray cascade. But  $^{202}\text{Os}$  case which have predicted cross section (GRAZING code calculation)  $2.08 \times 10^{-2} \text{ mb}$  assuming efficiency of 7.0% can have  $\gamma$ -ray cascade count  $\sim 20$  events/day was expected. In order to get the order of  $10^2$  count for the  $^{202}\text{Os}$ , the total six-days of machine time was requested. In the actual experiment the beam time of 4.5 days were achieved successfully.

### 3.3 VAMOS++ sepctrometer

### 3.3. VAMOS++ SEPCTROMETER

#### 3.3.1 Electro-Magmentic elements of VAMOS++

The VAMOS (VAriable MOde Spectrometer) spectrometer the electro-magnetic element consists of two quadrupole magnets, Wien-filter, and dipole magnet. (See figure 3.5) This relatively simple configuration was designed to maximize acceptance and enable more accurate software tracking which considers optical aberration [84, 85]. The configuration and spec of each magnetic elements are shown in Table 3.4. The first quadrupole is symmetric shaped, focusing though vertical (from ground) axis, while second quadrupole is oval shaped focusing though horizontal axis in order to maximize angular acceptance. The Wien filter which is used for better selectivity of reaction products was not used in the experiment. The magnetic dipole has large aperture for better acceptance. The spectrometer was used with focusing mode which maximizes the acceptance at the focal plane. The momentum dispersion at the focal plane can be varied by deflection angle between of the dipole magnet. The mean deflection angle was set to 45 ° in this experiment.

#### 3.3.2 Detectors of VAMOS++

The setup and position of the each detector are shown in table 3.5 and figure 3.6. In this subsection, the detailed description of each detectors and setup in the experiment will be discussed.

##### Multi-wire parallel plate avalanche counter

The timing measurement of reaction fragments were done by two MWPPACs (Multi-wire parallel plate avalanche counter), which are installed at near the target and the focal plane after the magnetic elements. When energetic charged particle passes

### 3.3. VAMOS++ SEPCTROMETER

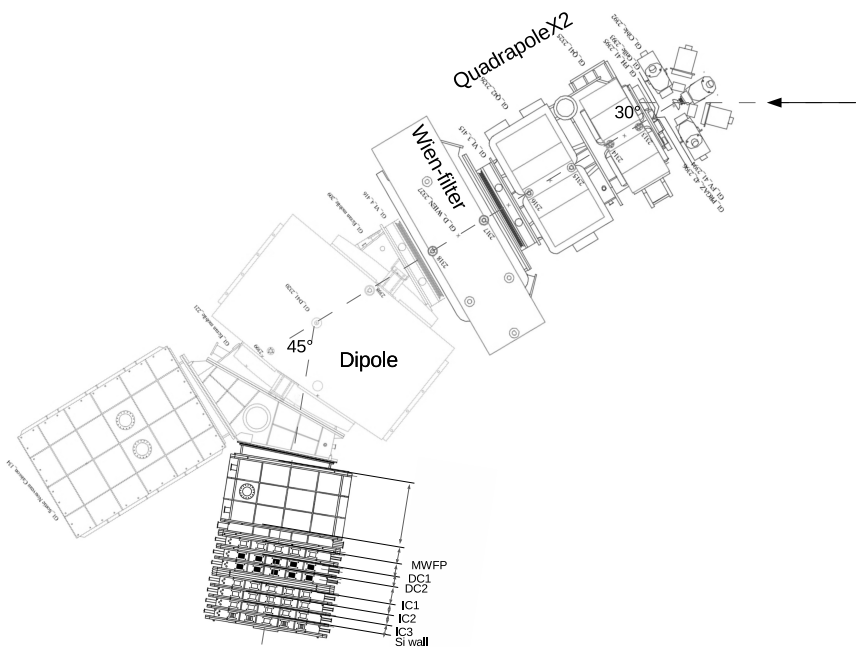


Figure 3.5 The setup of VAMOS spectrometer. Incoming beam direction is indicated as an arrow at the left side. The reaction fragments pass through electro-magnetic component consist of two quadrupoles, Wien filter ,and dipoles. Then detected by MWPPAC, two set of drift chambers, three sets of ionization chamber. and Si detector wall. The angle between electro-magnetic component axis and axis perpendicular to the detector face was  $45^\circ$ .

### 3.3. VAMOS++ SEPCTROMETER

Element name	Specification	
Quadrupole 1	Magnetic length	0.6 [m]
	Aperture diameter	$2G_0 = 300$ [ mm]
	Maximum magnetic field	1.05 [T]
Quadrupole 2	Drift length	0.3 [m]
	Magnetic length	0.9 [m]
	Horizontal aperture diameter	500 [ mm]
	Vertical aperture diameter	50 [ mm]
	Maximum magnetic field	1.0 [T]
Wien filter	Drift length	0.35 [m]
	Total length	1 [m]
	electrode height	0.32 [ mm]
	Effective E-field length	890 [ mm]
	Effective B-field length	1082 [ mm]
	Maximum voltage	$\pm 150$ [kV]
Dipole	Minimum magnetic field	0.2 [T]
	Drift length	0.70 [m]
	Magnetic length	1.0 [m]
	Magnetic length	1.57 [m]
	Angle of deflection at experiment	45 [°] (0~60°)
	Reference radius of deflection	1.9706 [m] (at 45 °)
	Maximum magnetic field	1.1 [T]

Table 3.4 Specification of electro-magnetic elements of VAMOS [90]

### 3.3. VAMOS++ SEPCTROMETER

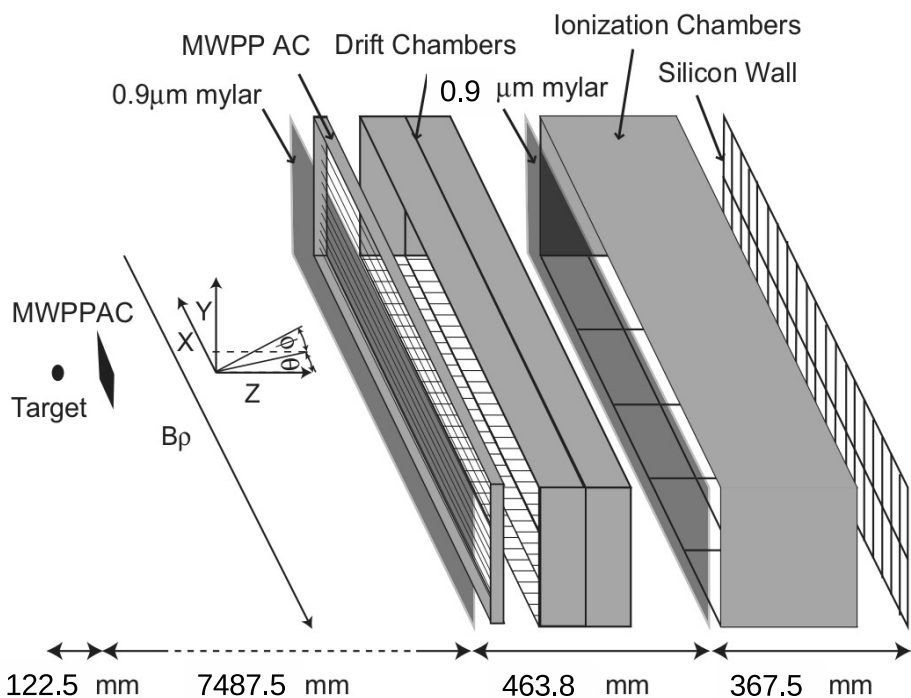


Figure 3.6 Schematic view of detector set of VAMOS near focal plane. The projectile from the reaction passes two PPACs near the target and near the focal plane detects the ToF. After the PPAC, the two sets of drift chamber detects position and angle of incident particle. Then the projectile travels and stops inside the series of ionization chamber, and Si detector to measure energy. [83]

### 3.3. VAMOS++ SEPCTROMETER

Detector	Specific part	Position from target [ mm]
	focal plane	7600.0
	mylar foil 0.9 $\mu\text{m}$	7610.0
Multi-wire chamber focal plane	entrance	7630.0
	center	7645.2
	exit	7749.7
Drift chamber 1	entrance	7770.0
	entrance of 1st pad	7645.2
	entrance of 2n pad	7830.1
	exit	7889.3
Drift chamber 2	entrance	7889.3
	entrance of 1st pad	7909.6
	entrance of 2n pad	7949.6
	exit	8008.9
	mylar foil 0.5 $\mu\text{m}$	8073.8
Ionization Chamber 1	entrance	8073.8
	drift field entrance	8074.2
	pad entrance	8094.2
	exit	8193.7
Ionization Chamber 2	entrance	8193.7
	pad entrance	8194.3
	exit	8314.0
Ionization Chamber 3	entrance	8314.0
	pad entrance	8314.2
	exit	8433.4
Si detector	entrance	8433.4
	Si detector surface	8441.4
	exit	8553.5

Table 3.5 Detector setup and position of VAMOS near focal plane.

### 3.3. VAMOS++ SEPCTROMETER

through MWPPAC, the electrons created from ionization of gas was drifted towards the cathode wire creating avalanche, very close to the wire. PPAC have advantage of good timing resolution and high count rate capability (typically  $10^6$  cps).

First MWPPAC at the target (MWT) with active area of 52 mm $\times$ 60 mm, was installed near target consist of one channel 122.5 mm away from the target. Permanent magnets were placed outside of the detector to avoid secondary electrons from the target.

The second MWPPAC which was installed at focal plane, have active area of 150 mm(height)  $\times$  1000 mm(width). The MWPPAC at the focal plane (MWFP) the 1000 mm long horizontal wires the 150 mm long vertical wires with diameter of 20  $\mu\text{m}$  were used with a pitch of 500  $\mu\text{m}$  and 1 mm for the central and external plane. The horizontal wires (cathode) were set to ground. And they were segmented into 20 independent sections for faster rise time by decreasing the capacity of detector.

$$V(t) = -\frac{q}{4\pi\epsilon} \ln\left(1 + \frac{\mu CV_0}{\pi\epsilon a^2} t\right) \quad (3.2)$$

$V_0$ =bias voltage,  $C$  = capacitance,  $q$  = charge from ionization,

$\epsilon$ =dielectric constant,  $\mu$ =mobility of charge,  $a$  = diameter of wire

The vertical wires (anode) were applied with – 500V bias. The signals from each segment of horizontal wires were fed in to fast voltage amplifiers.

Both of MWPPACs were filled with isobutane gas with pressure of 6.9 mbar. The MWPPAC at the target was covered with thin Mylar window of 0.5  $\mu\text{m}$ . The electronic circuits are showed in figure 3.17. The typical timing resolution was 0.5 ns.[83]

During the experiment, PPAC near the target suffered from the fast timing events due to the secondary electrons from Mylar foil in front of the detector. (See

### 3.3. VAMOS++ SEPCTROMETER

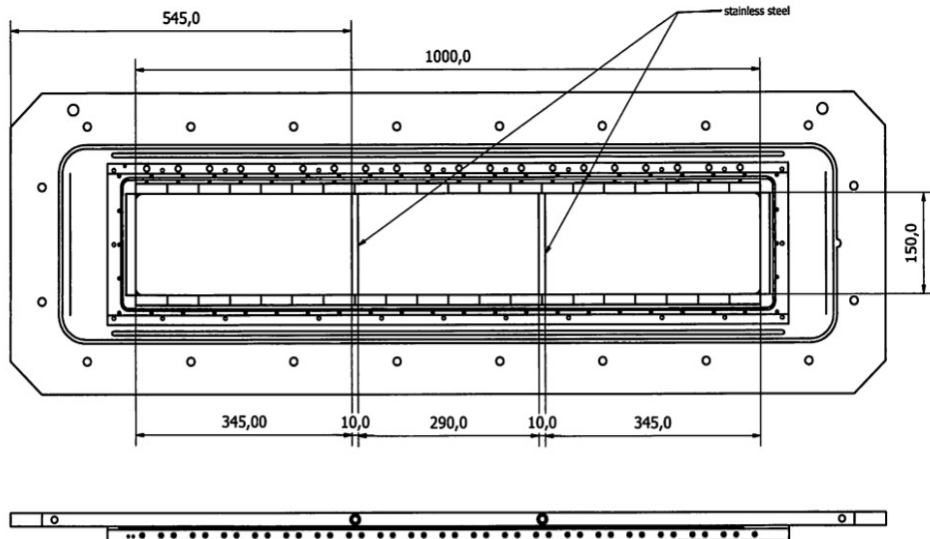


Figure 3.7 Schematic of multi-wire parallel plate avalanche chamber(MWPPAC) at focal plane.

Section 4.1.1)

### Drift chamber

The position (horizontal ( $x$ ) and vertical ( $y$ )) and incident angle ( $\theta, \phi$ ) of the PLF near the focal plane was measured, using two identical drift chambers shown in figure 3.8 3.9. When the charged particle passes through the drift chamber, electrons produced from ionization of the gas, drift towards Frisch grid. And then the positively charged amplification wires produces avalanche induced by high electric fields near the wire and collected. (See figure 3.9) The fast signal from the wire provides the time of arrival of the electrons with respect to the MWFP, which was used as a reference for the time measurement. The  $y$  position of the trajectory can be

### 3.3. VAMOS++ SEPCTROMETER

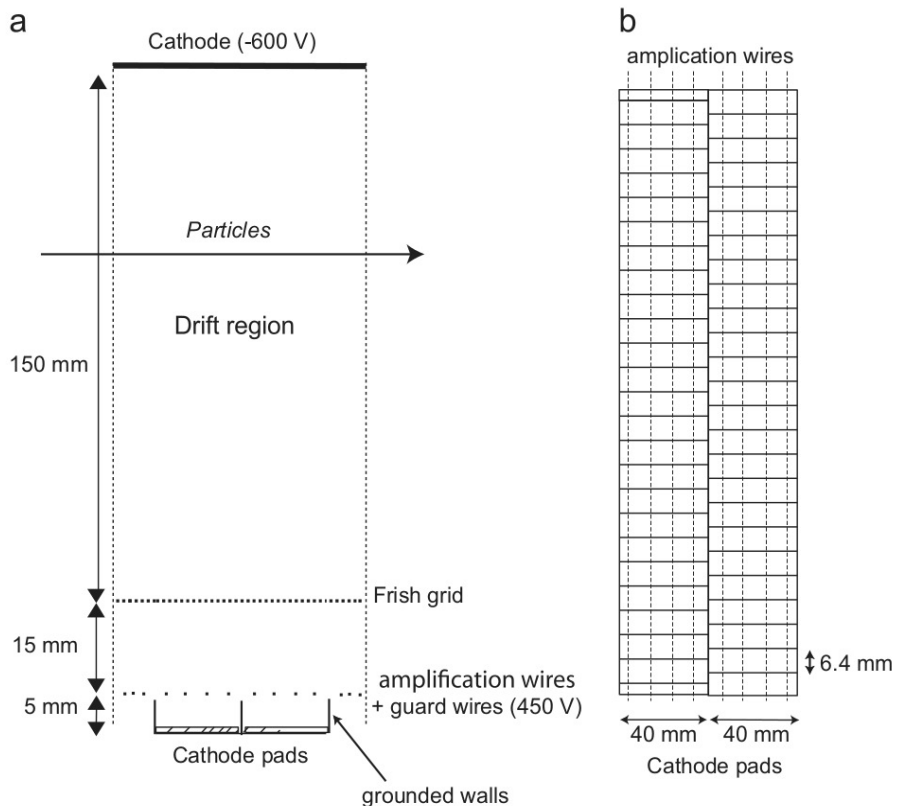


Figure 3.8 (right) Side view of drift chamber structure. Drift region, and amplification region is separated by Frisch grid can be seen.(left) Pad design of drift chamber for horizontal (X) position measurement. Two rows of pads are shifted to each other by half pad size.

### 3.3. VAMOS++ SEPCTROMETER

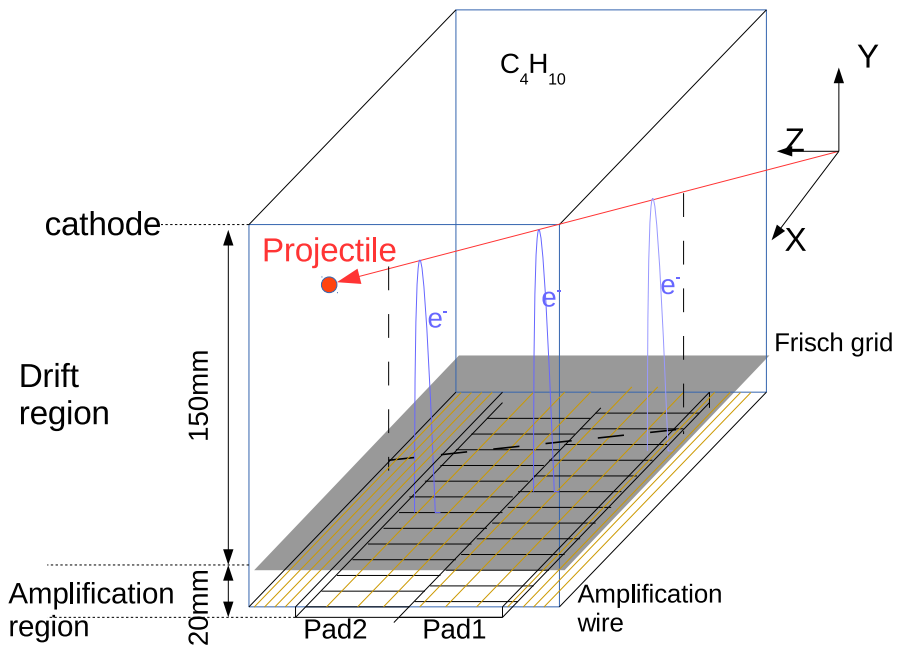


Figure 3.9 Schematic for demonstration of working principle of the drift chamber. Incident projectile passing through drift region creates ion pair. Electrons from ion pair travel through field inside drift region with constant speed. Then electrons are accelerated after Frisch grid and creates avalanche near the amplification wire inducing charge signal at the segmented pads. The drift time inside drift region is measured for position in vertical axis (Y), and charge induced in segmented pads decides horizontal position(X).

### **3.3. VAMOS++ SEPCTROMETER**

calculated by known drift velocity inside the drift region. The charge created from avalanche induces signal on nearby pads, and the charge from each pad is read out individually. The x position of the trajectory is then determined by the mean of relative strength of the charge distribution across the pads.

The drift chamber consists of a drift region and an amplification region, as illustrated in figure 3.8. The drift region has a cathode and a Frisch wire grid at ground potential which separates the drift region from the amplification region. The amplification wires were operated at a voltage of + 450 V while Frisch grid and the cathode pads were at ground potential. The amplification region has the similar structure of a proportional counter, consisting of a wire plane electrode of thick gold plated tungsten wires between the Frisch grid and the cathode of the chamber. The cathode of the drift chamber which detects the X position consists of two rows, each divided into 160 columns separate pads of 6 mm wide gold plated strips, with each pad separated by 6.4 mm along the dispersive direction. The second rows of pads are shifted from the first, by half a pad to reduce the non-linearity of the signal in between the strips.

The data readout of pads were done using ASIC chip, which reads signal from the pad and send them with clock of 500ns, converted in to serial data signal, in order to handle large number of channels. During the experiment, drift chambers were placed after the MWPPAC sharing same isobutane gas with pressure of 6.9 mbar. The typical position resolution for the drift chambers is 0.3 mm and 1 mm (FWHM) for x and y respectively.

### 3.3. VAMOS++ SEPCTROMETER

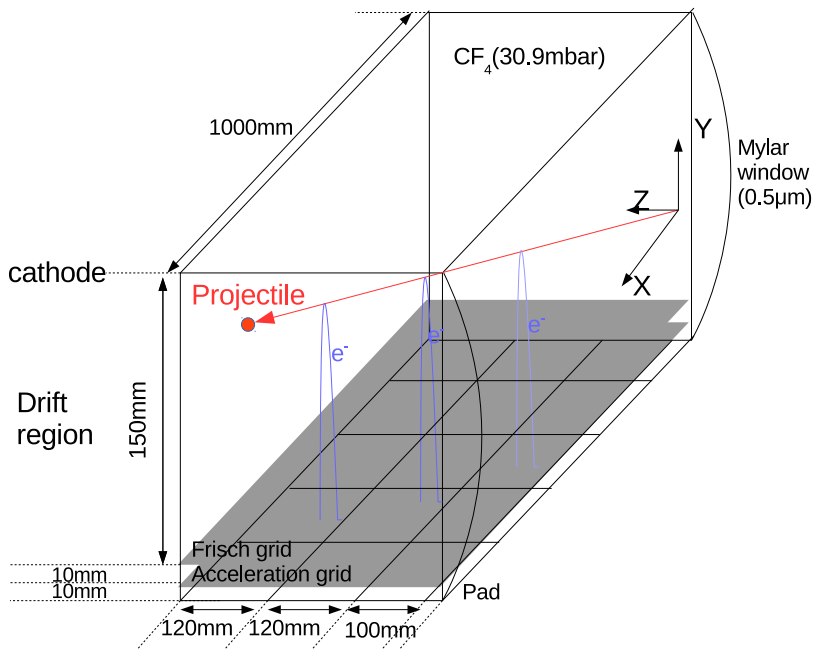


Figure 3.10 Schematic view showing working principle of ionization chamber. The energetic charged particle passes through gas,ion pair created proportional to the energy loss inside the gas. electrons are drifted inside drift region then accelerated in series by electric field from Frisch grid and acceleration grid. Finally electrons are collected at the pads. [83]

### 3.3. VAMOS++ SEPCTROMETER

#### **Ionization chamber**

The ionization chamber (IC) was used to measure the energy loss of the PLF through a volume of gas in order to measure energy loss inside the IC. From dE measurement, one can deduce the proton number of PLF. The Bethe-Bloch formula indicates that the energy charged particles passing through a medium is proportional to the square of the atomic number of the particle.

The ionization chamber consists of a cathode (150 mm from anode), Frisch grid (20 mm from anode), acceleration grid (10 mm from anode) and a segmented anode (See figure 3.10). The PLF passing through the ionization chamber, the electrons liberated from ionization of the gas proportional to the energy loss. The ionized electrons in the region between the cathode and the Frisch grid travel along the electric field without avalanche or recombination. Series of Frisch grid and acceleration grid helps to decrease the rise time, increasing the maximum rate of the detector can handle. The electrons which were collected by the pads in each rows creates the signal, with the amplitude proportional to the energy loss of the particle.

Frisch grid was made with gold coated tungsten wires with thickness of  $50 \mu\text{m}$ , and 1 mm pitch. The anode is divided into three segments (rows) along the beam axis with active area  $1000 \text{ mm} \times 150 \text{ mm}$ . The each row is segmented into 5 pads (columns) with each size of  $200 \text{ mm} \times 100$  (first row),  $200 \text{ mm} \times 120$  (second, third row) across the focal plane. The segmentation of the rows into individual pads enables the processing of simultaneous events whose trajectories pass over different pads. The chamber is filled with carbon tetrafluoride ( $\text{CF}_4$ ) gas (mean ionization energy 30eV) with a pressure of 30.9 mbar. The entrance widow was covered with  $0.5 \mu\text{m}$  Mylar window separating ionization chamber from drift chamber.

### 3.3. VAMOS++ SEPCTROMETER

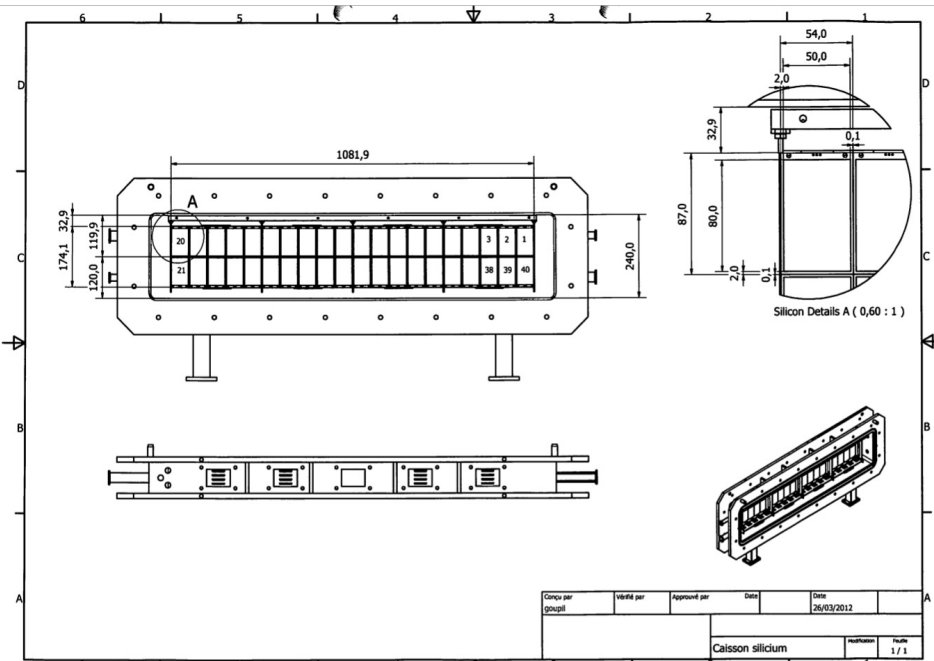


Figure 3.11 Si detector configuration inside the VAMOS spectrometer

During the experiment IC suffered from field leakage through Si detector which makes different electron collection efficiency depends on vertical position. (See figure 4.16) Correction process from this effect will be discussed in details at the Section 4.2.1.

#### Si detector

The Si-detector was used to determine the remaining energy of the PLF, after passing though the IC. Total number of 40 set of si-detectors closely packed together, were used to cover 1000 mm × 150 mm. (See figure 3.11) Each Si-detector size was with 54 mm × 87 mm with active area of 50 mm × 80 mm with thickness of 500

### **3.3. VAMOS++ SEPCTROMETER**

$\mu\text{m}$ . The Si-detector was separated about 0.1mm thus gap between each Si-detector active area is 4.1 mm. Each pre-amp was attached back of Si-detector inside vacuum chamber in order to decrease the noise. The PLF ions passing though Si-detector creates electron-hole pair inside the depleted region in the Si. The electron-hole pair is then collected by the electric field between the Si surface created by bias voltage.

Si-detector have smaller energy to create electron-hole pair(3.62eV) than IC chamber, having better energy resolution of the system. The typical resolution of Si-detector is 60 keV [83]. During the experiment four out of forty Si detectors at the side were broken due to mis-connection or, high noise from unknown reason.

#### **3.3.3 Event Reconstruction**

The VAMOS++ spectrometer, the reaction fragment position at the entrance was not measured, but only measured after passing though the magnetic elements. The trajectory of projectile after the reaction was needed to be reconstructed by software. This technique is often used to correct the higher order optical aberrations.[92] In order to reconstruct the full trajectory with high accuracy, VAMOS uses ray-tracing software to deduce the track of particles through the spectrometer.[85][90] This process was carried out by mapping of the full acceptance phase space(  $B\rho$ , flight path,  $\theta$ ,  $\phi$ ) to the focal plane ( $X_f$ ,  $Y_f$ ,  $\theta_f$ ,  $\phi_f$ ), building a database of these particle coordinates. Then by reverse mapping of the detected particles to phase space, one can deduce the track of each charged particle. This mapping was done by optical ray-tracing code ZGOUTI [93], used with the field map of each magnetic elements. The 3D field map of magnetic elements were calculated by computational code TOSCA [94].

### 3.3. VAMOS++ SEPCTROMETER

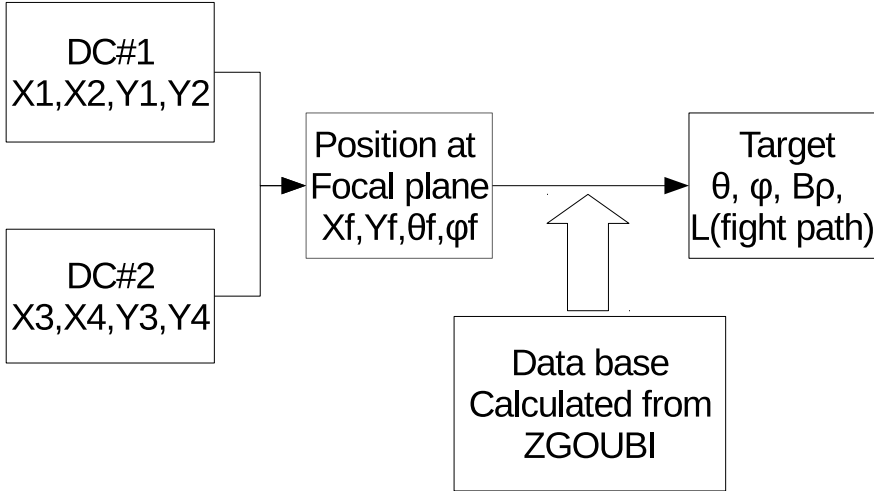


Figure 3.12 Flow chart showing reconstruction procedure

In the actual calculation database was generated by the initial phase space parameters  $X_{target}$ ,  $Y_{target}$ ,  $\theta_{target}$ ,  $\phi_{target}$ ,  $\delta$  ( $\delta$ : momentum deviation from the reference), which the trajectory is uniquely defined. The vectors fill a maximum angular and the momentum acceptance of the spectrometer defined within the range  $\Delta\theta$ ,  $\Delta\phi = \pm 160$  mrad and  $\delta = \pm 10\%$ .

But due to limited computational power, the reverse mapping of the coordinates is obtained by expressing the simplified mapping database, and a polynomial function. The  $B\rho$ , flight path,  $\theta_{target}$  is deduced directly from simplified database only containing data with  $Y_f=0$ , and  $\phi_f=0$ , since the dependence of these variable is small enough to achieve the resolution for this experiment. While the  $\phi_{target}$  is

### 3.4. EXOGAM GE-CLOVER ARRAY

determined by 10<sup>th</sup> order polynomial

$$F(X_f, Y_f, \theta_f, \phi_f) = \sum_{i,j,k,l}^{i+j+k+l=10} X_f^i Y_f^j \theta_f^k \phi_f^l \quad (3.3)$$

by fitting all the points in the database. The differences between original database and simplified database events can be observed by simulation using ray-tracing code. The generated event at the target, incident position and angle at the focal plane was calculated using Zugubi ray-tracing code. Then it was reanalyzed to get condition at the target by simplified mapping database, and polynomial fitting function. (See figure 3.13) The typical disagreement or the width of correlation distribution was  $\Delta B\rho=4.5\times10^{-3}$  T·m (FWHM),  $\Delta\theta=0.15^\circ$  (FWHM), and  $\Delta\phi=0.35^\circ$  (FWHM). The correlation result showed that they are in good agreement with each other.

## 3.4 EXOGAM Ge-clover Array

The Ge-clover detector array EXOGAM was used to detect the  $\gamma$ -rays from de-excitation of the reaction fragments. Each clover detector has 4 crystals with 4 electrodes in each crystal for better angular resolution. (See figure 3.14) The Ge-clover crystals were surrounded by BGO-crystal (side) and CsI-crystal (back) scintillator to detect Compton scattered gamma-ray from Ge-crystal which reduces the energy resolution. The collimator was used close to the target in order to avoid  $\gamma$ -rays from Compton scattering with materials outside of the target. (See figure 3.16) (The applying all shielding for Compton scattering mentioned above which was used in this experiment, is called configuration B.) The resolution and photo-peak efficiency of the EXOGAM is listed in Table 3.7.

The electric circuit of EXOGAM is presented in figure 3.21. The circuit consists

### 3.4. EXOGAM GE-CLOVER ARRAY

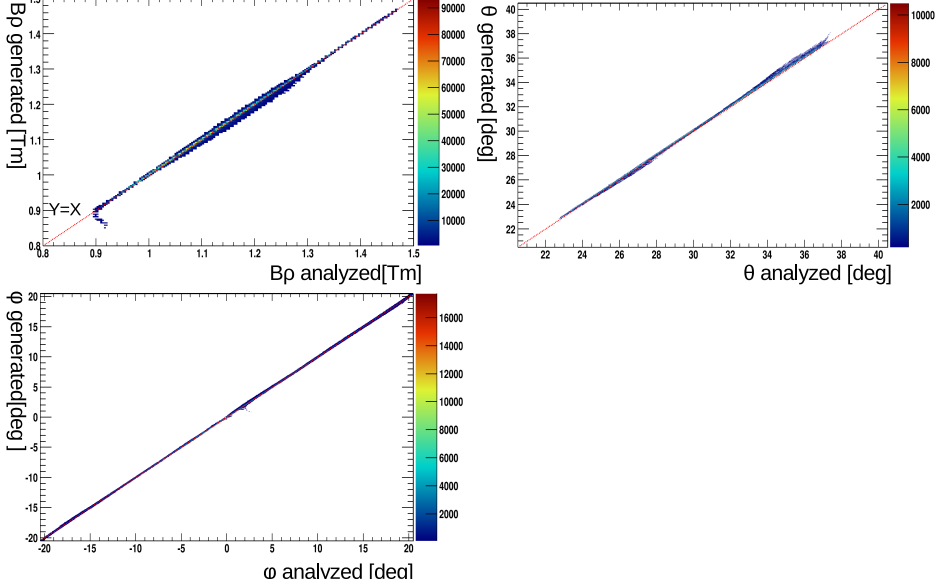


Figure 3.13 Correlation between generated event and analysed result using simplified database ( $B\rho, \theta$ ) and fitting ( $\phi$ ). (top left) Correlation between generated  $B\rho$  and analysed  $B\rho$  typical width was  $\Delta B\rho = 4.5 \times 10^{-3}$  T·m (FWHM). The red dashed line is  $Y=X$ . (top right) Correlation between generated  $\theta$  and analysed  $\theta$  typical width was  $\Delta\theta = 0.15^\circ$  (FWHM). (bottom left) Correlation between generated  $\phi$  and analysed  $\phi$  typical width was  $\Delta\phi = 0.35^\circ$  (FWHM).

System	$\beta$	Photo peak efficiency [%]		peak-to-total [%]	
		662 keV	1313 keV	662 keV	1313 keV
High spin (config. B)	0.075	13	10	57	47
Mass 100 (config. B)	0.063	13	10	60	49
Mass 60 (config. B)	0.045	15	10	64	52

Table 3.6 Photo peak efficiency, peak-to-total efficiency cases close to this experimental configuration[97]

### 3.4. EXOGAM GE-CLOVER ARRAY

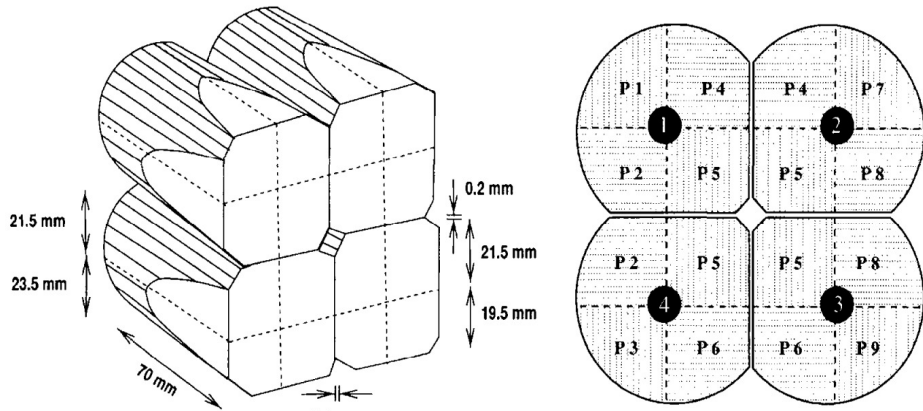


Figure 3.14 Clover crystal structure inside the EXOGAM Ge-clover detector. Set of 4 crystal consist one Ge-detector, each crystal has 4 electrode segments.(left figure) Side-view of crystal.(right figure)front view of Crystal. [96]

System	$\beta$	Resolution [keV]	
		662 keV	1313 keV
High spin (config. B)	0.075	2.7	4.3
Mass 100 (config. B)	0.063	5.6	10.7
Mass 60 (config. B)	0.045	4.2	7.8

Table 3.7 Resolution of  $\gamma$ -ray with cases close to this experimental configuration[97]

### 3.4. EXOGAM GE-CLOVER ARRAY

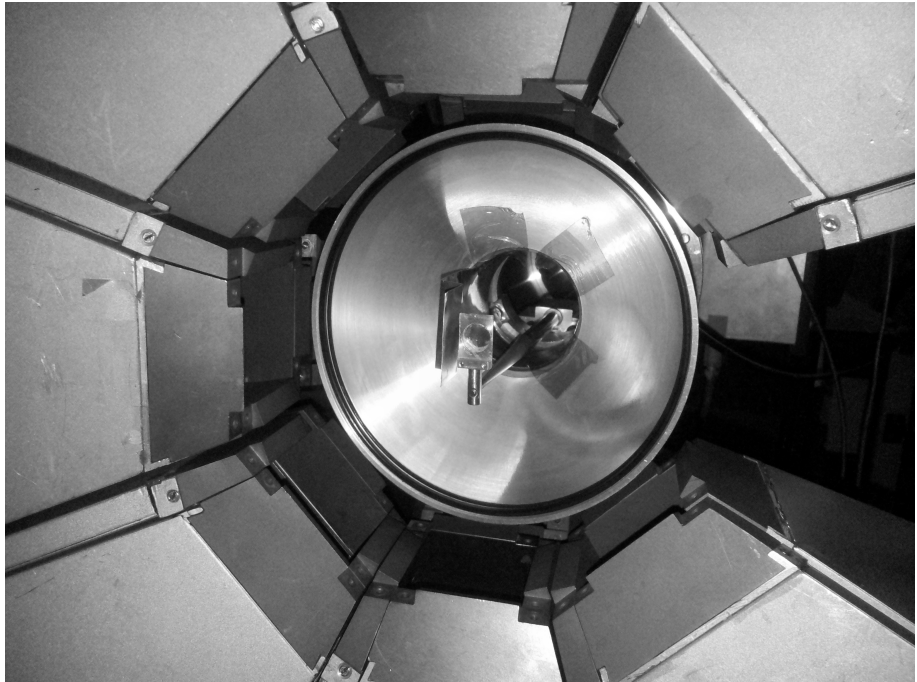


Figure 3.15 EXOGAM surrounding target chamber. Total seven Ge-clover detector near 90° can be seen

### 3.4. EXOGAM GE-CLOVER ARRAY

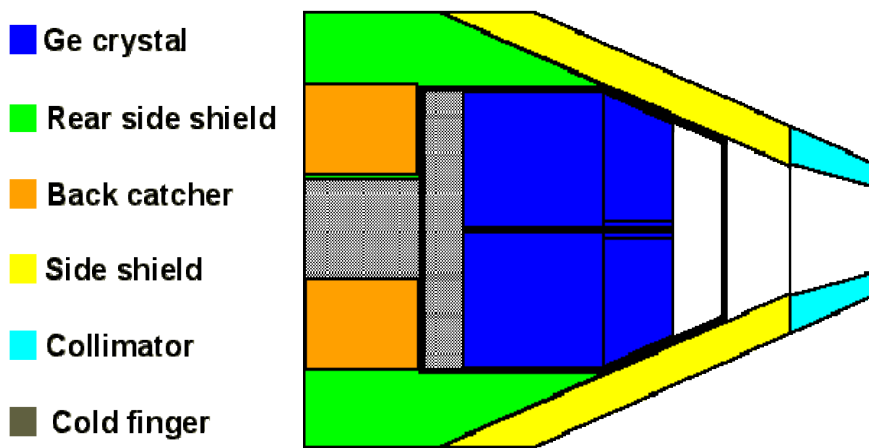


Figure 3.16 The Compton shielding of EXOGAM Ge-clover detector. Side ,and rear side shielding of the detector was made by BGO crystal which have large stopping power. While back catcher is made of CsI crystal(lower stopping power than CsI) which have larger space is available.[97]

### *3.4. EXOGAM GE-CLOVER ARRAY*

of circuit for Ge center contact ( $4 \times 10$  ch), Ge outer contact ( $4 \times 4 \times 10$  ch), BGO crystal ( $4 \times 10$  ch). The center contact records energy(0 6 MeV, 0 20 MeV), timing and triggering. The outer contact only measured energy. The BGO crystal measures energy or timing for summed over one Clover detector.

The trigger system was consisted of two level trigger. First level trigger was made to provide good timing, in this experiment it was made from multiplicity of all center contact (indicated as  $\Sigma$ Bus in figure). Second level trigger was made to validate or reject the good or bad events using programmable hardware. In this experiment coincident from VAMOS was made to ensure the event was from the reaction.

In the experiment total 10 Ge-clover detectors were used. They were placed 68.3 mm away from the target. The 7 Ge-clover detectors sets were at  $\theta=80$  100°. The 3 Ge-clover detectors sets were at  $\theta=120$  145°. (See Table 3.8 and 3.9 ) The coincident with VAMOS was made with 400ns width to collect  $\gamma$ -rays from isomer states.

#### **3.4.1 Electric circuit and trigger system**

The electric circuit of this experiment is presented in figure 3.17, 3.18. 3.19, 3.20, 3.21, 3.22, and 3.23

The signals from VAMOS and EXOGAM has stand alone DAQ, processed though GANIL data acquisition system [86]. The three triggers were made for experiment, trigger from VAMOS (indicated as VAMOS-hit), trigger from EXOGAM (indicated as EXOGAM-hit), and trigger from coincident of VAMOS, EXOGAM (indicated as EXOGAM AND VAMOS-hit). (See figure 3.22)

The main trigger used in the experiment is the trigger from VAMOS, to suit

### 3.4. EXOGAM GE-CLOVER ARRAY

Clover Detector	Ge crystal	$\theta[^\circ]$	$\phi[^\circ]$
1	A	76.8~85.7	256.5~265.6
	B	76.8~85.7	274.4~283.5
	C	94.4~103.5	274.4~283.5
	D	94.3~103.5	256.5~265.6
2	A	120.4~130.4	185.1~197.7
	B	137.6~146.3	186.8~204.5
	C	137.6~146.3	155.5~173.2
	D	120.4~130.4	162.3~174.9
3	A	137.6~148.6	96.9~ 114.8
	B	137.6~148.6	65.2~83.1
	C	120.2~130.4	72.1~84.9
	D	120.2~130.4	95.1~107.9
4	A	120.3~130.4	252.2~264.9
	B	85.7~120.3	275.1~285.5
	C	137.6~148.5	276.2~294.6
	D	137.6~148.5	245.4~263.2
5	A	76.3~85.7	184.5~193.8
	B	94.5~103.7	184.5~193.8
	C	94.5~103.7	166.2~175.5
	D	76.3~85.6	166.2~175.5

Table 3.8 Angular geometry coverage of each EXOGAM Clover detector 1 ~ 5.

### 3.4. EXOGAM GE-CLOVER ARRAY

Clover Detector	Ge crystal	$\theta[^{\circ}]$	$\phi[^{\circ}]$
6	A	76.5~85.7	229.4~238.6
	B	94.3~103.2	229.4~238.6
	C	94.4~103.5	211.4~220.6
	D	76.5~85.7	211.4~220.6
7	A	94.3~103.6	301.4~310.6
	B	76.8~85.7	301.4~310.6
	C	76.8~85.7	319.4~328.6
	D	94.3~103.6	319.4~328.6
9	A	94.3~103.7	31.2~40.5
	B	76.6~85.7	31.2~40.5
	C	76.6~85.7	49.5~58.8
	D	94.3~103.7	49.5~58.8
10	A	94.3~103.7	94.5~103.8
	B	94.4~103.7	76.2~85.5
	C	76.2~85.6	76.2~85.5
	D	76.3~85.5	94.5~103.8
11	A	76.3~85.7	139.5~148.8
	B	94.3~103.7	139.5~148.8
	C	94.3~103.7	121.2~130.5
	D	76.6~85.6	121.2~130.3

Table 3.9 Angular geometry coverage of each EXOGAM Clover detector 6 ~ 11.

### 3.4. EXOGAM GE-CLOVER ARRAY

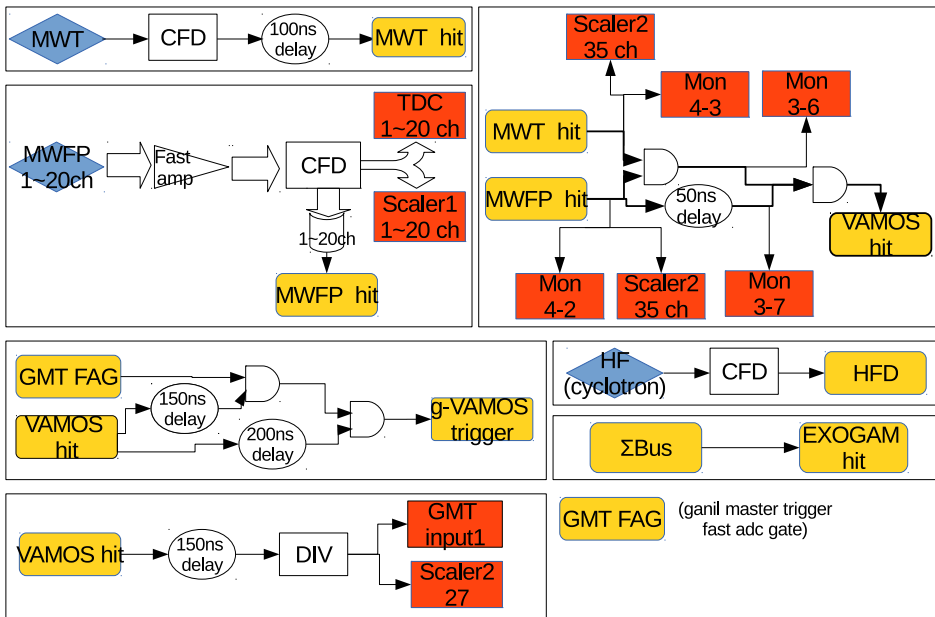


Figure 3.17 The electric circuit of two set of MWPPACs

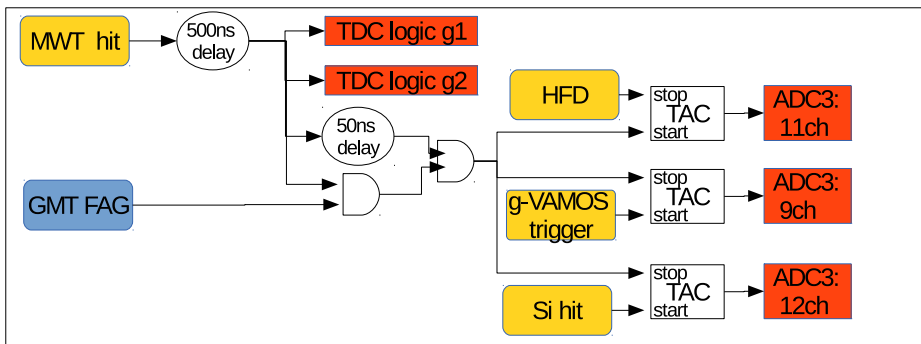


Figure 3.18 The electric circuit of two set of MWPPACs to the TDC and Scaler

### 3.4. EXOGAM GE-CLOVER ARRAY

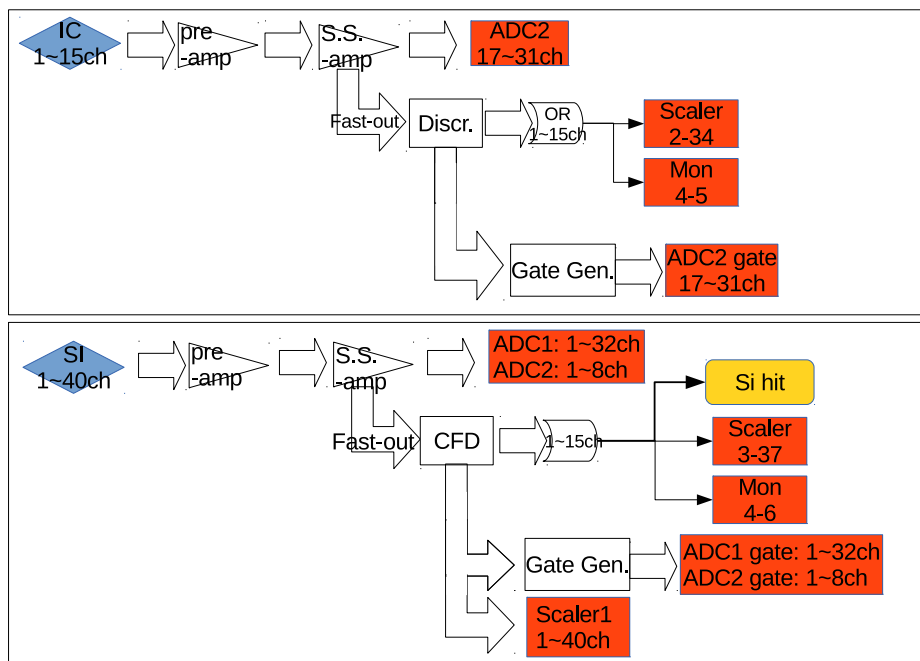


Figure 3.19 The electric circuit of ionization chamber (top), and Si detector (bottom)

### 3.4. EXOGAM GE-CLOVER ARRAY

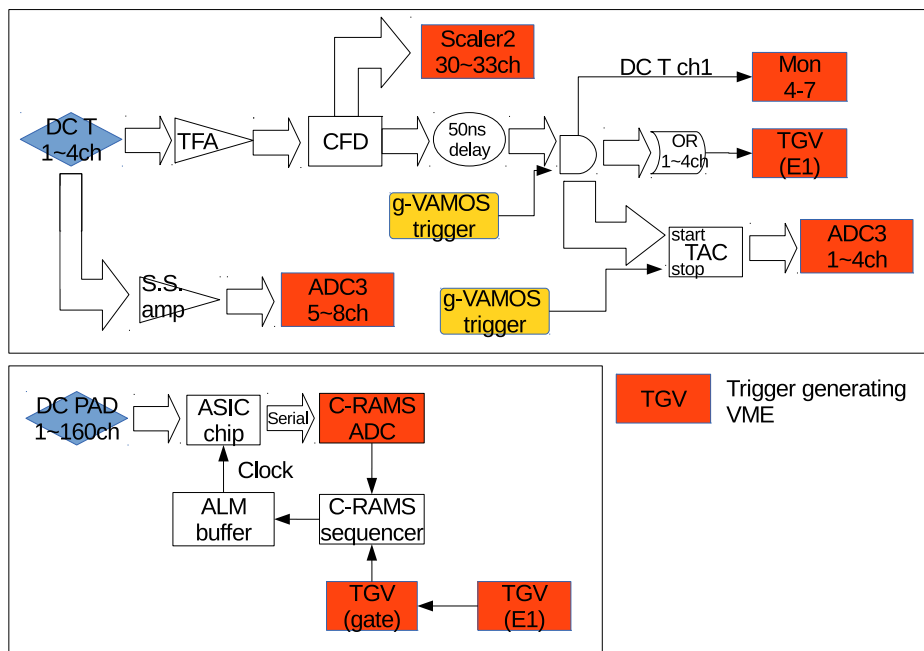


Figure 3.20 The electric circuit of drift chamber

### 3.4. EXOGAM GE-CLOVER ARRAY

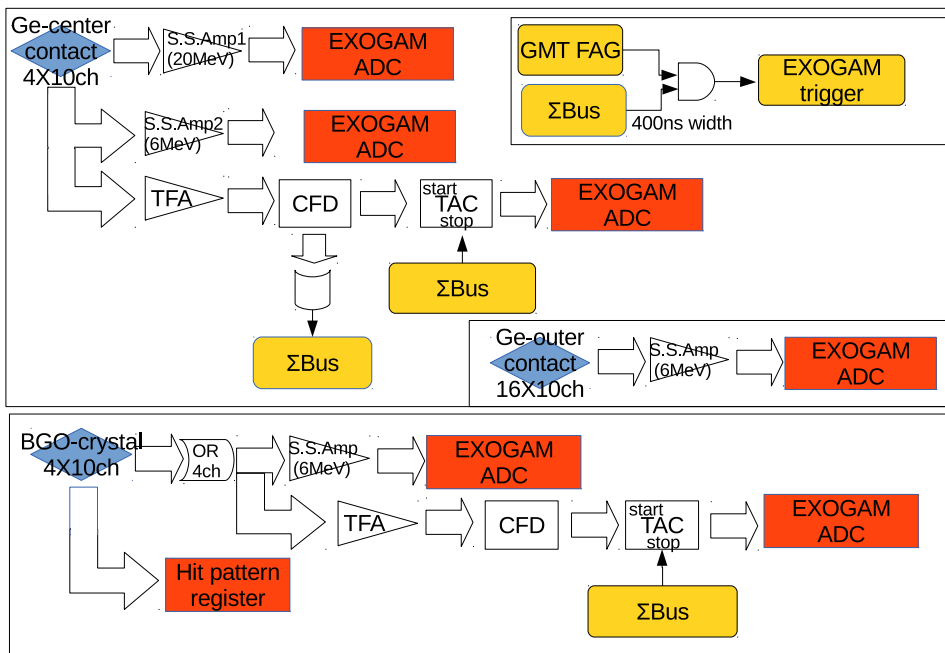


Figure 3.21 The electric circuit of EXOGAM

### 3.4. EXOGAM GE-CLOVER ARRAY

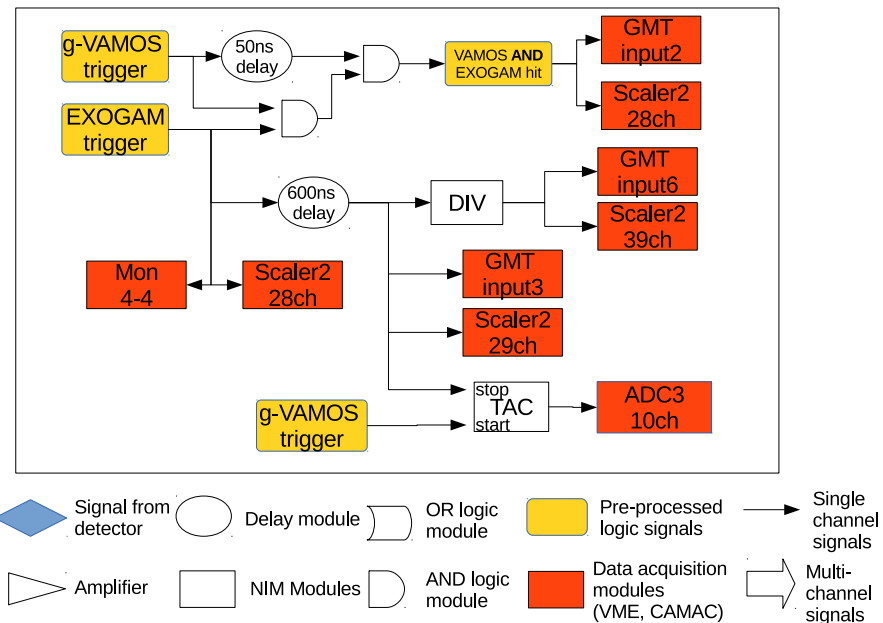


Figure 3.22 The electric circuit of trigger system

### 3.4. EXOGAM GE-CLOVER ARRAY

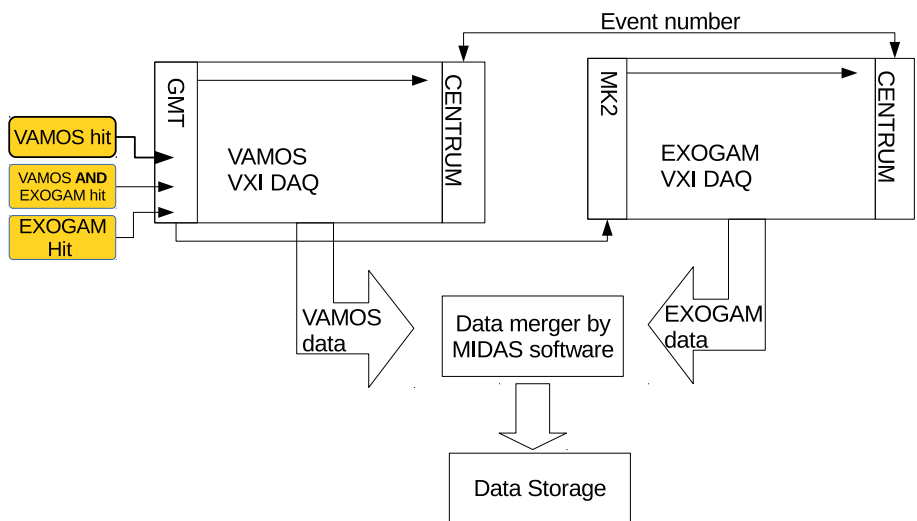


Figure 3.23 The electric system of scyncronization of different detector system

### *3.5. TANDEM EXPERIMENTAL RESULT*

the purpose of cross section measurement. It consists of coincident of MWT and MWFP, ensuring the particle(from reaction or scattering) was passed through magnetic elements. The coincident was made in order to set signal from MWFP to be the leading edge of the trigger. This is to insure the trigger is made from detector with best timing information.

In order to synchronize data from different complicated detector set, the events was validated by common trigger from GMT (Ganil Master Trigger)[88], which is indicated as GMT FAG (fast adc gate) resulting gVAMOS-trigger, EXOGAM-trigger. The veto in GMT was made from OR of individual DAQ dead time signal to ensure the data storage with common deadtime. Each events were numbered by CENTRUM (Clock and Event Number Transmitter Receiver Universal Module)[87] module in each VAMOS, EXOGAM DAQ controlled by GMT to make same numbering of event in VAMOS and EXOGAM events. Finally the data from different detectors was merged using event number by software MERGER and MIDAS[89]. (See figure 3.23)

## **3.5 Tandem experimental result**

The grazing angle and energy distribution of the fragment need to be known in order to maximize the detection efficiency of the reaction fragment using VAMOS spectrometer. The actual grazing angle and the angular distribution of the reaction fragments determines the potential energy and the kinetic energy of the reaction, which depends on the beam, target combination and beam energy.

The experiment with same beam target combination which will be used at the GANIL experiment was done in Tandem accelerator facility at JAEA.[81] The  $^{136}\text{Xe}$

### 3.5. TANDEM EXPERIMENTAL RESULT

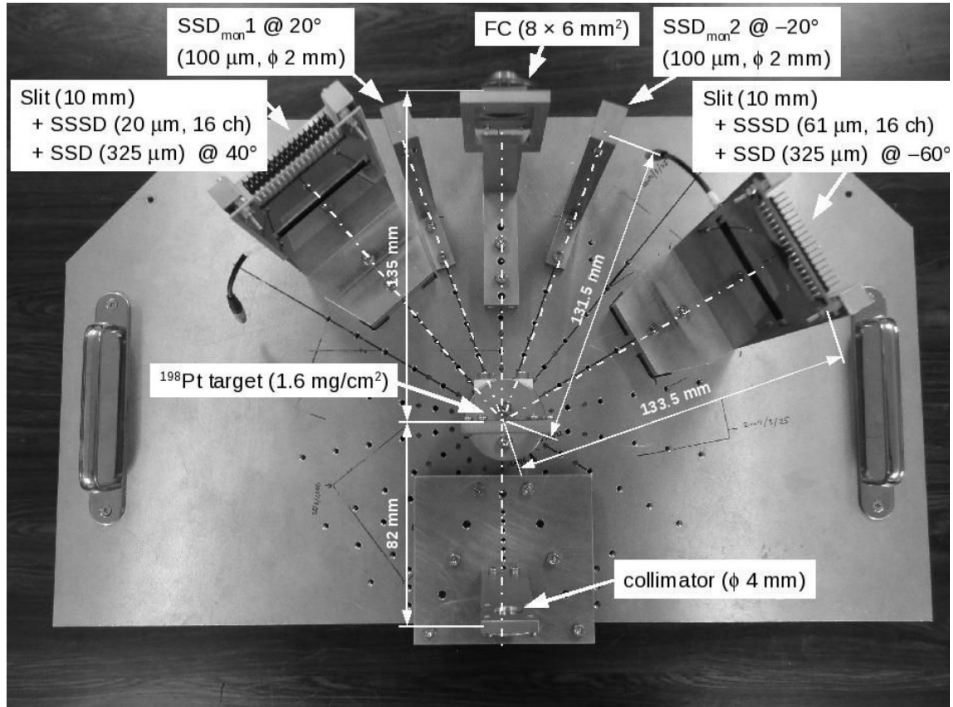


Figure 3.24 The setup of Tandem experiment. The  $^{198}\text{Pt}$  target with  $1.6 \text{ mg}/\text{cm}^2$  is placed at the center. Two set of detectors with consist of SSSD sandwiched with SSD was placed at  $30\sim 50^\circ$  ( $6.0\sim 7.0 \text{ MeV/u}$ ) /  $20\sim 40^\circ$  ( $7.5\sim 8.0 \text{ MeV/u}$ ) and  $50\sim 70^\circ$ . Two Si detectors for monitoring elastic scattering was placed at  $\pm 20^\circ$ . Faraday cup was placed at  $0^\circ$  deg to monitor the beam current.

### 3.5. TANDEM EXPERIMENTAL RESULT

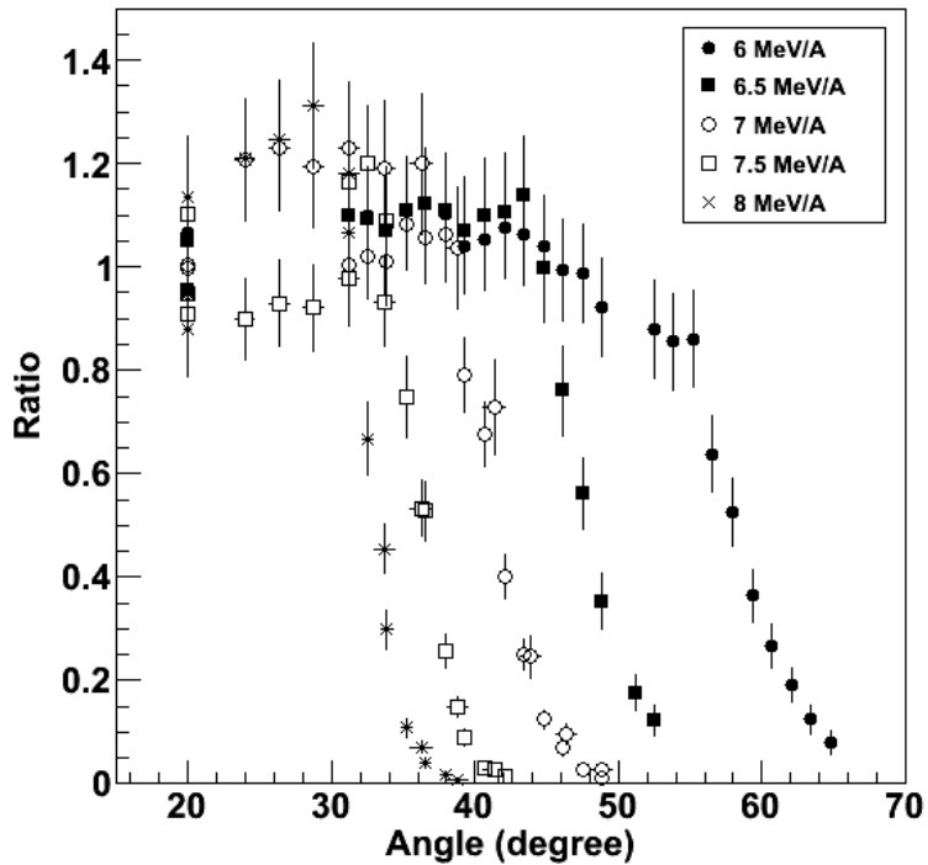


Figure 3.25 The angular distribution of elastic scattering channels with different beam energy. Angular distribution was normalized by Rutherford scattering at the  $20^\circ$  counts. Sudden decrease of cross section at the grazing angle can be observed.

### 3.5. TANDEM EXPERIMENTAL RESULT

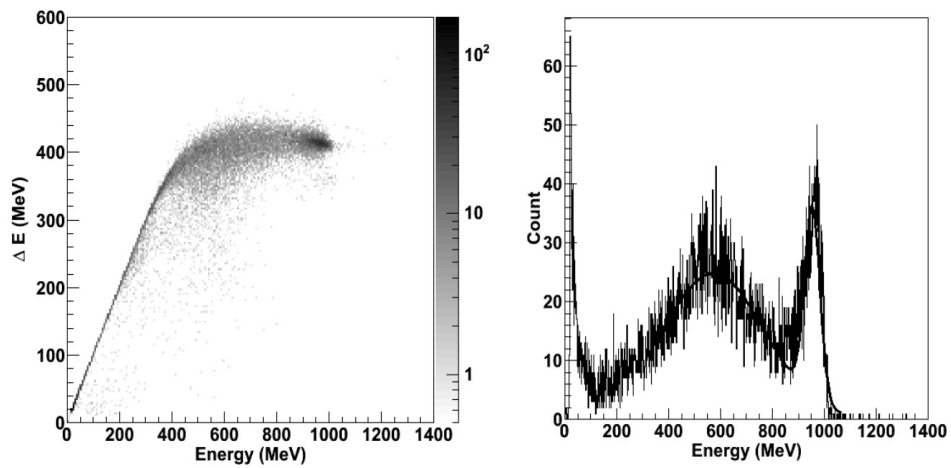


Figure 3.26 (left)dE-E distribution of one segment( $\sim 24^\circ$ ) in SSSD placed at  $40^\circ$ . (right)The energy distribution of Xe channels. The elastic scattering was decomposed from the rest of the reaction fragments by Gaussian fitting to the elastic channel and reaction channels. Both figures the beam energy was 8 MeV/u.

### *3.5. TANDEM EXPERIMENTAL RESULT*

beam with different energy of 6, 6.5, 7, 7.5, 8 MeV/u bombarded into  $^{198}\text{Pt}$  target with thickness of 1.6 mg/cm<sup>2</sup>. The two detector sets were used to detect the fragment angle, energy distribution and the charge number of both PLF, and TLF. In order to find the hint of the best setup possible, to maximize the acceptance.

The setup of this experiment can be seen at figure 3.24. For the beam energy of 8 MeV/u, the first detector set was placed at 40° to cover angle of 22 ~ 58°, and second detector set was placed at 50° to cover 40 ~ 60°. Each detector set was consisted of single sided Si strip detector (SSSD) which served as dE detector, and solid state Si detector(SSD) E detector was used. The first detector set the thickness of SSSD was 20  $\mu\text{m}$ . The second detector set was the thickness of SSSD was 61  $\mu\text{m}$ . Both thickness of SSD was 325  $\mu\text{m}$ , the area of two detector set of 50×50 mm<sup>2</sup>. To increase angular resolution detector set was covered with vertical slit of 10 mm. The two Si detectors were set at the angle – 20 ° and 20 ° to count the elastic scattered  $^{136}\text{Xe}$ . And Faraday cup was set at 0 ° to monitor the beam current.

The angular distribution and energy of distribution is presented in figure 3.25. The sudden drop of cross section showed that grazing angle of the system is at ~30 ° in the LAB frame(different from calculated grazing angle ~32.6°). The energy distribution showed very wide distribution of energy (See figure 3.26) at the forward angle where PLF dominates. The very wide energy distribution with separation between elastic peak near ~950MeV and reaction fragments from heavily damped energy peaked at ~ 550MeV can be seen. This experimental results were considered in the setup of VAMOS (angle and  $B\rho$ ). And the result was later compared with the GANIL experimental result.

# Chapter 4

## Presorted Experimental Data: Calibration, PID, and Corrections

### 4.1 Calibration

#### 4.1.1 Multi-wire parallel plate avalanche counter calibration

The calibration of time of flight (ToF) measured between two multi-wire parallel plate avalanche chambers was carried out. The VAMOS++ spectrometer was set at 0 degree. And the faint beam was with well defined energy (8 MeV/u) was bombarded to thin gold target. The elastic scattered projectile near  $0^\circ$  was used in order to send projectile to the all channels of the MWPPAC at the focal plane. The reference  $B\rho$  of spectrometer was set to 1.2 T·m. All the ToF of MWPPAC channels

#### 4.1. CALIBRATION

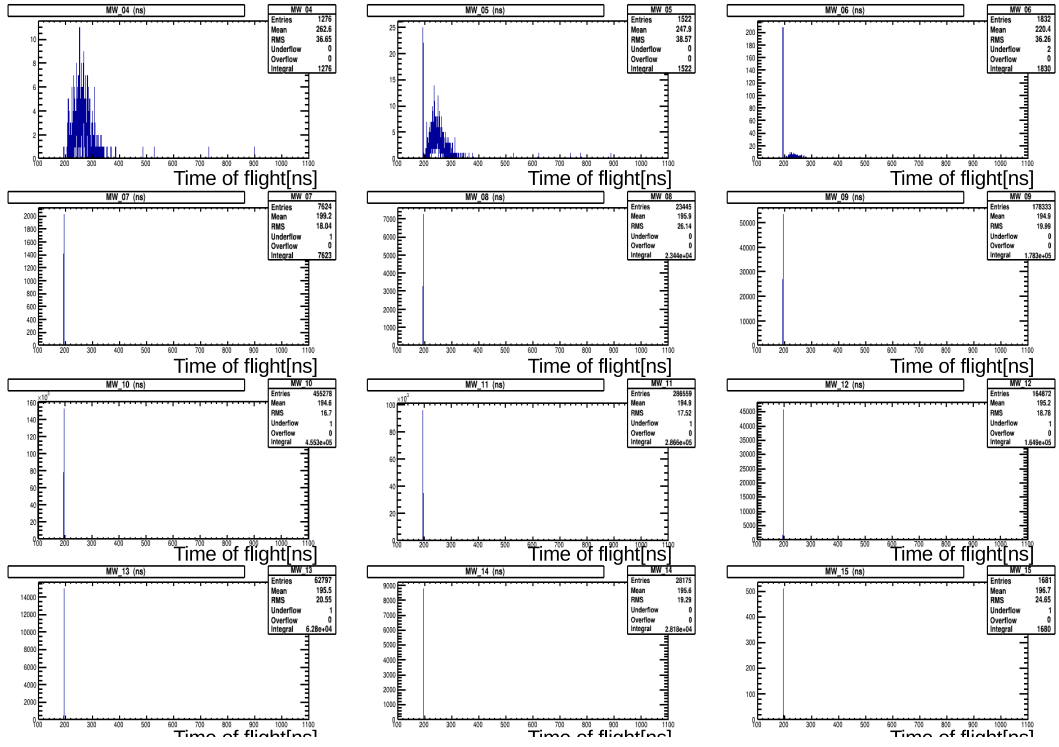


Figure 4.1 Time of flight calibration between two MWPPAC at focal plane and target using elastic scattered  $^{136}\text{Xe}$  near  $0^\circ$ . Different channels from 4<sup>th</sup>(top leftmost) to 15<sup>th</sup>(bottom rightmost) is shown

were calibrated as 194.7 ns, using the distance from MWPPAC at the target to the MWPPAC at the focal plane and velocity of projectile. (See figure 4.1) The small difference of flight path between different MWPPAC was later corrected by using mass distribution. (See section 4.2.2)

The event with timing few 10 ns faster than the normal events were observed. (See figure 4.2) This is presumed to be from the fast electrons from the target, which was not fully rejected from the magnet. These events were manually removed

#### 4.1. CALIBRATION

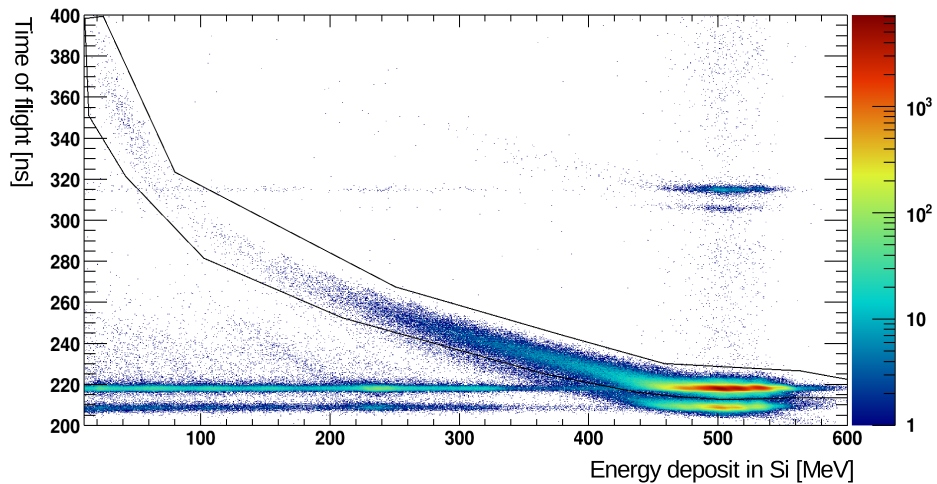


Figure 4.2 The correlation between energy deposit in Si (channel 7) and time of flight between two MWPPAC at focal plane and target. The fast timing event from MWPPAC showed similar energy distribution as the normal events indicating the false timing.

#### 4.1. CALIBRATION

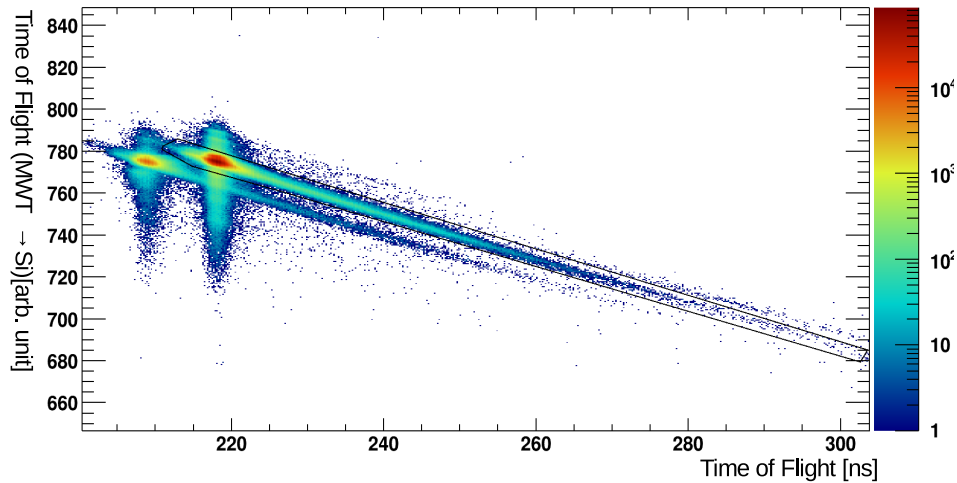


Figure 4.3 The correlation between time of flight between MWPPAC at focal plane and target and time of flight between MWPPAC at target and Si. the parallel transition shows that the timing in MWPPAC at the target had problem

by two dimensional cut in the correlation of time of flight and energy deposit in the Si detector. (See figure 4.2) The remaining fast timing events were removed by another two dimensional cut correlation of time of flight and time of flight from MWPPAC at target to Si detector. (See figure 4.3)

##### 4.1.2 Drift chamber calibration

The vertical(Y) position calibration of drift chamber was carried out based on the drift velocity of electrons inside the drift region of the chamber ( $5.645 \text{ cm}/\mu\text{s}$ ). The timing of the TAC was first calibrated by pulser signal. Then, the overall scale of the drift chamber was adjusted shadows from the wires in-front of the drift chamber.

#### 4.1. CALIBRATION

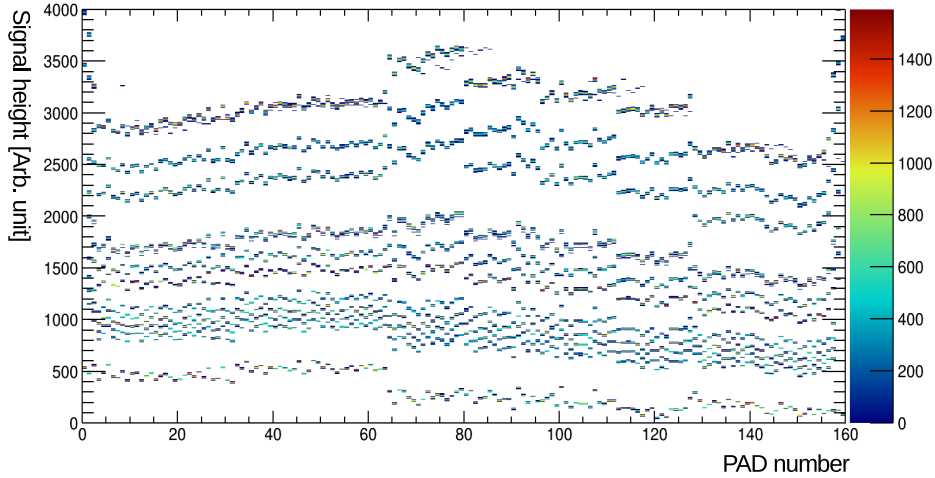


Figure 4.4 The drift chamber using pulser signal before calibration. The pulser with different signal height was used for better resolution.

(See figure 4.5) Then the vertical position can be calculated by following equation.

$$Y = V_{drift} * T + Y_{ref} \quad (4.1)$$

$Y_{ref}$  = offset position,  $V_{drift}$  = drift velocity,  $T$  = calibrated timing

The horizontal(X) position of the drift chamber was deduced from the pad signal of the detector. The diffusion of charge during drifting induces signal spread in multiple pad channels. The signal heights of the pads were matched by pedestal run and pulser signal input run of drift chamber. (See figure 4.4). The x position can be determined by the square root ratio of signal height from maximum signal pad and two pads right next to the maximum pads.

#### 4.1. CALIBRATION

$$v[0] = \text{sqrt}Q[Nmax]/Q[Nmax - 1], v[1] = \text{sqrt}Q[Nmax]/Q[Nmax + 1] \quad (4.2)$$

$$v[2] = \frac{v[0] + v[1]}{2}, v[3] = \log(v[2] + \text{sqrt}v[2]^2 - 1) \quad (4.3)$$

$$v[4] = \frac{v[0] - v[1]}{2\sinh(v[3])}, v[5] = \frac{1}{2}\log\left(\frac{1 + v[4]}{1 - v[4]}\right) \quad (4.4)$$

$$X = X_{\text{pad}}[Nmax] - (X_{\text{pad}}[Nmax] - X_{\text{pad}}[Nmax - 1])v[5]/v[3] \quad (4.5)$$

$X_{\text{pad}}[i]$ =position of i-th pad,  $N_{\text{max}}$ =pad number of maximum signal

The position calibration can be confirmed by extrapolated particle position, at the MWPPAC at focal plane and Si detector position. (See figure 4.5 and figure 4.6(si position x vs y))

The position of plastic pole of MWPPAC at focal plane is clearly seen. And the position of Si detector shows gap between different Si detectors corresponds to real physical size of the Si detector.

##### 4.1.3 Si, IC energy calibration

The Si detector and ionization chamber(IC) was calibrated first, with the pulser signal, matching the gain between different channels. And second procedure of the calibration was done using the calculated energy loss for rough energy calibration . Instead of precise calibration of each IC, and Si, the total energy was calibrated using charge states. (See Section 4.2.1).

#### 4.1. CALIBRATION

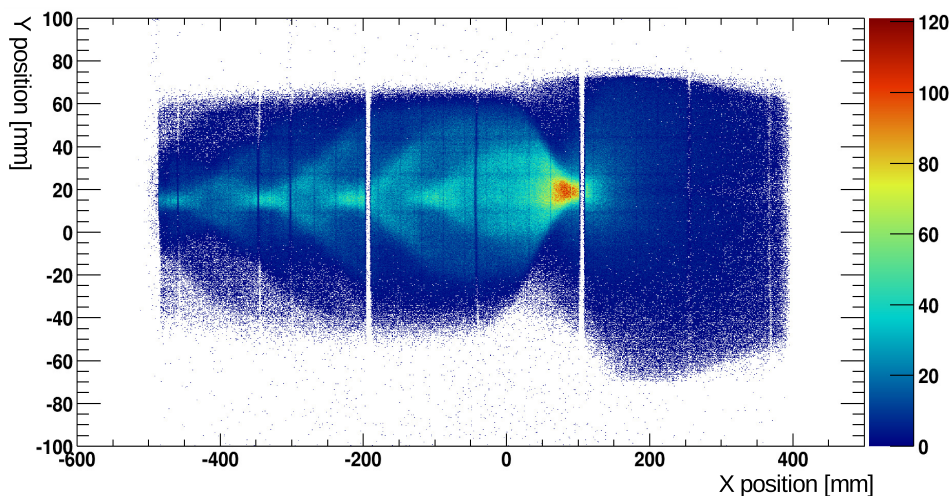


Figure 4.5 The hit position at the focal plane (30 mm in-front of MWPPAC at focal plane). The clear vertical shadows from the supporting pole inside the MWPPAC, and vertical/horizontal shadows from the field wires between exit of MWPPAC and entrance of drift chamber can be observed.

#### 4.1. CALIBRATION

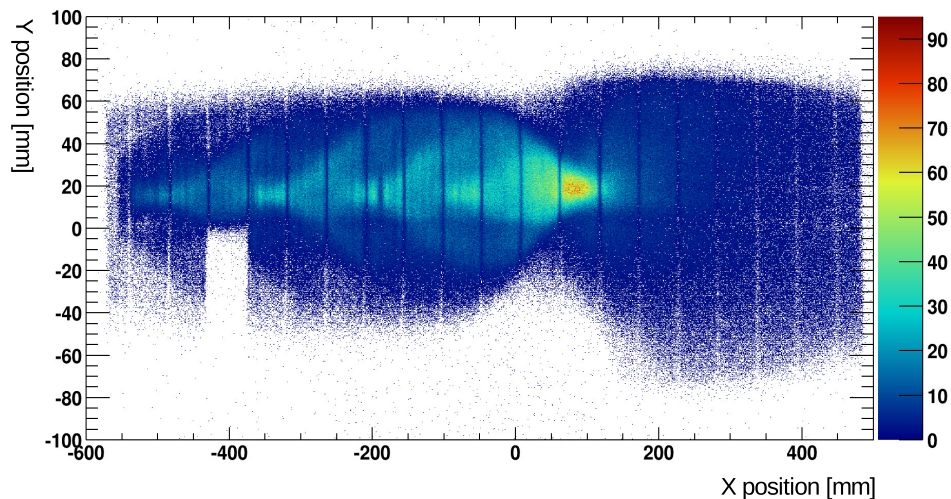


Figure 4.6 The hit position at the Si plane. The clear vertical shadows from the gap between different Si detector can be seen. The blank region in the left lower side is due to broken Si detector.

#### 4.1. CALIBRATION

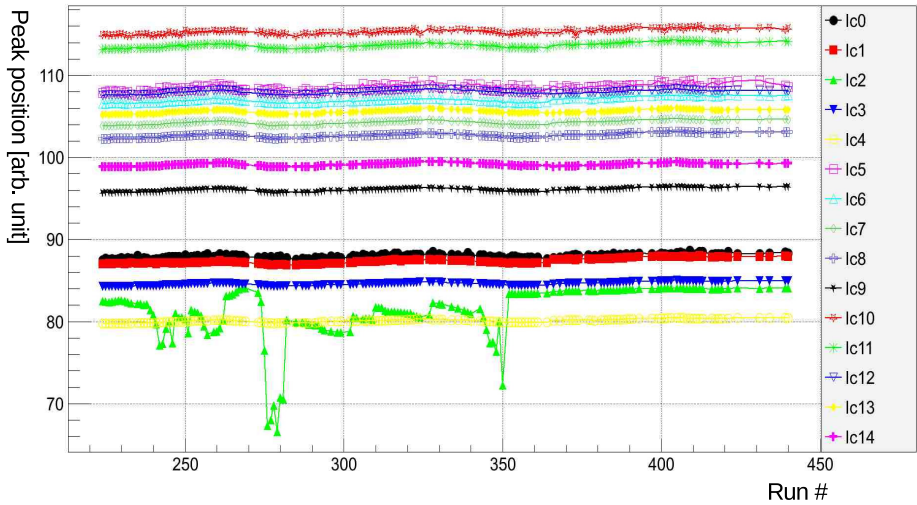


Figure 4.7 The ionization chamber(IC) energy peak from elastic scattering as function of run number. The unstalbe gain in the channel 2 can be seen, the other channels showed very small fluctuation order of few MeV. The gain was corrected run by run using the fitting result

This is due to the fact that energy calibration of Si, IC with conventional method (calibration source like  $^{241}Am$  alpha source which have energy of several MeV) is not appropriate, since the energy of the incoming projectile is order of several  $10^2$  MeV to *sim*  $10^3$  MeV.

During the experiment, the few channels in the ionization chamber and several channels in the Si detector suffered from unstable gain. The energy loss peak from the elastic scattering was used, to check the gain change through out the experiment run by run. (See figure 4.7, 4.8). The gain change during experiment was fixed using the fitting result.

#### 4.1. CALIBRATION

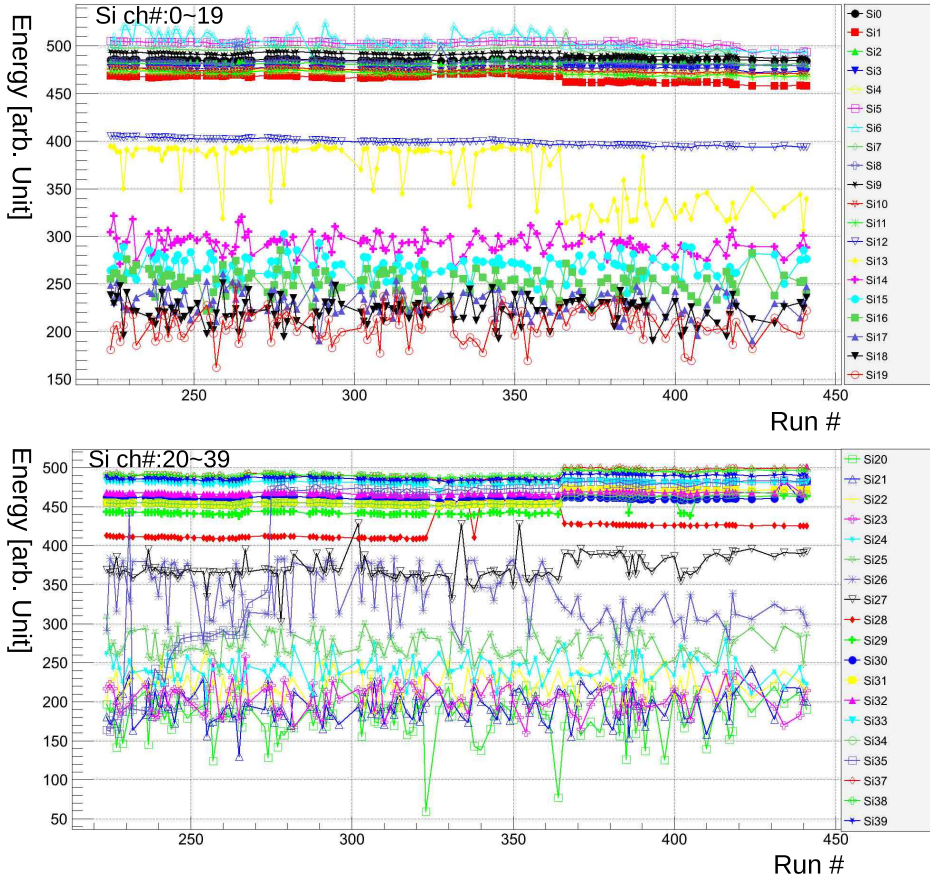


Figure 4.8 The Si detector energy peak(except for Si detector channel :15~24 which used mean of energy distribution) from elastic scattering as function of run number. The sudden change in the gain for different Si detectors can be observed. The instability of Si detectors in low  $B\rho$  regions (Si detector channel: 15~24) due to absent of elastic peak.

## 4.1. CALIBRATION

### 4.1.4 Ge detector

#### Energy calibration

The energy calibration of EXOGAM Ge clover array was executed after the beam time. The signal from each Ge-crystal, and outer contacts were calibrated using  $^{152}\text{Eu}$  source which has various  $\gamma$ -decay energy. The second order polynomial was used for deducing energy calibration parameter.

#### 4.1.5 Timing calibration

The  $\gamma$ -ray timing of EXOGAM was measured with respect to the MWPPAC at the focal plane(MWFP). Therefore time of flight of projectile is included in the measurement. Thus the time of flight from target to MWFP is needed to be excluded. The scale of timing was deduced from the pulser calibration. The peaks from the off coincident shows good matching with RF signal (10.32188MHz) from the CSS1 cyclotron which was 96.9105 ns. (See figure 4.9)

$$T_\gamma = a1T_{EXOGAM-MWFP} - a2T_{MWT-MWFP} - T_{target-MWT} \quad (4.6)$$

a1: Scale parameter of EXOGAM w.r.t MWPPAC at focal plane

a2: Scale parameter of MWPPAC at target

The signal height dependence of timing from the CFD causes energy dependence of timing. (although CFD is used to correct signal height dependence, small amount it still remains) The SLEW correction was carried out to correct this effect. The timing peak of each Ge-detector was investigated with 10keV slice of  $\gamma$ -ray energy of  $0 \sim 2000$  keV. The several crystals timing was independent from energy but some crystal had energy timing in order of few ns. (See figure 4.10) The timing was

#### 4.1. CALIBRATION

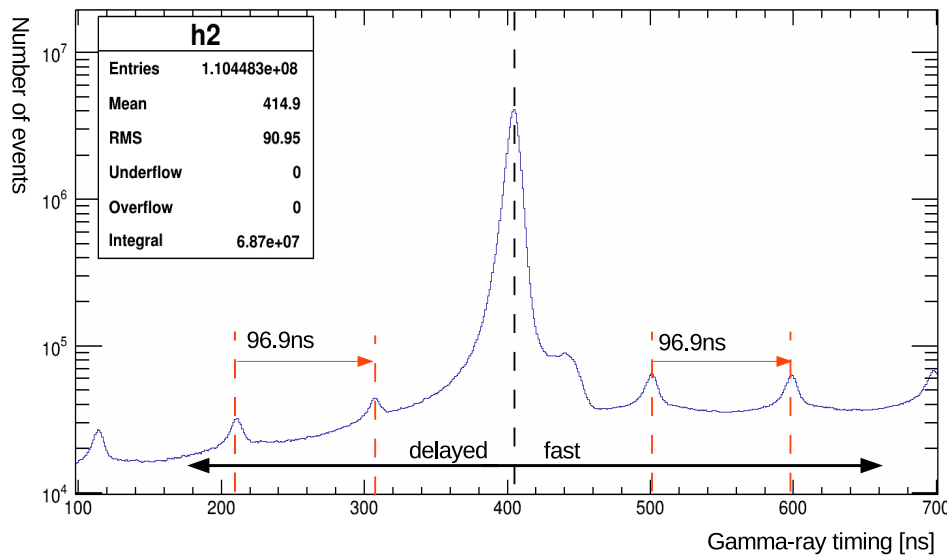


Figure 4.9 The timing of gamma-ray considering time of flight of PLF. The major peak from in beam gamma-ray events. The small peaks due to off coincident event with same period of RF signal from cyclotron

#### 4.1. CALIBRATION

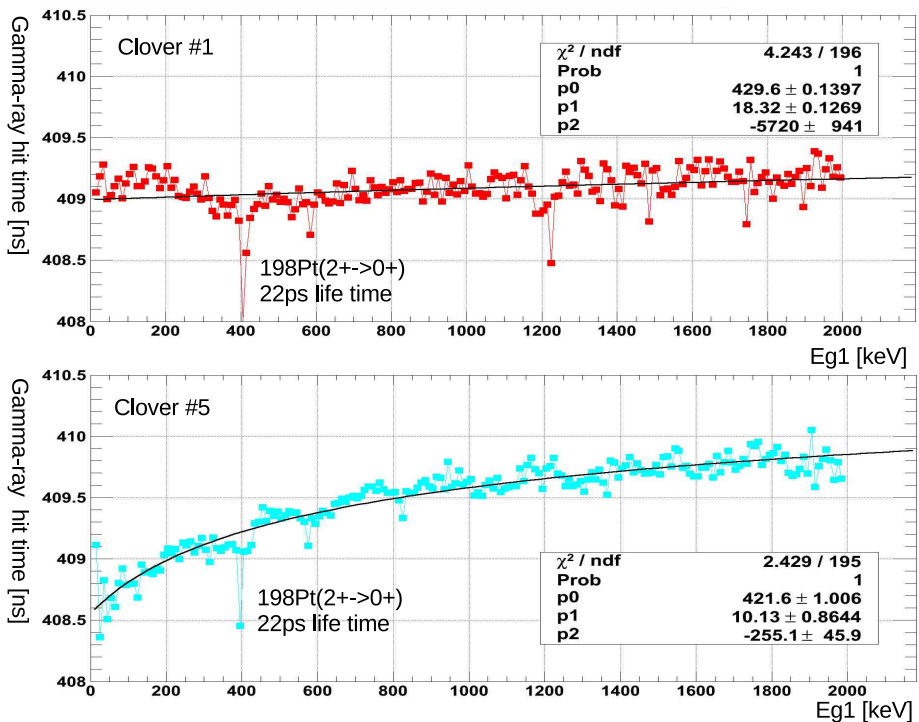


Figure 4.10 The energy dependence of timing in different Ge clover detectors. (top) timing dependence of energy of Clover detector 1 which shows almost no dependence. And (bottom) Clover detector 5 which shows  $\sim 1$  ns decrease in timing from 1000keV to 0keV

#### 4.1. CALIBRATION

corrected for each clover by fitting with empirical function.

$$\Delta T_{correction} = (a + b \exp(1/(E - c)^1/4)) \quad (4.7)$$

#### Geometrical calibration

The accurate angle between projectile and  $\gamma$ -ray is required, in order to apply Doppler correction. The position of each Ge detector was measured by detector holder angle and detector position relative to the holder. (See table 3.8 and 3.9) The geometrical calibration was confirmed by angular dependence of the Doppler corrected  $\gamma$ -ray. The de-excitation of first excited state of  $^{136}\text{Xe}$  ( $2+ \rightarrow 0+$ ), which has energy of 1313.023 keV shows same peak position over all angles. (See figure 4.12)

#### Doppler correction

The projectile-like fragments and target-like fragments have relativistic velocity after the reaction. The Doppler correction was applied, in order to detect the de-excitation energy of  $\gamma$ -ray from reaction fragments. The energy and angle of target-like fragments were not measured directly. The missing mass calculation was used to determine velocity and angle of target-like fragment, assuming two-body kinematics(See Appendix). The energy loss of projectile-like fragment from MWPPAC near target, and target was accounted event-by-event using SRIM code[117].

$$E_{corrected} = E_{detected} \times \gamma(1 - \beta \cos(\Theta_\gamma)) \quad (4.8)$$

$E_{detected}$  = energy detected in EXOGAM

$\Theta_\gamma$  = angle between  $\gamma$ -ray and projectile velocity

#### 4.1. CALIBRATION

The resolution of Doppler correction consists of three factors from the Doppler correction equation. First is from intrinsic energy resolution of the detector. The second factor is from velocity, and the last factor is from angular resolution, which can be written as equation below.

$$\left(\frac{\Delta E_{corrected}}{E_{corrected}}\right)^2 = \left(\frac{\Delta E_{detected}}{E_{detected}}\right)^2 + \left(\frac{\beta \sin \theta}{1 - \beta \cos \theta}\right)^2 \Delta \theta^2 + \left(\frac{\gamma(-\beta + \cos \theta)}{1 - \beta \cos \theta}\right)^2 \Delta \beta^2 \quad (4.9)$$

$$\beta: \text{speed of nuclei } (\beta = \frac{v}{c}), \gamma = \frac{1}{\sqrt{1-\beta^2}}$$

The intrinsic energy uncertainty ( $\sim 2.5$  keV at 1313 keV) was negligible compared to other two factors. The second and third term representing resolution from velocity and angle have different dependency of angle. (See figure 4.11) Where velocity term has minimum effect in the resolution at  $90^\circ$  while large effect at  $180^\circ$ . But in case of angular uncertainty it shows counter wise dependence on the angle.

In the practice the angular and velocity resolution were determined using this different angular dependence. The width of  $\gamma$ -ray from  $^{136}\text{Xe}$  with energy of 1313.023keV was measured as function of angle. (See figure 4.12)

This  $\gamma$ -ray peak was chosen since it has the largest statistics with high enough energy where change of peak position and width(resolution) could be measured clearly. The life time of this state was  $T_{\frac{1}{2}} = 0.36$  ps [125] and the typical  $\beta$  of  $^{136}\text{Xe}$  was  $\sim 0.12$ . The estimated position of decay is outside of the target. Thus the energy losses from target need to be accounted in the velocity of projectile. The width graph was fitted with the above equation by setting resolution of  $\beta, \theta$  as a free parameter. The fitting results are shown in figure 4.13 are summarized in Table 4.1.

The fitting result indicates that the main source of uncertainty of Doppler correction was caused by the angular uncertainty. This is factor  $\sim 3$  larger than the spec.

#### 4.1. CALIBRATION

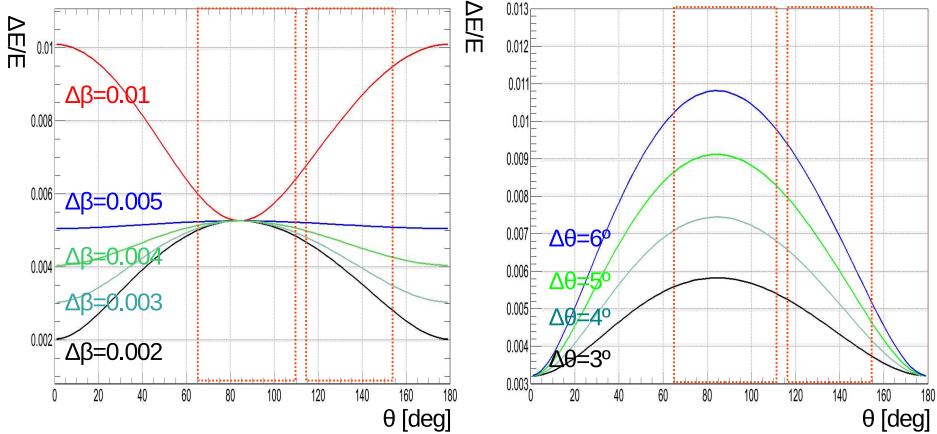


Figure 4.11 The energy dependence of timing in different Ge clover detectors. (top) timing dependence of energy of Clover detector 1 which shows almost no dependence. And (bottom) Clover detector 5 which shows  $\sim 1$  ns decrease in timing from 1000keV to 0keV

	EXOGAM spec.[97]	fitting result
$\Delta\theta$	$3^\circ$	$9.42^\circ$
$\Delta\beta$	$>0.002$	0.0059

Table 4.1 Fitting result of Doppler correction resolution.

#### 4.1. CALIBRATION

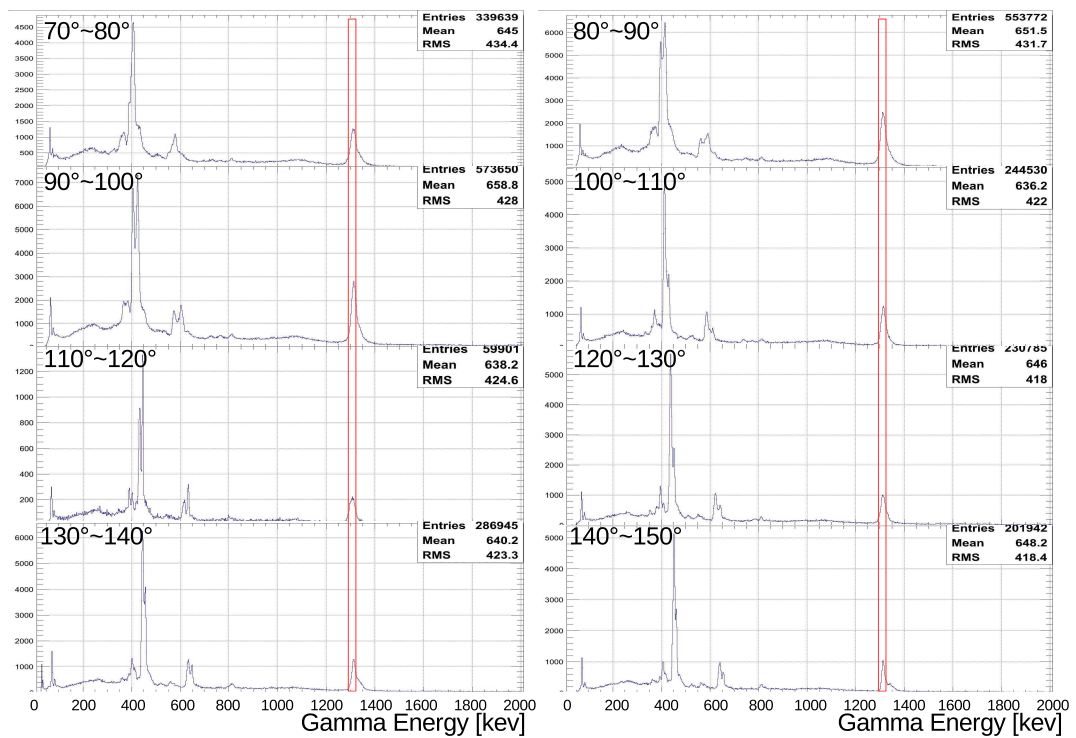


Figure 4.12 The energy of gamma-ray Doppler corrected for projectile-like fragment with angular distribution  $10^\circ$  cut from (top left)  $70^\circ \sim 80^\circ$  to (bottom right)  $140^\circ \sim 150^\circ$

#### 4.1. CALIBRATION

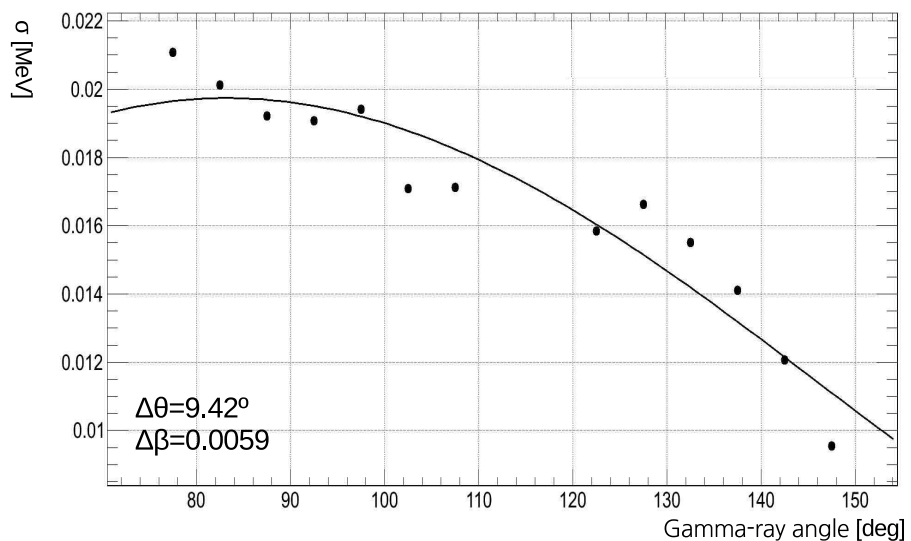


Figure 4.13 The graph of angular dependence of energy resolution  $\sigma$ )of gamma-ray peak 1313keV of  $^{136}\text{Xe}$ , Doppler corrected for projectile-like fragment . The graph was fitted with formula 4.9

## 4.2. PARTICLE IDENTIFICATION

of EXOGAM. This large angular uncertainty comes from the beam position uncertainty. The uncertainty of beam spot causes uncertainty in reconstruction, which leads to angular uncertainty in the Doppler correction. This will be discussed in more detail at Section 4.3. The velocity resolution was also larger than lower limit by factor  $\sim 3$ . But this was due to the uncertainty of the energy loss inside the target and MWPPAC near the target was larger, since we used heavy beam and target combination.

## 4.2 Particle Identification

The particle identification was carried out based on diagram Figure. 4.14

### 4.2.1 Total Energy Calibration and Charge state identification

The total energy was calibrated based on the detected energy from the Si and IC using charge states. The charge state can be determined directly from the total energy with equation 4.10

$$Q = \frac{E_{tot}/(\gamma - 1)}{M/Q} \quad (4.10)$$

$$\frac{M}{Q} = \frac{B\rho}{3.107\beta\gamma} \quad (4.11)$$

$E_{tot}$  = total energy of incident projectile detected from Si and IC.

The charge state in heavy nuclides with damped reaction results wide range of charge states. Thus the good calibration of charge state for all regions indicates

## 4.2. PARTICLE IDENTIFICATION

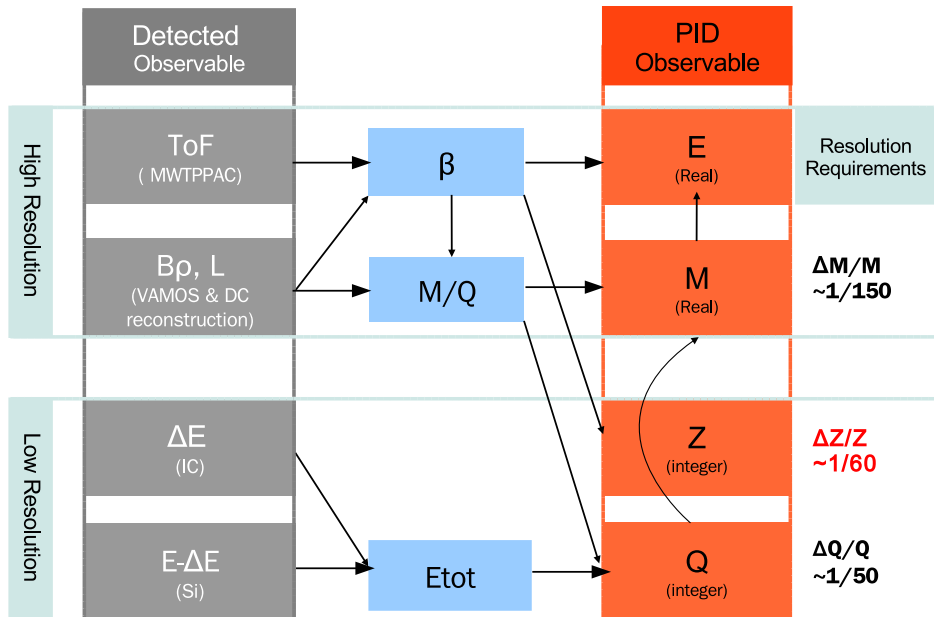


Figure 4.14 The flow chart of particle identification process. Each parameters were divided in to two by resolution (detection, requirement). The energy detected by Si and IC had low resolution, while time of flight,  $B\rho$ , and travel length from reconstruction had high resolution. While the particle identification parameters charge state and atomic number which is integer value required low resolution, while the energy and mass needs good resolution. The detected parameters were combined to produce PID parameters to satisfy the required resolution

## 4.2. PARTICLE IDENTIFICATION

good calibration of total energy. Besides the rough calibration of the IC, and Si, (see Section 4.1.3) the sum of detected energy of IC and Si is not the same as the actual projectile energy. The energy loss from MWPPAC at focal plane, drift chamber, Mylar foil, drift region in front of IC and the Si dead layer should be accounted. The inflated Mylar foil in front of the ionization chamber which makes position dependent energy loss was accounted. Thus the total energy can be described as

$$E_{tot} = a1E_{IC1} + a2E_{IC2} + a3E_{IC3} + a4E_{Si} + a5E_{IC1}(1 - \frac{Yf^2}{80}) \quad (4.12)$$

$E_{ICn}$ : Energy detected in n-th row of IC,  $E_{Si}$ : Energy detected in Si

$Yf$ : Horizontal position at focal plane

a1: Energy loss in front of IC, a2~a3: micro adjustment of IC row 2, 3(~1)

a4: Energy loss due to Si dead layer and drift region between Si, IC, ]

a5: Energy loss due to inflated Mylar foil(a5<<1).

First, the five coefficients (a1 ~ a5) were roughly deduced by energy loss calculation using SRIM[117]. The total energy was used to determine charge state.

$$Mass_{Etotal} = \frac{E_{total}}{\gamma - 1}, Q = \frac{Mass_{Etotal}}{M/Q} \quad (4.13)$$

Then the parameters were adjusted by fitting using unbinned chi-square minimization, by using software minuit2 to make Q peak near the integer value. (See figure 4.15) Although the charge state was determined by calibration of the total energy, improvements were needed for optimization the charge states due to various reasons. First the  $\frac{M}{Q}$  (of Mass dependence) in charge state due to the energy calibration in different energy regions. The high  $\frac{M}{Q}$  which has small velocity (and

## 4.2. PARTICLE IDENTIFICATION

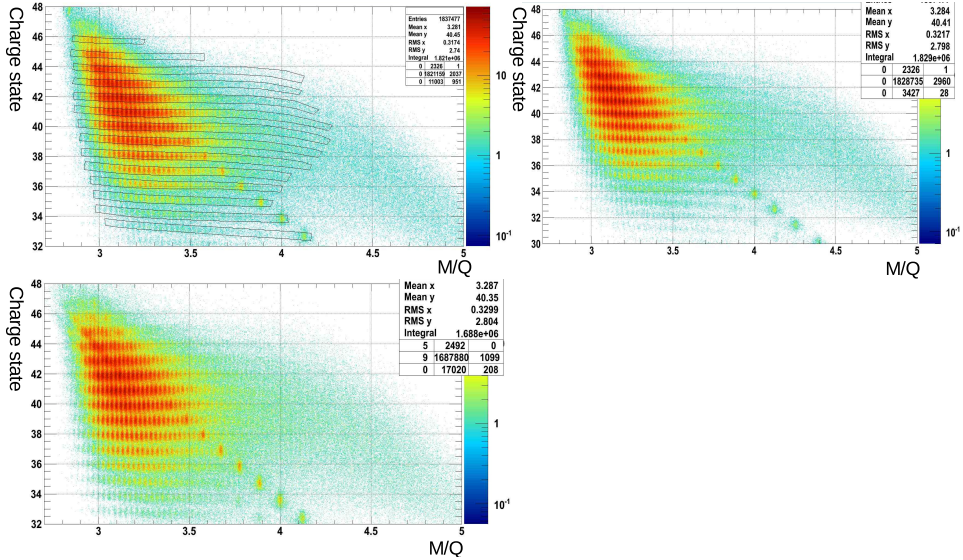


Figure 4.15 The total energy calibration using charge state distribution of events hitting Si detector channel 17. (top left) The correlation of charge state and  $\frac{M}{Q}$  from rough calibrated energy, the charge states dependence can be seen. The events selected by two dimensional cuts, which have clear charge states were used for fitting. (top right) The same histogram with applying fitting result using equation 4.12. (bottom left) The additional correction using equation 4.14.

## 4.2. PARTICLE IDENTIFICATION

energy) the energy calibration using above equation deviates from the real energy. This makes  $\frac{M}{Q}$  vs charge state distribution curved. (See figure 4.15) The charge state was corrected directly based on empirical equation below to make charge state independent on  $\frac{M}{Q}$  with same charge state.

$$\Delta Q = a1 \frac{M/Q}{Mass} (M/Q - a2)^3 + a3 \quad (4.14)$$

The each parameter was set by unbinned chi-square fitting of  $Q$  vs  $\frac{M}{Q}$  distribution using the program minuit2.

Second the position dependence of the charge state. This was due to the ionization chamber suffered from field leakage at the edge of exit plane. The projectile passing the edge of the ionization chamber detected energy is smaller since the charge collection efficiency decreases causing decrease in charge state distribution. (See figure 4.17, 4.18) This field leakage was confirmed by computer software GARFIELD[95]. (See figure 4.16) This position dependence of ionization chamber detection energy was corrected by making charge state independent from the IC position.

Finally the charge state distributions were integerized by fitting distribution with multiple Gaussian functions. (See figure 4.19) The crossing point of different Gaussian functions were used as a limit of each charge states. The charge state resolution was  $\frac{\Delta Q}{Q} = \frac{1}{77}(FWHM)$  which is higher than the requirement of this experiment. This indicates very small possibility of wrong determination of charge state, which causes misidentification of the mass.

## 4.2. PARTICLE IDENTIFICATION

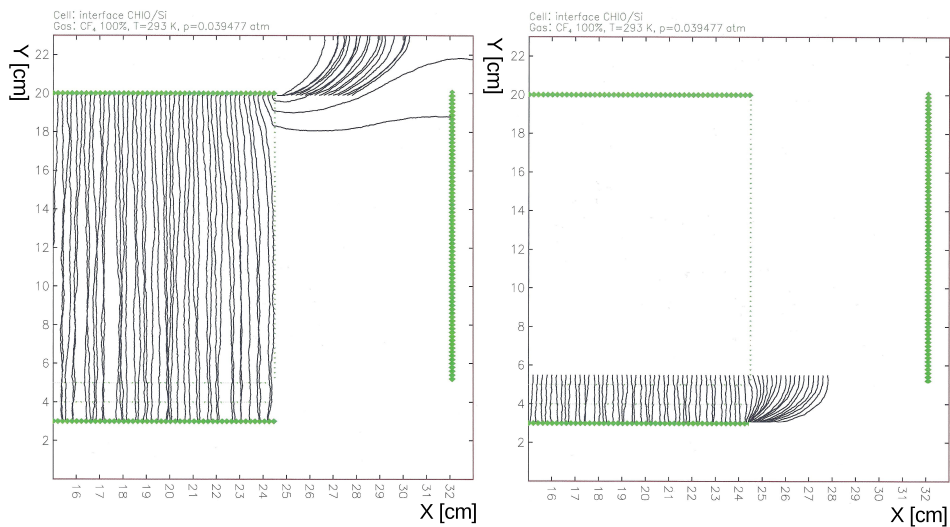


Figure 4.16 (left) Field leak of IC near the cathode. (right) Field leak of IC between Frisch grid, Amplification grid, and anode. The field leak in each regions showed different pattern.

## 4.2. PARTICLE IDENTIFICATION

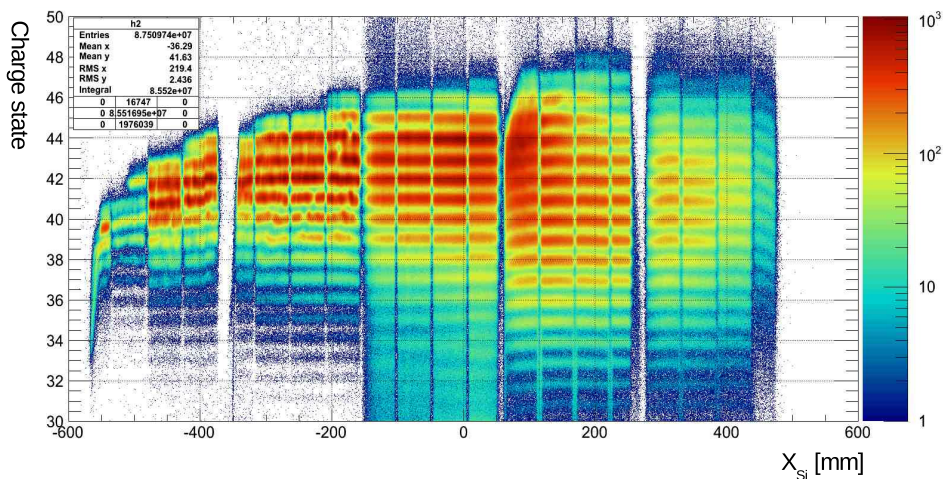


Figure 4.17 The correlation between charge state and X hit position at the exit position of IC. The sudden decrease in charge state at the edge of the IC chamber exit can be observed

## 4.2. PARTICLE IDENTIFICATION

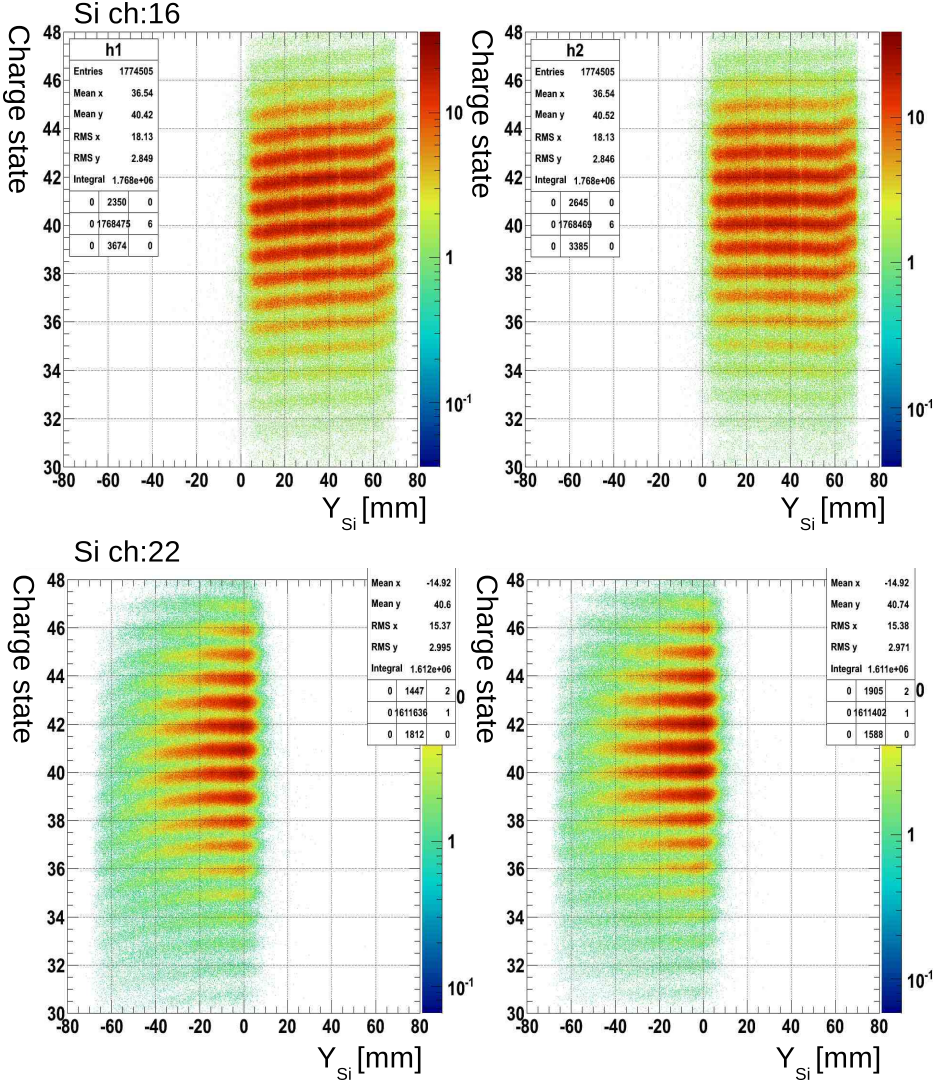


Figure 4.18 The correlation between charge state and Y hit position at the exit position of IC for typical Si detector(channel 17, 22) events before and after position dependence correction. (top left) Si detector channel :17 events before correction, overall tilt in the charge state and sudden change at the edge can be seen (top right) Si detector channel :17 after correction. (bottom left) Si detector channnel : 22 before correction, gradual decrease in the charge state can be seen due to different field leak pattern. (bottom right) Si detector channel : 22 after correction.

#### 4.2. PARTICLE IDENTIFICATION

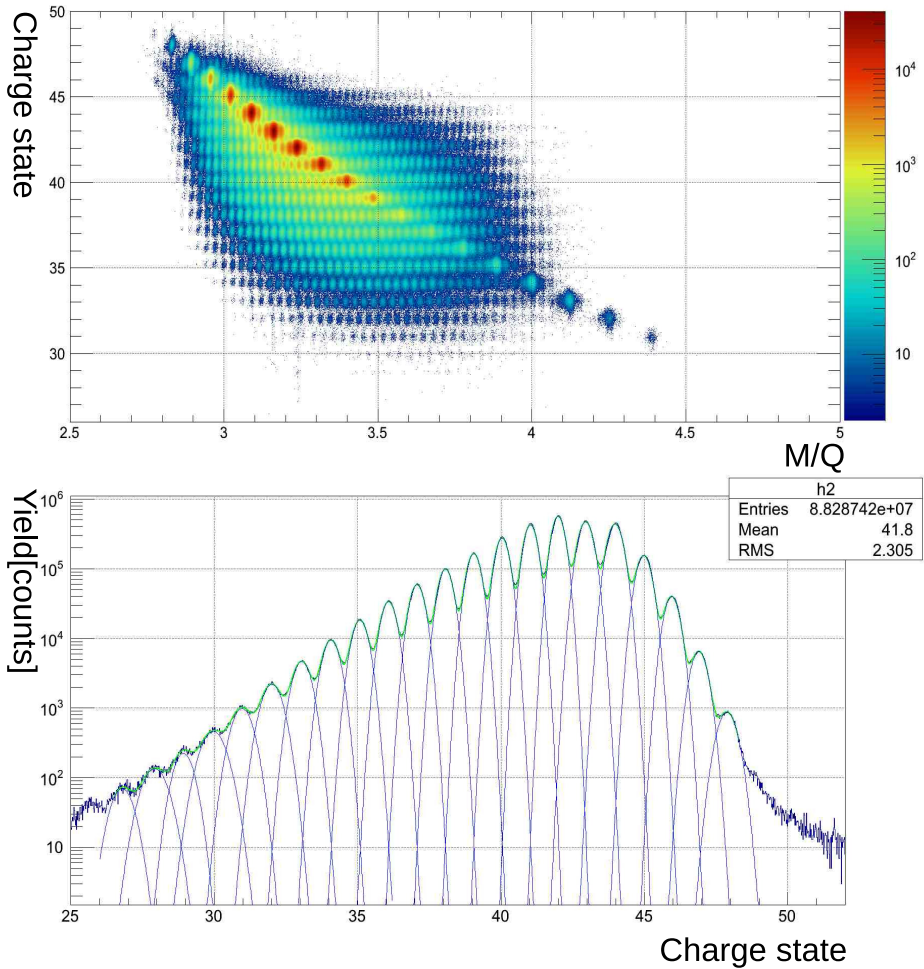


Figure 4.19 (top) The correlation of charge state and  $\frac{M}{Q}$  for all events. (Bottom) Charge state distribution fitted with multiple Gaussian function, resolution of  $\frac{\Delta Q}{Q} = \frac{1}{77}$  (FWHM) was achieved after all corrections.

## 4.2. PARTICLE IDENTIFICATION

### Blob Events

The small fraction ( $< 10\%$ ) of events from the elastic scattering suffered from malfunction of Si detector.(named as blob events for convenience) The blob events and normal events had no physical difference except for the Si detected energy was  $10\sim30\text{MeV}$  higher than the normal events. These caused events with same  $\frac{M}{Q}$  have different charge states, making isotopic distribution of Xe higher than 136 highly distorted from the elastic event. (See figure 4.20) The ratio between elastic peak and blob event was different for each Si detector channels and charge state channels. The blob events were observed even at the run with the stable gain. These two evidences indicate that the blob events were not caused from unstable gain of Si detector. The channels other than the elastic scattering, blob events were not observed. The blob events were corrected by the charge state vs mass distribution. (See figure 4.21) The blob events were manually selected by using graphical cut and making shift of charge state and energy. But this manual graphical cut also contains data from the neutron pickup channel of Xe. Thus the neutron pickup channel with mass larger than  $^{137}\text{Xe}$  contains high uncertainty.

#### 4.2.2 Mass number identification

The mass can be determined right after the charge state identification, by multiplying integerized charge state to the  $\frac{M}{Q}$ . The time of flight was adjusted to make mass peaks align to the integer value. (See figure 4.22) The mass was also fitted with multi-Gaussian function in order to determine the integerized mass and the resolution. (See figure 4.22) The resolution of the mass distribution was  $\frac{\Delta M}{M} = \frac{1}{203}$

#### 4.2. PARTICLE IDENTIFICATION

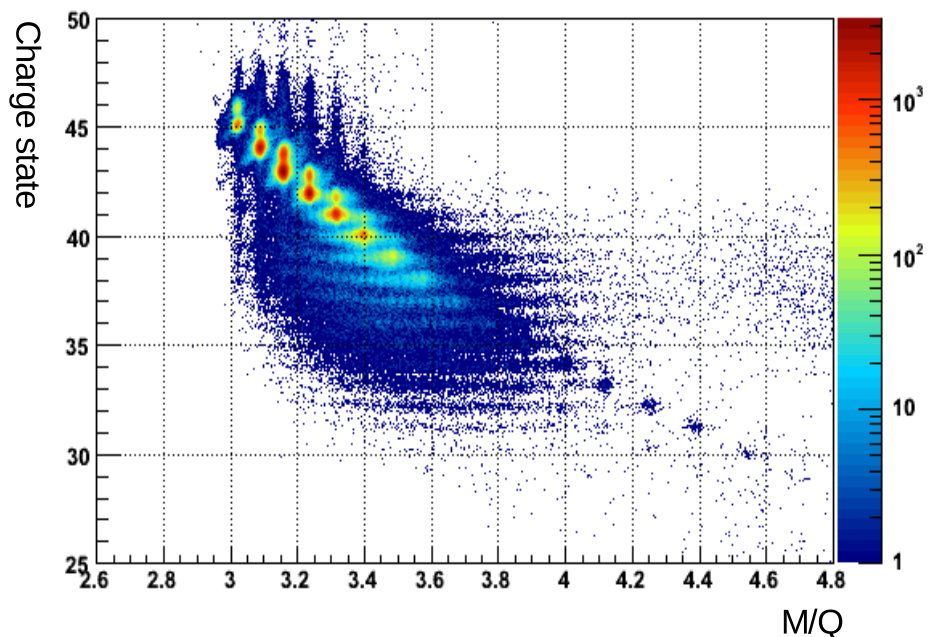


Figure 4.20 The correlation of charge state and  $\frac{M}{Q}$  in Si detector channel 7. Right above elastic peak smaller peak can be seen.

## 4.2. PARTICLE IDENTIFICATION

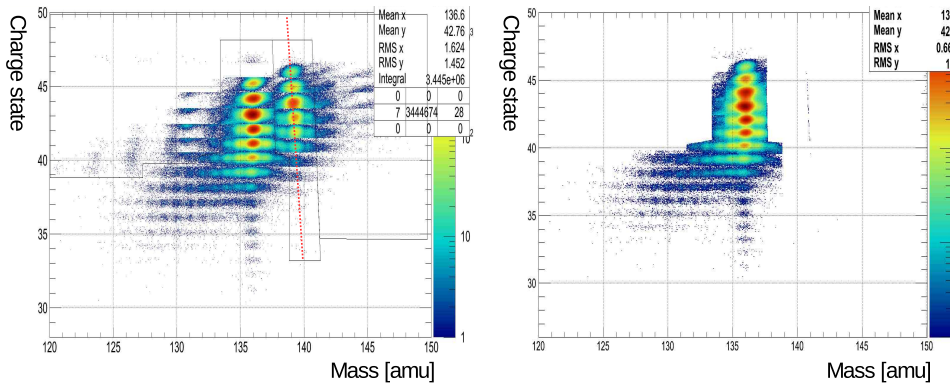


Figure 4.21 The correlation of charge state and Mass of Xe channels in Si detector channel 7.(right) Distribution before correction, the mis-identification of charge state of blob events (can be seen 2~4 neutron pickup channels) results mass dependence of charge state(red dotted line). The two dimensional cut for selecting blob events are shown as box. (left)The distribution after correction blob events by correcting charge state by -1.

## 4.2. PARTICLE IDENTIFICATION

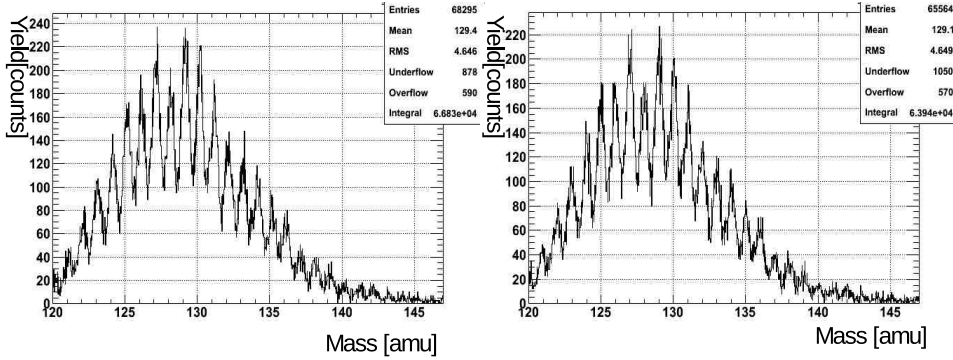


Figure 4.22 (left) Mass distribution of Si detector channel 11, with charge state 38 before fine calibration of time of flight. (right) Mass distribution after the fine calibration. The after the mass was aligned at the integer value (FWHM) which is higher than the requirement for this experiment. (See figure 4.23)

### 4.2.3 Atomic number identification

The atomic number of the PLF was determined by dE-E method. The dE measured in ionization chamber is square proportional effective charge of the projectile and inverse proportional to the squared velocity, which can be seen to the from Bethe-Bloch formula.

$$-\frac{dE}{dx} = \frac{4\pi}{m_e c^2} \frac{n Z_{effective}^2}{\beta^2} \left( \frac{e^2}{4\pi\epsilon_0} \right)^2 \left[ \ln \left( \frac{2m_e c^2 \beta^2}{I(1 - \beta^2)} \right) - \beta^2 \right] \quad (4.15)$$

n=electron density of material,  $m_e$ =rest mass of electron

I=mean excitation potential,Z=atomic number of projectile

## 4.2. PARTICLE IDENTIFICATION

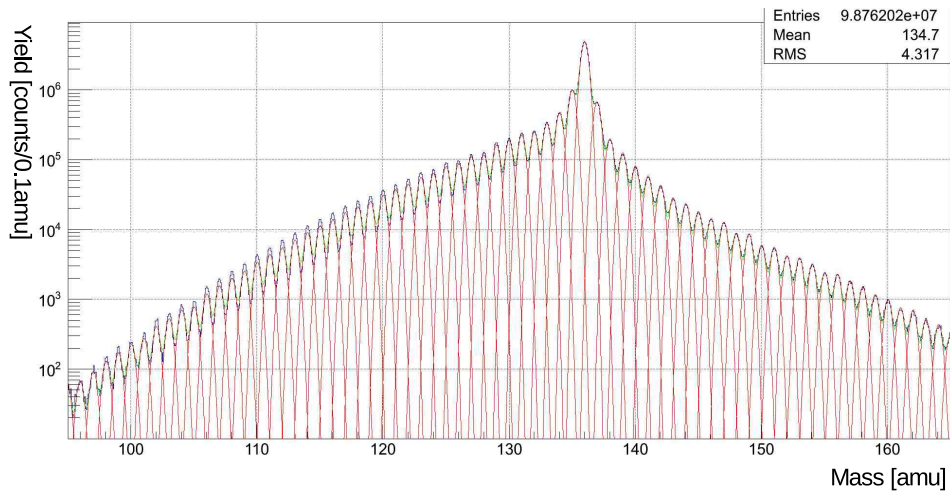


Figure 4.23 Mass distribution including all events. The mass peak are aligned at the integer indicating successful mass calibration. The distribution was fitted with multiple Gaussian function. The resolution from the fitting result was  $\frac{\Delta M}{M} = \frac{1}{203}(FWHM)$

## 4.2. PARTICLE IDENTIFICATION

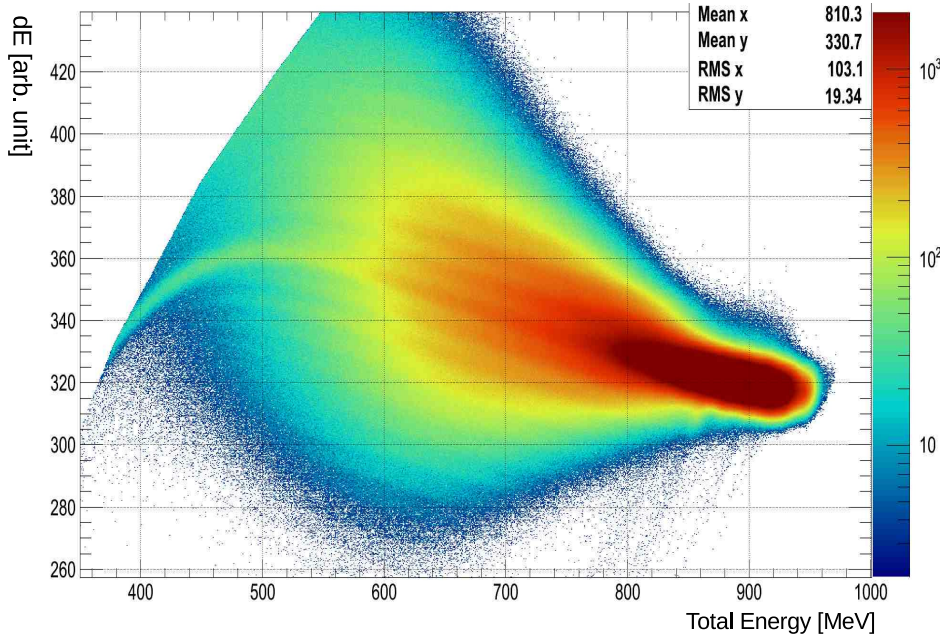


Figure 4.24 The correlation of dE and E. The each atomic numbers can be identified by curved bands.

The dE detected in ionization chamber depends on the path length for each incoming nuclides. In order to get  $\frac{dE}{dx}$ , it was converted to energy loss over same travel length of size of the ionization chamber.

$$\left(\frac{dE}{dx}\right)_{IC} = dE_{detected} \cos\theta \cos\phi \quad (4.16)$$

$X_{IC}$ : Depth of ionization chamber (100 + 120 + 120 mm)

And the energy of each ionization columns were further adjusted to match one another for better statistics. (See figure 4.24)

The the dE vs E distribution were converted to Z vs E distribution by using formula based on Bethe-Bloch formula. The additional terms were included for better

## 4.2. PARTICLE IDENTIFICATION

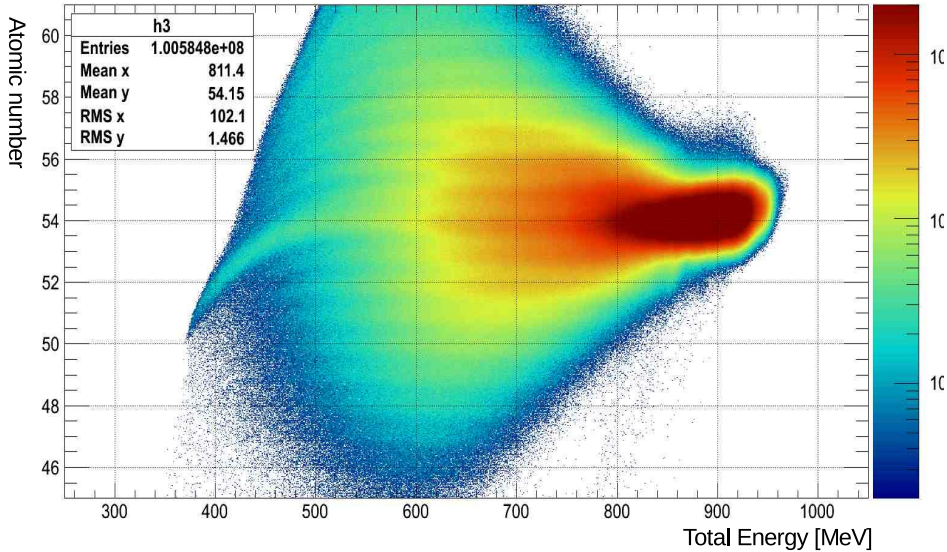


Figure 4.25 The two dimensional histogram of atomic number vs E. The each atomic numbers can be identified as parallel lines.

linearity of the atomic number and scaling to the integer value. The unbinned chi-square fitting by program minuit2 was used in order to determine the coefficients.

$$PI = \frac{(\frac{dE}{dx})X_{IC}\beta^2}{a1 + a2\beta^2 + a3\log(\beta^2/(1 - \beta^2))} \quad (4.17)$$

$$Z = a4(PI + a5M + a6)^{a7} \quad (4.18)$$

a1~a7: Fitting parameter,  $\beta$ :  $\beta$  of projectile, M: Mass of projectile

The clear distinction between different nuclide was not possible, due to the beam used in this experiment has the atomic number close to the detector resolution. (See figure 4.25) Thus the fitting is needed to distinguish each atomic number.

### **4.3. SPECTROMETER DETECTION EFFICIENCY**

The converted Z distribution was further sliced by energy. (See figure 4.26) This is due to large amount of elastic scattered events which dominates the whole distribution at high energy. The slicing the Z distribution over energy separates the energy regions dominated by elastic scattering, which has high total energy and reaction part which has smaller total energy. The energy sliced Z distribution was fitted with multi Gaussian function, where the crossing point was set as the border line of different atomic number. The fitting the total resolution of was fixed as the total resolution  $\frac{\Delta Z}{Z} = \frac{1}{60}$ . This is close to the limit of required resolution.

Finally two dimensional graphical cut was made using points determined from fitting of atomic number as function of total energy. (See figure 4.26) The integerized atomic number was deduced using graphical cuts. The error of parameters from the fitting was used to determine the 3 different sets of graphical cuts, which was used to determine the error of this method. The events smeared to the neighboring atomic number should be accounted, or only two dimensional histogram can be drawn. (See figure 4.27)

## **4.3 Spectrometer Detection Efficiency**

### **4.3.1 Simulation**

The detection efficiency and acceptance of the spectrometer was deduced, in order to determine number of events at the reaction. The detection efficiency is determined by the electro-magnetic field and setup of detector of the spectrometer. The detection efficiency was calculated based on Monte-Carlo simulation. The projectile

### 4.3. SPECTROMETER DETECTION EFFICIENCY

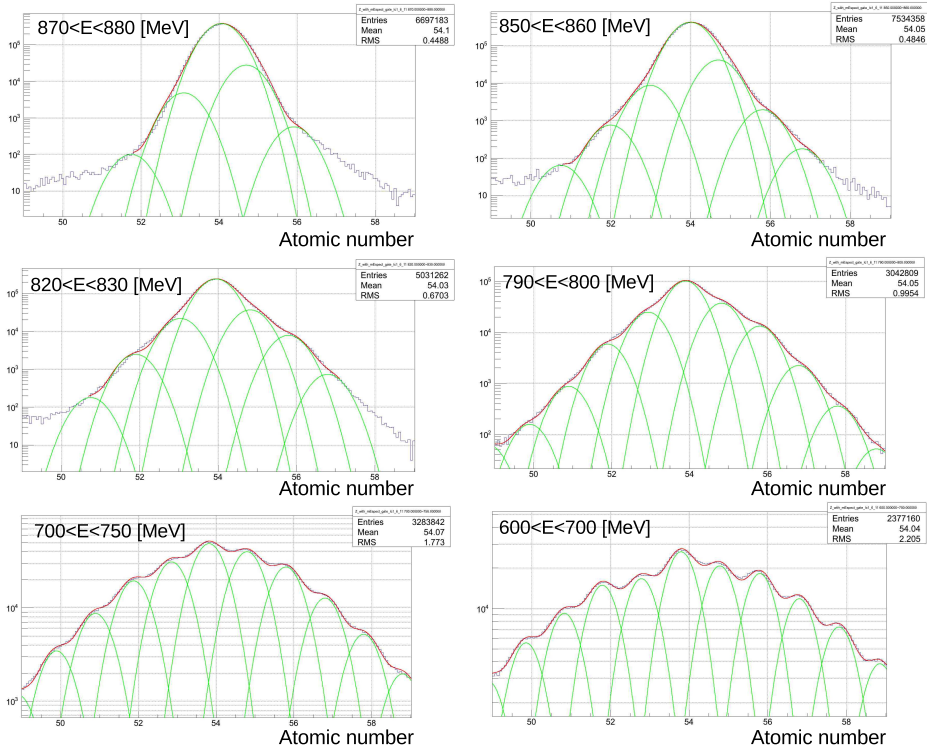


Figure 4.26 The energy sliced atomic number distribution. The each atomic numbers can be identified using fitting using multi Gaussian function. The width of fitting function was limited to the same value for all histograms with the resolution  $\frac{\Delta Z}{Z} = \frac{1}{60}$ .

### 4.3. SPECTROMETER DETECTION EFFICIENCY

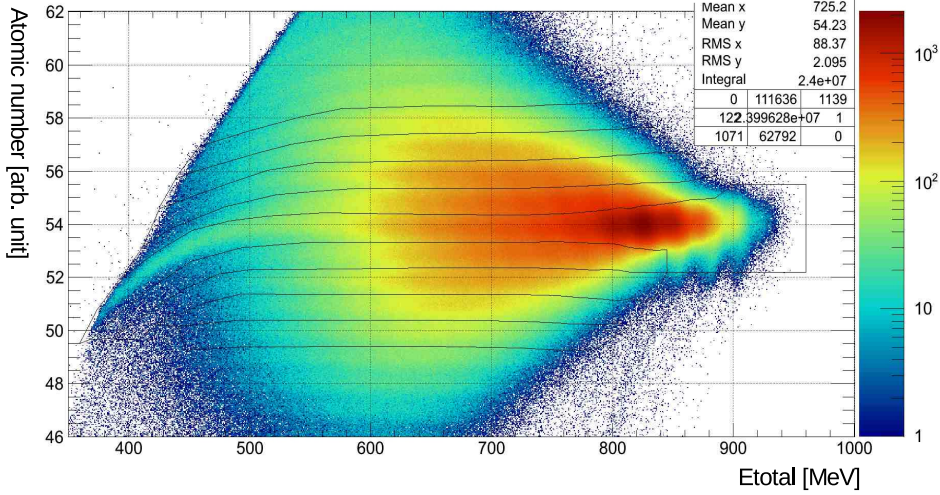


Figure 4.27 The correlation between atomic number and  $E$  with two dimensional cut based on the fitting result from energy sliced atomic number distribution.

trajectories were generated isotropically (i.e. uniform distribution of  $\cos\theta, \phi$ ), with uniform distribution of  $B\rho$ . (See figure 4.28) Since the track of projectile is fully determined by  $B\rho, \theta, \phi$  and fixed initial position at the target  $X_{target} = -2$  mm,  $Y_{target} = -2$  mm. (Named as X-2Y-2 optics for convenience) The total number of  $4.5 \times 10^8$  events was generated to reduce the statistical error. The trajectory of generated projectiles inside the spectrometer was determined by calculated database, which was explained at Section 3.3.3. The determination of whether the projectile trajectory was accepted in VAMOS or not, was decided first, by the physical size of the MWPPAC at focal plane(See figure 3.7). And second the position and gap between Si detector wall and missing Si detector channels(See figure 3.11). If the trajectory passes through active region of MWPPAC, and Si detectors, then it is regarded as accepted event. Then the detection efficiency was deduced by the ra-

#### 4.3. SPECTROMETER DETECTION EFFICIENCY

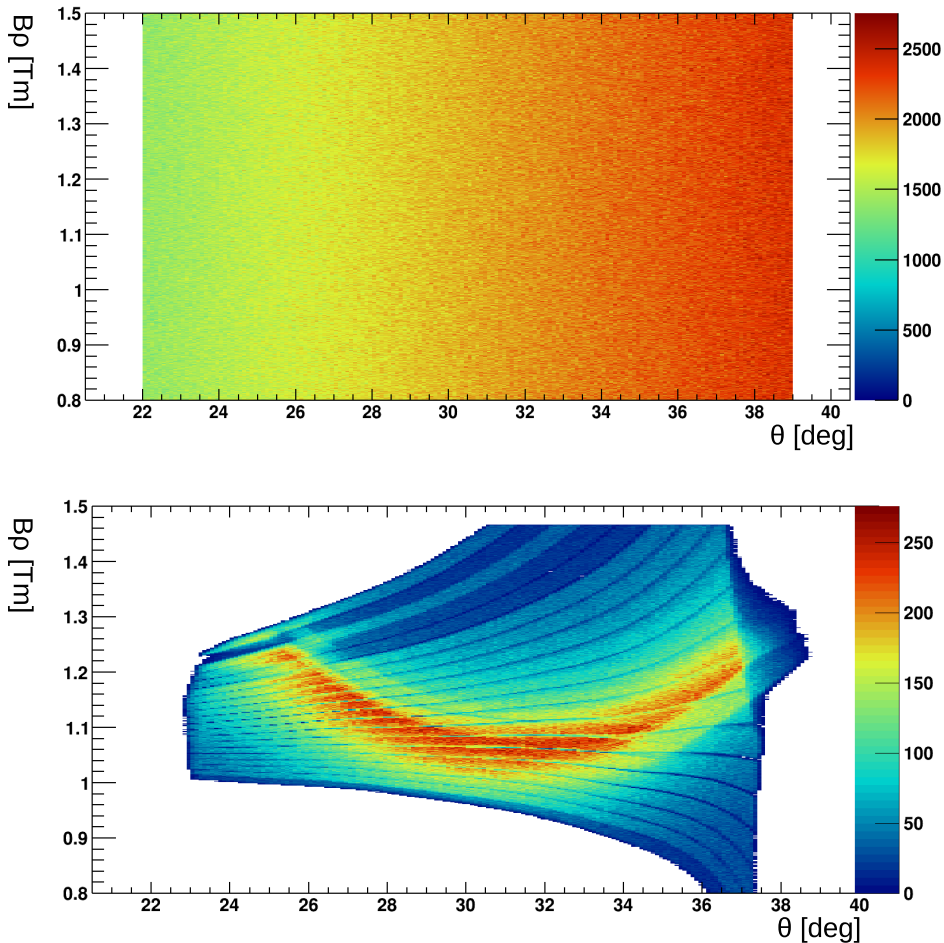


Figure 4.28 (top) The two dimensional histogram  $B\rho$  vs  $\theta$ (LAB frame) of generated events. Isotropic distribution of  $\theta$ , and uniform distribution of  $B\rho$  can be seen.  
 (bottom) The two dimensional histogram  $B\rho$  vs  $\theta$ (LAB frame) of accepted events of VAMOS. The shadows from supporting pole and missing Si detectors can be seen as curved bands.

### 4.3. SPECTROMETER DETECTION EFFICIENCY

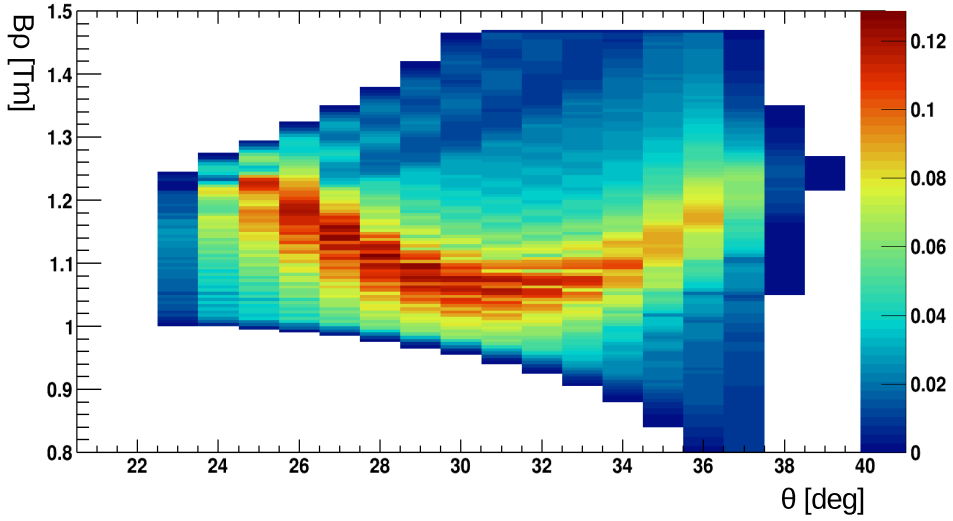


Figure 4.29 The two dimensional histogram of detection efficiency (  $B\rho$  vs  $\theta$ (LAB frame)) calculated by taking the ratio accepted events over generated events. The maximum acceptance shown as the curved band showed lowest  $B\rho$  near the  $30\sim 31^\circ$  at  $\sim 1.05$  T·m while angle at the side showed maximum acceptance at higher  $B\rho \sim 1.18$  T·m

tio between generated event and the number of accepted event. spectrometer. (See figure 4.28, 4.29) The curved gaps are due to gaps between different Si detectors and supporting pole in the MWPPAC at focal plane. And the wide band of small detection efficiency at the  $B\rho = 1.2 \sim 1.4$  T·m is due to the missing Si detector. The simulated result were used with 0.005 T·m and  $1^\circ$  bin size.

#### 4.3.2 Beam position uncertainty

During the beam time the beam spot at the target was unstable. Sometimes, beam position was so shifted it hit the target holder, causing large rate in gamma-ray

#### 4.3. SPECTROMETER DETECTION EFFICIENCY

array. (In such extreme case beam was stopped and readjusted.) The mean position of the beam spot was investigated after the beam time by inspecting the target. The burned mark showed the movement of the beam spot from the center of the target was at  $-2 \sim -3$  mm vertically and moved horizontal directions but staid mainly at the  $-2$  mm. Therefore the events are analyzed by database based on incident beam position different from true position by only few mm, the  $B\rho, \theta$ , will not be changed much.

But the small change in the incident position of the beam is essential to the  $\phi$  reconstruction. This is because the small position change in the beam position is not affect the deflection angle of dipoles. And the horizontal track inside the Dipole magnet (i.e.  $B\rho$ , and  $\theta$  reconstruction) will not be changed drastically. But the incident central position will affect the magnetic-field from the quadrupole experienced by projectile, thus affecting the  $\phi$  reconstruction.

This uncertainty in the acceptance can be confirmed from the simulation using ray-tracing code, similar to the simulation (see section 3.3.3) was carried out. The generated event at the target assuming incident target position ( $X = -2, Y = -2$  mm), incident position and angle at the focal plane was calculated using database created by Zugubi ray-tracing code. Then it was re-analyzed with database with different beam stop ( $X=0, Y=0$  mm) to calculate projectile condition at the target. (See figure 4.30)

The typical uncertainty (or disagreement) from the generated distribution was  $\Delta B\rho = 7.0 \times 10^{-3}$  Tm (FWHM),  $\Delta\theta = 0.27^\circ$  (FWHM) (1.5~1.8 times larger than right beam position reconstruction see Section 3.3.3). The only small disturbance in  $B\rho$  and  $\theta$  reconstruction from beam position means that the physical variables like

#### 4.3. SPECTROMETER DETECTION EFFICIENCY

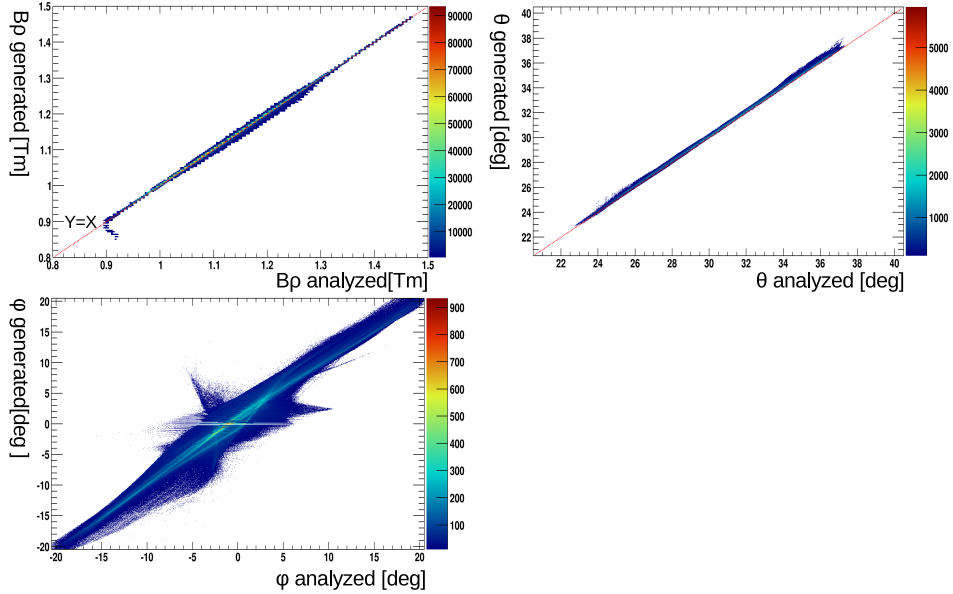


Figure 4.30 Correlation between generated event assuming beam position of  $X = -2$ ,  $Y = -2$  mm at the target and analyzed result assuming beam position  $X=0$ ,  $Y=0$  mm by simplified database(  $B\rho, \theta$  ) and fitting ( $\phi$ ). (top left) Correlation between generated  $B\rho$  and analyzed  $B\rho$  typical width was  $\Delta B\rho = 7.0 \times 10^{-3}$  Tm (FWHM).The red dashed line is  $Y=X$ . (top right) Correlation between generated  $\theta$  and analyzed  $\theta$  typical width was  $\Delta\theta=0.27^\circ$  (FWHM).(bottom left) Correlation between generated  $\phi_{generated}$  and analyzed  $\phi_{analyzed}$  typical width at the  $\phi_{generated} = 0^\circ$  was  $\Delta\phi_{analyzed} = 4.9^\circ$  (FWHM)

### 4.3. SPECTROMETER DETECTION EFFICIENCY

velocity, energy, Mass was not affected. This is proved by good resolution of Mass and charge states which are in good agreement from VAMOS++ spec. But the  $\phi$  shows uncertainty of typically  $\sim 5^\circ$  (FWHM) near  $\phi = 0$  which is  $\sim 14$  times larger than the right reconstruction. The factor 3 larger angular uncertainty in Doppler correction than the spec. value is another indication of this uncertainty. (See Section 4.1.4)

The evidence of distorted detection efficiency from beam position uncertainty could be observed by three independent observables. First angular distribution of elastic scattering after detection efficiency correction. (See figure 4.31) The angular dependence of elastic scattering of  $^{136}\text{Xe}$  at the forward angle should follow Rutherford cross section, where only the long ranged Coulomb interaction is affected. The angular dependence of elastic scattering accounting detection efficiency of spectrometer and missing event from acceptance limit and normalized Rutherford scattering was compared. (See figure 4.31) The experimental distribution shows steeper slope than the Rutherford. (The method used for selection of elastic scattering from  $^{136}\text{Xe}$  will be discussed in Section 5.1)

Second the angular dependence of charge state ratio for fixed velocity after efficiency correction. The charge state of same atomic number with same velocity should have same charge state distribution. [100] Thus the ratio between different charge state of fixed atomic number and velocity should be independent of angle. For certain isotope with fixed velocity the different charge states occupies different  $B\rho$  values. Thus the charge state distributions are very sensitive to the detection efficiency. This feature makes charge states the good indicator for the validity of detection efficiency. The typical case of  $^{136}\text{Xe}$  with  $\beta = 0.107 \sim 0.108$  and  $0.113 \sim$

#### 4.3. SPECTROMETER DETECTION EFFICIENCY

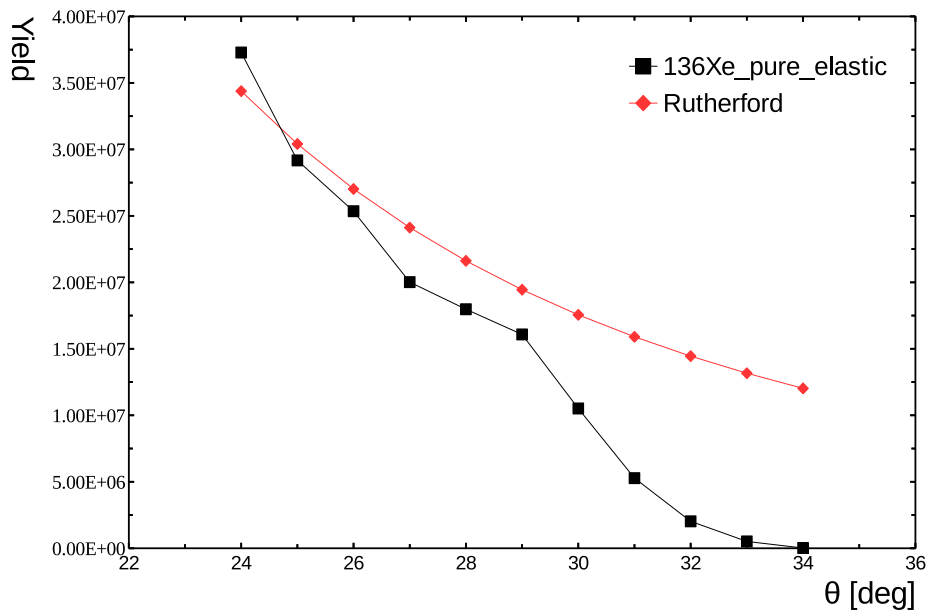


Figure 4.31 The angular distribution of elastic scattering compared with Rutherford angular distribution(scaled to experimental distribution in forward angle of  $24\sim26^\circ$ ).

### 4.3. SPECTROMETER DETECTION EFFICIENCY

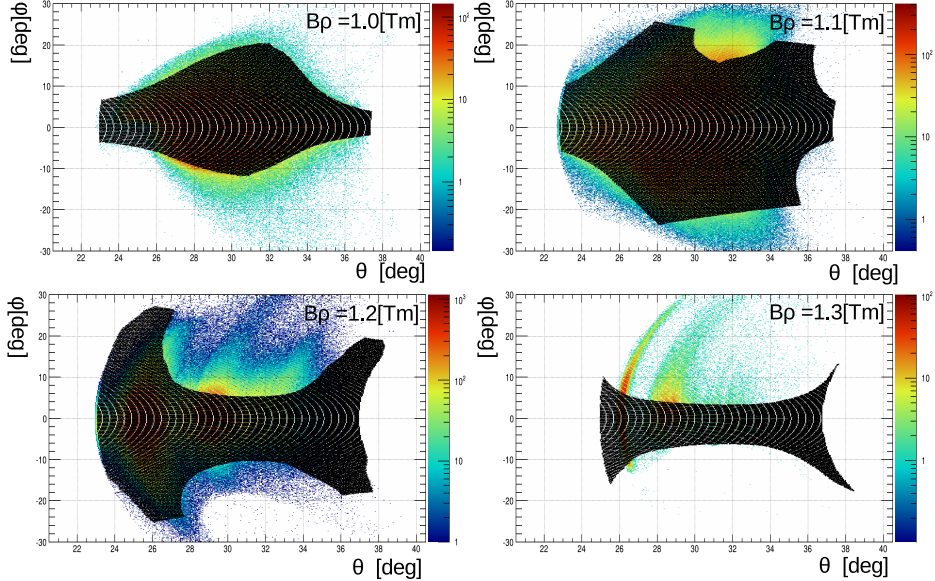


Figure 4.32 The two dimensional histogram of acceptance range ( $\theta$  vs  $\phi$ (LAB frame)) of different  $B\rho$  range.(top left)  $B\rho=0.95\sim 1.05$ , (top right)  $B\rho=1.05\sim 1.15$ , (bottom left)  $B\rho=1.15\sim 1.25$ , (bottom right)  $B\rho=1.25\sim 1.35$  T·m.

0.114, the ratio between different charge states in angle is shown in the left figures of 4.42 ,4.43. The seniority between different charge states change drastically for different angle, indicating large distortion in the acceptance correction.

Third the acceptance range in  $\theta$ , and  $\phi$  from the calculation are different from experimental value, especially at the  $B\rho$  larger than the reference value, which leads to uncertainty in acceptance correction. (See figure 4.32)

This distortion in the detection efficiency calculation can seriously distort the physical observables like cross section, angular dependence and result related to reaction mechanism. Thus correction for this acceptance was required to proceed for

### 4.3. SPECTROMETER DETECTION EFFICIENCY

further analysis.

#### 4.3.3 Detection efficiency correction using charge state

##### Correction method

The correction of detection efficiency of VAMOS was estimated by charge state distribution. The high sensitivity of the charge state ratio to the detection efficiency was used as a tool for deducing the detection efficiency. And (empirically deduced) theoretical charge state formula [103] was assumed.

The following assumption was used to deduce the acceptance correction. First, the charge state distribution follows the theoretical Gaussian distribution from [103] with the mean modified depending on Z by the experimental result within the theoretical uncertainty. (More detailed description of the modification of charge state mean are written in the section 4.3.3) Second, the detection efficiency calculated by simulation, assuming beam position at the target X = - 2, Y = - 2 mm (named X-2Y-2 efficiency afterwards) is true in at least near the acceptance maximum. (i.e. The velocity distribution with the events which have  $B\rho$  distribution maximum match with the maximum X-2Y-2 efficiency calculation. Then the corrected velocity distribution (Yield( $\beta, \theta$ )) using X-2Y-2 efficiency are assumed to be correct.)

The detection efficiency correction was preceded with the following method.

- (1) The isotopes with good statistics, and the maximum of  $B\rho$  distribution coincides with the maximum detection efficiency from simulation (X-2Y-2 efficiency) were selected. This condition for selecting isotope was set to make use of the second assumption for normalization of correction factor. In the practice  $^{134}\text{Xe}$ ,  $^{132}\text{Xe}$ ,  $^{132}\text{Cs}$  ( $Z=55$ ),  $^{134}\text{Cs}$ ,  $^{130}\text{I}$  ( $Z=53$ ),  $^{136}\text{Ba}$  ( $Z=56$ ),  $^{134}\text{Ba}$ ,  $^{130}\text{Te}$

### 4.3. SPECTROMETER DETECTION EFFICIENCY

(Z=52) were selected for the reference isotopes. Which were well accepted in VAMOS and have maximum count at the maximum detection efficiency (X-2Y-2) of VAMOS. These nuclides are mainly produced by reaction with small energy dissipation. Where the velocity distribution has well defined peak and angular peaked near grazing angle with small width (few degrees).

- (2) For selected isotope, with fixed  $\theta$  ( $\Delta\theta=1^\circ$ ) and velocity ( $\Delta\beta=0.001$ ), the  $B\rho$  distribution (bin size  $\Delta B\rho=0.01$  Tm corresponding to the bin size of  $\beta$ ) corresponds to seven major charge state (i.e. seven charge states with most statistics) were selected. (see top left figure 4.33)
- (3) The charge state near the maximum yield ( $Q_{MAX}\pm 2$ ), where the corresponding  $B\rho$  is near the maximum detection efficiency, was set as the reference point. (See top right figure 4.33)
- (4) The ratios between the each point and the theoretical calculation (normalized at the reference point) were calculated for each charge state. (See bottom right figure 4.33)
- (5) The ratio of charge states were converted in to the one bin at the  $B\rho$  distribution. (See (bottom left) Figure 4.33) and the reference point was set which is near the acceptance maximum of X-2Y-2.
- (6) Repeat (2)~(5) for different velocity with enough statistics to cover wide range of  $B\rho$  and deducing ratio multiple times for one bin in the  $B\rho$ . (See figure 4.34)
- (7) Each set of correction factors are normalized to match velocity distribution from X-2Y-2 velocity distribution. (See figure 4.35)

### 4.3. SPECTROMETER DETECTION EFFICIENCY

- (8) Take average of deduced correction factor for each bin of  $B\rho$ . (See figure 4.36) and take RMS(difference between average efficiency and individual points from different velocity) and statistical error as the error of the correction factor for each bin.
- (9) Repeat (2) ~ (8) for different angle with good statistics ( $24 \sim 34^\circ$ )
- (10) Repeat (2) ~ (9) for different isotopes. Take weighted average of deduced correction factor for different isotopes and error was summed from RMS (difference between average efficiency and individual points of different isotopes) and error (weighted) from different isotopes. (See figure 4.37)

The averaging process and error estimation over many isotopes can reduce the statistical error and cover large range of  $B\rho$ . The errors in the detection efficiency are presumed to be the effects from the internal uncertainty in the theoretical charge state estimation, and small mismatch between the bin size of  $B\rho$  and  $\beta$  cuts. (The internal uncertainty in the charge state distributions such as specific shell structures of different atoms[100], or the error from the theoretical charge state.)

The finally two dimensional histogram (  $B\rho$  vs  $\theta$ ) detection efficiency is shown in figure 4.38 The detection efficiency was similar from the X-2Y-2 at angle near  $30^\circ$  and the backward angle, which has clear maximum at the same position. On the other hand at the forward angles ( $24 \sim 26^\circ$ ), shows almost flat efficiency unlike X-2Y-2 which has clear maximum. The smaller range of acceptance using this empirical method is due to small statistics outside this region.

#### 4.3. SPECTROMETER DETECTION EFFICIENCY

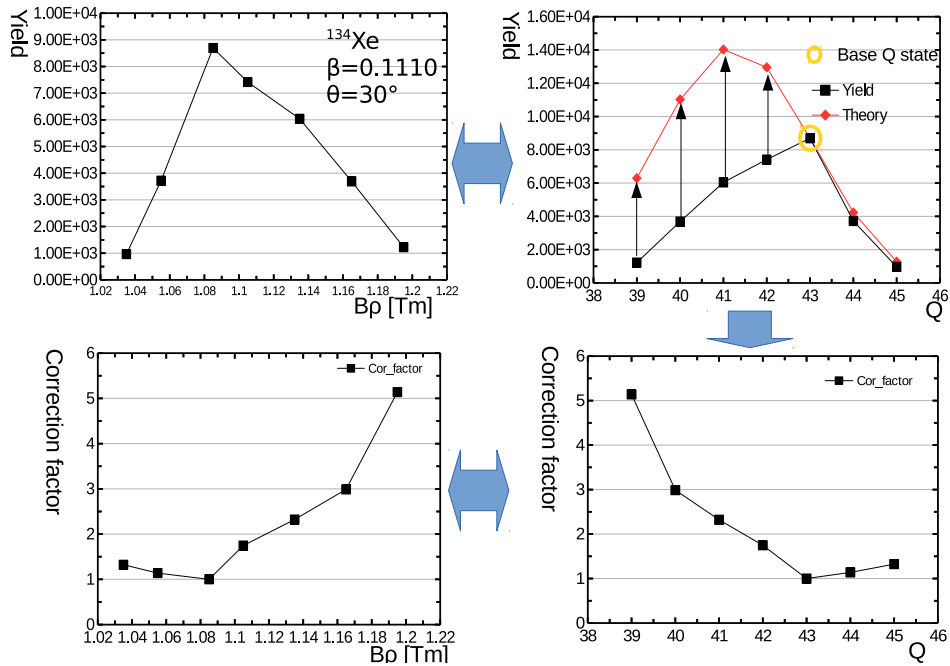


Figure 4.33 The method for detection efficiency using typical case of  $^{134}\text{Xe}$  with  $\beta=0.1110$  at  $30^\circ$ . (See the explanation in the text)

### 4.3. SPECTROMETER DETECTION EFFICIENCY

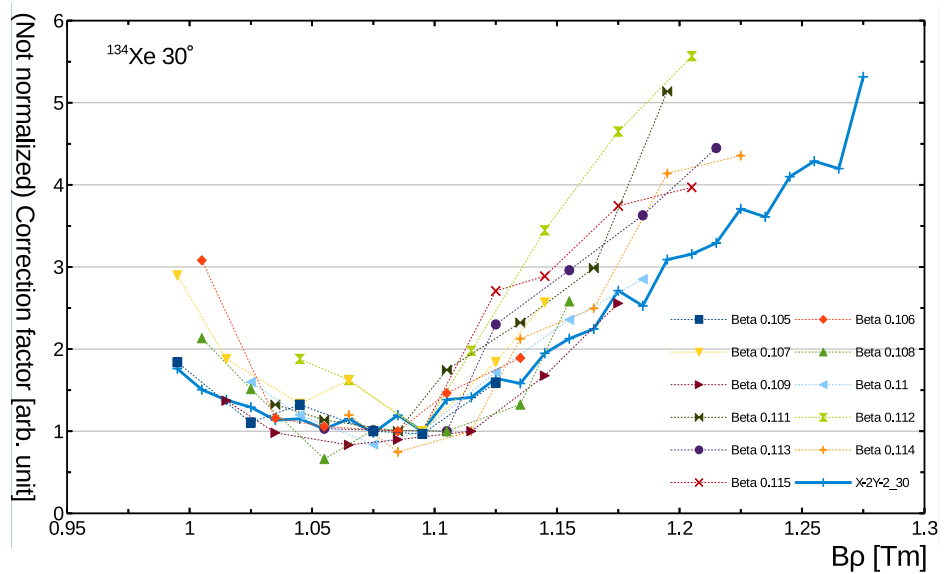


Figure 4.34 (Not normalized) Detection efficiency using  $^{134}\text{Xe}$  events with different velocity at  $30^\circ$  compared with scaled detection efficiency. (See the explanation in the text)

### 4.3. SPECTROMETER DETECTION EFFICIENCY

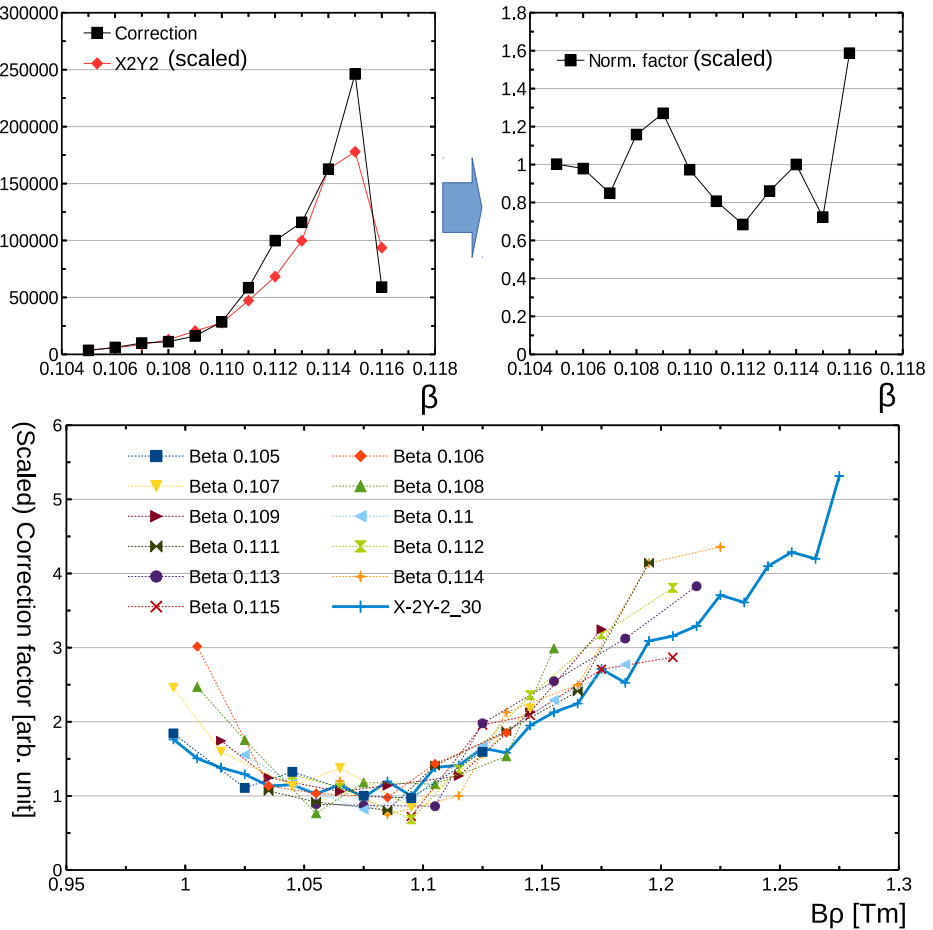


Figure 4.35 The normalization process of detection efficiency using typical case of  $^{132}\text{Xe}$  at  $30^\circ$ . (top left) the velocity distribution using simulated acceptance correction (red diamond) and empirically corrected velocity distribution (black square). (top right) The ratio between different corrections. (bottom) each correction factors from different velocities were normalized by ratio of velocity distribution. (see the explanation in the text)

#### 4.3. SPECTROMETER DETECTION EFFICIENCY

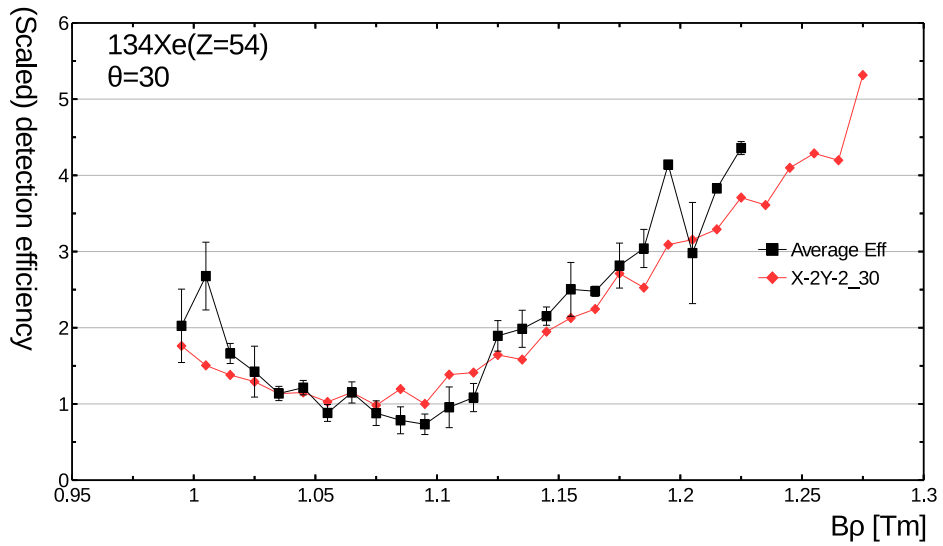


Figure 4.36 Averaged detection efficiency using  $^{134}\text{Xe}$  events with different velocity at  $30^\circ$  compared with (scaled) X-2Y-2 efficiency. (See the explanation in the text)

#### 4.3. SPECTROMETER DETECTION EFFICIENCY

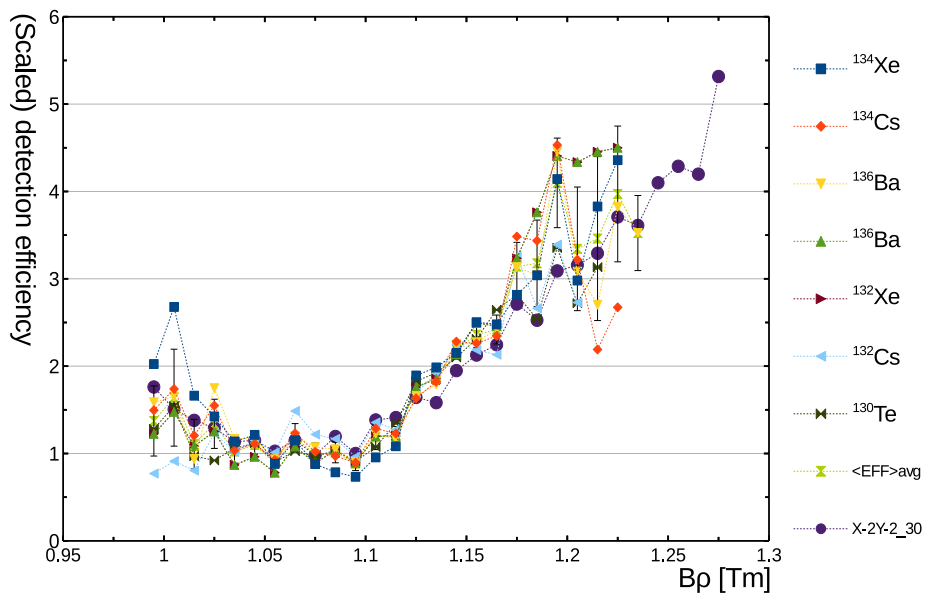


Figure 4.37 (scaled) Averaged detection efficiency of various isotopes ( $^{134}\text{Xe}$ ,  $^{132}\text{Xe}$ ,  $^{132}\text{Cs}$ ,  $^{134}\text{Cs}$ ,  $^{130}\text{I}$ ,  $^{136}\text{Ba}$ ,  $^{134}\text{Ba}$ ,  $^{130}\text{Te}$ ) compared with (scaled) X-2Y-2 efficiency

### 4.3. SPECTROMETER DETECTION EFFICIENCY

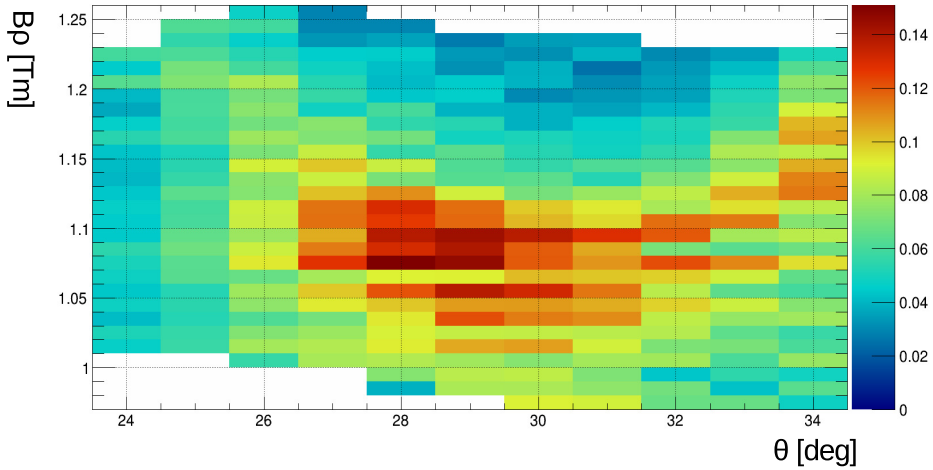


Figure 4.38 Two dimensional histogram of detection efficiency averaging over many isotopes.

#### Modification theoretical charge state mean

The theoretically determined charge states [103] are deduced empirically from comprehensively fitting the vast number of experimental results. This empirical methods has been used in many references.(e.g. [105, 101, 102, 104]) The large error exist in these theories, since the actual charge states depends on specific atomic shell structure and so on. [100] Thus mean value of the specific charge states in this experimental regions the correction is needed.

The mean value of the charge states were corrected in order to create consistent correction of detection efficiency and also coincide with the X-2Y-2 efficiency. The charge state shift was determined with following method.

- (1) The shift of the charge state was determined by calculating efficiency of single isotope at fixed velocity  $\beta, \theta$  using the method (2)~(5) in 4.3.3 with the original

### 4.3. SPECTROMETER DETECTION EFFICIENCY

formula of [103]. (see top figure 4.39)

- (2) Calculate the theoretical charge state shift, which minimize the chi-square between the X-2Y-2 efficiency. (See bottom figure 4.39)
- (3) Repeat (1)~(2) to different velocity  $\beta, \theta$  (See figure 4.40).
- (3) Calculate mean of the charge state shift distribution. (see right most bottom figure 4.40)
- (4) Repeat (1)~(3) to different isotopes with good statistics and condition satisfying second assumption described in section 4.3.3. (15 nuclides of  $^{126,124}\text{Sb}$ ,  $^{130,128}\text{Te}$ ,  $^{130}\text{I}$ ,  $^{134,132}\text{Xe}$ ,  $^{134,132}\text{Cs}$ ,  $^{136,134}\text{Ba}$ ,  $^{138,136}\text{La}$ ,  $^{140,139}\text{Ce}$  were used)  
(See figure 4.41)
- (5) Estimate the charge state shift over all distribution based on fitting.

The mass dependence shown in the figure 4.41 is due to the mismatch at the low velocity. This regions the mean position of  $B\rho$  distribution deviates from the maximum of the detection efficiency. Thus the distribution could be distorted by the X-2Y-2 efficiency in low  $B\rho$  (i.e. lower than the efficiency maximum) regions.

The calculated charge state shift showed angular dependence and the calculated minimum chi-square was very large at the angle far from the center( $\sim 30^\circ$ ). The charge state shift showed dependence of the atomic number, the linear fitting was made as the first order approximation. (See figure 4.41) The final result of the charge state correction was

$$Q_{corrected} = Q_{theory} + (-0.08884 * Z + 5.239) \quad (4.19)$$

### **4.3. SPECTROMETER DETECTION EFFICIENCY**

$Q_{theory}$ : calculated charge state of the formula from [103]

Z: atomic number of the PLF.

The width of the charge state distribution was also compared with the theory [103]. The efficiency correction of different isotopes showed good agreement with each other over all regions therefore correction was not applied. (See figure 4.38)

#### **Results of the detection efficiency**

The charge state ratio of typical distribution is shown in figure 4.42 4.43. The ratio from the X-2Y-2 detection efficiency shows clear change in the seniority respect to the angle. On the other hand the charge state ratio is still very unstable but the overall seniority of the charge state was kept the same within the error bars. The angular distribution of the elastic scattering was deduced and compared with Rutherford scattering distribution. (See figure 5.3) Good agreement can be seen at the forward angle. The confirmation was also carried out by optical potential fitting and the comparison with the tandem experiment (see section 5.1.3, and 5.1.4) These two evidences indicate the goodness of correction using charge state.

#### **4.3.4 Restoration of events out side of the acceptance**

The detection efficiency using charge state used isotopes with  $B\rho$  maximum coincide with the detection efficiency from simulation. Thus the region far from the  $B\rho$  maximum, statistics are low for selected isotopes. The smaller range of acceptance in the  $B\rho$  affected the total cross section. The heavily damped reaction part are affected most where distribution is concentrated at low  $B\rho$  ( $< 1.0 \text{ T}\cdot\text{m}$ ). Also

#### 4.3. SPECTROMETER DETECTION EFFICIENCY

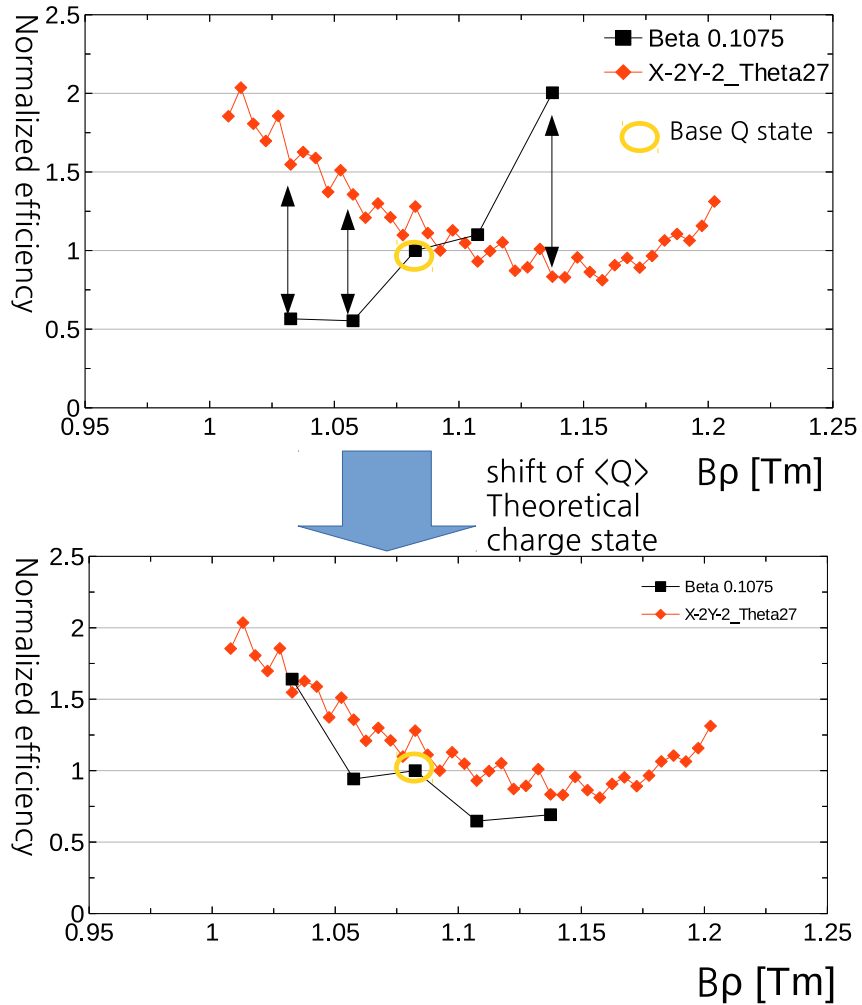


Figure 4.39 (top) (black square) calculated efficiency of  $^{134}\text{Xe}$  at  $\beta = 0.1075$ ,  $\theta = 27^\circ$  using the original formula from [103] and (red diamond) X-2Y-2 efficiency. (bottom) calculated efficiency by shifting which minimize the chi-square between X-2Y-2 efficiency and calculated efficiency.

### 4.3. SPECTROMETER DETECTION EFFICIENCY

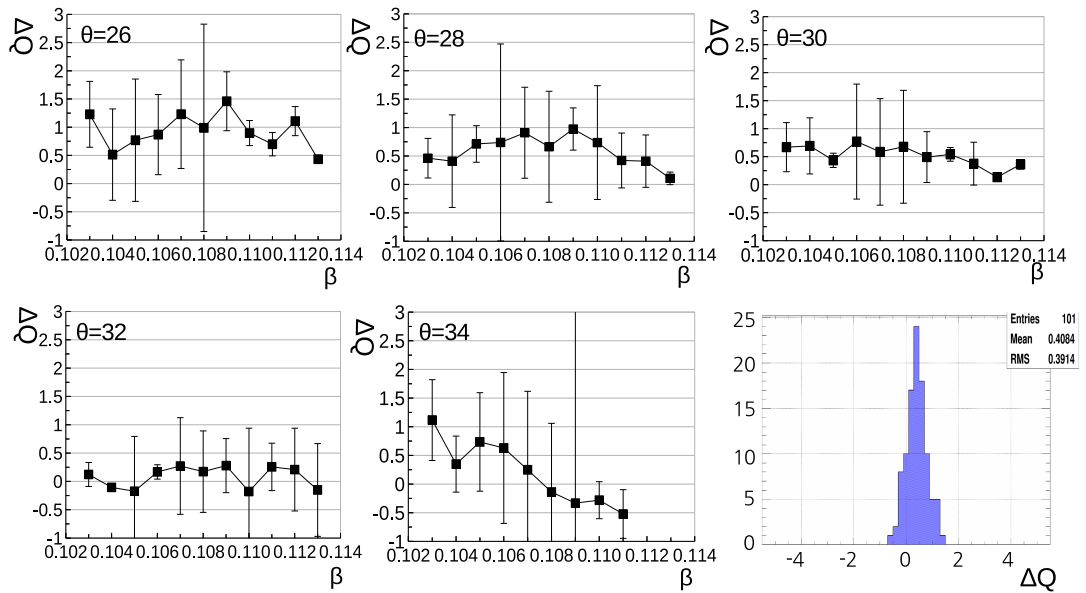


Figure 4.40 The calculated charge state shift of  $^{134}\text{Xe}$  of different velocity and (even number) angles of 26~34 (shown in order from top left to bottom right) the error bars indicate the calculated chi-squares after minimization with the X-2Y-2 efficiency described in the text. The bottom left figure is the distribution of the charge state shift.

#### 4.3. SPECTROMETER DETECTION EFFICIENCY

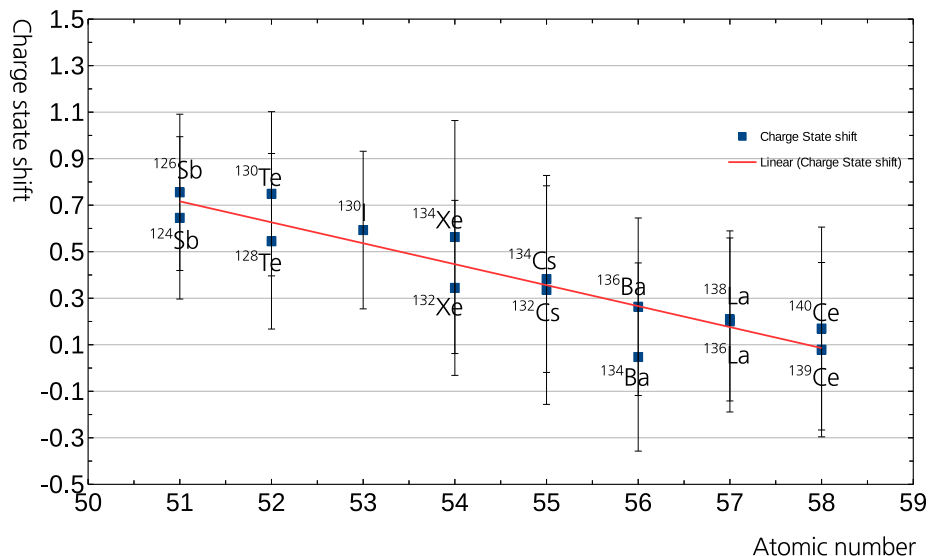


Figure 4.41 The averaged charge state shift of different isotopes indicated as the blue square ( $^{126,124}\text{Sb}$ ,  $^{130,128}\text{Te}$ ,  $^{130}\text{I}$ ,  $^{134,132}\text{Xe}$ ,  $^{134,132}\text{Cs}$ ,  $^{136,134}\text{Ba}$ ,  $^{138,136}\text{La}$ ,  $^{140,139}\text{Ce}$ ) with the linear fitting (red solid line). The error bars indicate the FWHM of the charge state shift distribution shown in the figure 4.40.

### 4.3. SPECTROMETER DETECTION EFFICIENCY

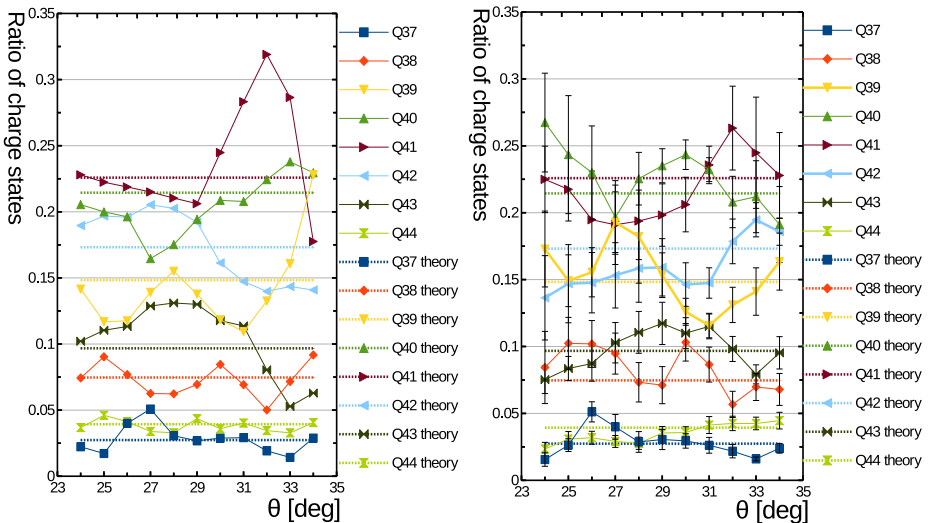


Figure 4.42 The ratio between charge state of  $^{136}\text{Xe}$  with  $\beta=0.107\sim0.108$  at different angle (left)using X-2Y-2 detection efficiency,(right)using averaged detection efficiency by charge states. The error bars include the statistical errors and the error from detection efficiency

### 4.3. SPECTROMETER DETECTION EFFICIENCY

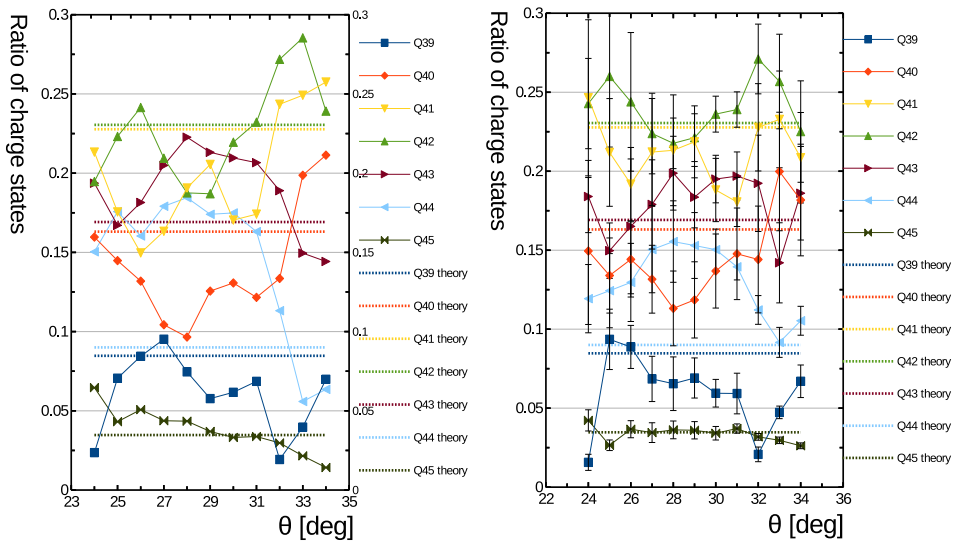


Figure 4.43 The ratio between charge state of  $^{136}\text{Xe}$  with  $\beta=0.113\sim0.114$  at different angle (left)using X-2Y-2 detection efficiency,(right)using averaged detection efficiency by charge states.

### 4.3. SPECTROMETER DETECTION EFFICIENCY

elastic scattering, which have fast velocity at the forward angle causing almost half of event outside of the acceptance limit ( $B\rho > 1.3$  Tm at  $24^\circ$ ). The restoration of event out of acceptance is needed in order to investigate the full range of reaction mechanism.

The charge state distribution was used to determine unaccepted events , similar to the detection efficiency determination. For each velocity cut( $\Delta\beta=0.001$ ) the charge state distribution was fitted with Gaussian distribution. (See figure 4.44) The charge state out side of the acceptance was restored based on the fitting result. In case of the charge state with maximum yield ( $Q_{MAX}$ ) is missing  $Q_{accepted} < Q_{MAX} + 1$ . Then the width was fixed with theoretical value [103] to avoid the wrong extrapolation. The restoration was carried out until the data point of detected charge state is less than 4 for avoid unreliable extrapolation. The restoration result from velocity distribution shows significant change in the distribution especially isotopes mainly produced from large damping. (See figure 4.46, 4.46) The restored angular distribution showed centroid similar to the accepted events with wider distribution, due to the restored events are mainly from reaction from heavily damped part. (See figure 4.46) Total restored event can be presented with two dimensional  $B\rho$  vs  $\theta$  distribution. (See figure 4.47) The isotopes with total number of restored events less than 30% was selected for this treatment to assure the reliability of the extrapolation.

### 4.3. SPECTROMETER DETECTION EFFICIENCY

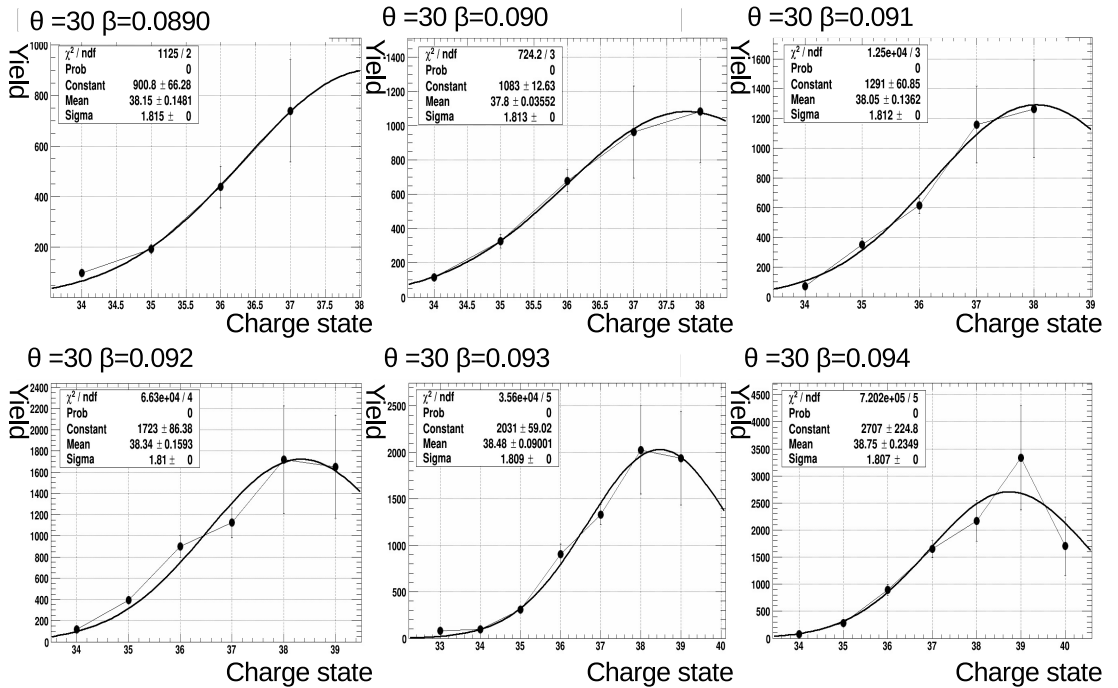


Figure 4.44 The charge state of  $^{133}\text{Ba}$  from  $\beta=0.089$ (top left) to  $\beta=0.094$ (bottom right).

The width was fixed using theoretical value[103].The experimental value and Gaussian function showed good agreement within error bar.

#### 4.3. SPECTROMETER DETECTION EFFICIENCY

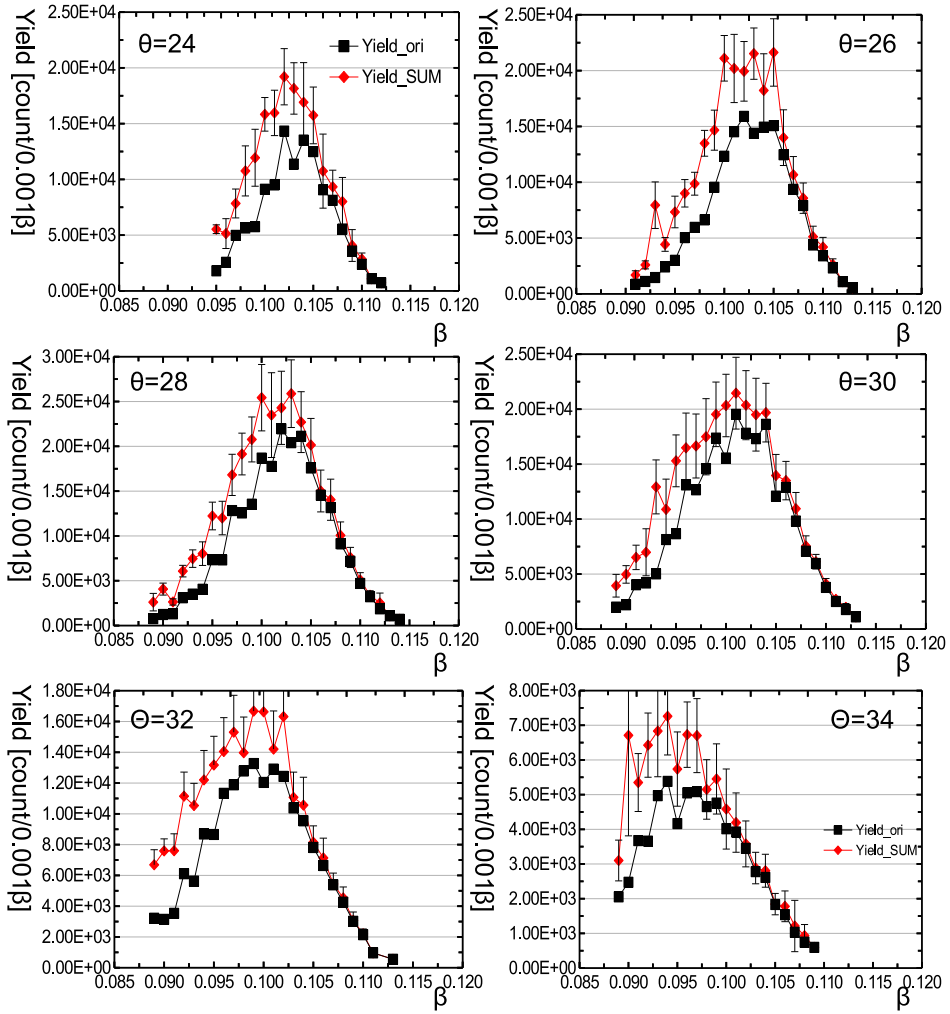


Figure 4.45 The velocity distribution of  $^{131}\text{Ba}$  from  $\theta=24$  (top left) to  $\theta=34$  (bottom right). The accepted yield are indicated as black square and yield including restored events are indicated as red diamond. The peak position and the yield of velocity changes, especially at the angle far from grazing angle.

#### 4.3. SPECTROMETER DETECTION EFFICIENCY

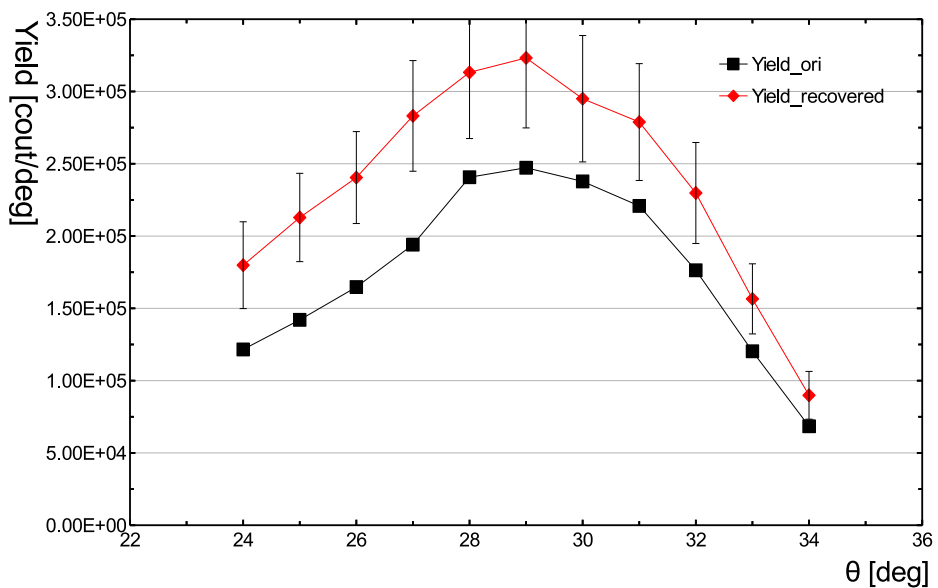


Figure 4.46 The angular distribution of  $^{131}\text{Ba}$ . The accepted yield are indicated as black square and yield including restored events are indicated as red diamond.

### 4.3. SPECTROMETER DETECTION EFFICIENCY

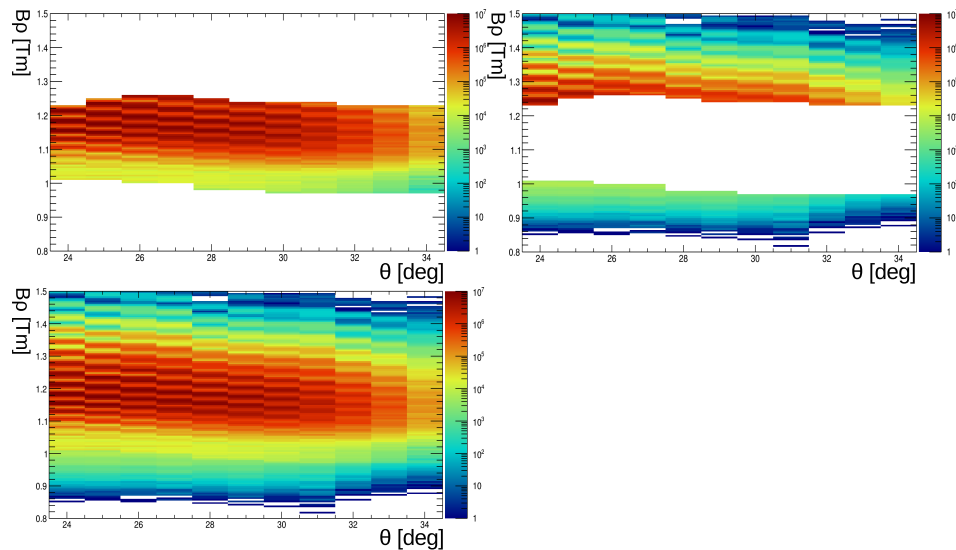


Figure 4.47 The two dimensional  $B\rho$  vs  $\theta$  distribution of  $^{136}Xe$ . (top left) Accepted events inside detection efficiency using charge states.(top right) Restored events outside the acceptance.(bottom left)Combined distribution of accepted distribution and restored distribution.

# **Chapter 5**

## **Analyzed Results and Discussion**

The result from the analysis and discussion of the experiment is presented. Since the scope of this study has many subjects, separating result and discussion would be confusing and inconvenient. Thus results and discussions are written under each subject.

### **5.1 Elastic Scattering**

The measurement of the elastic scattering distribution was used first, in order to determine the conversion factor from yield to cross section. Second, elastic scattering was used to check the consistency (or validity) of this experimental result (PID, spectrometer detection efficiency) by optical potential fitting and comparison with the other experimental data with similar system. The elastic scattering was the major component of the system accepted in the spectrometer which determined the beam current.

## 5.1. ELASTIC SCATTERING

### 5.1.1 Selection of elastic scattering channel from $^{136}\text{Xe}$

The elastic scattering was separated from other reaction channels in  $^{136}\text{Xe}$  by energy distribution corrected by the detection efficiency including out-of-acceptance events (See section 4.3.4). The three Gaussian fitting was used to the energy distribution for each angle to separate the elastic scattering from the D.I.C. and Q.E. (See figure 5.1).

This method serves as a kind of standard method for distinguishing elastic scattering from other reactions. And it was used in many previous experiments for distinguishing different reaction mechanisms (e.g. [56, 57, 51]). The elastic scattering yield was set as the integrated area of the fitted Gaussian corresponding to the elastic scattering.

The error was estimated by four systematic components.

- (1) The error from selecting elastic scattering. The width of the Gaussian representing elastic scattering was set to free parameter (see figure 5.1). And fixed width with the value from fitting result from 24 degree (see figure 5.2). The difference between them was set as and error.
- (2) The Yield difference from error of fitting parameter.
- (3) The error from out-of-acceptance event restoration using charge state (see section 4.3.4). The difference of elastic yield from which velocity the charge state distribution was fitted with fixed width using theoretical model.
- (4) The error of target thickness of 10%. The thickness of the target restrains the effective number of cross section to two digits.

## 5.1. ELASTIC SCATTERING

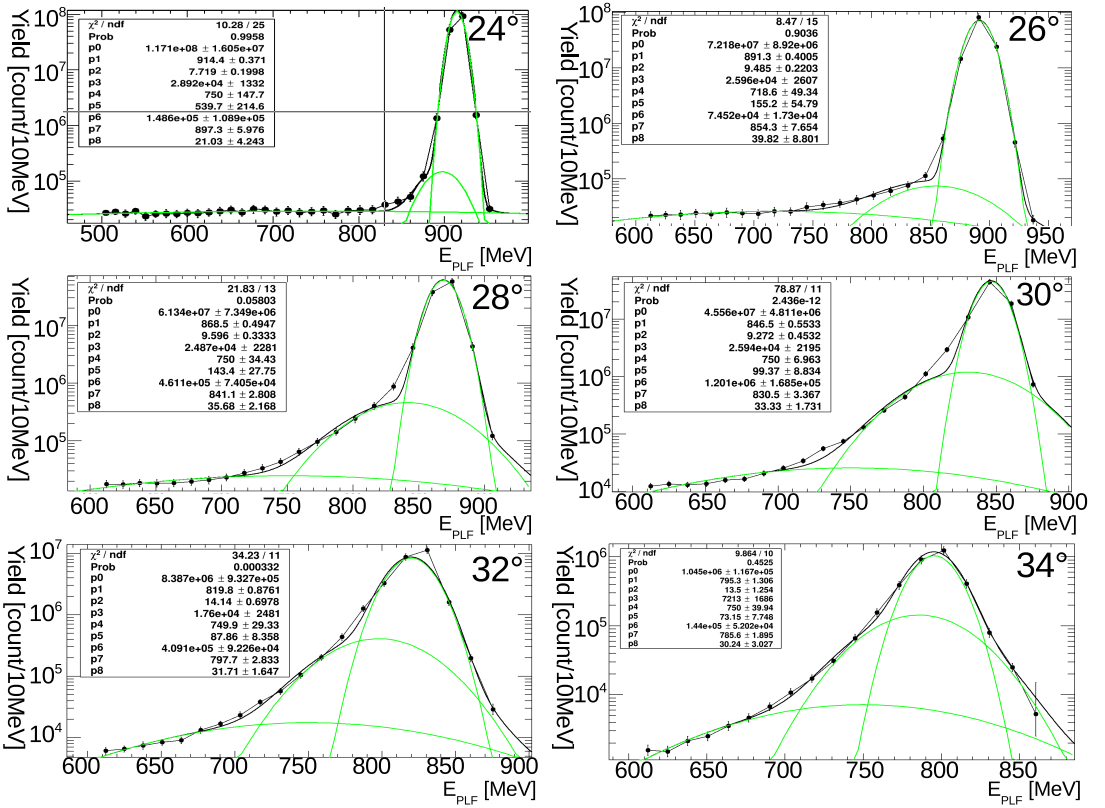


Figure 5.1 The energy distribution of  $^{136}\text{Xe}$  (from top left to bottom right) at even number angles  $\theta_{\text{LAB}} = 24, 26, 28, 30, 32$ , and  $34$  deg, fitted with three Gaussian distributions representing elastic, quasi-elastic, and deep inelastic collision.

### 5.1. ELASTIC SCATTERING

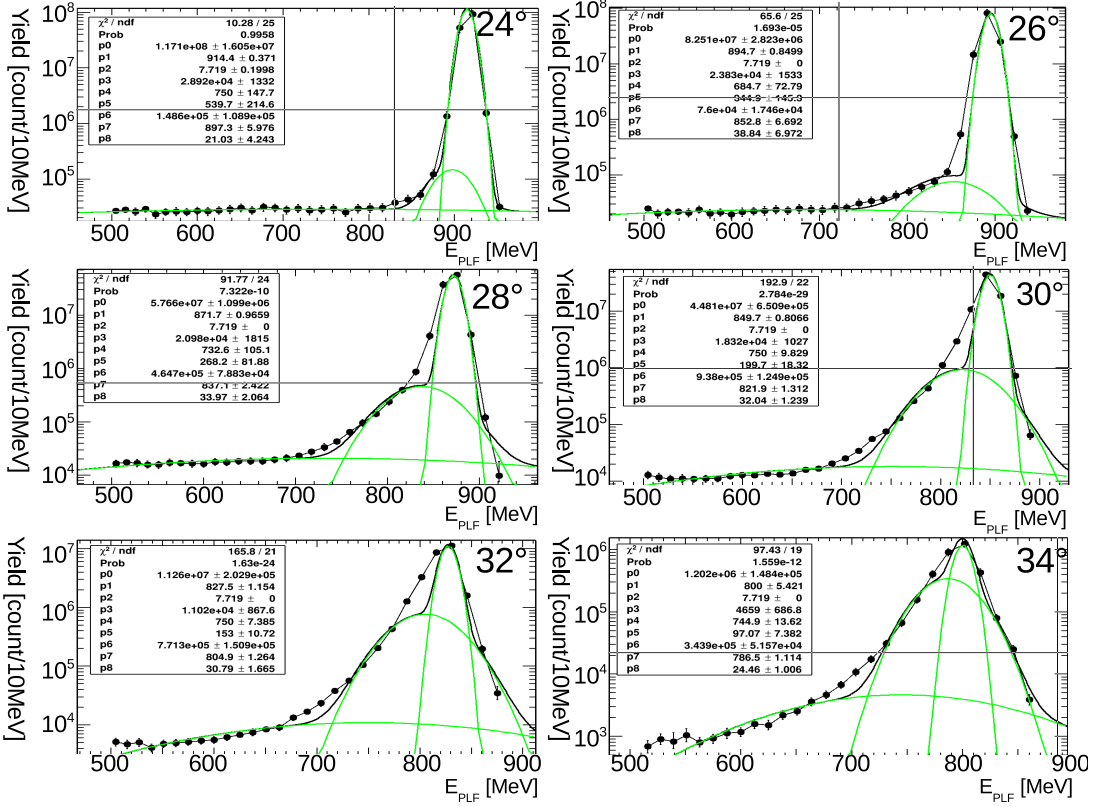


Figure 5.2 The energy distribution of  $^{136}\text{Xe}$  (from top left to bottom right) even number angles of  $\theta_{\text{LAB}} = 24, 26, 28, 30, 32$ , and  $34$  deg, fitted with three Gaussian distribution representing elastic, quasi-elastic, deep inelastic collision. The width of the Gaussian function which represents elastic scattering, was fixed to the value from angle 24.

## 5.1. ELASTIC SCATTERING

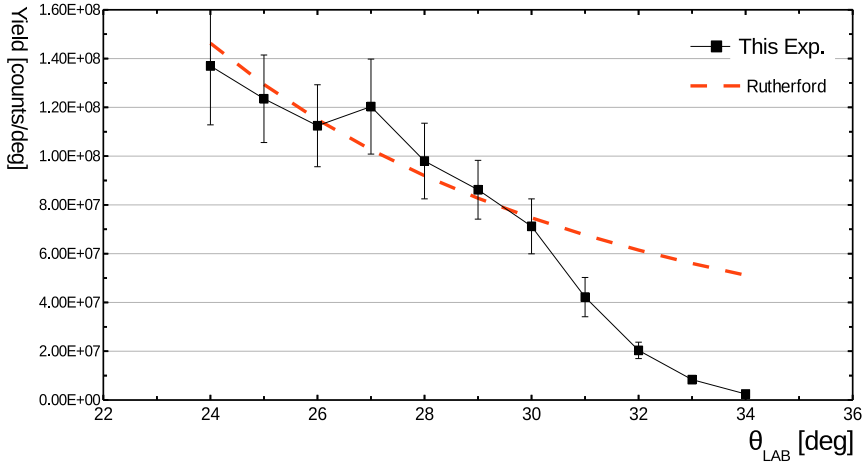


Figure 5.3 (black square) The angular distribution of elastic scattering component of  $^{136}\text{Xe}$  and (red dashed line) Rutherford scattering angular distribution normalized to  $\theta_{\text{LAB}}=24 \sim 27$  deg.

### 5.1.2 Conversion factor calculation

The angular distribution was deduced concerning fitting result of elastic scattering. The angular distribution of elastic scattering was normalized to the Rutherford scattering cross section at the forward angle  $24^\circ \sim 27^\circ$  (See figure 5.3). The measured elastic scattering at the forward angle showed good agreement with the Rutherford scattering. The angles near and backward to the grazing angle, the cross section decrease exponentially with respect to the Rutherford scattering. This decrease was due to the events escaped from the elastic scattering by the MNT reactions.

The error bar consists of uncertainty of yield concerning selecting elastic scattering by fitting(fitting parameter error difference from the fitting with fixed width), out-of-acceptance correction, and thickness of the target (10%) (other errors was not

## 5.1. ELASTIC SCATTERING

included to avoid the double counting the error). The estimated conversion factor was  $3.4_{-0.79}^{0.67} \times 10^{-6}$  showing  $20 \sim 23\%$  error.

### 5.1.3 Optical potential fitting

The confirmation of the elastic scattering and the conversion factor result was carried out by two independent methods.

- (1) The optical potential fitting of the angular distribution of the elastic scattering.
- (2) Comparison with the tandem experimental result (See section) with the same beam energy.
- (3) Comparison with fitting result (total reaction cross section and optical potential parameters), from this experimental result and also the references with the similar beam target combination.

The detail of the optical potential model can be found in the many textbooks (such as [5]). The program PTOLEMY [106] which is widely used for optical potential fitting and DWBA calculation were used for fitting. The PTOLEMY uses Woods-Saxon potential in both real and imaginary part of the nuclear potential. The depth, and width of the real and imaginary potential were fixed using theoretically predicted values [107] and only radii of potential were free parameters. (Since the fitting data contains only 11 points and total numbers of fitting parameters were 6. Thus it would be not reliable to set all parameters free.) The fitting result (potential energy parameter and the total cross section) is shown in figure 5.4 and summarized in the table 5.1.

### 5.1. ELASTIC SCATTERING

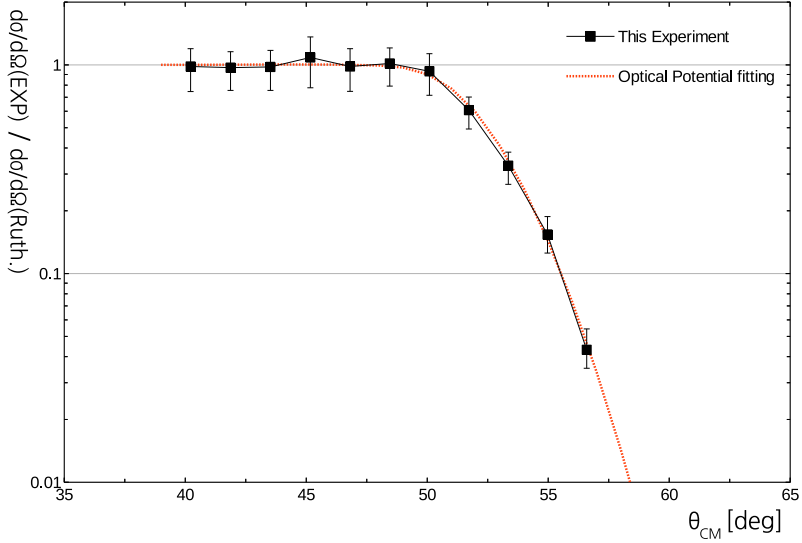


Figure 5.4 (black square) The angular distribution of elastic scattering component of  $^{136}\text{Xe}$  normalized by Rutherford scattering and (red dashed line) optical potential fitting result by program PTOLEMY.

$V_{Real}$ [MeV]	$R_{Real}^*$ [fm]	$A_{Real}$ [fm]	$\sigma_{Total}$ [mb]
30	1.21	0.6	2899.1
$V_{Imaginary}$ [MeV]	$R_{Imaginary}^*$ [fm]	$A_{Imaginary}$ [fm]	
20	1.30	0.4	

Table 5.1 The optical potential fitting result of elastic scattering angular distribution. The Real/Imaginary potential parameters are indicated with label. The V indicates the depth of potential, R indicates the radius parameter (Radius of nuclei =  $R^* A^{1/3}$ ), A is the diffusion parameter of Woods-Saxon potential ( $V(R) = \frac{V_0}{1 - \exp(-\frac{r-R}{A})}$ ). The depth and the diffusion constant of the both real and imaginary potential were fixed and only the radii of the potential were set as the free parameter.

## 5.2. CROSS SECTION OF PROJECTILE-LIKE FRAGMENTS

The total reaction cross section determines the events escaped from the elastic scattering, and it was compared to check the validity (or at least the inner consistency). The total reaction cross section of measured value from this experiment was  $2700 \pm 1000$  mb agreed with the optical potential fitting result of 2899.1 mb within the error bars. For example  $^{136}\text{Xe} + ^{208}\text{Pb}$  with  $^{136}\text{Xe}$  beam of 1120 MeV [61] case shows total reaction cross section of  $2520 \pm 200$  mb. And the  $^{136}\text{Xe} + ^{209}\text{Bi}$  with  $^{136}\text{Xe}$  beam of 1130 MeV [56] have total reaction cross section of  $2840 \pm 150$  mb. This confirms our procedure of the cross section determination (detection efficiency, conversion factors).

### 5.1.4 Comparison with tandem experiment

The tandem accelerator experiment (See section 3.5) was used to compare the angular distribution of elastic scattering. The tandem experiment cannot separate the mass due to the experimental setup. Thus the angular distribution of all Xe isotopes was used instead of  $^{136}\text{Xe}$  for comparison. Also the result from tandem experiment includes the Q.E. components. Thus the comparison of the angular distribution was made with components both elastic and elastic including Q.E. reactions. The angular distribution (See figure 5.5) showed good agreement within the error bars, between different experiments with same beam target combination. This result confirms the angular distribution and yield to cross section conversion factor calculation of this experiment.

## 5.2 Cross section of projectile-like fragments

## 5.2. CROSS SECTION OF PROJECTILE-LIKE FRAGMENTS

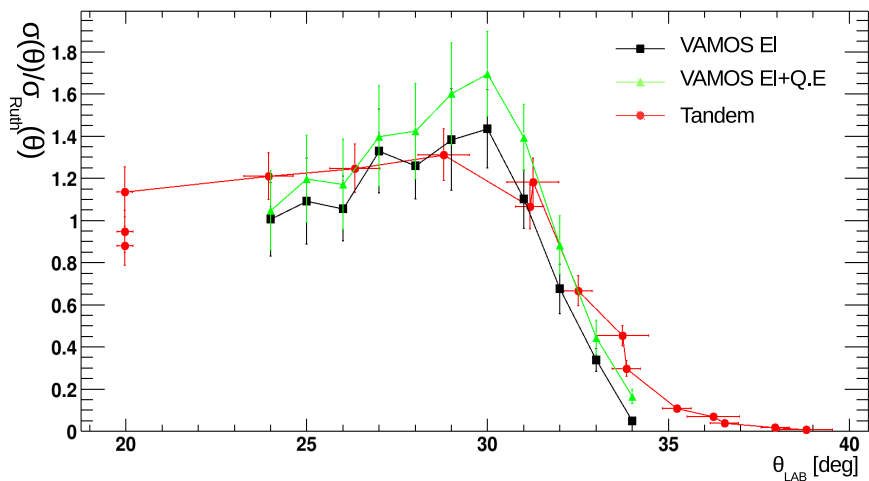


Figure 5.5 The angular distribution of elastic scattering (black square) and elastic and quasi elastic component (green square) of Xe normalized by Rutherford scattering and tandem experimental result (red circle).

## 5.2. CROSS SECTION OF PROJECTILE-LIKE FRAGMENTS

The production cross sections of the projectile-like fragments were calculated in different isotopes of Z=50 ~ 58 (See figure 5.6 and 5.7). The cross sections include the out-of-acceptance events using method mentioned in the chapter 4. The limit of the mass was set from the limit of out-of-acceptance events restored to be smaller than 30% of the total cross section. In case of the Xe isotopes the mass larger than  $^{138}\text{Xe}$  couldn't be deduced due to the blob events (See section 4.2.1).

The error estimations included statistical errors (0.73%), error from out-of-acceptance correction ( $-2.6 \sim +15\%$ ), PID cut error from atomic number Z and mass cut (0.047%), detection efficiency error (15%), and conversion factor error ( $-23 \sim +19\%$ ). Total (square root summed) error was on the average  $-27 \sim +28\%$ .

The proton pickup channels showed larger (factor 1.5 for two proton transfer channels) cross sections than the proton stripping channels. This enhancement in the proton pickup was also observed in the  $^{136}\text{Xe} + ^{209}\text{Bi}$  [56, 57, 58] case irrespective to the system energy. This result doesn't match with the theoretical estimation from GRAZING calculation. The more comprehensive discussion related to this will be presented in later sections 5.5.4.

The peak position and the width of the distribution showed quite different behavior in proton stripping channels and the proton pickup channels. For example the two-proton stripping channels (isotopes of Te) showed maximum cross section at the seven-neutron stripping channel ( $^{127}\text{Te}$ ). The distance of maximum cross section position from the pure proton transfer channel (channel without neutron transfer) increased as the number of transferred protons increase. On the other hand the two proton pickup channels (isotopes of Ba) showed peak cross section at the one-neutron stripping channel ( $^{137}\text{Ba}$ ). And the isotopic distributions of the proton pickup chan-

## 5.2. CROSS SECTION OF PROJECTILE-LIKE FRAGMENTS

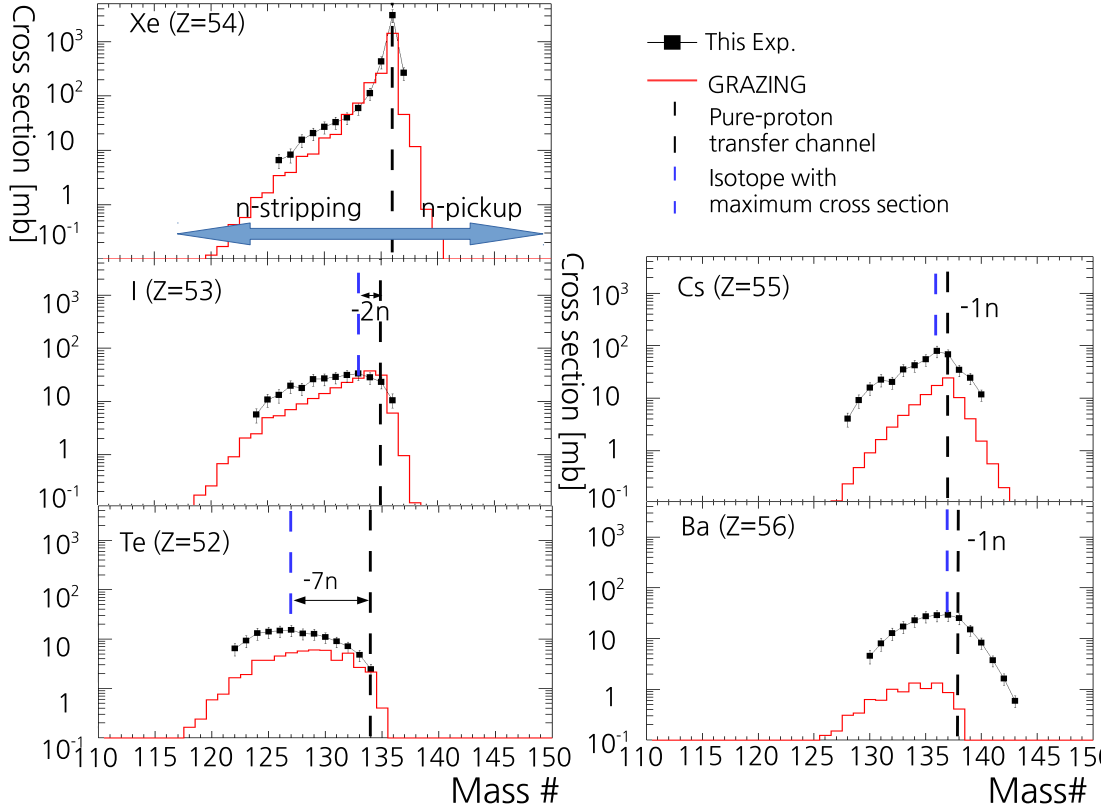


Figure 5.6 The production cross section of projectile-like fragment from 0p to 2p transfer channels indicated as black square with GRAZING code calculation [20] indicated as red solid line. The Xe (top left), I (middle left), Cs (middle right), Te (bottom left), Ba (bottom right) isotopes are presented. The black dashed line indicates pure proton transfer channel (channel without neutron transfer) and blue dashed line indicates isotope with maximum cross section.

## 5.2. CROSS SECTION OF PROJECTILE-LIKE FRAGMENTS

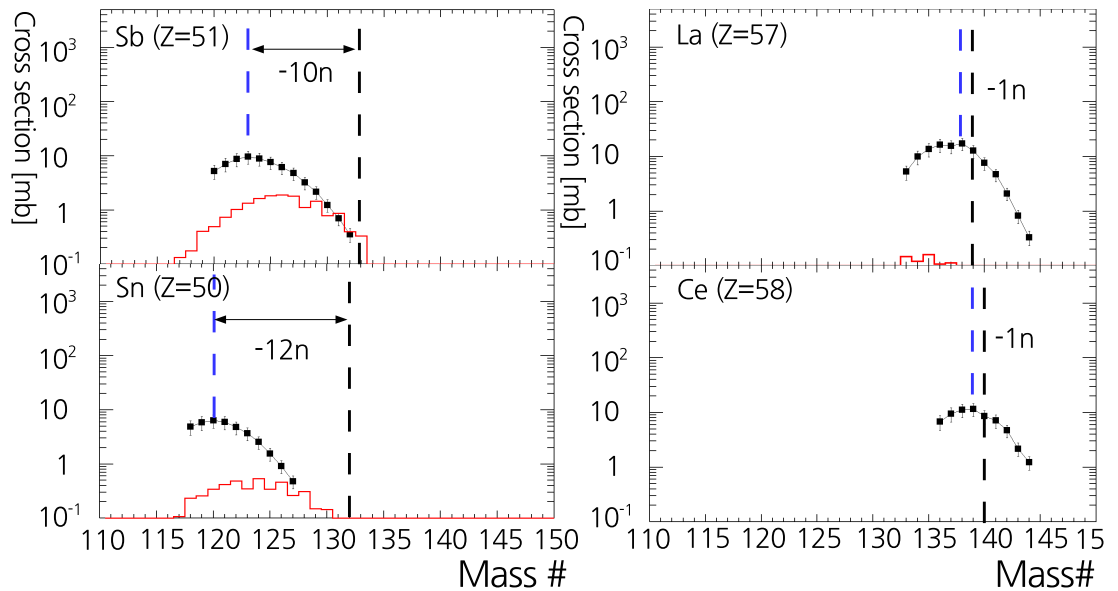


Figure 5.7 The production cross section of projectile-like fragment from  $3p$  to  $4p$  transfer channels. The Sb (top left), La (top right), Sn (bottom left), Ce (bottom right) isotopes are presented. The figures use same indication as the figure 5.6

### *5.3. DECOMPOSITION OF Q.E. AND D.I.C.*

nels present smaller width as compared with proton stripping channels. And the width of the distribution the proton pickup presented smaller than the two proton stripping channel. These differences are owing to the N/Z equilibrium and secondary evaporation processes, which will be discussed in more detail in the later sections (e.g. section 5.5).

## **5.3 Decomposition of Q.E. and D.I.C.**

Various methods were used in previous studies, for decomposition of the elastic, Q.E., and D.I.C. reactions ([15] and reference therein).

- (1) Manual cut off by excitation energy (or TKEL) [66, 59]
- (2) Fitting energy distribution[56, 77]
- (3) Fitting the mass distribution[75, 68]
- (4) Fitting Angular distribution[76]

The first, and the second method uses the same fact that Q.E. has smaller excitation energy close to elastic than D.I.C. This method is used widely especially for very heavy ions. And it is considered as a standard method for distinguishing the elastic scattering from the other reactions. The third method utilizes the property that the mass distribution from Q.E. reaction has narrow width than D.I.C.. The forth method utilize the fact that the angular distribution changes forward in light ions (backward in very heavy ions). Especially for light ions the angular distribution presents double peaked structure corresponding Q.E. and D.I.C. But it can be applied only in the reaction with light ( $A < 80$ ) (or very heavy ( $A > 200$ )) projectiles.

### *5.3. DECOMPOSITION OF Q.E. AND D.I.C.*

These methods are used depending on the scope of interest, experimental observables. But since there is no definite boundary determining the different reaction mechanism, especially for the reaction between heavy isotopes, the decomposition process should be treated carefully depending on the objective of the analysis. And its result should be treated as more or less qualitatively.

#### **5.3.1 Different factors of nucleon transfer dependency in Q.E. and D.I.C.**

The first of interest is the position of mean mass distribution of Q.E. and D.I.C. This was done in order to figure out what variable determines the nucleon transfer of Q.E. and D.I.C. Thus the third method of the decomposition of Q.E. and D.I.C. is most suitable. The decomposition of the quasi-elastic reaction and deep inelastic reactions were determined by fitting isotopic cross section distribution with Gaussian distribution (See figure 5.8).

The cross section of D.I.C. and Q.E. from decomposition using fitting of isotopic distribution is shown in figure 5.9 as function of atomic number. The decomposition shows that the D.I.C. reaction dominates over Q.E. reaction in all transfer channels of more than one proton. The both Q.E. and D.I.C. component the proton pickup channel is enhanced than the proton stripping channels. Thus the enhancement in the proton pickup channels could be originated from more compound like reaction component.

This result agrees with TDHF calculation which indicates the enhancement in the proton pickup channels in the quasi-fission component [35], which GRAZING code calculation was not taking into account. But enhancement of p-pickup channel

### 5.3. DECOMPOSITION OF Q.E. AND D.I.C.

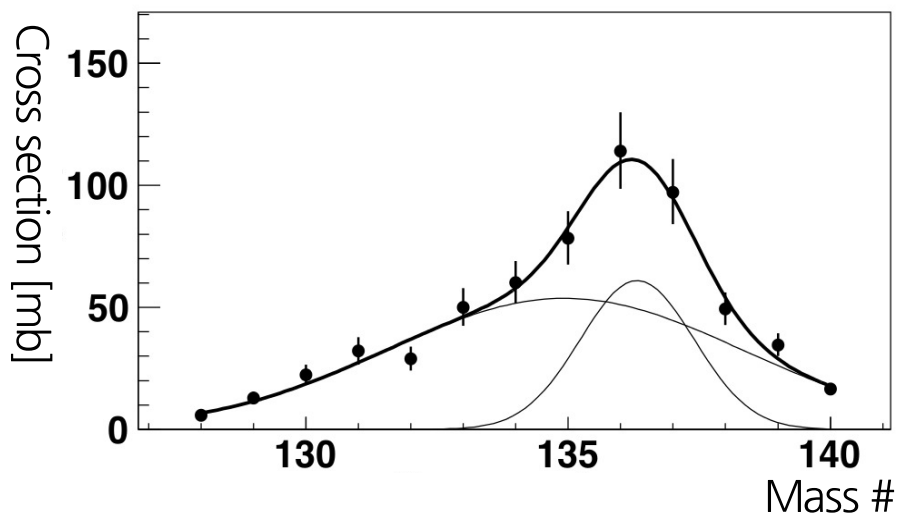


Figure 5.8 The cross section of Cs ( $Z = 55$ ) fitted with two Gaussian distribution. The narrow distribution was assigned as a reaction from Q.E. and wider width was assigned as a reaction fragments from D.I.C.

### 5.3. DECOMPOSITION OF Q.E. AND D.I.C.

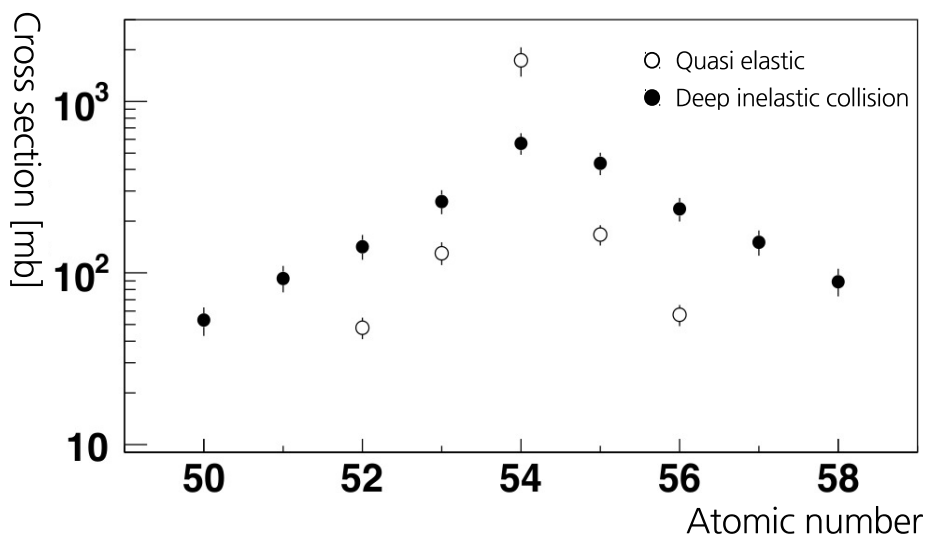


Figure 5.9 The result of decomposition of Q.E. and D.I.C. component of the cross section in proton transfer channels. The error bars indicate uncertainty of cross sections from the fitting errors.

### 5.3. DECOMPOSITION OF Q.E. AND D.I.C.

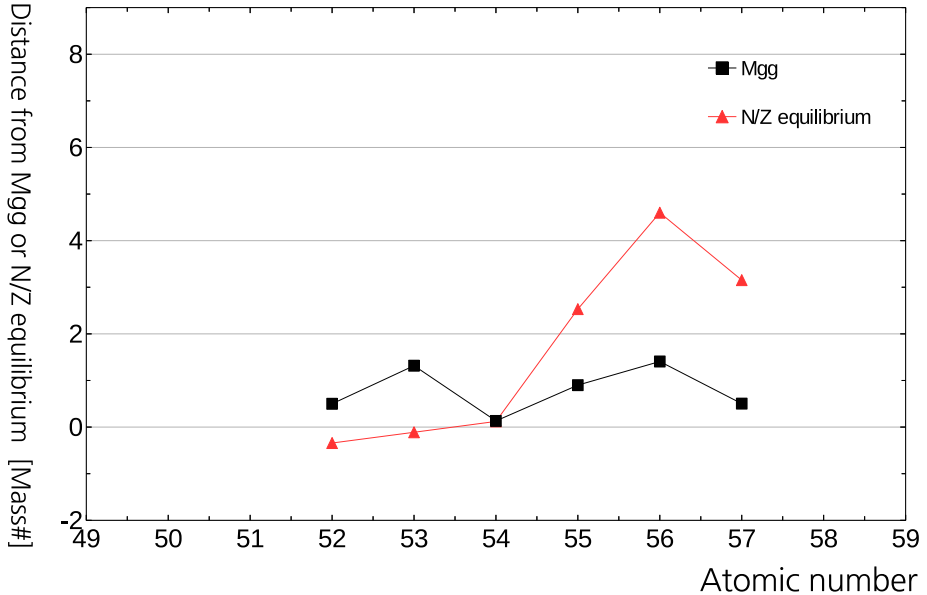


Figure 5.10 The distance of mean mass number of Q.E. component from mass of largest ground-to-ground state Q-value and N/Z equilibrium (See table 2.1).

in Q.E. component was not expected in GRAZIGN code calculation.

The correlation between atomic numbers and the mean mass difference from isotope with maximum local ground-to-ground state Q-values ( $M_{gg}$ ) or N/Z equilibrium position ( $M_{N/Z}$ ) (determined by global effective Q-value) is presented in figure 5.10.

The dependency of the most probable mass number on the atomic number can be identified if the distance from the  $M_{gg}$  or  $M_{N/Z}$  coincide or at least constant considering the neutron evaporation. The Q.E. channels in  $+2p \sim -2p$  showed independent distance ( $-1n$ ) from  $M_{gg}$ . This suggest that neutron transfer in Q.E.

### 5.3. DECOMPOSITION OF Q.E. AND D.I.C.

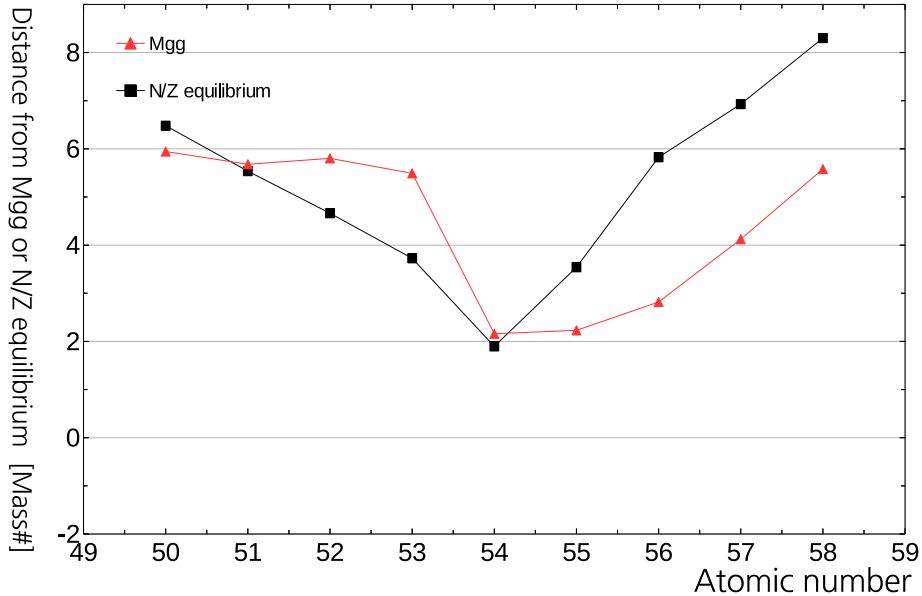


Figure 5.11 The distance of mean mass number of D.I.C. component from mass of largest ground-to-ground state Q-value and N/Z equilibrium (See table 2.1).

follows ground-to-ground state Q-value considering the neutron evaporation. This result is in coincidence with the result from the introduced in section 2.1.1. This can be interpreted as the ground state shell effect remained due to the low excitation energy in Q.E. reactions.

The case of D.I.C. was quite unclear at this stage of analysis due to the effect from secondary processes. But it could be inferred from these facts and the result in the later sections 5.5 that

- (1) The mean TKEL or excitation energy in later section depends approximately linearly as the number of transferred protons.

#### 5.4. REACTION KINEMATICS OF PLFS

- (2) And the number of evaporated neutrons are also depends (approximately) linearly to the TKEL.
- (3) Thus dependence of neutron transfer in D.I.C. can be determined by whether the distance from the M<sub>gg</sub> or M<sub>N/Z</sub> as function of number of transferred proton number is linear.

From figure 5.11 we can identify the D.I.C. depends (approximately) linearly on N/Z equilibrium not on the ground state Q-value. The more detailed description of the N/Z equilibrium will be discussed in the later sections.

### 5.4 Reaction kinematics of PLFs

#### 5.4.1 Wilczynski plot

The Wilczynski plot is the two dimensional histogram of total kinetic energy loss (TKEL) correlated with  $\theta_{CM}$  distribution, which was first plotted by J. Wilczynski [29]. (The calculation of TKEL is written in the appendix A.) It characterizes the different reaction mechanism of quasi-elastic and deep inelastic collision and quasi-fission (although there is no clear cut). This Q.E. has characteristic features of small excitation energy with angular distribution concentrated vicinity of the grazing angle. On the other hand, the D.I.C. has the massive excitation energy and wide angular distribution.

This experiment presented smooth transition (i.e. no double peak in TKE distribution) of reaction from low TKEL Q.E. to D.I.C. (See figure 5.12). The width of

#### 5.4. REACTION KINEMATICS OF PLFS

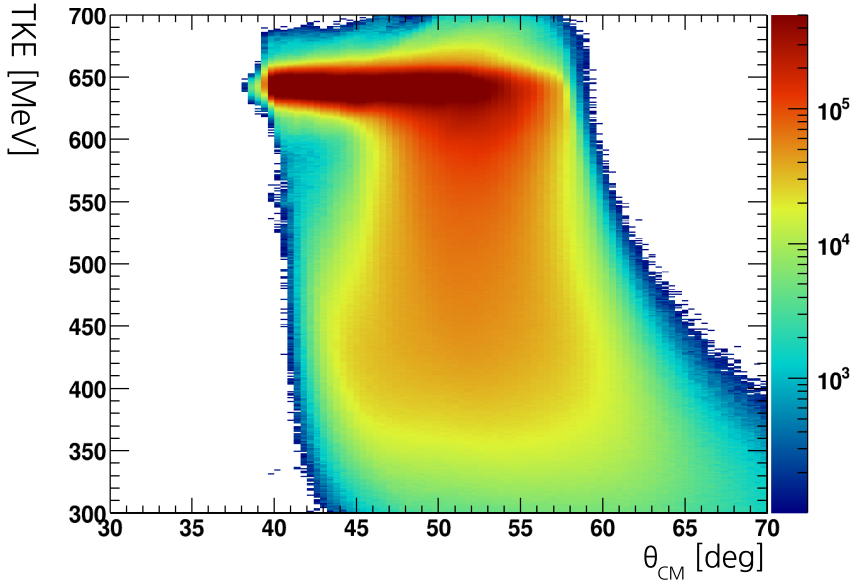


Figure 5.12 The Wilczynski plot of this system. drift to backward angle in TKEL<350 was due to the acceptance cut off of the spectrometer.

the angular distribution monotonically increased as the total kinetic energy (TKE) decreased, considering the strong elastic component near the TKE  $\sim 643$  MeV. It is contrasting to the light system (figure 5.13) which has more clear transition from Q.E. and D. I. C could be observed due to the change in the angular distribution and double peaked energy distribution. The Wilczynski plot also shows differences in the kinematics of entrance channels. In this experiment and references similar to this experiment, presents the constant mean angular over all TKEL regions. (See figure 5.12)

The mean angular distribution of the light projectile ( $A = 20 \sim 50$ ) with targets similar to this experiment (e.g.  $^{40}\text{Ar} + ^{232}\text{Th} = \text{K} + \text{Ac}$  [65]) drifted to forward angle

#### 5.4. REACTION KINEMATICS OF PLFS

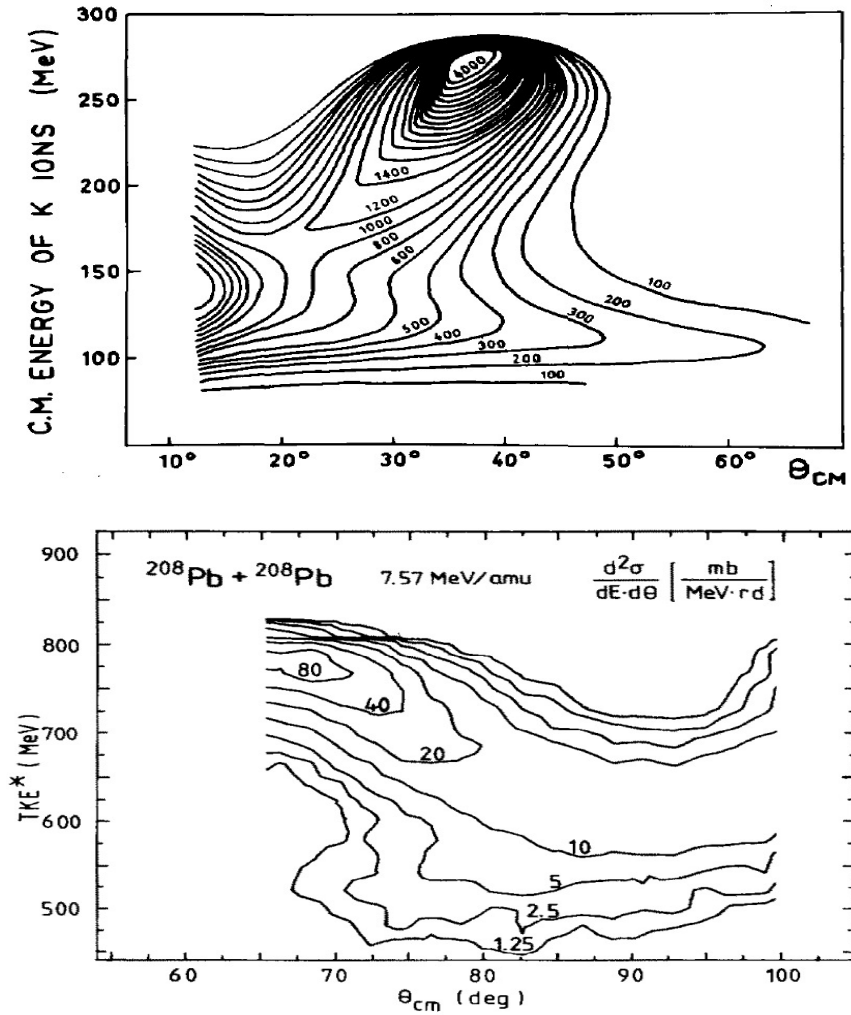


Figure 5.13 The Wilczynski plot (TKE (or  $E_{CM}$ ) vs  $\theta_{CM}$ ) of typical cases of light projectile system ( $^{40}\text{Ar} + ^{232}\text{Th} = \text{K} + \text{Ac}$  [65]) (top) and very heavy projectile system ( $^{208}\text{Pb} + ^{208}\text{Pb}$ ) [66] (bottom ).

## 5.4. REACTION KINEMATICS OF PLFS

as the TKEL increases. (See top figure 5.13) On the other hand, in the case with heavy projectile with targets drifted to the backward angle as the TKEL increased. (See bottom figure 5.13)

This is due to the interplay between repulsive Coulomb force and attractive nuclear force. Where as the system proton number increases close to this experimental system, then the repulsive Coulomb potential increases, thus the attractive nuclear force is canceled out in all range TKEL (i.e. for all impact parameter). And in the reaction with heavier nuclei Coulomb force is dominant causing angular distribution to more backward angle as dissipation energy increased.

### 5.4.2 n,p-transfer dependence of Wilczynski plot

The TKEL dependence of proton transfer were investigated. (See figure 5.14) The proton transfer showed peaked close to Xe ( $Z=54$ ) but slightly enhanced distribution to proton pickup channels irrespective to the TKE. The width of the distribution increased monotonically as TKE decreases. And more discussion about the mean, width will be presented in section 5.6.3, 5.6.1. The TKEL smaller than the ion-ion potential energy with Bass model (equation (7.37)  $\sim$  (7.39), (7.51) in Ref. [1])) at the distance of the closest approach between two colliding ions was observed. This indicates the massive deformation between TLF and PLF at the scission point [9].

The centroids of the Wilczynski plot of different isotopes of each proton transfer channel were surveyed. (See figure 5.15)

The proton stripping and pickup channels presented different behavior. First the angular distribution in proton stripping channels drifted to more forward angle than the Xe (0p transfer) channels as the number of transferred proton increased.

#### 5.4. REACTION KINEMATICS OF PLFS

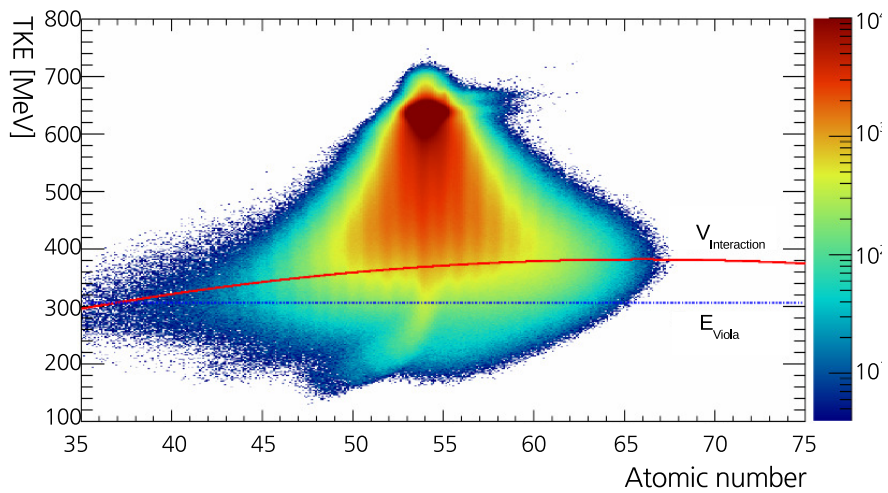


Figure 5.14 The atomic number vs TKE distribution . The potential energy ( $V_{\text{Interaction}}$ ) at the distance of the closest approach (red solid line) and fully damped energy calculated by Viola systematics [108] (blue dotted line) are indicated.

#### 5.4. REACTION KINEMATICS OF PLFS

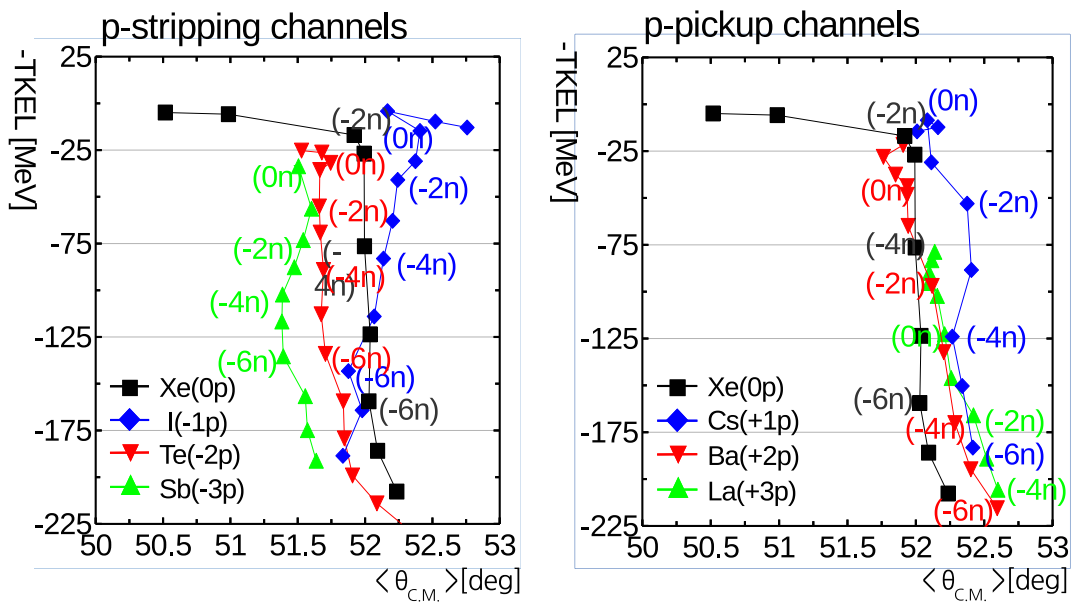


Figure 5.15 The mean position of  $\langle \text{TKEL} \rangle$  and  $\langle \theta_{\text{CM}} \rangle$  of proton stripping channels (left figure) and proton pickup channels (right figure). The isotope with even number of transferred neutrons are marked to indicate the position of different nuclides.

#### 5.4. REACTION KINEMATICS OF PLFS

While on the other hand the proton pickup channels stayed in the backward angle than the Xe channels. This can be interpreted that the Coulomb repulsion was decreased in proton stripping results trajectory to more forward angle. On the other hand, repulsive force was increased in proton pickup channels causing the angle drift towards backward angle.

The mean of the TKEL distribution ( $\langle \text{TKEL} \rangle$ ) becomes greater as the number of transferred neutrons (protons) increases among nuclides with the same number of transferred protons (neutrons). But when we look at the dependence of  $\langle \text{TKEL} \rangle$  on the number of transferred nucleons more closely, very At the proton stripping channels, the  $\langle \text{TKEL} \rangle$  increases slowly as the number of transferred protons increases among nuclei with the same number of transferred neutrons (e.g. -4n channels  $^{132}\text{Xe}$ : -76.5,  $^{131}\text{I}$ : -83.1,  $^{130}\text{Te}$ : -89.1,  $^{129}\text{Sb}$ : -102.2 MeV). On the other hand, at the proton pickup channels, the increase in the  $\langle \text{TKEL} \rangle$  is rapidly changed (e.g. -4n channels  $^{132}\text{Xe}$ : -76.5 ,  $^{133}\text{Cs}$ : -124.0,  $^{134}\text{Ba}$ : -170.1,  $^{135}\text{La}$ : -205.7 MeV). This behavior is due to the N/Z equilibrium and the secondary process after the nucleon transfer, details of which will be explained in the section 5.5.

The width of angular distribution is monotonically increased as the TKEL increases in all systems. The TKEL dependence of the width of the angular distribution shows similar tendencies among the different proton transfer channels (see figure 5.16), which are also observed in other systems similar to this [56]. This independence of angular distribution confirms the fact that the primary parameter for describing the nuclear reaction kinematics is the TKEL (or later excitation energy). And the number of transferred protons is the secondary term correlated to the TKEL.

#### 5.4. REACTION KINEMATICS OF PLFS

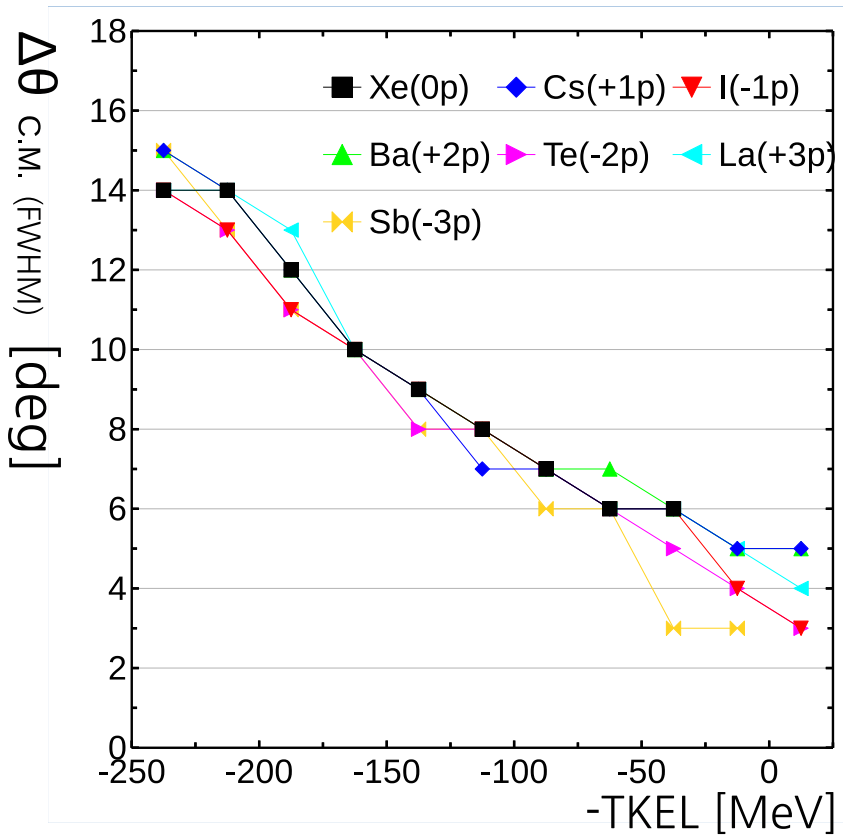


Figure 5.16 The FWHM of angular distribution of different proton transfer channels.

## *5.5. PRE-EVAPORATION FRAGMENT AND EXCITATION ENERGY DETERMINATION*

### **5.5 pre-evaporation fragment and Excitation Energy Determination**

The MNT reaction process results reaction fragment with exit energy ranging from elastic to fully damped energy, where the kinetic energy of projectile is converted to the internal excitation energy through nucleon transfer (friction) or strong deformation of nucleus (depending on model interpretation (See chapter 2)). The excitation energy after scission of compound system to PLF and TLF is consumed by light particle evaporation.

The name evaporation comes from the fact that the energy distributions of the light particles are similar to the Maxwell-Boltzmann distribution resembling black body radiation (e.g. equation 1 of [110], and figure 8 of [112]). The particle evaporation during the MNT reaction so called non equilibrated evaporation is negligible from the previous experimental results [110], confirming the evaporation process occurs after the nucleon transfer.

The detected fragments from VAMOS spectrometer are the PLF after secondary process. The excitation energy, TLF mass and kinematics directly calculated from the PLF assuming two body kinematics will be distorted without considering secondary process (see figure 5.17).

Thus the correction of the secondary process is necessary in order to determine the TLF information and the properties of the nucleon transfer without the effect from the secondary process. But the evaporated light particles were not detected directly from the experiment due to the lack of setup. Therefore the correction for secondary process needs to be based on some assumptions.

In this analysis four assumptions were configured, an iteration method (similar

## 5.5. PRE-EVAPORATION FRAGMENT AND EXCITATION ENERGY DETERMINATION

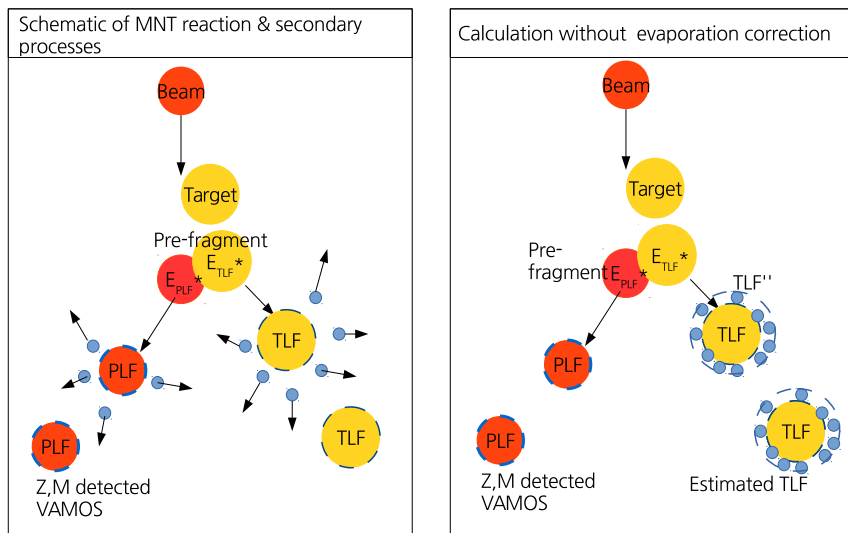


Figure 5.17 (right) Schematics of MNT reaction and secondary process. Evaporated light particles are indicated as blue circle. (left) Schematics of kinematical calculation without correcting secondary process.

## 5.5. PRE-EVAPORATION FRAGMENT AND EXCITATION ENERGY DETERMINATION

to the H. Breuer *et al.* [116]) was used to calculate the excitation energy and the number of evaporated light particles.

The four assumptions are,

- (1) The excitation energies are divided with mass ratio of the system.
- (2) Only neutrons are evaporated in the PLF.
- (3) The evaporated neutrons are emitted isotropically.
- (4) The light particles are evaporated based on the theoretical calculation of PACE4 [113].

The first assumption indicates the excitation energy of the system is equilibrated between PLF and TLF (i.e. having the same temperature). It is expressed by  $E_{\text{PLF}}^*/E_{\text{TLF}}^* = A_{\text{PLF}}/A_{\text{TLF}}$ . This assumption is valid since the typical reaction time ( $10^{-21}\sim-19$ ) is smaller than the time scale of the energy equilibrium ( $10^{-22}$ : time of proton with Fermi energy travel twice the nuclear radius) [1]. This assumption has been very widely used in the previous references [58, 59, 66, 73, 68]. The experimental results which were investigated by neutron multiplicity support such picture [82, 109]. In the region of the low excitation energies, where the reaction time scale is comparable to the energy equilibrium time, this assumption could be questionable. There is another assumption also used in the previous literatures which includes temperature [69, 70], where it is expressed by  $E_{\text{PLF}}^*/E_{\text{TLF}}^* = (A_{\text{PLF}}T_{\text{PLF}})/(A_{\text{TLF}}T_{\text{TLF}})$ . But this assumption includes another assumptions and uncertainty by using the theoretical models to determine the different temperatures of PLF and TLF (e.g. reference [69] used nucleon exchange trajectory model [39]). In this experiment the main part of the reaction occurs in the D.I.C. where the

## 5.5. PRE-EVAPORATION FRAGMENT AND EXCITATION ENERGY DETERMINATION

reaction time is larger than the time for energy equilibrium. And the low excitation energy region has a very small effect of the evaporation ( $1 \sim 2$  neutron evaporation). Thus in this experiment the mass ratio was used to evaluate excitation energies.

The second assumption indicates the competition between neutron and charged particle evaporation. It can be investigated by difference between neutron separation energy ( $S_n$ ) and proton separation energy ( $S_p$ ) including Coulomb barrier for the proton ( $V_{Cp}$ ). This can be categorized by [116];

$$S_p + V_{Cp} - S_n < 0. \text{ [MeV]: dominant proton evaporation}$$

$$S_p + V_{Cp} - S_n \simeq 0. \text{ [MeV]: equal contributions of proton, neutron evaporation}$$

$$S_p + V_{Cp} - S_n > 0. \text{ [MeV]: dominant neutron evaporation}$$

In this experiment we used neutron rich projectile and the target with large Coulomb barrier thus  $(S_n) + V_{Cp} - S_n > 0.$  for all reaction fragments. (e.g.  $^{136}\text{Xe}$  has  $S_p=9.929 \text{ MeV}$ ,  $V_{Cp}=7.154$  and  $S_n=8.084 \text{ MeV}$  and the most n-deficient nuclei measured  $^{110}\text{Sn}$   $S_p=6.643 \text{ MeV}$ ,  $V_{Cp}=6.904$  and  $S_n=11.282 \text{ MeV}$  [125],[1]). Which is much larger than 0. MeV, thus second assumption is justified. This assumption is used in many previous experimental references [58, 59, 66, 73, 61, 68] using neutron rich nuclides. This assumption holds also in the PACE4 calculations, even at the  $E_{\text{PLF}}^*=100 \text{ MeV}$  ( $E_{\text{total}}^* \sim 250 \text{ MeV}$  in case of PLF mass number 136), where more than 80% of the evaporation occurs by neutrons. The second assumption is very useful since the multi-channel calculation is difficult in reverse transfer from evaporated event to pre-evaporation fragment. The fission process can be another source of the secondary process in the target-like fragments. But PACE4 and recent GRAZING-F calculation [23] showed negligible probability of fission for our reaction system. The

## 5.5. PRE-EVAPORATION FRAGMENT AND EXCITATION ENERGY DETERMINATION

another source of energy consumption is the  $\gamma$ -ray during the evaporation process. The experimental result showed number of  $\gamma$ -ray coincidence is proportional to the excitation energy [116]. But the amount of the energy consumed by the  $\gamma$ -ray emission is negligible ( $<1$  MeV) compared to the particle evaporation (few tens MeV depending on the kinetic energy of evaporated particle).

The isotropic emission of the neutron evaporation is the natural assumption if the evaporation process is purely statistical process (not from the reaction or direct process in the spontaneous particle emission). This assumption makes the average velocity of fragment unchanged during the secondary process. This assumption coincided with the experimental results.

The PACE4 [113] calculation is considered as one of the standard fusion evaporation codes. A distribution of nuclides after the evaporation is obtained as the result of the calculation by PACE4, where the statistical model is used. The validity of the PACE4 can be seen in many experiments (See figure 5.18 for experiment similar to this system).

In this experiment it was used to calculate the mean numbers of evaporated neutrons (and charged particles in case of TLF evaporation) as function of excitation energy. The mean number of neutrons were calculated for N/Z equilibrium nuclides for different atomic number and fitted with 7th order polynomial function. And ratio of channel from charged particle evaporation was calculated for TLF nuclides (e.g.  $^{193}\text{Os}$  case, see figure 5.20, and 5.21).

The uncertainty of particle evaporation was deduced changing the mean number of evaporated neutrons by a standard deviation ( $\sigma_{\text{ev}}$ ) of the particle evaporation calculated at each excitation energy (see figure 5.22).

## 5.5. PRE-EVAPORATION FRAGMENT AND EXCITATION ENERGY DETERMINATION

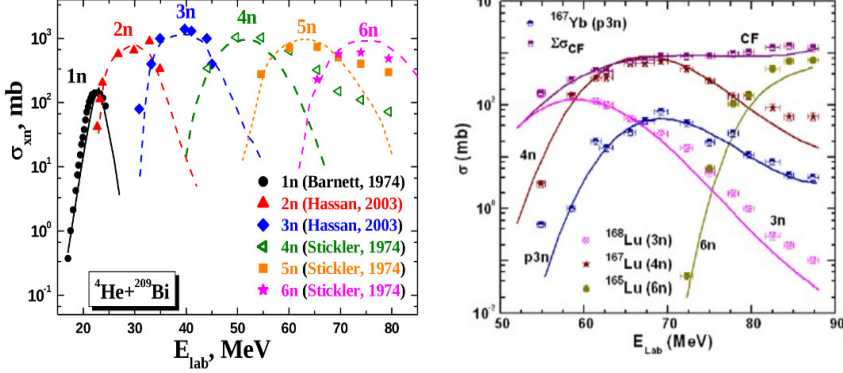


Figure 5.18 (left) Experimental result of fusion evaporation of  ${}^4\text{He} + {}^{209}\text{Bi} \rightarrow {}^{213}\text{At} \rightarrow {}^{213-x}\text{At} + xn$ -evaporation with PACE4 calculation. [114] (right) Experimental result of fusion evaporation of  ${}^8\text{Be} + {}^{124}\text{Sn} \rightarrow {}^{132}\text{Xe} \rightarrow {}^{132-x}\text{Xe} + xn$ -evaporation and  ${}^{126}\text{Te} + \alpha + 2n$ -evaporation with PACE4 calculation [115].

The two different set of data are calculated from the mean number of evaporated neutrons  $\pm \sigma_{ev}$ . The difference between calculated data using only curve of mean number of evaporation and  $\pm \sigma_{ev}$  was set as uncertainty of particle evaporation.

### 5.5.1 Iteration method

Based on the four assumptions, the number of evaporated neutrons in PLF ( $dN_{PLF}$ ), the excitation energies in PLF ( $E_{PLF}^*$ ), and kinematical information of TLF ( $M_{TLF}$ ,  $E_{TLF}^*$ ,  $\vec{P}_{TLF}$ ) before secondary process are calculated iteratively. The method is shown in diagrams (See figure 5.23) and described below.

- (1) In the beginning ( $i=0$ ), the detected PLF was assumed as the pre-evaporated fragment PLF (i.e. PLF in 0-th iteration) with no neutron evaporation ( $dN_{PLF}[0] = 0$ ) and no excitation energy ( $E_{PLF}[0] = 0$ ).

## 5.5. PRE-EVAPORATION FRAGMENT AND EXCITATION ENERGY DETERMINATION

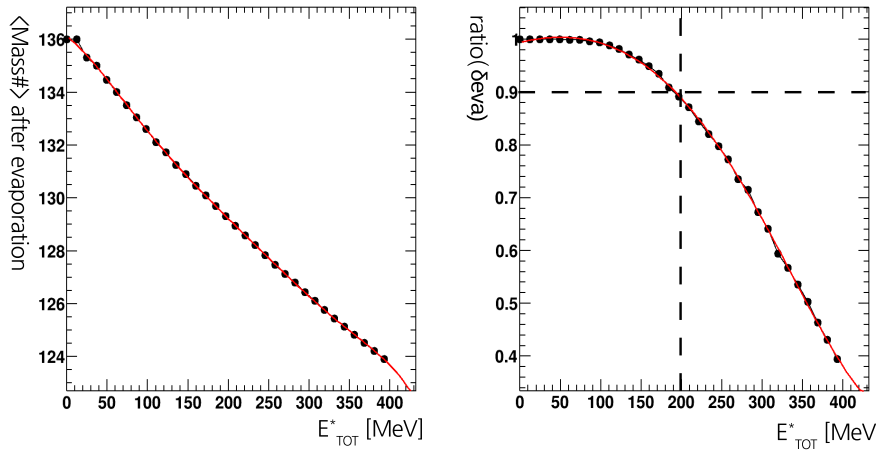


Figure 5.19 (right) The PACE4 calculation of evaporation curve ( $E^*_{TOT}$  as an x-axis) of  $^{136}\text{Xe}$  (mean mass after evaporation as function of excitation energy) which are indicated with black solid circle with 7th order polynomial fitting (solid line) (left) The ratio of  $^{136}\text{Xe}$  evaporation channel without any particle evaporation (neutron evaporation only) from total cross section as function of excitation energy.

## 5.5. PRE-EVAPORATION FRAGMENT AND EXCITATION ENERGY DETERMINATION

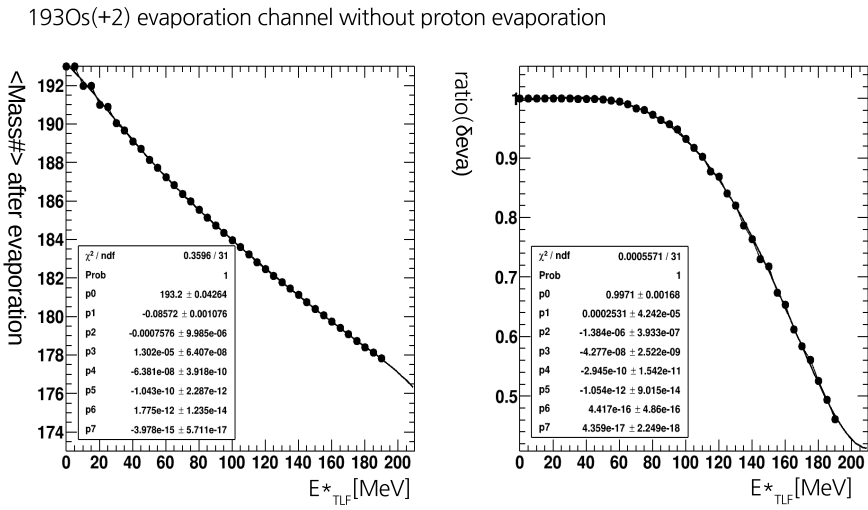


Figure 5.20 (left) The PACE4 calculation of evaporation curve of  $^{193}\text{Os}$  (mean mass after evaporation as function of excitation energy) which are indicated with black solid circle with 7th order polynomial fitting (solid line) (right) The ratio of  $^{193}\text{Os}$  evaporation channel without any particle evaporation (neutron evaporation only) to the total cross section as function of excitation energy.

## 5.5. PRE-EVAPORATION FRAGMENT AND EXCITATION ENERGY DETERMINATION

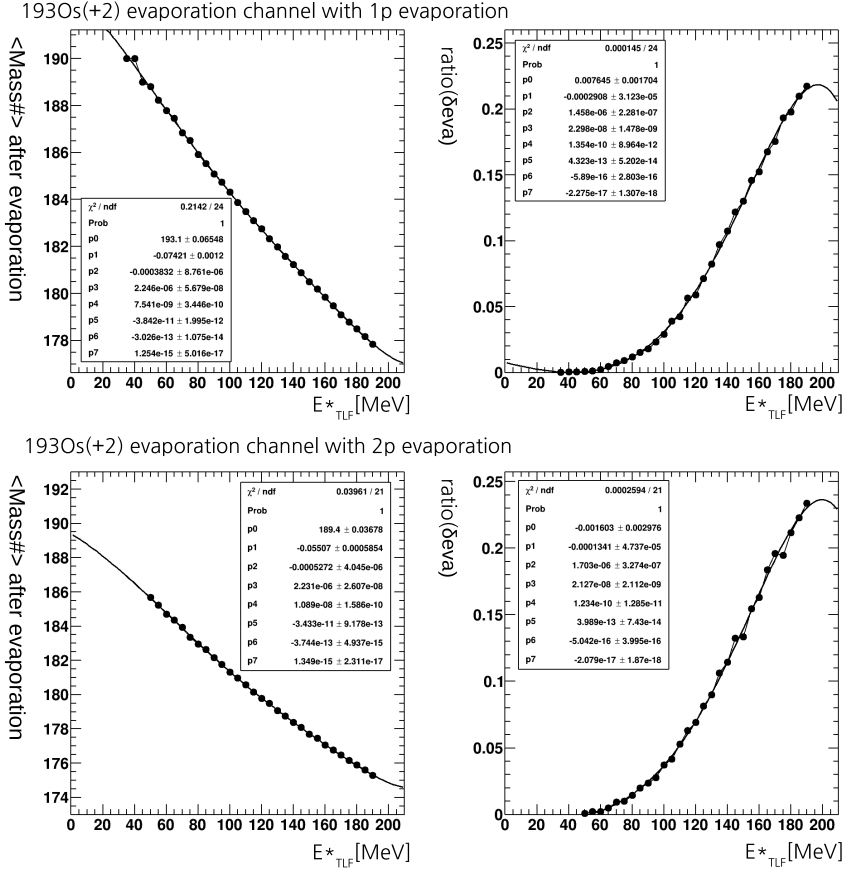


Figure 5.21 Evaporation curve of  $^{193}\text{Os}$  with one proton and multiple neutrons, (top left) mean mass , (top right) ratio to the total evaporation channels as function of excitation energy of TLF, with two proton and multiple neutrons, (bottom left) mean mass , (bottom right) ratio to the total evaporation channels as function of excitation energy of TLF.

## 5.5. PRE-EVAPORATION FRAGMENT AND EXCITATION ENERGY DETERMINATION

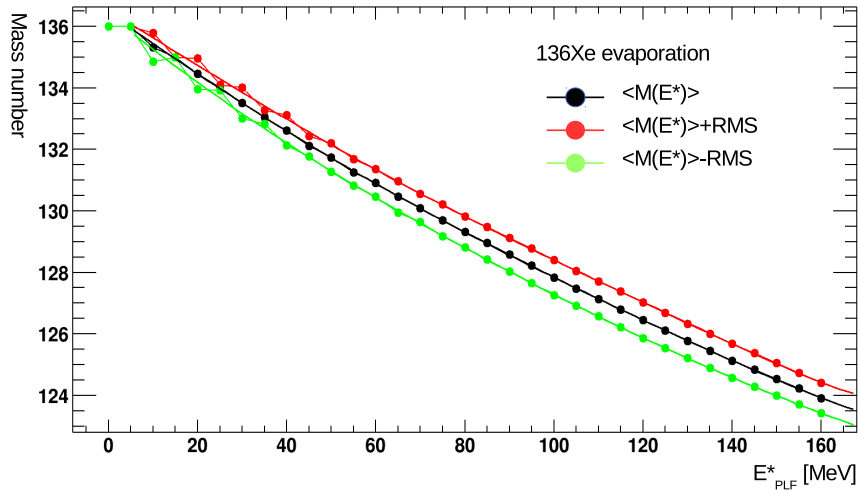


Figure 5.22 Mass number of the nucleus after neutron evaporation from  $^{136}\text{Xe}$  calculated by PACE4 (black solid circle) with 7th order polynomial fitting (black solid line) red/green solid circle indicate upper/lower limit deduced by adding/subtracting standard deviation of the mass distribution after evaporation with fitting result (solid line).

## 5.5. PRE-EVAPORATION FRAGMENT AND EXCITATION ENERGY DETERMINATION

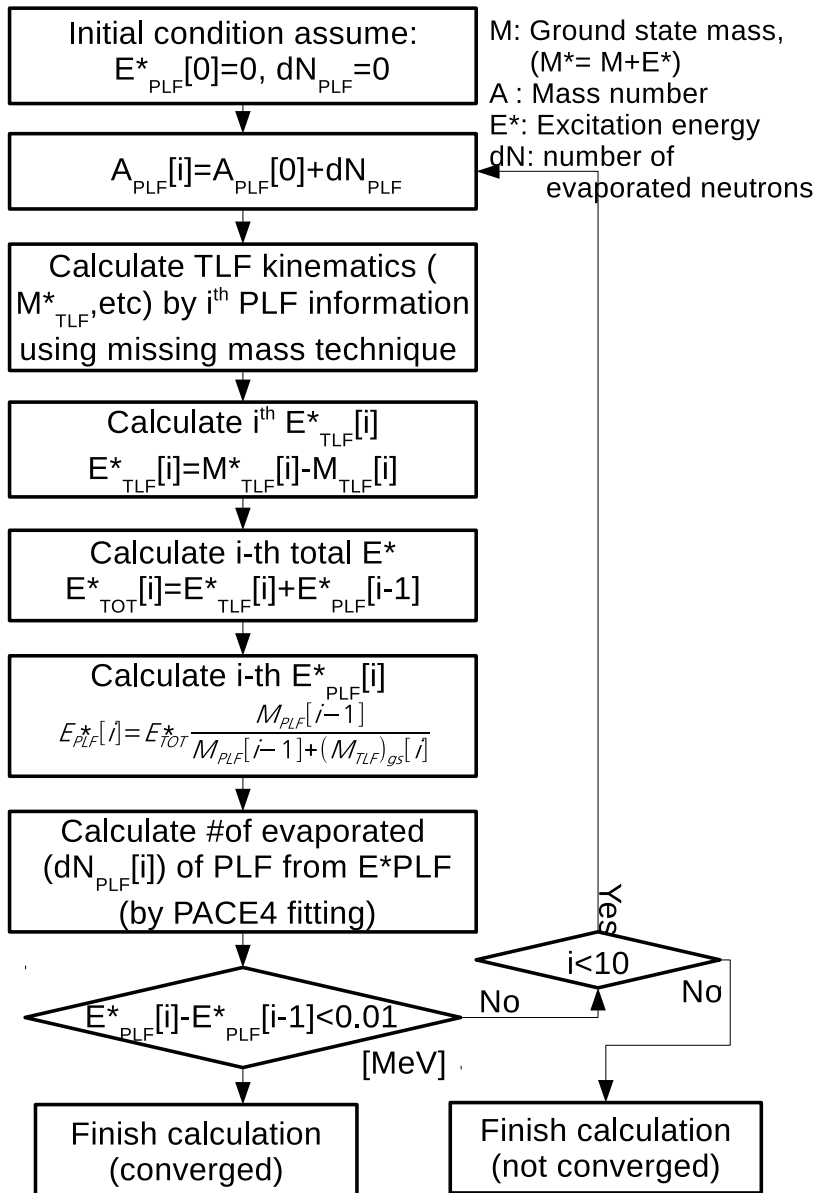


Figure 5.23 The flow chart describing the iteration method for correcting neutron evaporation and deducing excitation energy of the system. (See text for more detailed explanation)

## 5.5. PRE-EVAPORATION FRAGMENT AND EXCITATION ENERGY DETERMINATION

- (2) (i-th iteration) Mass number of the primary PLF was deduced by adding  $dN_{PLF}[i]$  to the detected mass number of the PLF.
- (3) Calculate i<sup>th</sup> TLF kinematics ( $M_{TLF}^*[i]$ ,  $\vec{P}_{TLF}[i]$ ) using i-1<sup>th</sup> iteration data of PLF assuming two body kinematics.
- (4) Calculate the total excitation energy.

$$E_{TOT}^* = E_{PLF}^*[i - 1] + E_{TLF}^*[i] \quad (5.1)$$

- (5) Determine TLF excitation energy ( $E_{TLF}^*[i]$ ) by difference from calculated mass and ground state mass using i-1<sup>th</sup> iteration

$$E_{TLF}^*[i] = M_{TLF}[i](calculated) - M_{TLF}[i](groundstate). \quad (5.2)$$

- (6) From calculated  $E_{TLF}^*[i]$ , calculate  $E_{PLF}^*[i]$  by mass ratio

$$E_{PLF}^*[i] = (M_{PLF}[i - 1]/(M_{TLF}[i] + M_{PLF}[i - 1]))E_{TOT}^*[i] \quad (5.3)$$

- (7) Calculate number of evaporated neutrons  $dN_{PLF}[i]$  from PLF using the result from PACE4 calculation fitting.

- (8) Repeat (2-7) until event converges (convergence condition:  $M_{PLF}[i] = M_{PLF}[i - 1]$ , and  $E_{PLF}^*[i] - E_{PLF}^*[i - 1] < 0.01MeV$ ) during the iteration. If the event doesn't converge (vibrate ( $M_{PLF}[i] - M_{PLF}[i - 1] = \pm 1$ ) or diverges) after tenth iteration the events are assumed to be not converged.

The most of the events (> 90%) coverage at the fifth ~ sixth iteration, and the events which are not converged vibrates one mass to another. The vibrated events are divided in to half and included to different mass. (The vibrated events are included as an error)

## 5.5. PRE-EVAPORATION FRAGMENT AND EXCITATION ENERGY DETERMINATION

### 5.5.2 Resolution of the $E_{total}^*$ calculation

The resolution of the total excitation energy is determined by two main uncertainties. First the target thickness, since we don't know where the reaction occurred inside of the target. This uncertainty gives 14.6 MeV which is the difference between excitation energy(Lab angle 30°) reaction occurred in the front and the back of the target. The energy loss uncertainty is large since we used large atomic number beam target combination with relatively low beam energy. Second the angular resolution of our system is 1°. The energy uncertainty of the elastic scattering in the + 0.5° and the -0.5° results in 9.5MeV. And the intrinsic energy resolution of the IC and Si is order of a few 100 keV which can be ignored in comparison with other two resolutions. Combination of this two resolution results in total energy resolution of 17.4 MeV. Thus in the following sections the excitation energy cut was done with 20 MeV intervals.

### 5.5.3 Limit of the $E_{total}^*$ calculation

The pre-evaporation fragment of PLF cannot restore the yield using the same method as the production cross section determination. (See section 4.3.4, and 5.2) This is because events out of the restored mass range are included in the calculation.  $E^{*total}$  is limited in the range where restored mass region does not participate in mean, width of the distribution. And values such as cross section including outside of this region should be treated as the lower limit.

The limit of valid region of total excitation energy  $E_{total}^*$  are determined by two main factors. The first factor is the acceptance of the spectrometer. The limit of the spectrometer acceptance is determined by  $B\rho$  and  $\theta$  ( $\phi$  acceptance is corrected by

## 5.5. PRE-EVAPORATION FRAGMENT AND EXCITATION ENERGY DETERMINATION

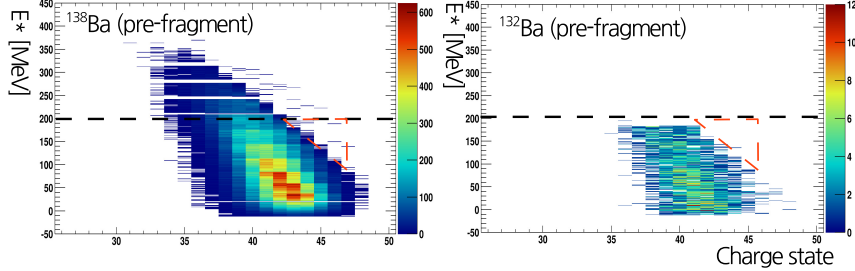


Figure 5.24 The charge state vs total exciation energy ( $E_{TOT}^*$ ) distribution of pre-evaporation fragment(left figure) $^{138}\text{Ba}$ , (right figure) $^{132}\text{Ba}$ . The cutoff below  $E_{TOT}^* < 200$  MeV are indicated as a red triangle. The missing event in  $^{132}\text{Ba}$  distribution at  $E_{TOT}^* > 200$  MeV are due to the (integer) mass identification was not determined, isotopes in that mass range after evaporation (isotope with mass smaller than  $^{126}\text{Ba}$ ) due to the small statistic.

detection efficiency). For fixed PLF isotope with fixed charge state, as the  $E_{total}^*$  increases the  $B\rho$  decreases. The cutoff can be determined by correlation of charge state and  $E_{total}^*$ (See figure 5.24). There is cutoff (red triangle region) in the region of  $E_{TOT}^* < 200$  MeV. But it is less than 10% even in the heavy isotopes like  $^{138}\text{Ba}$ . The second is due to the assumption in the calculation that the all particles evaporated from the PLF are neutron. The PACE4 calculation below 200 MeV presented that evaporation other than neutrons was less than  $8 \sim 15\%$  (see figure 5.19).

From this the  $E_{total}^*$  limit was set as the 200 MeV to ensure the acceptance and the validity of the neutron evaporation correction. And the cross sections or yield distribution without  $E_{total}^*$  limit should be treated as the lower limit.

## 5.5. PRE-EVAPORATION FRAGMENT AND EXCITATION ENERGY DETERMINATION

### 5.5.4 Pre-evaporated fragment cross section

The cross section before secondary process (neutron evaporation) is presented in figure 5.25 and 5.26. As mentioned in the previous section the out-of-acceptance events were not accounted due to the limit of the correction method. (Thus the cross section could be treated as a lower limit of the real total cross section.) For the blue open circles ( $A = 138 \sim 145$ ) in the figure 5.25 Xe ( $\leftrightarrow$  Pt) are underestimated due to the removal of events in mass regions due to the blob events explained in the section 4.2.1.

The errors in the cross section includes the statistical error, acceptance correction error, the error of conversion factor, the error from atomic number cut, error from neutron evaporation model (See section 5.5), and the error from vibrating event during iteration (See section 5.5.1).

The peak position of the experimental cross section showed mass rather far from the pure proton transfer channel but between the isotope with local Q-value maximum and the N/Z equilibrium(except for the Xe channels where elastic and quasi-elastic dominates). This means the strong N/Z equilibrium drives the transfer of nucleon. (The N/Z equilibrium mass was calculated from the effective Q-value by V. V. Volkov in section 2.1.1) This result is due to the dominance of the deep inelastic collision over the quasi-elastic reaction. (See section in the proton transferred channels 5.3.1)

The experimental cross section is compared to the GRAZING code calculation [20] and TDHF [35] calculation. First, the amount of the cross section between experiment and the theoretical calculation was compared. The GRAZING code calculation underestimated the cross section for all channels. In the proton stripping

## 5.5. PRE-EVAPORATION FRAGMENT AND EXCITATION ENERGY DETERMINATION

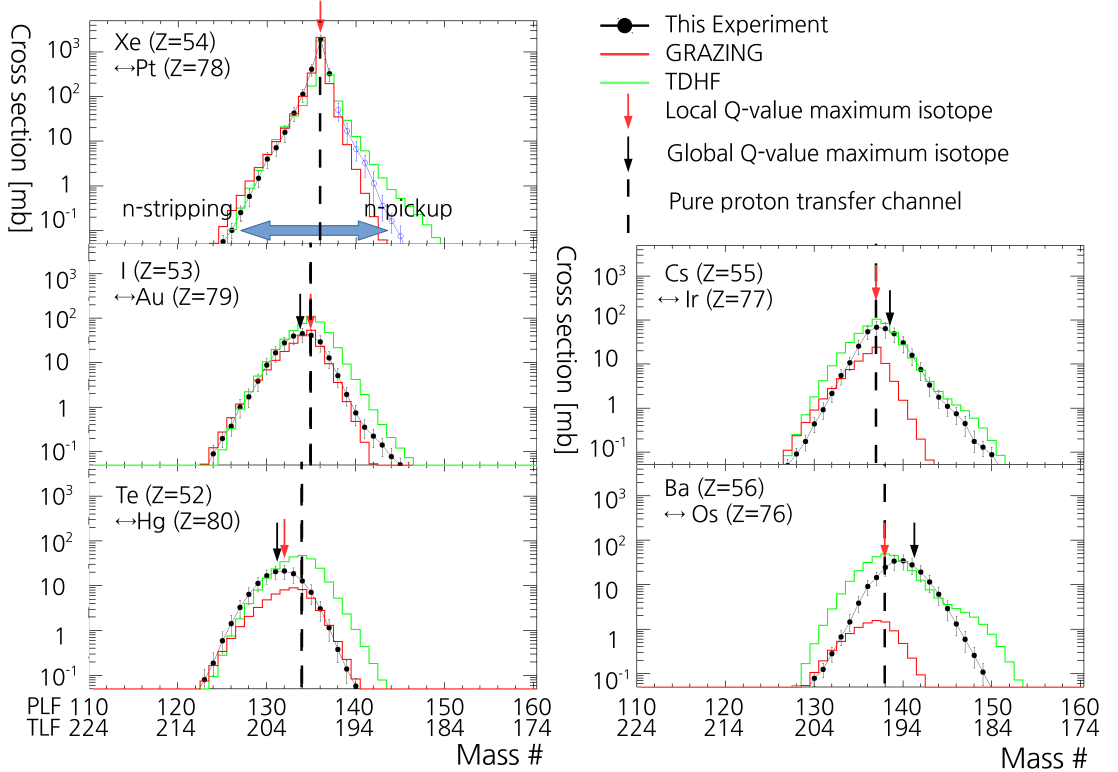


Figure 5.25 The cross section of pre-evaporation fragments before secondary process. The (top left)  $Xe (Z=54)$ , (middle left)  $I (Z=53)$ , (middle right)  $Cs (Z=55)$ , (bottom left)  $Te (Z=52)$ , (bottom right)  $Ba (Z=56)$  isotopes are presented. Experimental results are indicated as an black solid circle. (Blue open circles are measured lower limits of the cross section for more explanation read the text) The theoretical calculation of GRAZING are indicated as red solid line, and TDHF calculations are indicated as an green solid line. The black vertical dashed line indicates the pure proton transfer channel. The isotope with local Q-value maximum are indicated as red arrows, and global Q-value maximum ( $N/Z$  equilibrium) isotope are indicated as black arrows.

## 5.5. PRE-EVAPORATION FRAGMENT AND EXCITATION ENERGY DETERMINATION

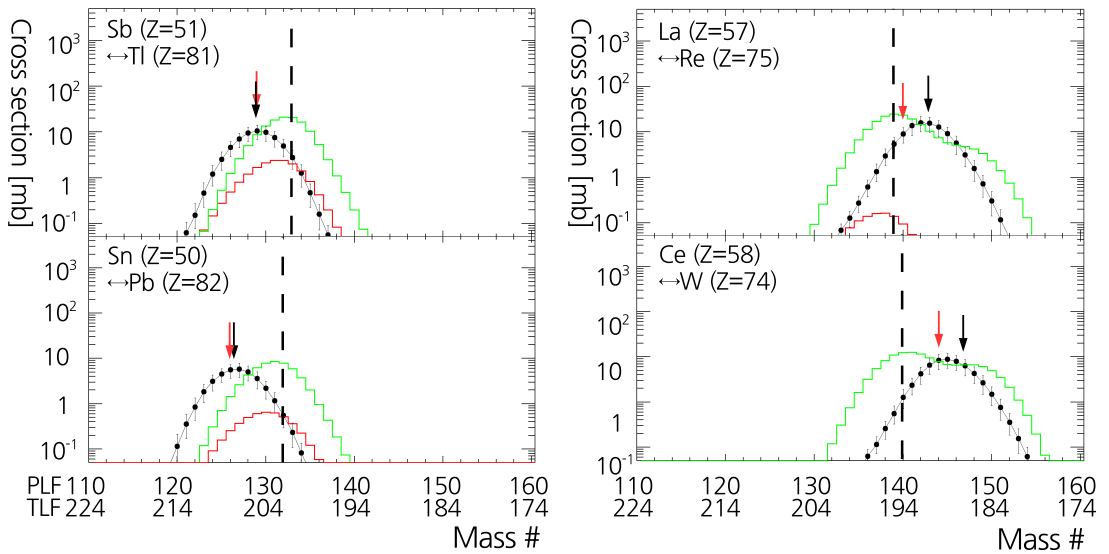


Figure 5.26 The cross section of pre-evaporation fragments before secondary process.

The (top left) Sb ( $Z=51$ ), (top right) La ( $Z=57$ ), (bottom left) Sn ( $Z=50$ ), (bottom right) Ce ( $Z=58$ ) isotopes are presented. The figure follows the same notation as figure 5.25.

## *5.5. PRE-EVAPORATION FRAGMENT AND EXCITATION ENERGY DETERMINATION*

channels, the discrepancy was larger as the number of transferred proton increases, and the number of neutron stripped (or evaporated). The discrepancy between experiment and the GRAZING code calculation in the proton stripping channel can be partially explained by the calculation limit in the GRAZING code. First is due to this GRAZING calculation is limited to the impact parameter larger than the nuclear rainbow in this case  $> 14$  fm. (See figure 2.6 in chapter 2.) Second the initial deformation of nuclides in the entrance channels were not accounted. ( $^{136}\text{Xe}$ ,  $^{198}\text{Pt}$  case the deformation is negligible) This can be confirmed in the following section 5.5.5.

The underestimation of cross section from GRAZING calculation was especially large at the proton pickup channels which showed orders of magnitude difference. This underestimation in the proton pickup channels can be observed in the other experimental results (e.g.  $^{64}\text{Ni} + ^{238}\text{U}$  [51]). The recent GRAZING code [23] based calculation which includes transfer induced fission in the secondary process presented good agreement depending on the reaction systems, limited within the three proton stripping channels. (transfer of proton from light projectile to the heavy target) But it also failed to reproduce proton pickup channels since the underestimation of GRAZING code in pickup side. Currently the reason for this under-estimation in the proton pickup channels is not clear at this moment [9].

The cross section estimated from the TDHF [35] calculation showed good agreement to the experimental result (within factor two). The TDHF presented larger cross section in the proton pickup channels with respect to the proton stripping channels, which coincides with the experimental results. This good agreement of cross section height was similar over all proton transfer channels. This better agree-

## 5.5. PRE-EVAPORATION FRAGMENT AND EXCITATION ENERGY DETERMINATION

ment of the TDHF than GRAZING is partially due to the fact that TDHF calculation doesn't have limit in the impact parameter like GRAZING code calculation (see the flowing subsections). The another major contribution in the proton pickup channel is the quasi-fission in the very damped regions.[35] This quasi-fission causes the minor peak of the isotopic distribution in the proton pickup channel.

Second, the position of isotope with maximum cross section of the experiment and the theoretical calculation was compared. The peak position of the GRAZING calculation and the TDHF calculation are near pure proton transfer channels for all proton transfer channels. The strong tendency towards N/Z equilibrium shown in the experiment was not expected by theoretical calculation of GRAZING and the TDHF. The both of the model predictions show the mean of mass distribution stays in the same position near the pure proton transfer channels (channel with only proton transfer).

These differences of the model calculation from the experiment are not clear at this moment, and only some speculation could be made. The GRAZING assumes the form factor which is main term of the transfer probability much smaller than unity. Thus the cross section will be largest for channels with least number of nucleon transferred. Thus for different cross section for channels of different proton number, the peak position of mass was at the pure proton transfer channel.

The transfer probabilities in the TDHF calculations are not small as the GRAZING. But the similar N/Z equilibrium keeps the net number of transferred nucleon close to the entrance channel. Thus the peak position close to the pure proton transfer channels instead of the N/Z equilibrium mass. (But in case of the reaction system with asymmetric N/Z ratio (e.g.  $^{58}Ni + ^{208}Pb$  [52]) TDHF presents mean

## 5.5. PRE-EVAPORATION FRAGMENT AND EXCITATION ENERGY DETERMINATION

mass position close to the experimental results.)

### 5.5.5 Pre-evaporation fragment cross section $E_{total}^* < 100\text{MeV}$

The GRAZING calculation assumes the classical trajectory using Woods-Saxon and Coulomb potential assuming point like charge. This assumption breaks down as the impact parameter decreases where closest distance approach becomes similar to the sum of projectile and target nuclei radius. Due to this GRAZING calculation is limited to the impact parameter larger than the nuclear rainbow in this case  $> 14 \text{ fm}$ . (See figure 2.6) This corresponds to the excitation energy  $< 80 \sim 100 \text{ MeV}$ . Thus for fair comparison with the GRAZING calculation the cross section below this excitation energy needs to be compared.

The figure 5.27, and 5.28 are the cross section with excitation energy lower than 100 MeV. The cross sections in the proton pickup channels are still underestimated in order of magnitude. But the cross section in the proton stripping channels agrees very well even at the four-proton stripping channels, considering the cross section value and the peak position. (Although width is larger than the experiment)

The good agreements of GRAZING in proton stripping channels are also seen in the other experimental results with system energy close to the Coulomb barrier, (e.g.  $^{64}\text{Ni} + ^{238}\text{U}$ ,  $^{58}\text{Ni} + ^{208}\text{Pb}$ ) where system satisfies the limits of the GRAZING calculation limits. (i.e. reaction occurs below the nuclear rainbow and available excitation energy is small and effect from attractive nuclear force is small.) This result is another indication of validity of the pre-evaporation fragment calculation.

## 5.5. PRE-EVAPORATION FRAGMENT AND EXCITATION ENERGY DETERMINATION

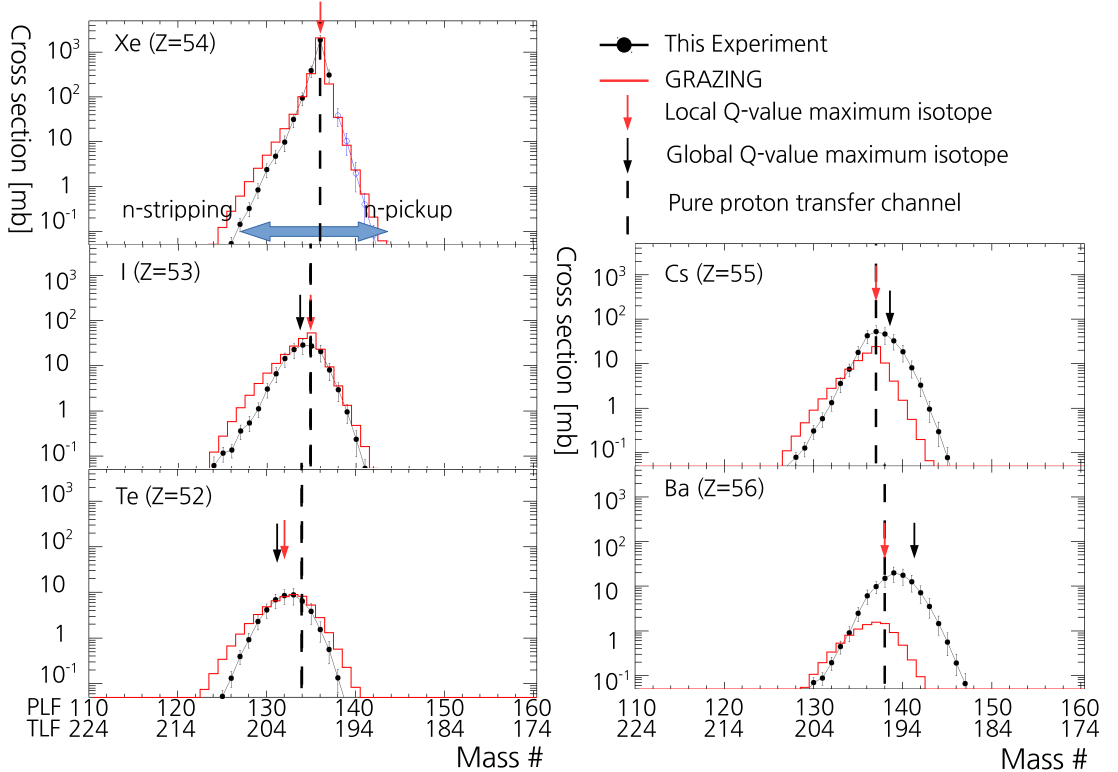


Figure 5.27 The cross section of pre-evaporation fragments before secondary processm with limit range of  $E_{total}^* < 100$  MeV. The (top left) Xe ( $Z = 54$ ), (middle left) I ( $Z = 53$ ), (middle right) Cs ( $Z = 55$ ), (bottom left) Te ( $Z = 52$ ), (bottom right) Ba ( $Z = 56$ ) isotopes are presented. Experimental results are indicated as an black solid circle. The theoretical calculation of GRAZING are indicated as and red solid line. The black vertical dashed line indicates the pure proton transfer channel. The isotope with local Q-value maximum are indicated as red arrows, and global Q-value maximum ( $N/Z$  equilibrium) isotope are indicated as black arrows.

## 5.5. PRE-EVAPORATION FRAGMENT AND EXCITATION ENERGY DETERMINATION

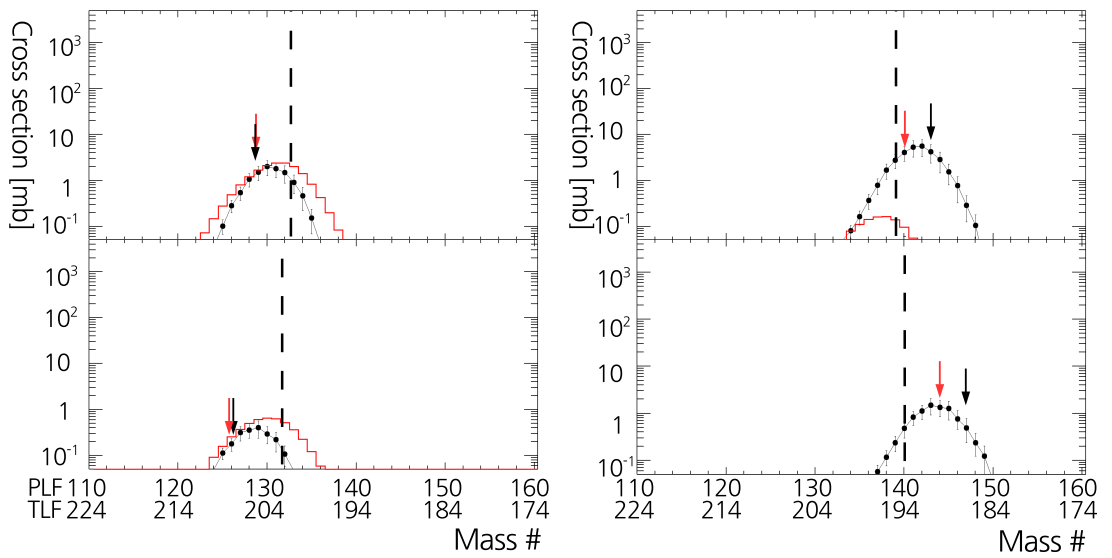


Figure 5.28 The cross section of pre-evaporation fragments before secondary process with limit range of  $E_{total}^* < 100$  MeV. The (top left) Sb ( $Z = 51$ ), (top right) La ( $Z = 57$ ), (bottom left) Sn ( $Z = 50$ ), (bottom right) Ce ( $Z = 58$ ) isotopes are presented . The figure follows the same notation as figure 5.27.

## 5.6. EVOLUTION OF REACTION AS FUNCTION OF $E_{TOTAL}^*$

### 5.6 Evolution of Reaction as Function of $E_{total}^*$

The change of the cross section as function of  $E_{total}^*$  was investigated from the result of the iteration method. (See figure 5.29)

The overall cross section decreased as the excitation energy increased. The low excitation energy lies near the pure proton transfer channels and maximum Q<sub>gg</sub>-value isotope. The cross section is larger in proton pickup channels, and neutron stripping channels in Xe channels. As the excitation energy gets higher, mean isotope position moves towards N/Z equilibrium isotope.

For more clear and organized view of this cross section, the moment study of this distribution (mean, width of distribution) was carried out and presented in the following subsections.

#### 5.6.1 $\langle M \rangle$ , $\langle Z \rangle$ and $\langle N \rangle$ of the distribution

The mean position of the atomic number, neutron distributions as function of  $E_{TOT}^*$  were deduced in the limit of  $E_{TOT}^* < 200$  MeV (See figure 5.31, and 5.32).

The mean position was determined by fitting with Gaussian distribution to avoid the effect from the edge of the distribution. The error was determined from the fitting.

Both atomic number and the neutron number (after the neutron evaporation correction) were constant near the entrance channel over different  $E_{TOT}^*$  regions. The constant atomic number and neutron number were observed in other experiments with similar beam target combination. (e.g. Atomic number distribution of  $^{136}\text{Xe}$  +  $^{209}\text{Bi}$  [55], mass distribution of  $^{136}\text{Xe}$  +  $^{208}\text{Pb}$ [42] see figure 1.10, 1.8)

This constant mean atomic number over excitation energy is also observed in the

## 5.6. EVOLUTION OF REACTION AS FUNCTION OF $E_{TOTAL}^*$

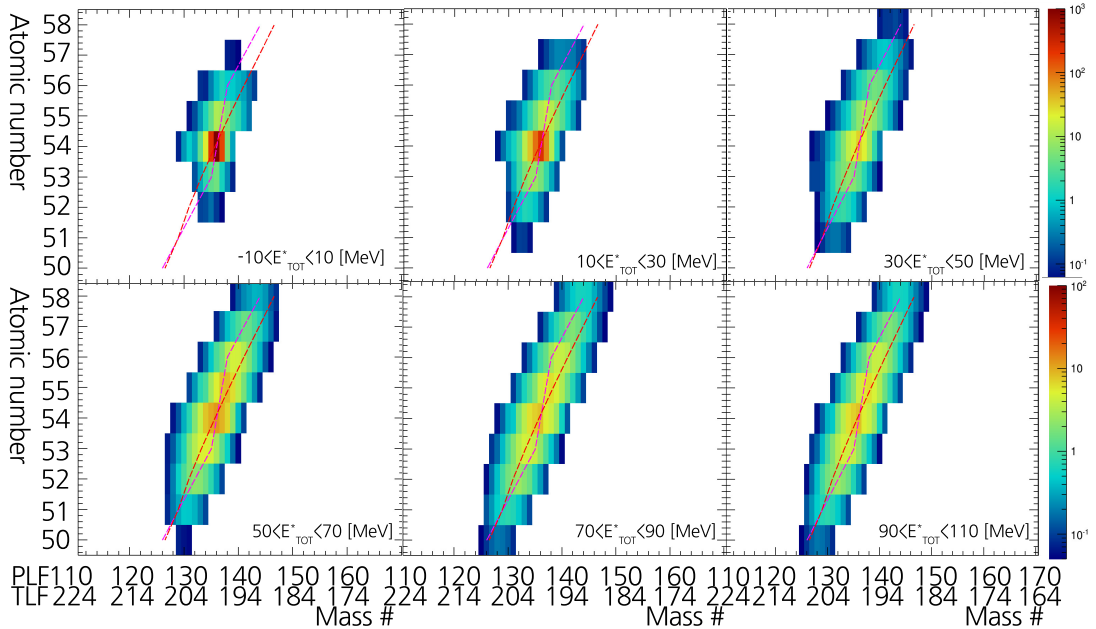


Figure 5.29 The two dimensional pre-evaporation fragment cross section of atomic number versus mass number for different total excitation energy range ( $E_{total}^*$ ). (top left)  $-10 < E_{total}^* < 10$ , (top middle)  $10 < E_{total}^* < 30$ , (top right)  $30 < E_{total}^* < 50$ , (bottom left)  $50 < E_{total}^* < 70$ , (top middle)  $70 < E_{total}^* < 90$ , and (top right)  $90 < E_{total}^* < 110$ . The range of cross section in the top row was matched from  $0.05 < \sigma < 1000$  mb, while the bottom row the range of cross section was matched from  $0.05 < \sigma < 100$  mb. The red dashed line indicates N/Z equilibrium mass and magenta dashed line indicates isotope with largest Q-value (Mgg)

## 5.6. EVOLUTION OF REACTION AS FUNCTION OF $E_{TOTAL}^*$

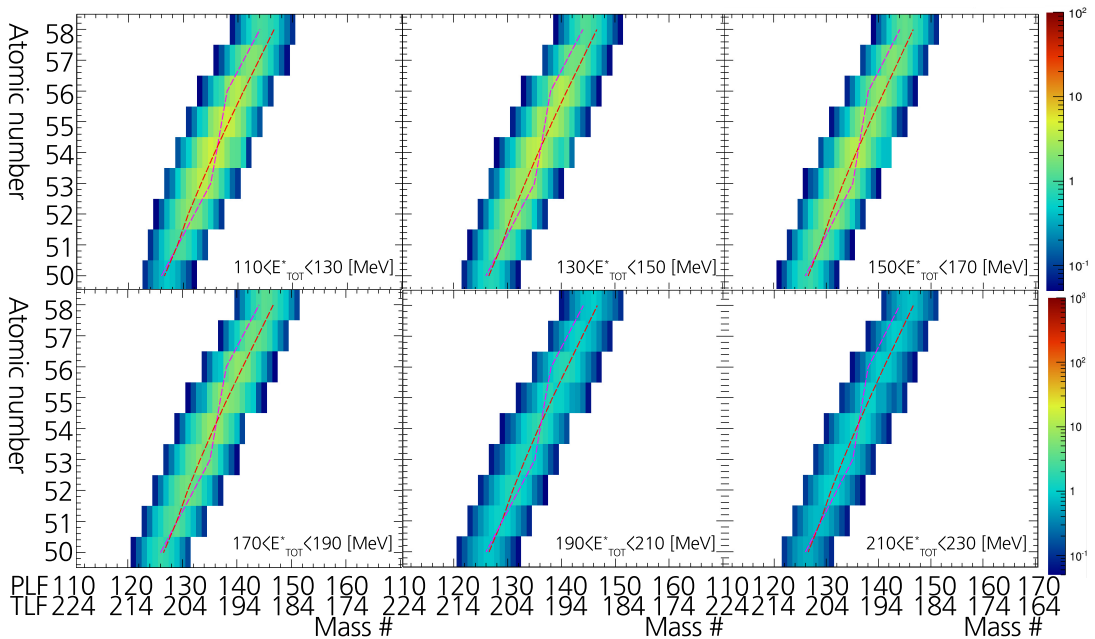


Figure 5.30 The two dimensional pre-evaporation fragment cross section of atomic number versus mass number for different total excitation energy range ( $E_{total}^*$ ). (top left)  $110 < E_{total}^* < 130$ , (top middle)  $130 < E_{total}^* < 150$ , (top right)  $150 < E_{total}^* < 170$ , (bottom left)  $170 < E_{total}^* < 190$ , (top middle)  $190 < E_{total}^* < 210$ , and (top right)  $210 < E_{total}^* < 230$ . The the range of cross section was matched from  $0.05 < \sigma < 100$  mb. The red dashed line indicates N/Z equilibrium mass and magenta dashed line indicates isotope with largest Q-value (Mgg)

### 5.6. EVOLUTION OF REACTION AS FUNCTION OF $E_{TOTAL}^*$

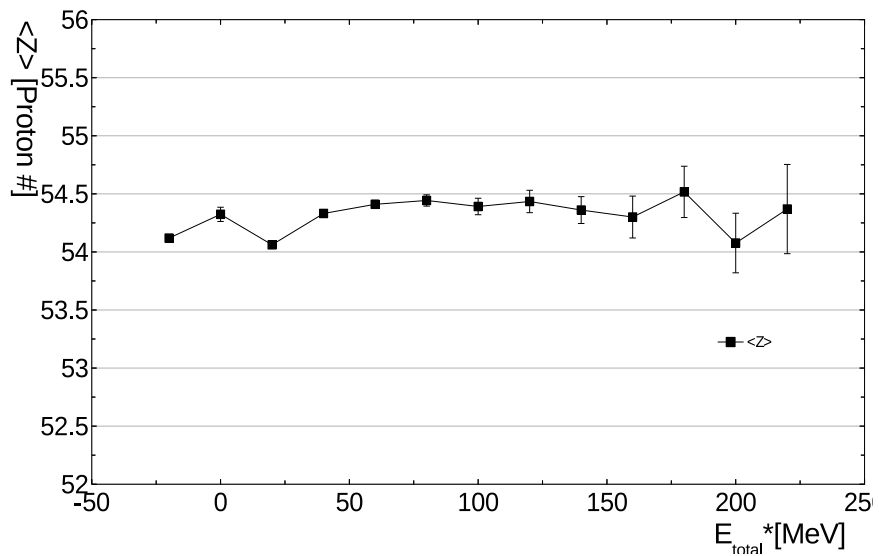


Figure 5.31 The mean of atomic number distribution as function of  $E_{TOT}^*$  with 20 MeV bin.

### 5.6. EVOLUTION OF REACTION AS FUNCTION OF $E_{TOTAL}^*$

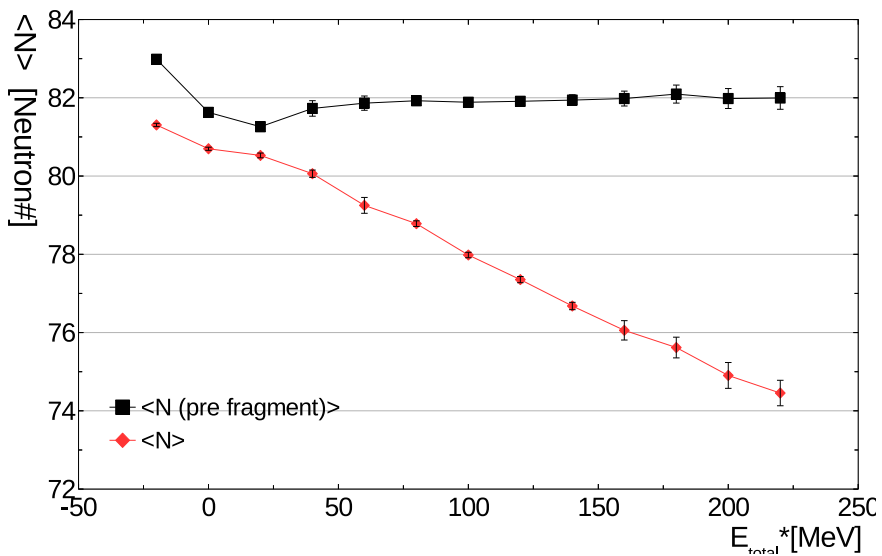


Figure 5.32 The mean of neutron number distribution as function of  $E_{TOTAL}^*$  with 20 MeV bin.

## 5.6. EVOLUTION OF REACTION AS FUNCTION OF $E_{TOT}^*$

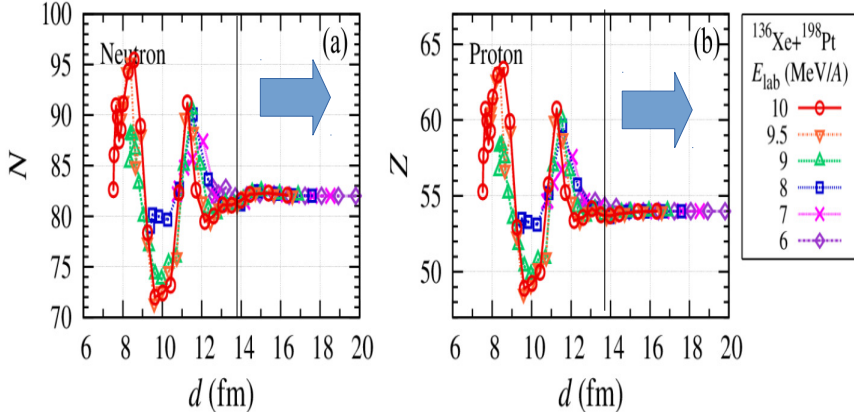


Figure 5.33 The TDHF calculated mean of (left) neutron number distribution (right) proton number distribution as function of closest distance approach. The black dashed line indicates the closest distance approach corresponds to the  $E_{TOT}^* < 200 \text{ MeV}$ .

TDHF calculation within the limit of this experiment. (See figure 5.33) This result can be explained by similar N/Z ratio between beam and target. The similar N/Z ratio of projectile and target makes net transfer of the both proton and neutron to zero.

### 5.6.2 $\langle M(E_{TOT}^*, Z) \rangle$ distance from N/Z equilibrium mass

The distance from the N/Z equilibration mass was surveyed for different atomic number as function of the excitation energy ( $\langle M(E_{TOT}^*) \rangle - \langle M(N/Z - equilibrium) \rangle$ ). (See figure 5.34) The mean of the mass distribution in the low excitation energy were close to the pure proton transfer channels. And as the excitation energy increases the mean mass distribution converged towards N/Z equi-

## 5.6. EVOLUTION OF REACTION AS FUNCTION OF $E_{TOTAL}^*$

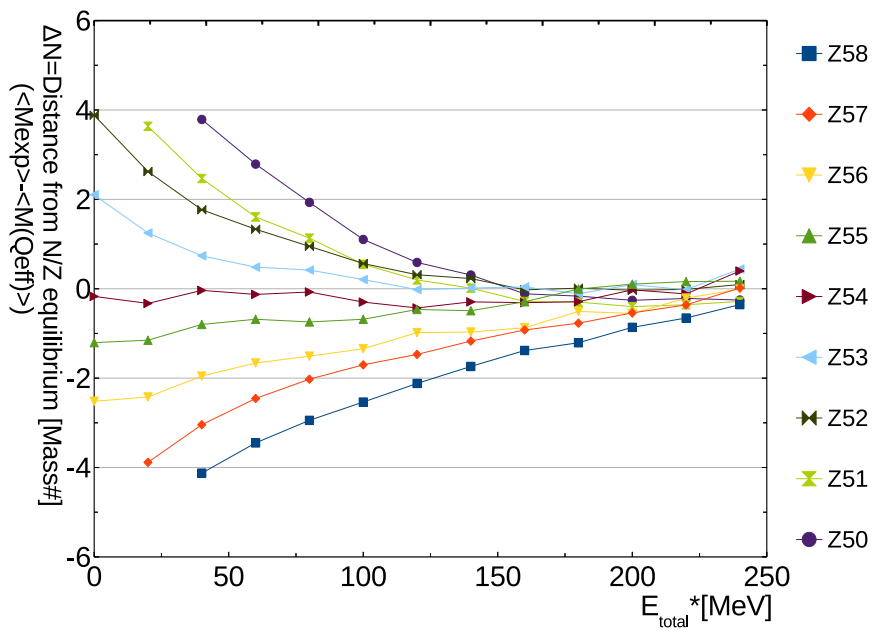


Figure 5.34 The distance of mean of mass distribution of different isotopic channels from N/Z equilibrium mass as function of  $E_{TOT}^*$ .

## *5.6. EVOLUTION OF REACTION AS FUNCTION OF $E_{TOTAL}^*$*

librium irrespective to the number of transferred protons. The clear convergence demonstrates the N/Z equilibrium is the driving force of the direction of the nucleon transfer. The difference between proton pickup and proton stripping channels presented so far, such as the peak position of the cross section (section 5.2), or the mean TKEL distribution (section 5.4) can be understood by the tendency towards N/Z equilibrium and secondary process.

The proton pickup accompanied by neutron pickup and massive neutron evaporation causes the cross section peak mass position close to the pure proton transfer channel. While the proton stripping accompanied by neutron stripping and neutron evaporation presents the cross section peak mass position far from the pure proton transfer channel.

The close inspection of the curve towards the N/Z equilibrium, the proton pickup channels and proton stripping channels shows different behavior as the number of transferred proton increases. The proton stripping channels as the number of transferred proton increases, the curvature increased. Thus they arrive to N/Z equilibrium at the similar excitation energy.

However, in the proton pickup channels the curvature didn't increase as the number of transferred protons. Thus the arrival excitation energy at the N/Z equilibrium mass was higher as the number of transferred proton increased.

This behavior can be speculated qualitatively by picture of potential energy surface calculated by effective Q-value. (See section 2.1.1 and figure 5.35) The proton stripping channels, the effective Q-value from the pure proton transfer channel to the N/Z equilibrium channel (global Q-value maximum) increases monotonically. While the proton pickup channels, the effective Q-value from pure proton transfer channels

### 5.6. EVOLUTION OF REACTION AS FUNCTION OF $E_{TOTAL}^*$

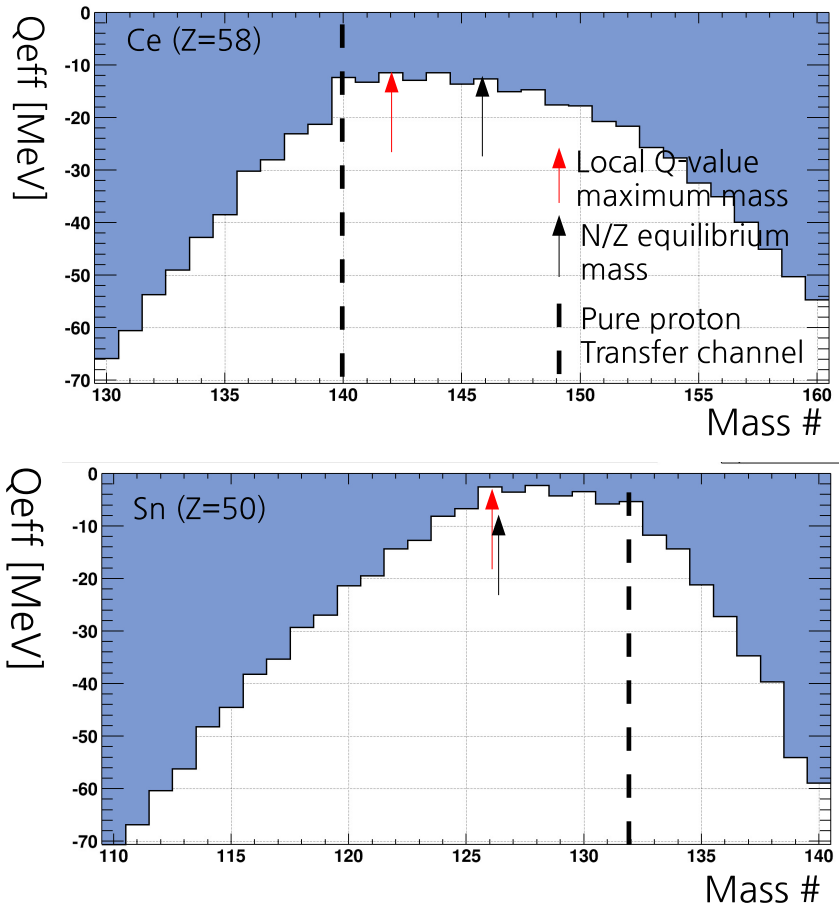


Figure 5.35 The effective Q-value distribution of (top) Ce ( $Z = 58$ ) , (bottom) Sn ( $Z = 50$ ). The vertical dashed line indicates the pure proton transfer channel, black arrow indicates the mass of global maximum effective Q-value, red arrow indicates the mass of local maximum of effective Q-value.

## 5.6. EVOLUTION OF REACTION AS FUNCTION OF $E_{TOTAL}^*$

to the N/Z equilibrium channel increased till local Q-value maximum and decreased to the N/Z equilibrium channel. And the curvature of the effective Q-value was larger than the proton stripping channels. This smaller curvature and unmatched local and global Q-value maximum in the proton pickup side, causes driving force towards the N/Z equilibrium smaller than the proton stripping side.

### 5.6.3 Variance of proton, neutron distribution

From the statistical model point of view, the variance of the atomic number and neutron number ( $\sigma_Z^2$  and  $\sigma_M^2$ ) distribution can be interpreted as the number of nucleon exchange. This is valid in the limit of the Poisson distribution where the probability of the particle exchange is small and the number of trial is large. The proton and neutron variance of experimental distribution are presented in figure 5.36. The proton, neutron and mass variance were increased exponentially as the excitation energy increased. The variance of atomic number distributions was always smaller than the neutron variance showing that the mobility of the proton is smaller than the mobility of the neutrons.

The proton variance was compared to the vast number of experiments. (See figure 5.37) For matching the different system energy of references, the normalized total kinetic energy over angular momentum at the grazing collision was used [60].

$$TKE/l_g + C(l_g)[MeV/\hbar] \quad (5.4)$$

$$C(l_g) = 1.393E_{CM}/l_g | 0.651[MeV/\hbar] \quad (5.5)$$

where  $E_{CM}$  = center of mass energy and  $l_g$  is the grazing angular moment of this experiment.

## 5.6. EVOLUTION OF REACTION AS FUNCTION OF $E_{TOTAL}^*$

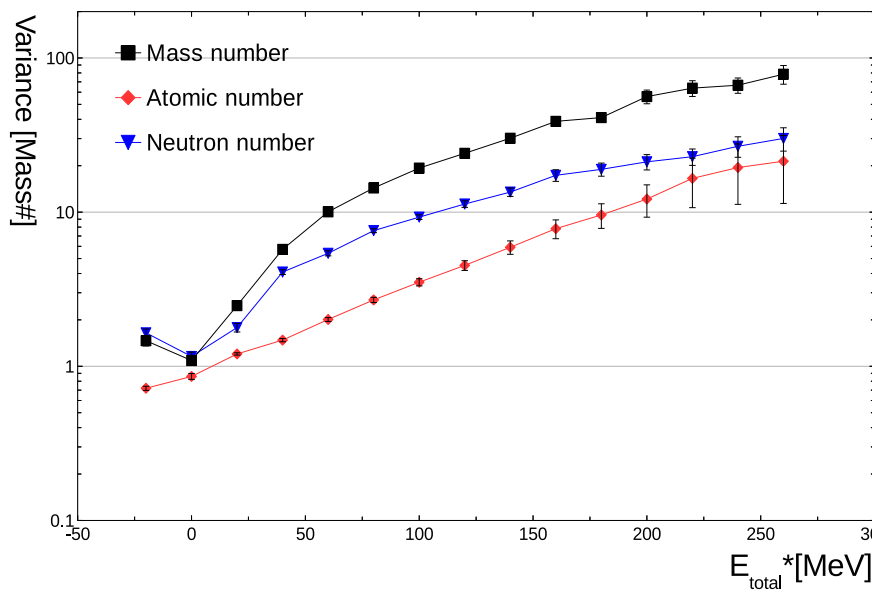


Figure 5.36 The variance of (red diamond) atomic number, (black square) mass, (blue triangle) neutron number as function of excitation energy.

## 5.6. EVOLUTION OF REACTION AS FUNCTION OF $E_{TOTAL}^*$

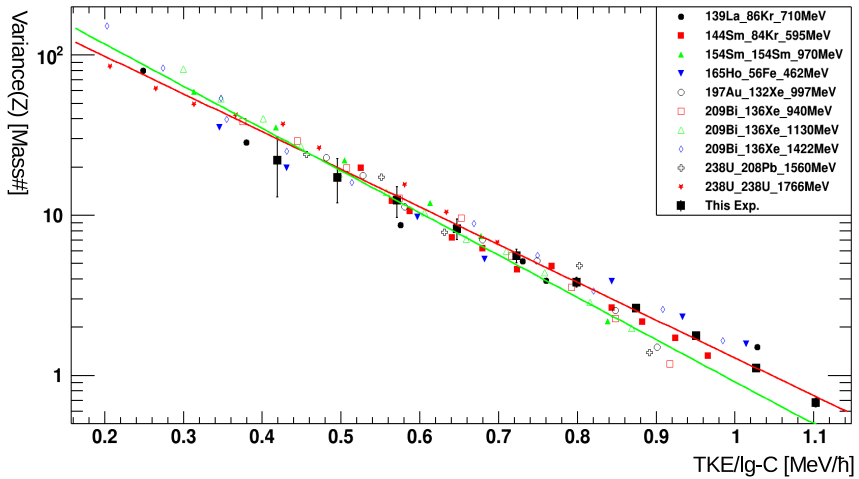


Figure 5.37 The atomic number variance as function of normalized total kinetic energy over grazing angular momentum compared with vast number of references[60] and reference therein. The green line indicates the exponential fitting of different references, while the red line indicates the exponential function fitting result of this experiment.

## 5.6. EVOLUTION OF REACTION AS FUNCTION OF $E_{TOTAL}^*$

The grazing angular momentum ( $l_g$ ) was determined as  $460.81 \hbar$  by quarter point angle of elastic scattering data (see equation 3.24, and 3.25 in reference [1]). The result presented good agreement between this experiment and the references. This indicates similar mobility (or in terms of statistical models diffusion coefficient) of proton for different systems. [60]

The neutron width compared with the references will be surveyed in the future studies. But the result from the following discussion (the mass, proton number variance) indicates there will be a disagreement with the references due to the shell closure in  $^{136}\text{Xe}$ .

The ratio of mass number variance over atomic number variance was deduced. (See figure 5.38) Adopting the statistical point of view the ratio between n,p flow between PLF and TLF can be investigated by  $\sigma^2(A)/\sigma^2(Z)$  of the distribution. And the criteria whether the nucleon flow between PLF and TLF is neutron rich or proton rich was set as  $(A/Z)^2$ . (i.e. if the  $\sigma^2(A)/\sigma^2(Z) > (A/Z)^2$  then the flow is determined as neutron rich on the other hand, if  $\sigma^2(A)/\sigma^2(Z) < (A/Z)^2$  was determined as proton rich.) This criteria is following from the one used in the reference [15]. The  $(A/Z)^2$  was originally set as the criteria deciding whether the N/Z equilibrium is reached (see equation 35 ~ 41 in reference [38]). Thus it can be considered as a nominal value of p, n exchange ratio.

In the small excitation energy regions the ratio is close to  $1.5 \sim 2$ . And as the excitation energy increased from 0 to 100 MeV, the variance ratio was also increased and it was saturated with the value close to the  $(A/Z)^2$  of compound system. The small ratio in the low excitation energy indicates the flow of nucleon transfer was proton rich. The proton rich flow is not common between heavy systems ( $A > 100$ ),

## 5.6. EVOLUTION OF REACTION AS FUNCTION OF $E_{TOTAL}^*$

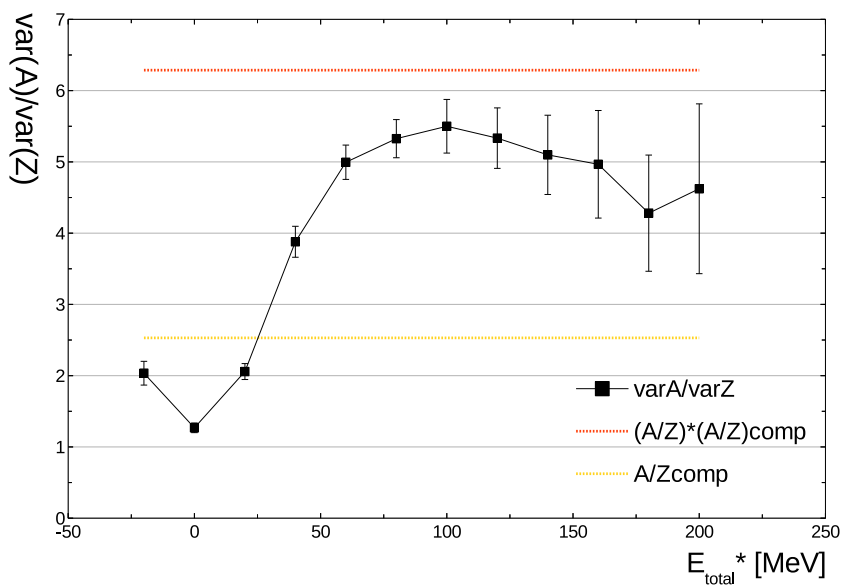


Figure 5.38 The ratio variance of mass number over atomic number as function of excitation energy indicated as a black square. The yellow dashed line indicates  $A/Z$ , and the red dashed line indicates  $(A/Z)^2$  of compound system.

## 5.6. EVOLUTION OF REACTION AS FUNCTION OF $E_{TOTAL}^*$

since the neutron is easier to be transferred than the proton due to the Coulomb interactions, and the larger radius of neutron in the nucleus. This neutron rich flow could be seen in many systems (e.g.  $^{129}\text{Xe} + ^{116,124}\text{Sn}$  [74] ).

But entrance nuclei close to the neutron magic number like this experiment ( $^{136}\text{Xe}_{82}$ ) present proton rich flow. This shell closure effect is clearly observed in comparison of  $^{154}\text{Sm} + ^{154}\text{Sm}$  and  $^{144}\text{Sm} + ^{144}\text{Sm}$  system.

The neutron magic nuclei  $^{144}\text{Sm}$  system presents proton rich flow while the  $^{154}\text{Sm}$  system presents the neutron rich flow at the low excitation energy. ([63, 72]) This magic number nuclei has more tightly bound neutrons with low level density in the neutron particle states. Also the neutron radius is smaller than the non-magic nuclei. Thus the neutron transfer probability is hindered than the normal (non-magic number) nuclides.

The saturation in the high excitation energy indicates that the ratio number of proton and neutrons transferred were fixed meaning that the nucleon transfer was dominated by the N/Z equilibrium. Since the distribution at N/Z equilibrium is aligned in N/Z equilibrium line following potential energy surface essentially parallel to the UCD prediction. Thus linear relation between A and Z close to A/Z could be seen.[15]

Since the saturation is originated from the N/Z equilibrium, this is commonly observed irrespective to the entrance channels and system energies.(e.g.  $^{56}\text{Fe} + ^{56}\text{Fe}$ ,  $^{65}\text{Ho}$ ,  $^{209}\text{Bi}$ ,  $^{238}\text{U}$  systems [73],  $^{129}\text{Xe} + ^{116,124}\text{Sn}$ , [74]) This is related to the correlation between proton and neutron transfer described in the next section.

## 5.6. EVOLUTION OF REACTION AS FUNCTION OF $E_{TOTAL}^*$

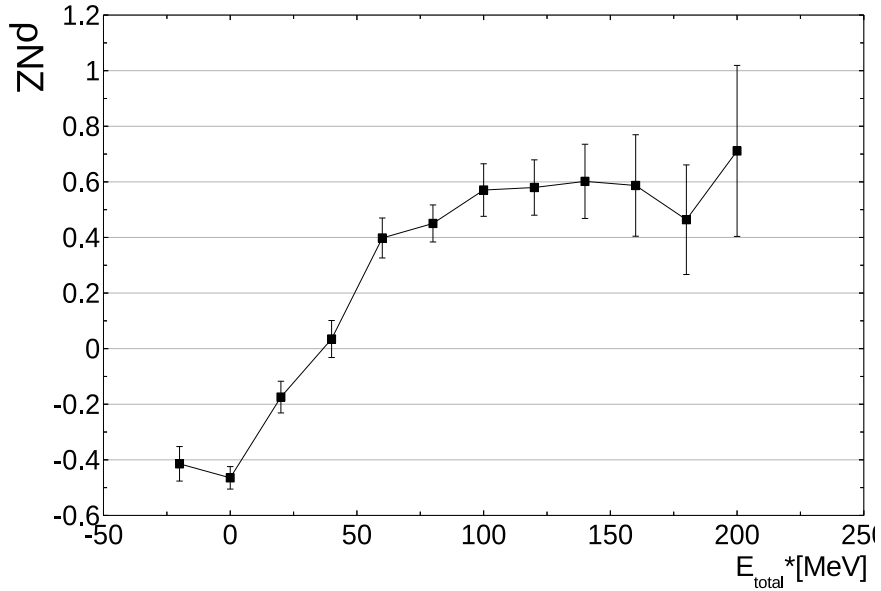


Figure 5.39 The correlation coefficient of neutron and proton variance as function of excitation energy.

### 5.6.4 Correlation of proton and neutron transfer

The (first order) correlation coefficient  $\rho$  of the proton and neutron transfer was calculated by equation 5.6.

$$\sigma_A^2 = \sigma_Z^2 + \sigma_N^2 + 2\rho\sigma_N\sigma_Z \quad (5.6)$$

The evolution of correlation coefficients is presented in the figure 5.39. The saturation of correlation coefficient occurs around 0.6, in the region with excitation energy  $\sim$  100 MeV. This value was less than the energy where the mean mass converges to the N/Z equilibrium. The saturation of correlation coefficient at the high excitation was commonly observed in many heavy ion MNT reactions. (e.g.  $^{132}\text{Xe} + ^{197}\text{Au}$  [68],  $^{56}\text{Fe}$

### 5.7. TLF CROSS SECTION AND FEASIBILITY OF N-RICH NUCLIDES

+  $^{136}\text{Xe}$ [74], and  $^{154}\text{Sm} + ^{154}\text{Sm}$  and  $^{144}\text{Sm} + ^{144}\text{Sm}$  [63, 72]) This was caused by the N/Z equilibrium makes the mass distribution align along the N/Z equilibrium line, even though the proton and neutron are not fundamentally correlated [15]. (Even the the proton and neutron was correlated in the order of nucleon pairing energy ( $\sim 1$  MeV order) the system energy was much higher this could not be observed in the highly damped regions)

The negative or anti-correlation in the low excitation energy of  $E_{total}^* < 20$  MeV could be observed. This means that at the low excitation energies the proton and the neutrons were transferred to the opposite directions, in our case proton was picked up while the neutrons were stripped. This anti-correlation was observed only few cases in previous references. (e.g. See reference  $^{56}\text{Fe} + ^{56}\text{Fe}$ ,  $^{165}\text{Ho}$ ,  $^{209}\text{Bi}$ , and  $^{238}\text{U}$  [73]) The reason why this anti-correlation was observed in only few experiments are not clear at this moment [15]. This clear difference are presumed to be from the Q-value dependence in the Q.E. [73]. This proton, neutron transfer to the opposite direction cannot be explained by models using the frictional energy dissipation with classical diffusion equations Langevin, Fokker-Plank [15]. This result supports the microscopic models which use collective motion (GDR, GQR etc.) as the main source of the energy dissipation.

## 5.7 TLF cross section and feasibility of n-rich nuclides

## 5.7. TLF CROSS SECTION AND FEASIBILITY OF N-RICH NUCLIDES

### 5.7.1 TLF cross section after evaporation

The cross sections of TLF were calculated with pre-evaporation fragment information of PLF. The excitation energy was shared by the mass ratio. Due to this property, the TLF takes larger portion of the excitation energy than the PLF. Thus the charged particle evaporation ( $p, d, \alpha$ ) cannot be ignored in the TLF.

The PACE4 calculation which accounts  $p, d, \alpha$  was carried out. The most significant channels after evaporation which is  $0p$  ( $n$  evaporation),  $1p$  ( $p$ , and  $d + n$  evaporation) , and  $2p$  ( $\alpha$  or two independent  $p,d + n$  evaporation) channels were accounted which consists more than 85% of total reactions. (See figure 5.20 ,and 5.21)

The event-by-event estimation of excitation energy and pre-evaporation fragment carried out from iteration method, was used for number of evaporation and the ratio of different charge evaporated channels was weighted. The fission was also accounted but the portion was very small in the PACE4 calculation, this was also pointed out in the recent study [23].

Using this method the  $4p$  ( $Sn \leftrightarrow Pb$ ), and  $3p$  ( $Sb \leftrightarrow Tl$ ) stripping channel was underestimated due to the mis-account of  $6p$  and  $5p$  stripping channels. And the acceptance and mis-account of charged particle emission in PLF in excitation energy higher than 200 MeV also cause underestimation. Thus the two dimensional cross section (mass number vs atomic number) of limited range of excitation energy less than 200 MeV was presented. (See figure 5.40) And the two dimensional cross section with out limit, which can be accepted as a lower limit is also shown in figure 5.41. The cross section in the neutron deficient side was enhanced with out excitation energy limit while there was no difference in the neutron rich side. This

## 5.7. TLF CROSS SECTION AND FEASIBILITY OF N-RICH NUCLIDES

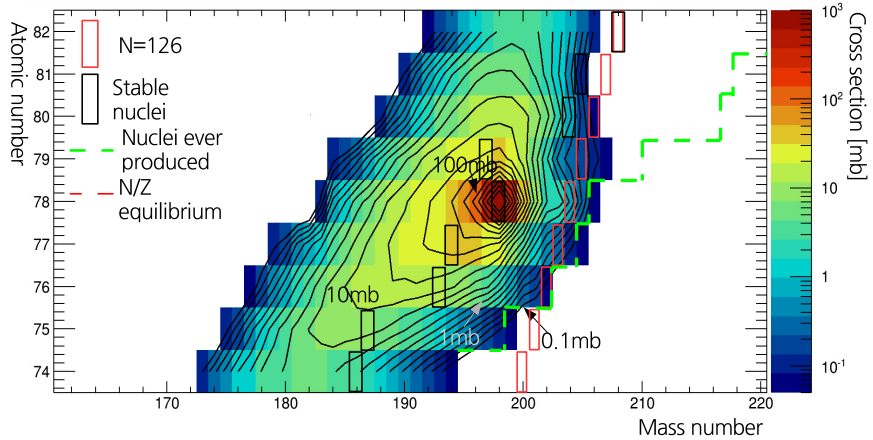


Figure 5.40 The two dimensional TLF cross section of atomic number versus mass number with limit of  $E_{total}^* < 200$  MeV. The range of cross section was matched from  $0.05 < \sigma < 1000$  mb.

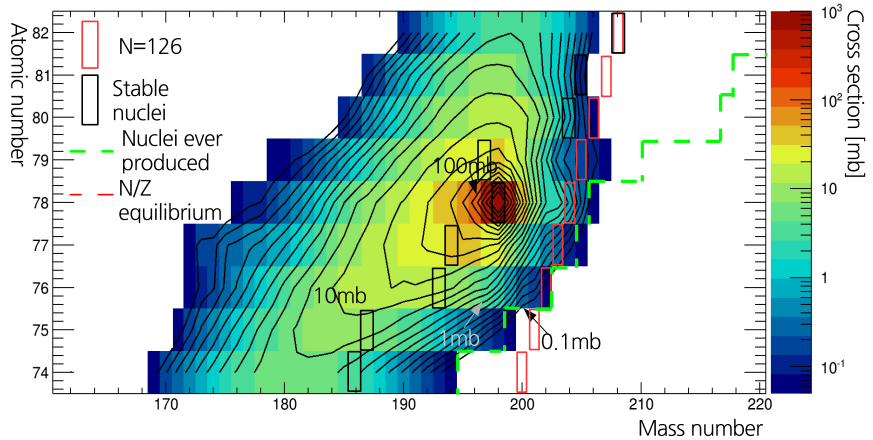


Figure 5.41 The two dimensional TLF cross section of atomic number versus mass number with no limit of  $E_{total}^*$ . The range of cross section was matched from  $0.05 < \sigma < 1000$  mb.

## 5.7. TLF CROSS SECTION AND FEASIBILITY OF N-RICH NUCLIDES

is due to the different regions of excitation energy contributes to each channels by N/Z equilibrium and secondary process after reaction. (See section 5.7.5 for more detailed description)

The one dimensional cross section of 4p stripping  $\sim$  4p pickup channel with no excitation energy limit is presented in figure 5.42, 5.43 for better comparison with the theory.

The same consideration of uncertainty was carried out from pre-evaporation fragment error estimation with additional uncertainty from using another PACE4 calculation was included with the same method. The cross section error of the Os isotopes are presented as a band in figure 5.44. The significant error in the neutron rich side came from conversion factor detection efficiency of VAMOS . And for the neutron deficient regions the uncertainty from secondary process calculation was also becomes significant effect. (e.g. The typical error was  $\sim 30\%$  in the neutron rich side (e.g.  $\frac{\Delta\sigma}{\sigma}(^{202}\text{Os}) = + 27.5 - 28.8\%$ ) and  $\sim 50\%$  neutron deficient side (e.g.  $\frac{\Delta\sigma}{\sigma}(^{180}\text{Os}) = + 54.9 - 52.3\%$ ).)

This was due to the uncertainty from PACE4 calculation, fitting procedure, and "integerization" in the mass determination from PLF (after evaporation) to pre-evaporation fragment to TLF (after evaporation). And especially the sudden changes in the evaporation curve from PACE4 calculation at the low excitation energies were not well reproduced by fitting.

In the neutron rich side the most significant error was from conversion factor error which alone results more than 20% error. On the other hand neutron deficient side, the error from neutron evaporation calculation with acceptance correction had large effect . Since the heavily damped event have large influence from neutron

## 5.7. TLF CROSS SECTION AND FEASIBILITY OF N-RICH NUCLIDES

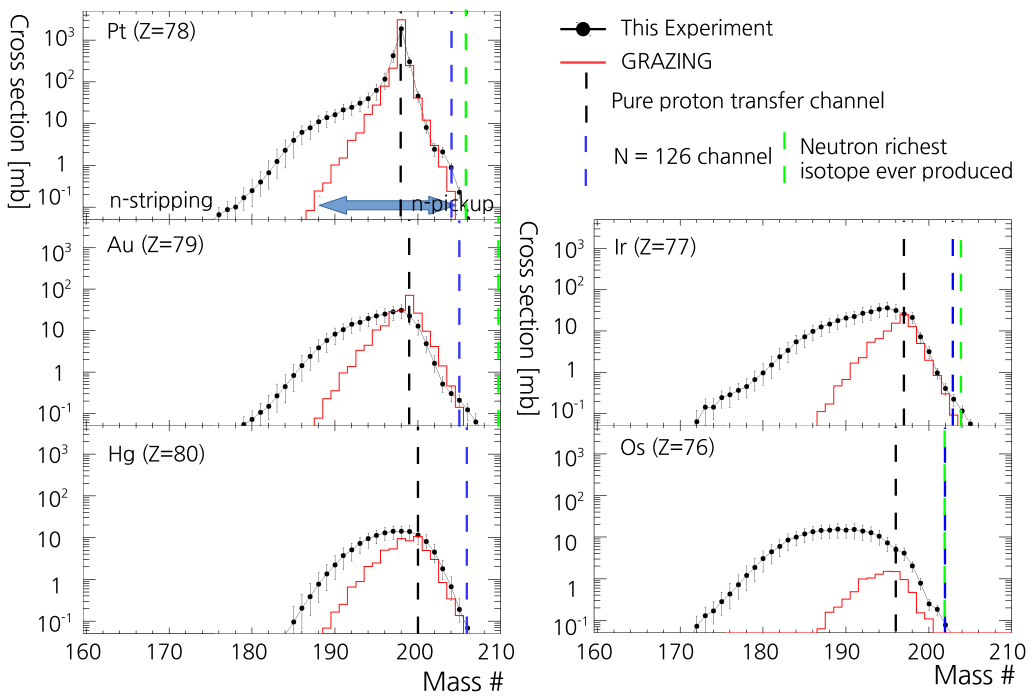


Figure 5.42 The one dimensional cross section of TLF of (top left) Pt (0p), (middle left) Au (-1p), (middle right) Ir (+1p), (bottom left) Hg (-2p), and (bottom right) Os (-2p) without cutoff or restoration. The proton transfer channel without neutron transfer are indicated as a black dashed line. The isotope with  $N = 126$  are indicated with blue dashed line. And the most neutron richest isotope ever produced are indicated as a green dashed line.

## 5.7. TLF CROSS SECTION AND FEASIBILITY OF N-RICH NUCLIDES

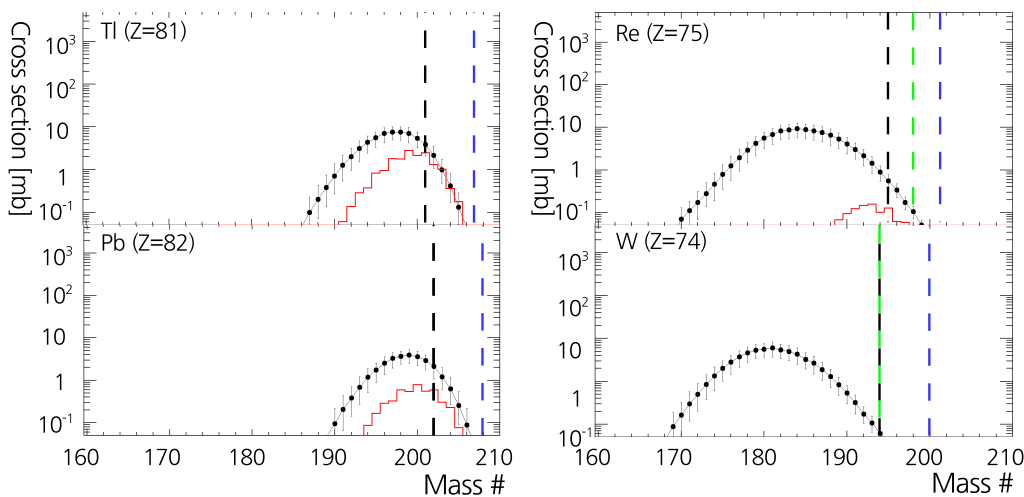


Figure 5.43 The one dimensional cross section of TLF of (top left) Tl ( $-3p$ ), (top right) Re ( $+3p$ ), (bottom left) Pb ( $-4p$ ), and (bottom right) W ( $-4p$ ) without cutoff or restoration. The isotope with  $N=126$  are indicated with blue dashed line. And the most neutron richest isotope ever produced are indicated as a green dashed line.

## 5.7. TLF CROSS SECTION AND FEASIBILITY OF N-RICH NUCLIDES

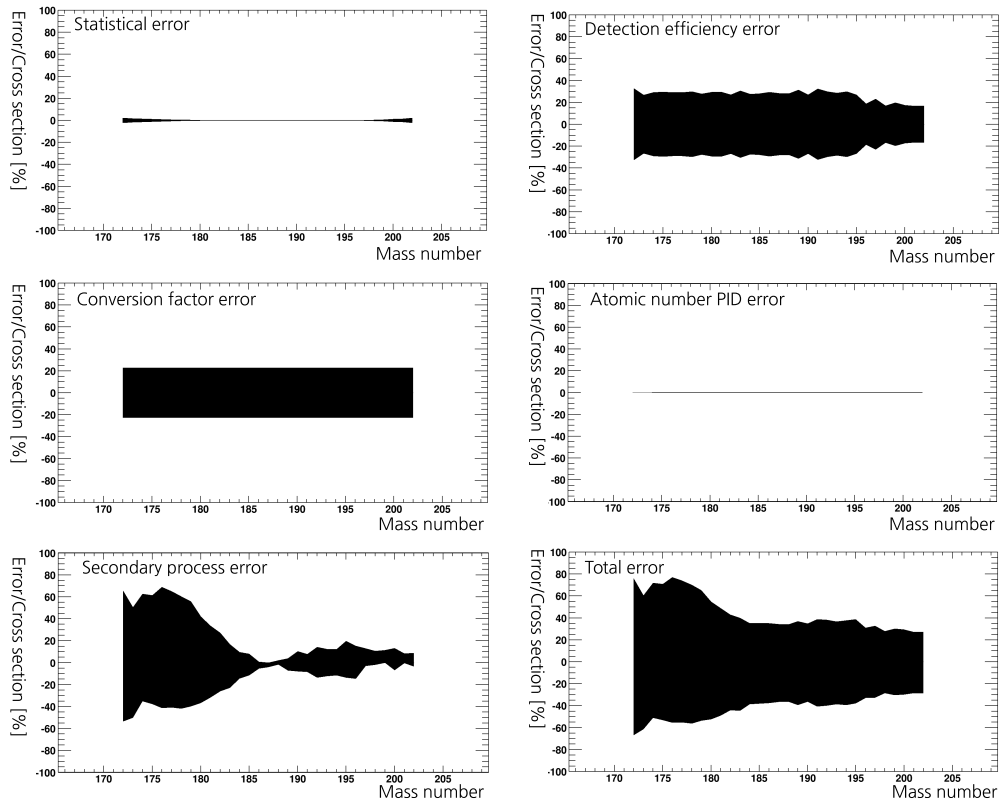


Figure 5.44 The different causes of errors of (top left) statistical, (top right) detection efficiency (middle left) conversion factor, (middle right) atomic number PID, (bottom left) secondary process, and (bottom left) sum of all errors in unit of %.

## 5.7. TLF CROSS SECTION AND FEASIBILITY OF N-RICH NUCLIDES

evaporation close to the acceptance cut off which have large error in the detection efficiency.

### 5.7.2 Evolution of TLF as function of excitation energy

The cross section of TLF was investigated as function of excitation energy. (See figure 5.45 and 5.46)

The proton pickup side and Pt channels exhibited decrease of mean mass position as the function of excitation energy. The most neutron rich side was produced from reaction with low excitation energy. This is due to low neutron evaporation and N/Z-equilibrium that favors neutron pickup channels causing neutron deficient TLF at high excitation energies.

On the other hand, proton stripping channels presents neutron richest side were consists of excitation energy  $>25$  MeV. And as the number of transferred proton increases the excitation energy that forms neutron richest nuclides increased. This was due to N/Z equilibrium which favors neutron stripping channels causing neutron rich TLF and neutron evaporation. This interplay between N/Z-equilibrium neutron evaporation causes different distribution of TLF in proton stripping and proton pickup channels. For example smaller width of isotopic distribution in proton stripping channel.

### 5.7.3 TLF PID confirmation

The confirmation of particle identification of TLF by gamma-ray (work carried out by work of H. S. Jung [122]) in  $^{192,194,196}\text{Os}$ . (See figure 5.47) The  $^{196}\text{Os}$  was selected because it was the neutron richest isotope previously identified with MNT reaction

## 5.7. TLF CROSS SECTION AND FEASIBILITY OF N-RICH NUCLIDES

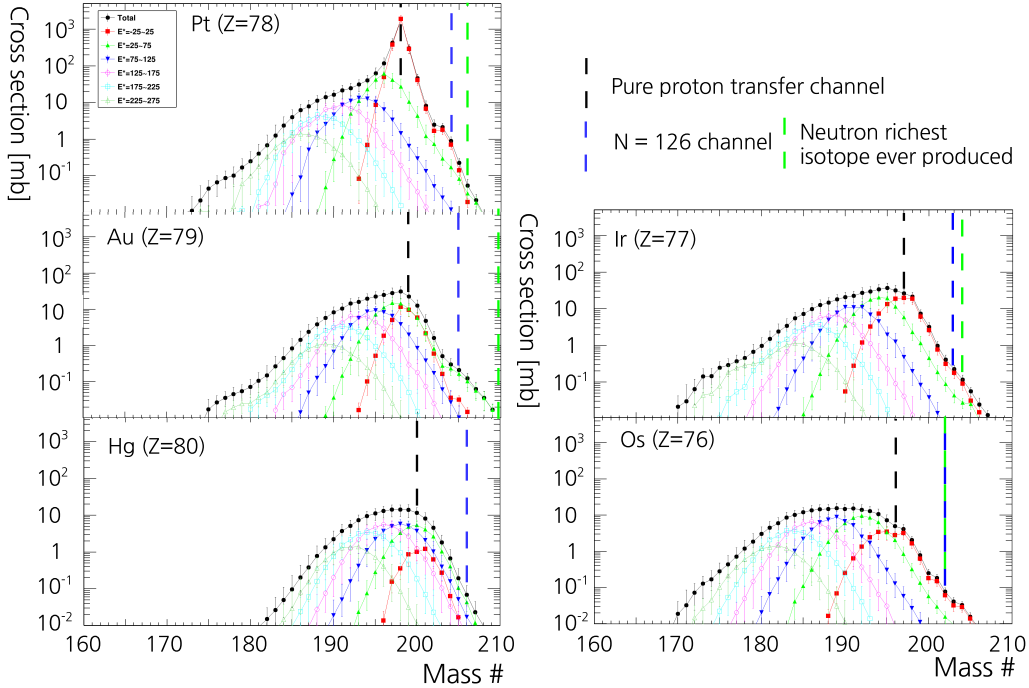


Figure 5.45 The one dimensional cross section of TLF of (top left) Pt (0p), (middle left) Au (-1p), (middle right) Ir (+1p), (bottom left) Hg (-2p), and (bottom right) Os (-2p) without cutoff or restoration. For each figures, cross section with different excitation energy range are indicated with (black solid circle) Sum of all cross section, (red square)  $-25 < E_{total}^* < 25$  (green triangle)  $25 < E_{total}^* < 75$  MeV, (blue inverted triangle)  $75 < E_{total}^* < 125$ , (magenta empty circle)  $125 < E_{total}^* < 175$  MeV, (skyblue empty square)  $175 < E_{total}^* < 225$  MeV, (forest green empty triangle)  $225 < E_{total}^* < 275$  MeV. The proton transfer channel without neutron transfer are indicated as a black dashed line. The isotope with  $N = 126$  are indicated with blue dashed line. And the most neutron richest isotope ever produced are indicated as a green dashed line.

## 5.7. TLF CROSS SECTION AND FEASIBILITY OF N-RICH NUCLIDES

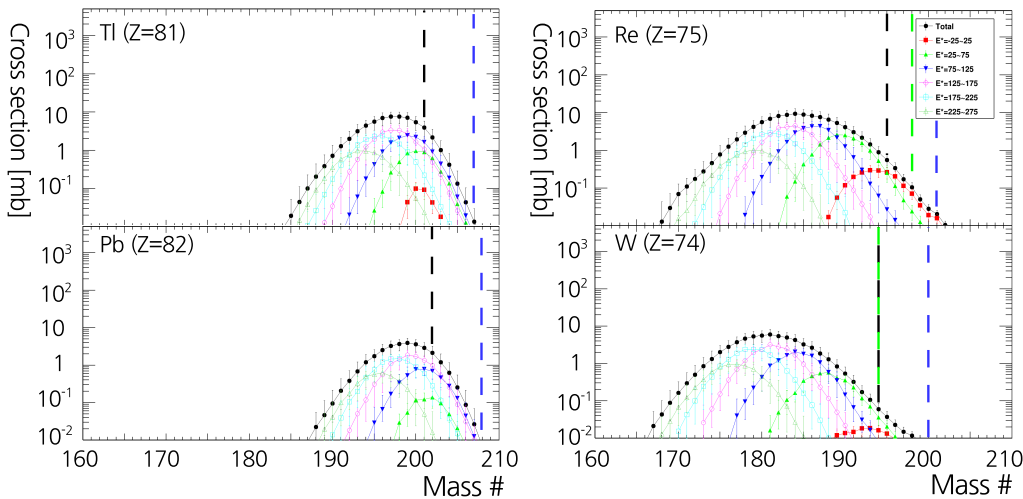


Figure 5.46 The one dimensional cross section of TLF of (top left) Tl ( $-3p$ ), (top right) Re ( $+3p$ ), (bottom left) Pb ( $-4p$ ), and (bottom right) W ( $-4p$ ) without cutoff or restoration. The marker and lines follow same notation as figure 5.45.

## 5.7. TLF CROSS SECTION AND FEASIBILITY OF N-RICH NUCLIDES

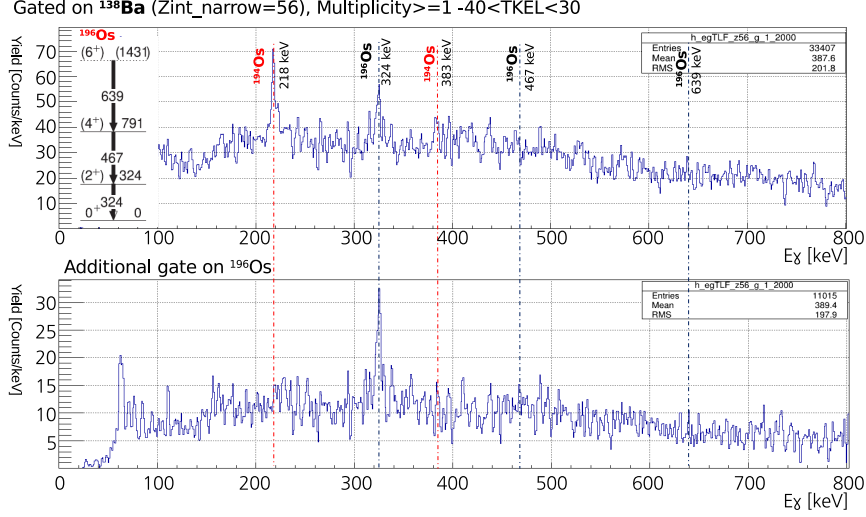


Figure 5.47 (top left) level diagram of  $^{196}\text{Os}$  [123]. (top)  $\gamma$ -ray energy distribution gated on  $^{138}\text{Ba}$  in  $-40 < \text{TKEL} < 30$  MeV. (bottom) additional gate in TLF  $^{196}\text{Os}$ . Blue dotted line indicates  $\gamma$ -ray energy of  $^{196}\text{Os}$ , and red dotted line indicates  $\gamma$ -ray energy from  $^{194}\text{Os}$ .

with well known  $\gamma$ -ray energy. Here, the preliminary results are presented in order to justify the iteration methods and figure out the errors of the method. The  $\gamma$ -ray energy distribution gated with PLF partner  $^{138}\text{Ba}$  showed  $\gamma$ -ray from  $^{196}\text{Os}$  and contamination from  $^{194}\text{Os}$ . But after TLF gate on the  $^{196}\text{Os}$  presented peak only from  $2+ \rightarrow 0+$  transitions of  $^{196}\text{Os}$ .

The events with TKEL with range of  $15 < \text{TKEL} < 40$  MeV were investigated, first PLF  $^{137}\text{Ba}$  with and without  $^{196}\text{Os}$  gate. (See figure 5.48) But  $\gamma$ -ray was not filtered out by  $^{196}\text{Os}$  gate. On the other hand  $\gamma$ -ray could be observed by  $^{195}\text{Os}$  gate. Second, in case of  $^{136}\text{Ba}$  gate with higher TKEL range of  $20 < \text{TKEL} < 60$  MeV

## 5.7. TLF CROSS SECTION AND FEASIBILITY OF N-RICH NUCLIDES

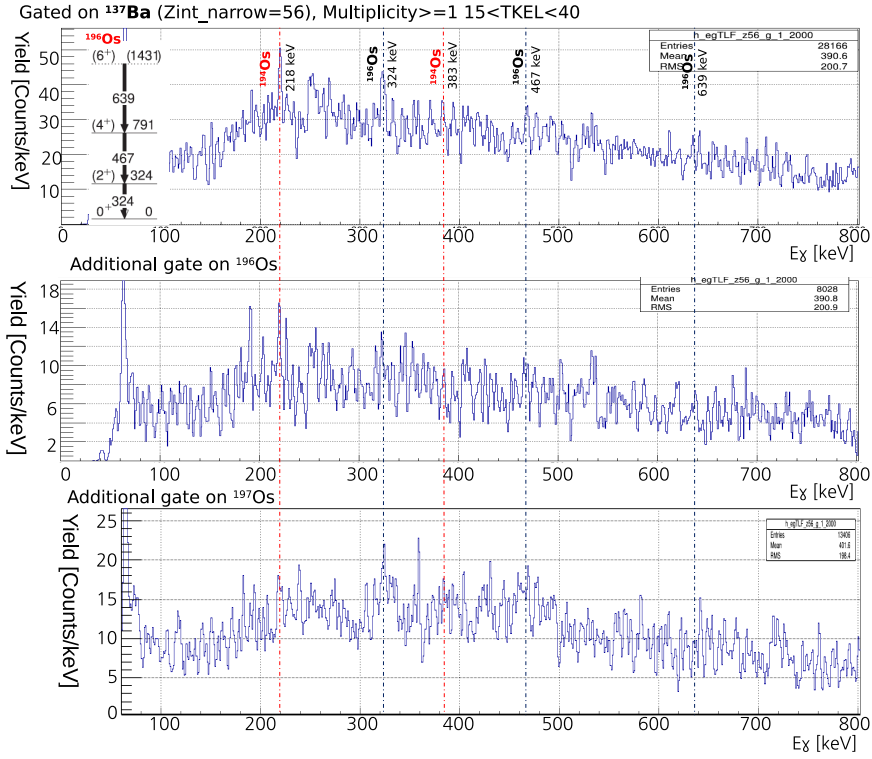


Figure 5.48 (top left) level diagram of  $^{196}\text{Os}$  ||. (top)  $\gamma$ -ray energy distribution gated on  $^{137}\text{Ba}$  in  $15 < \text{TKEL} < 40$  MeV. (middle) Additional gate with TLF  $^{196}\text{Os}$  on the top figure. (bottom) Additional gate with TLF  $^{197}\text{Os}$  on the top figure. Blue dotted line indicates  $\gamma$ -ray energy of  $^{196}\text{Os}$ , and red dotted line indicates  $\gamma$ -ray energy from  $^{194}\text{Os}$ .

## 5.7. TLF CROSS SECTION AND FEASIBILITY OF N-RICH NUCLIDES

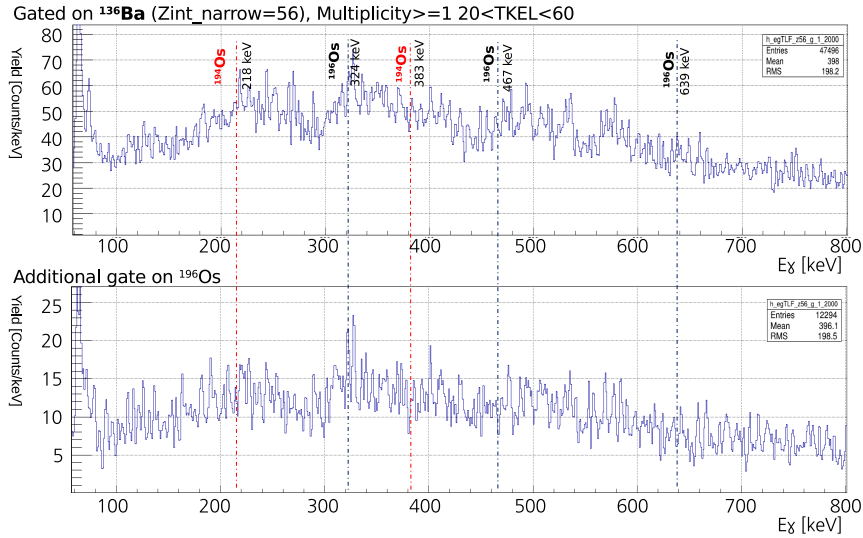


Figure 5.49 (top)  $\gamma$ -ray energy distribution gated on  $^{136}\text{Ba}$  in  $20 < \text{TKEL} < 60$  MeV. (bottom) Additional gate with TLF  $^{196}\text{Os}$  on the top figure. Blue dotted line indicates  $\gamma$ -ray energy of  $^{196}\text{Os}$ , and red dotted line indicates  $\gamma$ -ray energy from  $^{194}\text{Os}$ .

showed  $\gamma$ -rays from  $^{196}\text{Os}$ , after  $^{196}\text{Os}$  gate. (See figure 5.49)

The TKEL higher than was not investigated due to increase of multiplicity caused peak-to-total efficiency much smaller than expected. (Not evaluated yet)

The  $\gamma$ -ray from  $^{194}\text{Os}$  and  $^{192}\text{Os}$  was also observed. (See figure 5.50)

More extensive research is necessary in order to doubly confirm the PID of isotopes with different proton numbers. And  $\gamma$ -rays in more neutron rich side with smaller cross sections.

## 5.7. TLF CROSS SECTION AND FEASIBILITY OF N-RICH NUCLIDES

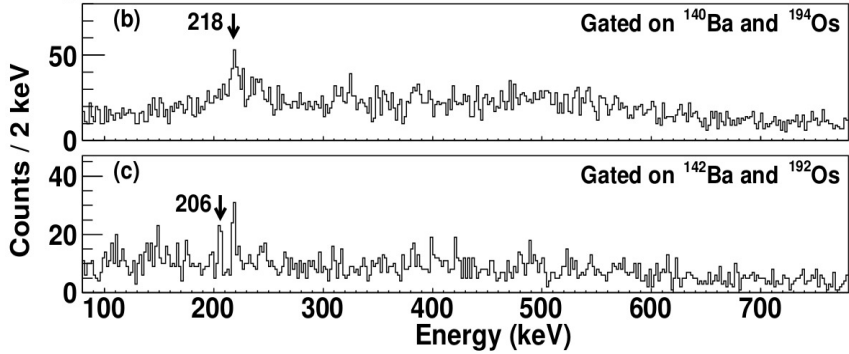


Figure 5.50 (top)  $\gamma$ -ray energy distribution gated on  $^{140}\text{Ba}$  and gated on  $^{194}\text{Os}$ . (bottom)  $\gamma$ -ray energy distribution gated on  $^{142}\text{Ba}$  and gated on  $^{192}\text{Os}$ .

### 5.7.4 Feasibility of producing n-rich TLF

The neutron rich nuclides in proton pickup channels are consists of low energy region of the reaction thus it was less affected by the evaporation process thus two-body figure was well applied. (See figure 5.45 and 5.46) This property ensures the particle identification in the TLF of neutron-rich side even though the cross section was low relative from the peak. Although the  $\gamma$ -ray was not observed in the  $^{202}\text{Os}$  due to the low statistics.

The result showed several factor larger cross sections than the GRAZING calculation result. This was caused from the underestimation of calculation in the proton pickup channels which was discussed in the previous sections. This cross section was  $\sim 6$  orders of magnitude larger than the cross section estimated from the (cold) fragmentation method [42].

The other proton pickup channels of neutron richest channels with cross section larger than 0.05 mb matched with limit of isotope ever reported.

## 5.7. TLF CROSS SECTION AND FEASIBILITY OF N-RICH NUCLIDES

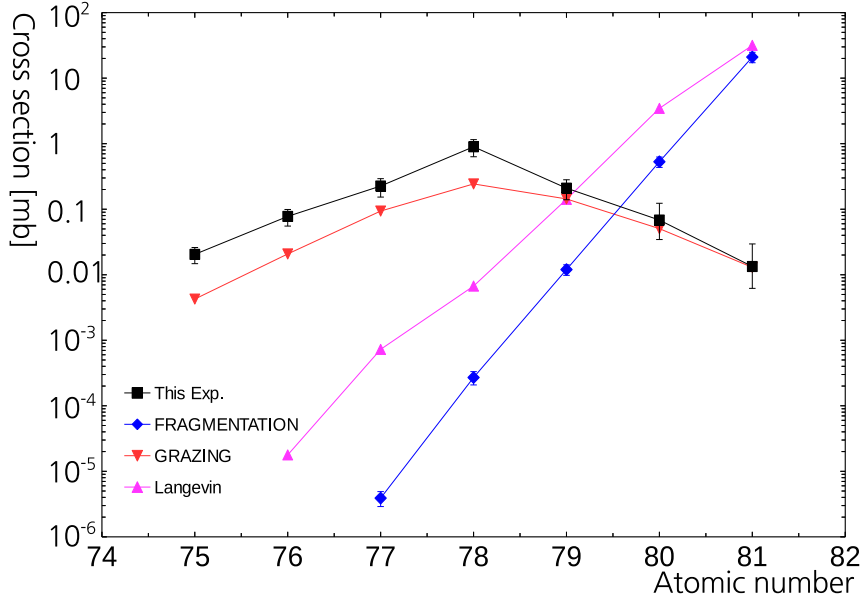


Figure 5.51 The cross section of  $N=126$  isotones of  $Z=75$  to  $81$  channels. (black square) This experiment, (blue diamond) Fragmentation experimental result [42], (red inverse triangle) GRAZING code calculation ( $^{136}\text{Xe}+^{198}\text{Pt}$ , 8 MeV/u), (magenta triangle) Langevin equation calculation [27] ( $^{136}\text{Xe}+^{208}\text{Pb}$ ,  $E_{CM}$  450 MeV).

The cross sections of  $N=126$  isotones compared with fragmentation experimental result [42] compared with GRAZING code calculation [20] ( $^{136}\text{Xe}+^{198}\text{Pt}$ , 8 MeV/u) and Langevin equation [27] ( $^{136}\text{Xe}+^{208}\text{Pb}$ ,  $E_{CM}$  450 MeV) is presented below. The experiment result reaction results shows exponential decrease in the cross section as the number of transferred protons increases. The cross section was symmetric within few factor larger in proton pickup channels relative to proton stripping channels. The n-rich side was consisted by the low excitation energy part of the reaction which neutron evaporation were suppressed. And the direct reaction dominates,

## 5.7. TLF CROSS SECTION AND FEASIBILITY OF N-RICH NUCLIDES

this could be confirmed by exponential decrease of cross section.

The fragmentation result also presented exponential decrease. The MNT reaction from this experiment presents much more gentle slope than the fragmentation. This makes cross section  $\sim 10^3$  times enhancement (from fragmentation) in  $^{204}\text{Pt}$ , and  $\sim 10^5$  in  $^{203}\text{Ir}$  case. And it is expected this enhancement will be increased in  $^{202}\text{Os}$ , 200W and so on.

The GRAZING code calculation [20] presents cross sections similar to the experimental data within few factors in proton stripping channels, while in proton pickup channels agrees within several factors. This coincides the discussion in previous sections 5.5.5.

The Langevin equation calculation [27] calculation shows also enhancement of cross section in MNT over fragmentation. This doesn't explain the result from this experiment, since the Langevin equation calculation expects optimum condition for producing neutron rich nuclei is energy close to the Coulomb barrier. (although there is no calculation result that coincide with this experiment.)

### 5.7.5 The kinematics of the TLF

The kinematic of TLF was estimated in order to provide information to the new facilities for better collection efficiency. The raw distribution was distorted (zig-saw shaped distribution) due to "integerization" of mass. (See figure 5.52, and 5.53) The real distribution should be smoothed from the statistical nature of evaporation process. But current method could not include statistical factor in the iteration, because the convergence cannot be reached.

The peak position of the distribution was estimated using fitting the distribution

## 5.7. TLF CROSS SECTION AND FEASIBILITY OF N-RICH NUCLIDES

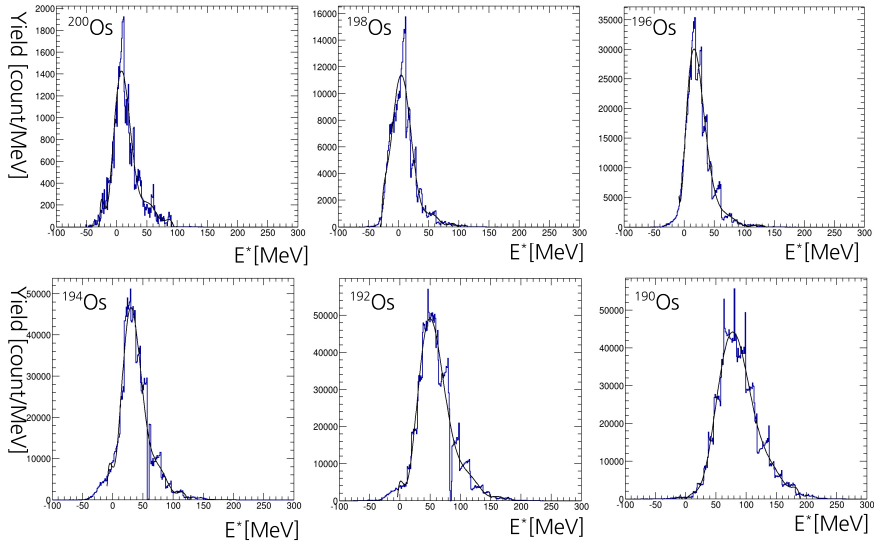


Figure 5.52 The excitation energy distributions of Os isotopes with (black solid line) ninth order polynomial fit of (top left)  $^{200}\text{Os}$ , (top middle)  $^{198}\text{Os}$ , (top right)  $^{196}\text{Os}$ , (bottom left)  $^{194}\text{Os}$ , (bottom middle)  $^{192}\text{Os}$ , (bottom right)  $^{190}\text{Os}$ .

## 5.7. TLF CROSS SECTION AND FEASIBILITY OF N-RICH NUCLIDES

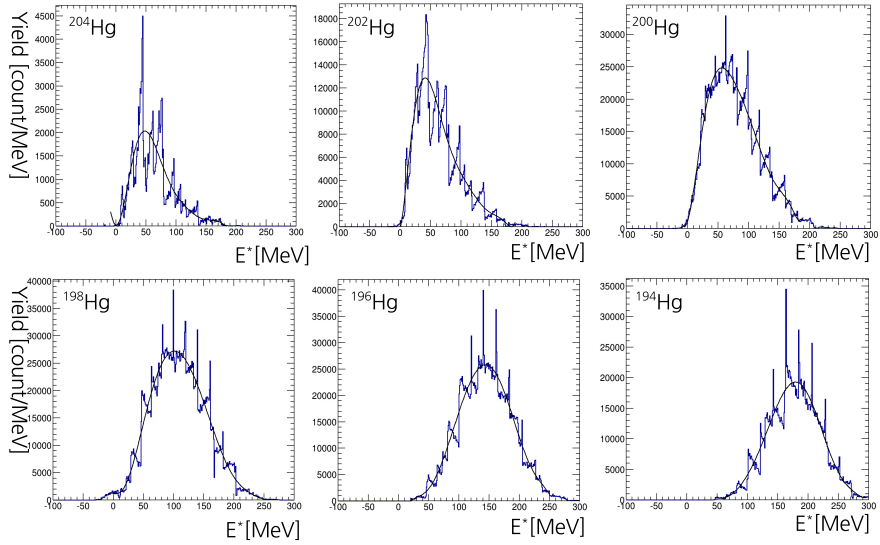


Figure 5.53 The excitation energy distributions of Os isotopes with (black solid line) ninth order polynomial fit of (top left)  $^{204}\text{Hg}$ , (top middle)  $^{202}\text{Hg}$ , (top right)  $^{200}\text{Hg}$ , (bottom left)  $^{198}\text{Hg}$ , (bottom middle)  $^{196}\text{Hg}$ , (bottom right)  $^{194}\text{Hg}$ .

### *5.7. TLF CROSS SECTION AND FEASIBILITY OF N-RICH NUCLIDES*

with 9th order polynomial function. The function was selected only since polynomial function empirically reproduces the distribution. And the angular distribution peak position was estimated using Gaussian function. The peak position of TLF nuclides in the Wilczynski plot was estimated. (See figure 5.54)

In proton stripping channels the angular distribution moved to forward as the number of proton picked up increased. On the other hand, proton pickup channels were opposite, which was the same as the result from PLF side. The excitation energy number of transferred neutrons were different from PLF side. The proton stripping channels for same number of transferred neutrons, excitation energy increased as the number of transferred proton increased. But in proton pickup channels it was opposite. This was opposite to the intuitive picture which number of transferred protons (or neutrons) increase excitation energy increases. This would be owing to the tendency of fast neutron pickup (from TLF to PLF) towards N/Z equilibrium in the proton pickup side and the interplay of neutron evaporation. Since first, as the number of transferred proton was picked up, larger number of neutrons were also picked up, this would drive TLF to more neutron deficient side. Than the shared excitation energy was lower than the channel with smaller number of protons picked up (vice versa for the neutrons). Second, the TLF has large portion of the total excitation energy it is more vulnerable to the neutron evaporation. These results the lower excitation energy as number of transferred proton increased with same number of transferred neutrons.

In channels other than Pt the neutron-rich channels showed low excitation energy close to 0 with angular distribution transition from forward to backward angle with respect to the main part of the reaction products as the number of neutron decreased.

## 5.7. TLF CROSS SECTION AND FEASIBILITY OF N-RICH NUCLIDES

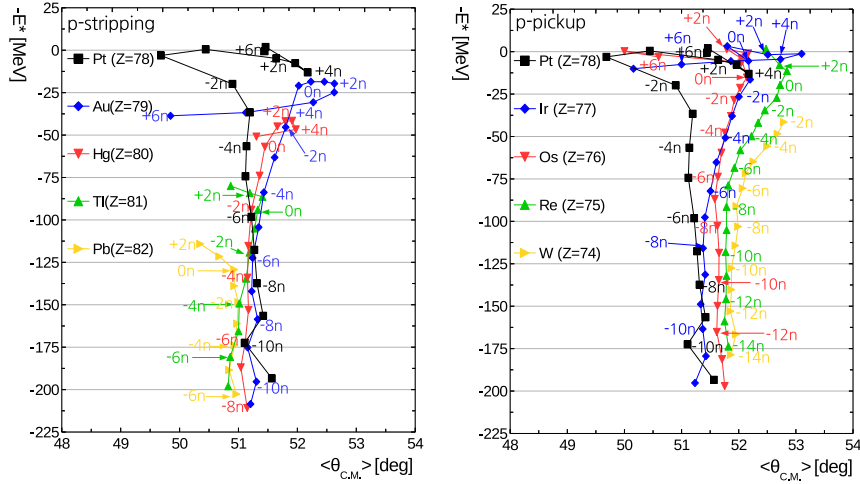


Figure 5.54 Mean excitation energy correlated with mean angular distribution of TLF nuclides (left) in proton stripping channels of (black square) Pt (0p), (blue diamond) Au (-1p), (red inverse triangle) Hg (-2p), (green triangle) Tl (-3p), and (yellow rotated triangle) Pb (-4p). (right) The same graph as the left figure with proton stripping channels of (black square) Pt (0p), (blue diamond) Ir (+1p), (red inverse triangle) Os (+2p), (green triangle) Re (+3p), and (yellow rotated triangle) W (+4p). The lines are drawn to guide eyes. The channels with even number neutron transferred are indicated with same color of the graph.

### *5.7. TLF CROSS SECTION AND FEASIBILITY OF N-RICH NUCLIDES*

This transition of angular distribution is the indication that the impact parameter dependence of the number of neutron transfer.

# Chapter 6

## Conclusions

The multi-nucleon transfer reaction between  $^{136}\text{Xe} + ^{198}\text{Pt}$  above 55% of Coulomb barrier was successfully carried out. The experiment was conducted in the interest of first, to test the feasibility of producing neutron rich target like fragments (TLF) with MNT reaction vicinity of neutron magic number 126. Second, investigate the reaction mechanism between heavy neutron rich beam, and target system with similar N/Z ratio concerning proton and neutron transfer. The experiment is distinguishable from previous experiments (concerning reaction between heavy ions close to this experiment) by event-by-event full identification of PLF and TLF with large acceptance. This was possible by using combination of wide acceptance spectrometer VAMOS and clover Ge-detector array EXOGAM.

The calibration of detectors in VAMOS (multi-wire PPACs near target, and focal plane , drift chamber, ionization chamber, Si detector wall) and EXOGAM detectors were successfully carried out. The complete particle identification of the PLF were

conducted successfully with good resolution of  $\frac{\Delta Z}{Z} = \frac{1}{60}$ ,  $\frac{\Delta M}{M} = \frac{1}{203}$ .

The detection efficiency of VAMOS spectrometer was investigated, the new technique was developed based on simulation and the empirical theory of charge state distribution. The detection efficiency was confirmed by first, comparison with Rutherford scattering at the forward angles. Second, the comparison between angular distribution of elastic scattering of this experiment and tandem experiment. Third consistent result from total reaction cross section between measured value and optical potential fitting result also previous experimental result with similar to this experiment.

The projectile like fragment (PLF) cross section was measured. The enhancements of proton pickup channels respect to the proton stripping channels were observed. This result was unexpected from prediction of GRAZING calculation.

The large effect from neutron evaporation in the PLF was corrected using newly developed iteration method. The pre-fragment right after reaction was determined event-by-event with full kinematics. The cross section reviled large effect from N/Z equilibrium which was not expected in both GRAZING and TDHF calculation. The TDHF calculation showed good agreement in the cross section in both proton pickup and stripping side within few factors of magnitude. And GRAZING calculation exhibited good agreement in the proton stripping channels after matching the experimental result to the calculation limit.

The reaction mechanism evolution of atomic number and mass distribution was studied as function of excitation energy using moment study. The mean position of the mass (after evaporation correction) and atomic number was constant over all region of excitation. This is due to the similar N/Z equilibrium of the projectile and

target. On the other hand, for fixed number of protons, the mass distribution changed from pure proton transfer channel in the low excitation energy and converged to the N/Z equilibrium mass at excitation energy at  $150 \sim 200$  [MeV].

The width of the atomic, neutron, and mass number distribution presented exponential increase to the excitation energy increase. The ratio between neutron and proton number width showed low excitation energy showed proton-rich flow in the low excitation energy owing to the neutron shell closure  $N = 82$  of projectile. The negative correlation coefficient in low excitation energy more favorable result to the microscopic models such as TDHF and GRAZING instead of the macroscopic models.

This experimental result confirmed for the first time that the MNT reaction between  $^{136}\text{Xe} + ^{198}\text{Pt}$  system could be used as effective tool to reach neutron rich nuclei  $N \sim 126$ . The targeted  $N = 126$  neutron rich TLF from proton pickup and neutron stripping reaction channel presented cross section result several orders of magnitude higher than the fragmentation reaction. And the cross section was enhanced by several factor relative to the GRAZING code calculation. The TLF cross section was determined accounting pre-fragment cross section result with neutron and charged particle evaporation. And the PID in TLF was confirmed by  $\gamma$ -ray spectroscopy.

In order to confirm TLF cross section more extensively, the experiment with more count rate or Ge detector array with better efficiency such as AGATA, or GRETINA (GRETA in near future). Since the  $\gamma$ -ray was not detected due to the low statistics and the high multiplicity  $\gamma$ -ray property of MNT reaction caused low detection efficiency.

Futher study is nessary to investigate the optimum condition of MNT reaction to produce  $N = 126$  nuclei. Such as system energy dependence and beam target combination.

This promising result will enable new facility which utilize the MNT reaction to reach n-rich nuclides around  $N = 126$ . Such as KEK Isotope Separation System (KISS) in RIKEN which is currently operational [14], and isotope factory CARIBU in Argonne national laboratory [124]. The same reaction between  $^{136}\text{Xe} + ^{198}\text{Pt}$  are the highest candidate which will be used in these facilities. Also encourage theoretical predictions with better prediction power of MNT reaction between heavy ions with similar N/Z ratio.

## Bibliography

- [1] R. Bass, Nuclear Reactions with Heavy Ions, Springer-Verlag, Berlin Heidelberg Newyork, 1980
- [2] W. von Oertzen, Cold Multinuclear Transfer and Synthesis of New Elements, Hahn-Meitner-Institut, Berlin, 1998
- [3] W. U. Schröder, J. R. Huizenga, and D. Allan Bromley, Treatise on Heavy-Ion Science Vol2:Damped Nuclear Reactions, Springer-Verlag, Berlin Heidelberg Newyork, 1985
- [4] A. Gobbi and W. Noënberg, Heavy Ion Collisions Vol2, ed R. Bock, North-Holland, Amsterdam, 1980, p.127
- [5] K. S. Krane, Introductory Nuclear Physics, John Wiley & Sons, Inc., Hoboken, 1988, p68
- [6] J. M. Blatt and V. F. Weisskopf, Theoretical nuclear physics, John Wiley & Sons, New York, 1952 p367
- [7] E. M. Burbidge, G. R. Burbidge, W. A. Fowler, and F. Hoyle, Rev. Mod. Phys. **29**, 547-650 (1957)

## BIBLIOGRAPHY

- [8] R. Krucken,Contem. Phys. **52**, 101–120 (2011) Nucasto
- [9] L. Corradi, G. Pollarolo, and S. Szilner,J. Phys. G: Nucl. Part. Phys. **36**, 113101 (2009)
- [10] L. Corradi,Journal of Physics: Conference Series **282**, 012005 (2011)
- [11] W. Reisdorf,J. Phys. G: Nucl. Part. Phys. **20**, 1297 (1994)
- [12] K. E. Rehm,Annu. Rev. Nucl. Part. Sci. **41**, 429 (1991)
- [13] V. V. Volkov,Phys. Rep. **44**, 93—157 (1978)
- [14] S. C. Jeong *et al.*,KEK Report **2**, (2010)
- [15] H. Freiesleben, and J. V. Kratz, Phys. Rep. **106**, 1-120 (1984)
- [16] W. U. Schroder, and J. R. Huizenga, Ann. Rev. Nucl. Sci. **27**, 465-547 (1977)
- [17] H. A. Bethe,Rev. Mod. Phys. **9**, 69 (1939)
- [18] J. R. Huizenga, and L. C. Moretto,Annu. Rev. Nucl. Sci. **22**, 427-464 (1972)
- [19] J. P. Bondorf *et al.*,J. de Phys **32**, C6-145 (1971)
- [20] A. Winther, program GRAZING, <http://www.to.infn.it/~nanni/grazing> (unpublished) A. Winther,Nucl. Phys. A **572**, 191-235 (1994)  
A. Winther,Nucl. Phys. A **594**, 203-245 (1995)
- [21] C. H. Dasso, G. Pollarolo, and A. Winther, Phys. Rev. Lett. **73**, 1907-1910 (1994)
- [22] W. von Oertzen,Z. Phys. A **342**, 177-182 (1992)

## BIBLIOGRAPHY

- [23] R. Yanez , and W. Loveland, Phys. Rev. C **91**, 044608 (2015)
- [24] J. Wilczynski,Phys. Lett. **47B**, 484 (1978)
- [25] R. Beck, and D. H. E. Gross,Phys. Lett. **47B**, 143 (1978)
- [26] V. Zagrebaev, and W. Greiner, Phys. Rev. Lett. **101**, 122701 (2008)
- [27] V. Zagrebaev, and W. Greiner, Nucl. Phys. A **834**, 366c-369c (2010)
- [28] V. Zagrebaev, and W. Greiner, J. Phys. G: Nucl. Part. Phys. **34**, 1-25 (2007)  
V. Zagrebaev, and W. Greiner, Lecture Notes in Physics 818, Clusters in 1st Ed. C. Beck, 267, Springer, Heidelberg, 2010.
- [29] J. Wilczynski,Phys. Lett. **47B**, 484 (1973)
- [30] R. Beck, and D. H. E. Gross,Phys. Lett. **47B**, 143 (1973)
- [31] C. Simenel,Eur. Phys. J. A **48**, 152 (2012)
- [32] C. Simenel,Phys. Rev. Lett. **105**, 192701 (2010)
- [33] K. Sekizawa,Phys. Rev. C **88**, 014614 (2013)
- [34] Y. Iwata *et al.*,Phys. Rev. Lett. **104**, 252501 (2010)
- [35] K. Sekizawa, private communication.
- [36] P. Bonche, H. Flocard, and P. Heenen,Nucl. Phys. A **467**, 115 (1987)
- [37] H. FeldmeierRep. Prog. Phys. **50**, 915-994 (1987)
- [38] F. Beck, M. Dworzecka, and H. Feldmeier Z. Physik A **289**, 113-119 (1978)

## BIBLIOGRAPHY

- [39] W. U. Schroder *et al.*, Proceedings of the International Symposium on 1 clear Fission and Heavy-Ion-Induced Reactions, Rochester, New York, 1986 (Harwood Academic, New York, 1987), p. 255.
- [40] D. Montanari, Ph. D thesis of Universita Degli Studi Di Milano (2009)
- [41] J. J. Valiente-Dobón, Ph. D thesis of University of Surrey (2007)
- [42] T. Kurtukian-Nieto, Phys. Rev. C **89**, 024616 (2014)
- [43] J. Steer *et al.*, Phys. Rev. C **84**, 044313 (2011)
- [44] D. A. Mayorov *et al.*, Phys. Rev. C **90**, 024602 (2014)
- [45] A. G. Arutkh *et al.*, Nucl. Phys. A **176**, 284 (1971)
- [46] R. Kirchner *et al.*, Nucl. Phys. A **378**, 549 (1982)
- [47] P. H. Regan *et al.*, Laser Phys. Lett. **1**, No. 6 (317) 2004
- [48] J. S. Barrett *et al.*, Phys. Rev. C **91**, 064615 (2015)
- [49] E. M. Kozulin *et al.*, Phys. Rev. C **86**, 044611 (2012)
- [50] J. Speer *et al.*, Phys. Lett. B **259**, 422 (1991)
- [51] L. Corradi *et al.*, Phys. Rev. C **59**, 261 (1999)
- [52] L. Corradi *et al.*, Phys. Rev. C **66**, 024606 (2002)
- [53] L. Corradi *et al.*, Phys. Rev. C **63**, 021601 (2001)
- [54] S. Szilner *et al.*, Phys. Rev. C **76**, 024604 (2007)

## BIBLIOGRAPHY

- [55] W. U. Schröder *et al.*, Phys. Rev. Lett. **36**, 514-517 (1976)
- [56] W. U. Schröder *et al.*, Phys. Rev. C **16**, 623-628 (1977)
- [57] W. U. Schröder *et al.*, Phys. Rep. **45**, 301-343 (1978)
- [58] W. W. Wilcke *et al.*, Phys. Rev. C **22**, 128-147 (1980)
- [59] H. J. Wollersheim *et al.*, Phys. Rev. C **24**, 2114-2126 (1981)
- [60] H. J. Wollersheim *et al.*, Phys. Rev. C **25**, 338-349 (1982)
- [61] R. Vandenbosch *et al.*, Nucl. Phys. A **269**, 210-222 (1976)
- [62] R. J. Otto *et al.*, Phys. Rev. Lett. **36**, 135-138 (1976)
- [63] K. D. Hindenbrand *et al.*, Nucl. Phys. A **405**, 179 (1983)
- [64] E. C. Wu *et al.*, Phys. Rev. Lett. **47**, 1874 (1981)
- [65] J. Wilczynski *et al.*, Phys. Lett. B **47**, 484 (1973)
- [66] T. Tanabe *et al.*, Nucl. Phys. A **342**, 194-212 (1980)
- [67] V. V. Volkov *et al.*, Nucl. Phys. A **126**, 1 (1969)
- [68] J. V. Kratz *et al.*, Nucl. Phys. A **332**, 477-500 (1979)
- [69] R. Planeta *et al.*, Phys. Rev. C **38**, 195-209 (1988)
- [70] D. R. Benton *et al.*, Phys. Lett. B **185**, 326 (1987) T. C. Awes *et al.*, Phys. Rev. Lett. **52**, 251 (1984) S. Sohlbach *et al.*, Phys. Lett. B **153**, 386 (1985) Y. Eyal, G. Rudolf I. Rode and H. Stelzer, Phys. Rev. Lett. **42** (1979) 826.

## BIBLIOGRAPHY

- [71] W. Królas *et al.*, Nucl. Phys. A **724**, 289-312 (2003)
- [72] E. C. Wu *et al.*, Phys. Rev. Lett. **47**, 1874 (1981)
- [73] H. Breuer *et al.*, Phys. Rev. C **28**, 1080 (1983)
- [74] D. Schiill *et al.*, GSI-Annual-Report , 18 (1980) D. Schiill *et al.*, Phys. Lett. B **102**, 116 (1981)
- [75] D. J. Morrissey, W. Loveland, R. J. Otto, and G. T. Seaborg, Phys. Lett. 74B:35 (1978).
- [76] K. E. Rehmet *et al.*, Phys. Rev. C **37**, 2629 (1988)
- [77] J. R. Birkelund *et al.*, Phys. Rev. C **13**, 133 (1976)
- [78] J. Speer *et al.*, Phys. Lett. B **259**, 422-426 (1991)
- [79] R. Kiinkel *et al.*, Z. Phys. A **336**, 71-89 (1990)
- [80] L. Corradi *et al.*, Phys. Rev. C **84**, 034603 (2011)
- [81] Y. X. Watanabe *et al.*, KEK Reports **12**, 12 (12)
- [82] D. Hilscher *et al.*, Phys. Rev. C **20**, 576 (1979) Y. Eyal *et al.*, Phys. Rev. Lett. **41**, 625 (1978) B. Tamain *et al.*, Nucl. Phys. A **330**, 253 (1979)
- [83] M. Rejmund *et al.*, Nucl. Instr. Meth. A **646**, 184 (2011)
- [84] S. Pullanhiotan *et al.*, Nucl. Instr. Meth. A **593**, 343 (2008)
- [85] S. Pullanhiotan *et al.*, Nucl. Instr. Meth. B **266**, 4148 (2008)

## BIBLIOGRAPHY

- [86] B. Raine, M. Tripone and B. Piquet, IEEE Transactions on Nucl. Sci. **41**, 55 (1994)
- [87] G. Wittwer *et al.*, Merging Several Data Acquisition Systems at GANIL, Proceedings of 14th. IEEE NPSS Real-Time. Conference, Stockholm, Sweden, 4–10 Juin 2005, <http://wiki.ganil.fr> G. Wittwer, CENTRUM User's Manual, <http://wiki.ganil.fr>
- [88] Groupe Acquisition pour la Physique, TRIGGER VXI-C GMT User's Manual, <http://wiki.ganil.fr>
- [89] V. F. Pucknell, MIDAS software, Daresbury Laboratory.
- [90] VAMOS homepage, <http://pro.ganil-spiral2.eu/laboratory/experimental-areas/g1-vamos>
- [91] GANIL homepage, <http://pro.ganil-spiral2.eu/users-guide/accelerators/available-stable-ion-beams-at-ganil>
- [92] H. Blok *et al.*, Nucl. Instr. and Meth. A **262**, 291 (1987) M. Berz *et al.*, Phys. Rev. C **47**, 537 (1993).
- [93] F. Meót, Nucl. Instr. Meth. A **427**, 353 (1999)
- [94] TOSCA Static Field Analysis OPERA-3D, Vector Fields, 24, Bankside Kidlington, Oxford, England.
- [95] GARFIELD homepage, <http://garfield.web.cern.ch/garfield/>
- [96] J. Simpson *et al.*, Heavy Ion Phys. **11**, 159 (2000)

## BIBLIOGRAPHY

- [97] EXOGAM homepage, <http://pro.ganil-spiral2.eu/> laboratory/ detectors/ exogam/
- [98] S. Beghini *et al.*, Nucl. Phys. A **551**, 364 (2005)
- [99] A. Cunsolo *et al.*, Nucl. Phys. A **484**, 56 (2002)
- [100] H. D. Betz, Rev. Mod. Phys. **44**, 465-539 (1972)
- [101] K. Shima, Nucl. Instr. Meth. B **10**, 45-48 (1985)
- [102] K. Shima, T. Ishihara ,and T. Mikumo, Nucl. Instr. Meth. **200**, 605-608 (1982)
- [103] G. Schiwietz, and P. L. Grande, Nucl. Instr. Meth. B **175-177**, 125-131 (2001)
- [104] E. Baron, M. Bajard, and Ch. Ricaud, Nucl. Instr. Meth. A **328**, 177-182 (1993)
- [105] I. S. Dmitriev, and V. S. Nikolaev, Soviet. Phys. JETP **20**, 409-415 (1965)
- [106] M. H. Macfarlane, S. C. Pieper, computer code PTOLEMY: a program for heavy-ion direct-reaction calculations, Argonne National Laboratory Report ANL-76-11-rev-1, 1978
- [107] J. Randrup , W. J. Swiatecki and C. F. Tsang, Lawrence Berkeley Laboratory Report LBL **3603**, 1974 (u)npublished C. Ngo ^ *et al.*, Nucl. Phys. A **252**, 237 (1975)
- [108] V.E. Viola, Jr. Nucl. Data A **1**, 391 (1966) V.E. Viola, K. Kwiatkowski, and M. Walker, Phys. Rev. C **31**, 1550 (1985)
- [109] C. R. Gould *et al.*, Z. Phys. A **284**, 353-354 (1978)

## BIBLIOGRAPHY

- [110] G. A. Petitt *et al.*, Phys. Rev. C **40**, 602-705 (1989)
- [111] P. Russo *et al.*, Phys. Lett. **28**, 155-157 (1977)
- [112] H. Machner *et al.*, Phys. Rev. C **33**, 91 (1986)
- [113] A.Gavron, Phys. Rev. C **21**, 230-236 (1980) O.B.Tarasov, and D.Bazin, Nucl. Instr. Meth. B **204**, 174-178 (2003)
- [114] A.R. Barnett and J.S. Lilley, Phys. Rev C **9**, 2010 (1974) J.D. Stichler and K.J. Hofstetter, Phys. Rev C **9**, 3 (1974) A.A. Hassan et al., Preprint JINR, Dubna **P15-2004-122**, 2004 (.)
- [115] V. V. Parkar *et al.*, Proc. Radiochim. Acta **1**, 131–134 (2011)
- [116] H. Breuer *et al.*, Nucl. Instr. Meth **204**, 419 (1983)
- [117] J. F. Ziegler, J. P. Biersack, and M. D. Ziegler, SRIM - The Stopping and Range of Ions in Solids, Lulu Press Co., Morrisville, 1985
- [118] A. M. Baldin, V. I. Goldanskii, and I. L. Rozental, Kinematics of Nuclear Reactions, Oxford University Press, London, 1961
- [119] Y. X. Watanabe *et al.*, Nucl. Instr. Meth. B **317**, 752-755 (2013)
- [120] Y. H. Kim *et al.*, EPJ Web of Conferences **66**, 03044 (2014)
- [121] Y. X. Watanabe and S. C. Jeong, experiment proposal Production of Heavy Neutron-Rich Nuclei by Multinucleon Transfer Reactions of  $^{136}\text{Xe} + ^{198}\text{Pt}$ , 2010
- [122] H. S. Jung, private communication.

## BIBLIOGRAPHY

- [123] P. R. John *et al.*, Phys. Rev. C **90**, 021301 (2014) G. Savard, Nucl. Instr. Meth. B **266**, 4086–4091 (2008)
- [124] G. Savard, ATLAS Users Metting, Argonne National Lab. **May**, 15-16 (2014)
- [125] A. A. Sonzogni,Nuclear Data Sheets **95**, 837 (2002)
- [126] R. Krucken,Contemporary Physics **52**, 101–120 (2011)

## 국문 초록

핵도표에서 안정된 핵종들이 이루는 골짜기에서 멀리 떨어져있는 질량 번호 200 근처의 중성자 과잉 핵자는, 철에서 우라늄까지의 무거운 원소 생성 과정중 하나인 r-process (빠른 중성자 포획 과정)의 마지막 병목 지점을 이룬다. 하지만 이 핵자들을 기준의 방법들로 생성하는 것이 어려워서, 중요함에 비해서 특성이 (예를 들어 반감기, 질량 등등) 알려진 핵종들은 안정된 핵종 근처에 한정되어 있었다. 최근 다중 핵 전달 반응은 이 질량 번호 200 근처의 중성자 과잉 핵자를 생성할 수 있는 반응의 후보로 많은 관심을 끌게 되었다. 특히, 무겁고 중성자가 많은 핵종사이의 예를 들어서  $^{136}\text{Xe}$  빔과  $^{208}\text{Pb}$  또는  $^{198}\text{Pt}$  표적 사이의 반응에서 생성된 표적과 비슷한 핵종들의(target-like fragments) 중성자 과잉 핵자의 산란 단면적이 클 것으로 기대되고 있다[9, 14, 26]. 하지만 이와 같은 무거운 핵사이의 다중 핵 전달 반응은 잘 알려지지 않은 점이 많았다.

이 실험은  $8\text{MeV/u}$   $^{136}\text{Xe} + ^{198}\text{Pt}$  표적을 사용했다 ( $\sim 55\%$  쿨롬 장벽 위의 에너지). 실험은 큰 acceptance를 가지는 VAMOS++와 EXOGAM 계르마늄 검출기 배열을 가지고 측정하였다. 실험의 목적은 첫 번째, 무거운 핵사이의 다중 핵 전달 반응이 질량 번호 200 근처의 중성자 과잉 핵자를 생성할 수 있는지 확인 해 보는 것이다. 두 번째, 무거운 핵사이의 다중 핵 전달 반응이 어떻게 진행되는지 그 특성을 알아보는 것이다.

실험에서 측정한 빔과 비슷한 핵자(projectile-like fragments)의 식별은 각각의 이벤트 별로 성공적으로 이루어 졌다 [119]. 빔과 비슷한 핵종과(projectile-like fragments)

## BIBLIOGRAPHY

산란 단면적과 표적과 비슷한 핵종의 산란 단면적을 빔과 비슷한 핵종의 측정 결과로 계산하였다. 심함의 산란 단면적은 GRAZING 이론 계산과 TDHF(time dependent Hartree Fork)계산과 비교 하였다. 핵자의 전달과 관련된 핵반응의 특성이 질량 번호와 원소번호의 분포의 모멘트 분석 (예를 들어 평균, 표준 편차, 상관관계 계수 등등)으로 분석되었다.

이 실험을 통해 처음으로  $^{136}\text{Xe}$  빔과  $^{198}\text{Pt}$  표적 사이의 다중 핵 전달 반응이 중성자 마법수 126의 중성자 과잉 핵종을 만들 수 있다는 것을 확인 하였다. 또한 이 중성자 과잉 핵종들이 N/Z-평형(N/Z-equilibrium)에 이르기 전의 낮은 내부 에너지를 가지는 반응에 의해서 생성 된다는 것을 확인 하였다. 이 연구는 천문학뿐만 아니라 핵물리학적으로 중요한 새로운 핵종들의 영역을 연구하는 가능성을 제시했다. 그리고 다중 핵 전달 반응을 이용해 새로운 핵종 빔을 만들려고 하고 있는 시설들에 도움이 될 것이다. **주요어:** 다중 핵 전달 반응, 중이온 사이의 핵반응, 핵 반응 특성,r-process, 중성자 마법수  $N = 126$ ,  $^{136}\text{Xe}$ ,  $^{198}\text{Pt}$ , 산란 단면적, N/Z equilibrium